THE ^{8}LI CALIBRATION SOURCE AND THROUGH-GOING MUON ANALYSIS IN THE SUDBURY NEUTRINO OBSERVATORY

A Thesis

Presented to

The Faculty of Graduate Studies

of

The University of Guelph

by

NATHANIEL TAGG

In partial fulfilment of requirements

for the degree of

Doctor of Philosophy

January, 2001

ABSTRACT

The ^{8}Li Calibration Source and Through-Going Muon Analysis in the Sudbury Neutrino Observatory

Nathaniel Tagg
University of Guelph, 2001

Advisor:
Professor J. J. Simpson

This thesis deals with two topics of relevance to the Sudbury Neutrino Observatory (SNO).

The first part describes the concept, design, testing, deployment, and preliminary data analysis of a ^{8}Li source deployed in the SNO detector. This source is a short-lifetime beta-emitting radioactive source is used to measure the detector position resolution, and the efficiency (i.e. sacrifice) of solar neutrino analysis data reduction schemes. The utility of this source to perform energy calibrations assisting in measurement of ^{8}B neutrino energy spectral distortions is also discussed.

The second part is an analysis of through-going muons in SNO. An algorithm for reconstruction muon tracks was implemented and tested using a Monte Carlo program, then applied to 149 days of SNO data. The distribution of muon directions was analyzed in two contexts: down-going muons from atmospheric cosmic rays, and atmospheric neutrino-induced muons.

Atmospheric muons are analyzed to obtain a value for the power index of the

primary all-nucleon spectrum of $\gamma = 2.80 \pm 0.04(stat) \pm 0.08(sys)$. A limit on prompt muon flux cannot be made without assumptions, but a limit of $R_c < 5.0 \times 10^{-3}$ can be set if γ is constrained to be less than 2.9.

Neutrino-induced muon data is given a preliminary analysis which is inconclusive due to limited statistics, but indicative that SNO will be able to produce a model-independent measurement of the absolute high-energy neutrino flux by looking at the component of neutrino-induced muons coming from zenith angles above the horizon. Early data exclude oscillations with $\Delta m^2 > 0.1\mathrm{eV}^2$ at $\sin^2 2\theta_V = 1$.

Acknowledgements

There are many people who deserve credit for helping me with this thesis.

Foremost among these are my committee members, who managed to push through my thesis defense process in a whirlwind. John Simpson, my advisor, gave me the freedom and the resources to get the research done. In particular he freed me from teaching duties, which sped my work enormously and for which I am grateful. Chris Waltham was a constant encouragement in the muon studies. Jimmy Law dealt with my incessant computing requests. Gabriel Karl and Ian MacKenzie provided valuable advice at various stages of work.

The ^{8}Li work simply would not have been possible without the hard work of Andre Hamer, who did many thankless tasks to help move ^{8}Li from a good idea to a working system. I also need to thank Baskar Sur for getting me into the whole ^{8}Li mess, Rich Helmer for moral support during our darkest hours, and a whole lot of people from the Queens University group who put in many hours of nuts-and-bolts work in the deployment of the source.

In fact, I want to thank everyone in the SNO collaboration for making a fun and engrossing experiment to work on. Anyone and everyone who answered my incessant, nagging, often stupid questions about things SNO-related has my gratitude.

Guelph is a great place to work and to live. This is in part due to the faculty (Bernie Nickel in particular helped me with many tricky mathematical difficulties) and also the staff. Thanks to Reggi Vallillee, Carol Croft, Brenda McLeod, and Bonnie Snider for helping me with all things administrative, clerical, and financial. The shops were of enormous help, due to the patient help of Bill Morton, Tom Riddols, Case Gielen and the rest.

My friends helped get me through it all. My good friend Al Richardson is to be commended for not killing his roommate. Christian Gigault gave me his LaTeX scripts, denying me many hours of foolish messing with files.

My parents have supported me emotionally and in other ways throughout my long education. Mom, I finally got me a good education - I don't need to work down the mine no more.

Bonnie Ward gives me the reasons to believe in life after thesis; I look forward to living it with her.

Contents

List of figures

List of tables

1

Introduction: The Sudbury Neutrino Observatory

This thesis consists of two parts, both of which are concerned with aspects of the Sudbury Neutrino Observatory (SNO). The first part details the development of the ^{8}Li calibration source designed to assist in the measurements of solar neutrinos. The second part deals with analysis of through-going muons observed in the SNO detector. These two topics, although independent, have similarities in their ends and means. Both are attempts to assist in measurements of neutrino oscillations, and both employ the SNO detector as the instrument for the measurement.

The SNO detector is a 1 kiloton heavy water Cherenkov detector, located in the Creighton nickel mine in Sudbury, Ontario, Canada. This detector has been described in great detail elsewhere [1, 2, 3] so only a brief sketch of the experiment will be presented here.

SNO is located 2070 meters underground. The detector resides in a large, barrelshaped cavity, represented in Figure 1.1. This cavity is filled with ultrapure light water (H_2O). Suspended in the center is a $\sim$2 inch thick acrylic vessel (AV) containing approximately one kiloton of heavy water (D_2O). This vessel is surrounded by an array of approximately 9400 photomultiplier tubes (PMTs) facing inward, on a geodesic PMT support structure (PSUP). The PSUP is separated from both the AV and from the external walls by the H_2O, which acts to shield the inner detector from radiation in the rock walls and from the PSUP and PMT materials.

Charged particles are detected in the water by Cherenkov radiation, which is detected by the PMTs. For low-energy particles($\sim$10 MeV), the detected Cherenkov light is proportional to the path length of the particle in water, which is in turn roughly proportional to the energy. The simplest measure of Cherenkov light is NHIT, or number of coincident phototubes that are triggered in a time window of $\sim$400 ns. The basic energy response of the detector has been measured using a ^{16}N source [4], and is approximately 9 NHIT per MeV of kinetic energy. This is complicated by the optical complexity of the detector. Energy response of the detector varies with event position (because of the complex optics in the detector), and with event topology (because NHIT is not a good measure of light production if the light is concentrated on a small area of the PSUP).

The model of PMT used is the Hamamatsu model R1408, which has a nominal timing resolution of 1.6 ns, and stable gain characteristics. Each PMT is augmented

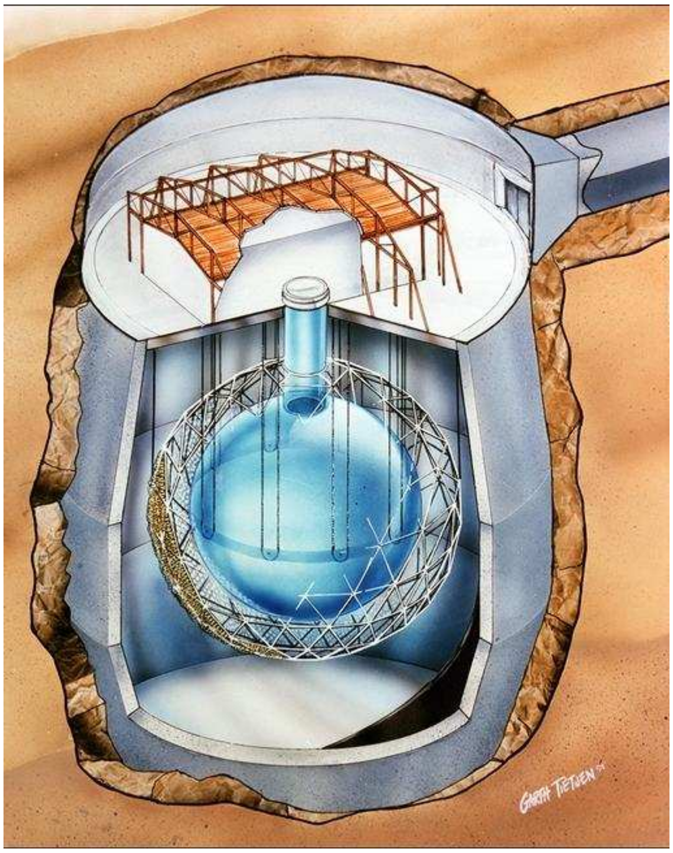

Figure 1.1: Sketch of SNO Detector. A 12 meter diameter acrylic vessel contains one kiloton of heavy water, and is surrounded by a 17 meter diameter geodesic array of photomultipliers. The rest of the cavity is full of light water. Above the detector is a the deck, which has space of for the front end electronics, and clean room from which calibration sources can be deployed.

by a concentrator 'bucket', which contains a set of nonlinear aluminum reflectors (i.e. Winston cones [5]). These reflectors increase the effective light collection area of each PMT by a factor of 2. The buckets also serve to limit the field of view of each PMT so that it is sensitive only to events in the inner 7 meters radius of the detector.

Besides the 9438 inward-looking PMTs, there also exist 91 outward looking (OWL) PMTs. These tubes have no concentrators, and look out towards the cavity walls. In addition, there are four tubes in the AV chimney and pipe boxes above the deck used to look for instrumental light (the 'neck' tubes), and there is a small array of tubes outside the PSUP used for testing that are dubbed the Berkeley Underwater Tube Test Sleds[1].

Each tube is connected by a single cable (carrying both high-voltage and signal) to a channel in the front-end electronics located on the deck above the water. Each channel has a fast discriminator used to generate an analog current pulse 100 ns long when the phototube generates a pulse above a trigger level of approximately 1/4 photoelectron. The analog sum of these current pulses is taken over all 10 000 channels to create the main detector trigger, which fires if more than 20 channels fire within the 100ns coincidence window. This, the "NHIT100" trigger, is the most important trigger method used in SNO, although other triggers are also employed. (See [6].) Once a trigger has been generated, the front end electronics receive a global

[1] Prurient acronym courtesy of Alan Poon.

trigger pulse, which is used to find the relative time of the PMT pulse to the trigger, and which signals the front-end cards to store the tube time and integrated anode charge for later read-out by the data acquisition system. Four values are recorded: the tube time relative to the global trigger, the anode charge integrated over a short time with high gain (QHS), the charge with the same gain over long time (QHL), and a low-gain integration (QLX). Any PMT triggers within 400 ns of the global trigger are accepted into a given event.

SNO was designed to look for solar neutrinos. The detection methods are described in Chapter 2. The ^{8}Li calibration source (a tagged beta source) was designed to assist in this search by performing several important calibrations. These are: ^{8}B shape analysis, event reconstruction characterization, and data cleaning sacrifice estimation. Each of these applications is discussed, but historically the source was first conceived (by Emanuel Bonvin) to perform energy shape discrimination, and this shaped the development of the source. Each of these motivations are directed at supporting SNO in looking for solutions to the solar neutrino problem (described in the next chapter)

In order to make high-precision measurements of the solar neutrino spectrum, and to do the important job of looking for neutral-current solar neutrino interactions, the detector was built with low intrinsic radioactive background by careful choice of materials and a high-quality water purification system. Equally important is to remove backgrounds associated with cosmic rays. The SNO detector, with a 6100 meter water equivalent overburden, is considerably deeper than most other detectors.[2] This large overburden allows for good measurements of high-energy atmospheric muons, as well as a unique measurement of the 'upward'-going muon flux (due to high energy atmospheric neutrinos) to zenith angles above the horizon. These measurements are described in Part II.

[2] Notable exceptions are the Kolar Gold Fields detector [7], which was located at approximately the same depth as SNO, and the CASE-WITS experiment [8], which was located at 8890 meters water equivalent.

Part I

The ^{8}Li Calibration Source

2

Introduction

This chapter deals with the basic physical questions that SNO is designed to answer, and the role that the ^{8}Li source has to play in finding these answers. In Chapter 3 the system of generating and delivering ^{8}Li isotope to SNO is described. Chapter 4 describes the decay chamber, the actual source container that is deployed in the D_2O to contain the isotope. This is followed by a description of empirical tests carried out on the decay chamber and the system as a whole to ensure that the source was sound, and to optimize the system for the most effective use of SNO live time. Chapter 6 discusses Monte Carlo predictions for using this source, in order to determine its utility once deployed. The actual data taken with the source is presented in Chapter 7. Finally, a comparative discussion is made about how to improve the source.

2.1 The Solar Neutrino Problems

SNO is built with the express purpose of looking for the solution to the Solar Neutrino Problem (SNP), with an emphasis on proving one of various neutrino oscillation solutions. [2]

The Solar Neutrino Problem can be briefly summed up by stating that the measured rate of interactions in neutrino detectors is much less than the number predicted. The predicted neutrino rate is calculated given a thorough knowledge of the sun and the nuclear processes involved in neutrino genesis. Solar neutrinos are generated by several processes in the p-p solar nuclear cycle, whose ultimate product is to burn protons into helium, and is the dominant energy-producing process in the sun. Solar physics and nuclear physics are believed to be well-enough advanced that the number of these neutrinos can be accurately calculated [9, 10], but experiments consistently show measured fluxes substantially smaller than the calculations.

Moreover, this loss appears to be *energy dependent*. This is shown in Figure 2.1, which summarizes the results from several neutrino experiments. Besides the obvious deficit of detected neutrinos, one can also see two other features. First, the number of neutrinos detected by the water-cherenkov detectors (Kamiokande[11], Super-Kamiokande[12], etc.) is larger than the number of neutrinos seen in the chlorine experiments [13]. Second, the gallium experiments [14, 15] show a measured flux just large enough to account for the precisely-calculated flux of pp solar neutrinos, but not the ^{7}Be neutrinos.

The dominant theory currently held to explain these data is one of neutrino oscillations. Simply put, the theory describes how electron-flavor neutrinos produced by

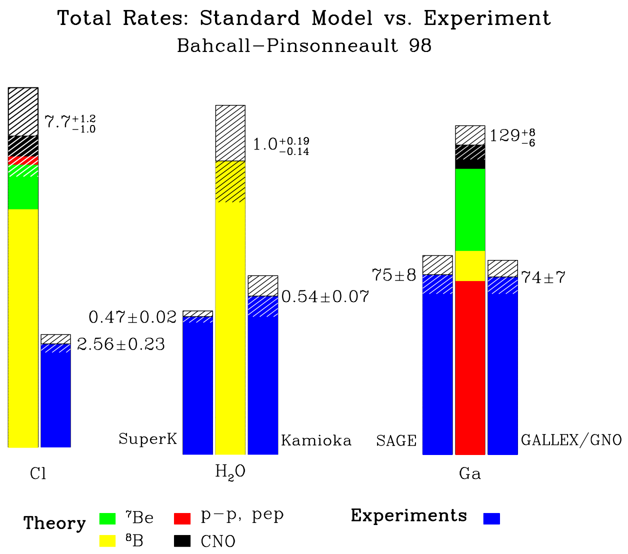

Figure 2.1: Solar Neutrino Theory Vs. Experiment. Taken from Bahcall [16]. The colored bars represent theoretical neutrino rates as determined by the standard solar model (SSM). The blue bars represent experimental results. Cross-hatching represents one sigma uncertainties.

the sun change into neutrinos of another flavor by a process known as flavor-mixing. If neutrinos are given non-zero masses, and furthermore the mass eigenstates are assigned to be different from the weak flavor eigenstates, a physical situation results in which one flavor may oscillate into another. The oscillations are due to phase-shifts caused by the different velocities of the different mass components. [1]

For a simplified case involving only two neutrino species, the probability of an electron neutrino being detected as such at time t (or distance L) from the source can be calculated. Two sets of eigenstates are defined: one for the masses and one for the flavors. These are constructed such that the mass eigenstates are rotated away from

[1] Many good descriptions of this theory exist elsewhere. For instance, a good pedagogical description can be found in [17].

the flavor eigenstates by mixing angle θ_V.

$$\begin{aligned} |\nu_e\rangle &= \cos\theta_V|m_1\rangle + \sin\theta_V|m_2\rangle \\ |\nu_\mu\rangle &= \sin\theta_V|m_1\rangle - \cos\theta_V|m_2\rangle \end{aligned} \tag{2.1}$$

An electron neutrino is generated at time t=0, and consists of an admixture of the two mass eigenstates. E_1 and E_2 are assigned to be the total energies of the mass 1 and mass 2 eigenstates respectively. Propagating these eigenstates through space with a vacuum Hamiltonian generates two different phases.

$$\begin{aligned} \langle\nu_e|\nu_e,t\rangle &= \langle\nu_e|e^{-iEt/\hbar}|\nu_e\rangle \\ &= \langle\nu_e|e^{-iE_1t/\hbar}\cos\theta_V|m_1\rangle + \langle\nu_e|e^{-iE_2t/\hbar}\sin\theta_V|m_2\rangle \\ &= e^{-iE_1t/\hbar}\cos^2\theta + e^{-iE_2t/\hbar}\sin^2\theta_V \\ &\vdots \\ |\langle\nu_e|\nu_e,t\rangle|^2 &= 1 - \sin^2 2\theta_V\ \sin^2(\tfrac{1}{2}(E_1 - E_2)t/\hbar) \end{aligned} \tag{2.2}$$

For the energy scale under consideration, $p \gg m_{1,2}$ so the parameter Δm^2 can be defined as in Equation 2.3.

$$\begin{aligned} E_1 - E_2 &= \sqrt{p^2c^2 + m_1^2c^4} - \sqrt{p^2c^2 + m_2^2c^4} \\ &\simeq \tfrac{m_2^2 - m_1^2}{2pc} \simeq \tfrac{\Delta m^2}{2E} \end{aligned} \tag{2.3}$$

Finally, equation 2.2 is rewritten to arrive at the probability that an electron neutrino will remain such at distance L from the source, since $v \sim c$.

$$|\langle \nu_e | \nu_e \rangle|^2 = 1 - \sin^2 2\theta_V \ \sin^2 \left(\frac{L \Delta m^2}{4E} \right) \tag{2.4}$$

This simple formulation shows the main features of the model. For each pair of neutrinos, a mass mixing angle and a mass-squared difference may be defined, which gives two independent free parameters to be determined experimentally. The L/E parameter defines a relationship between energy and distance, which leads naturally to spectral shape distortions when the source is at constant distance. It leads as well as a possible "smoking gun" of being able to see oscillatory behavior as an experimental baseline changes length or a beam changes energy. This is not simple to do in practice, however, and the oscillation theory remains unproven (although very appealing).

This theory has been substantially expanded by Wolfenstein [18] as well as Mikheyev and Smirnov [19], in which they proposed that these oscillations could become further enhanced when neutrinos travel through matter. Coherent scattering of electron neutrinos (ν_e) cannot occur for the other two flavors (ν_μ, ν_τ) which causes a 'drag' on the electron flavor neutrinos, changing the phase shift by changing the electron-flavor Hamiltonian. This addition to the theory allows for a much greater parameter space of θ_V and Δm^2 to be allowed as a solution to the SNP.

Using all of the experimental data available, various global fits have been made. [20, 21] Figure 2.2 shows the allowed regions of parameter space when this is done, using 2-neutrino flavor solutions. 3- and 4-neutrino flavor solutions [22, 23] require more complicated pictures of which flavors oscillate into which, but the basic features of these parameters spaces remain the same. (See, for example, Figures 6 and 7 in Giunti [24].) The possible solutions are known as the SMA (small mixing angle), LMA (large mixing angle), LOW (Low Δm^2), and the VAC (Vacuum oscillation) solutions.

2.2 SNO and Solar Neutrinos

SNO uses heavy water (D_2O) as the neutrino target, which gives a unique means to test the neutrino oscillation solutions. Solar neutrinos on D_2O result in one of three interaction modes:

(1) $\nu_x + \mathrm{e}^- \rightarrow \nu_\mathrm{x} + \mathrm{e}^-$ (elastic scattering)

(2) $\nu_e + \mathrm{d}^+ \rightarrow \mathrm{p}^+ + \mathrm{p}^+ + \mathrm{e}^-$ (charged current)

(3) $\nu_x + \mathrm{d}^+ \rightarrow \mathrm{p}^+ + \mathrm{n} + \nu_\mathrm{x}$ (neutral current)

The most direct test of neutrino oscillations comes from comparing the ratio of rates of interactions (2) and (3).[2] This neutral current to charged current ratio provides a direct test of the neutrino oscillation hypothesis. If the NC/CC ratio is unity, this would indicate that either neutrino oscillation does not occur, or that the

[2] Taking a ratio of these two quantities is a sensitive test, because it removes many sources of systematic error that crop up when finding absolute rates.

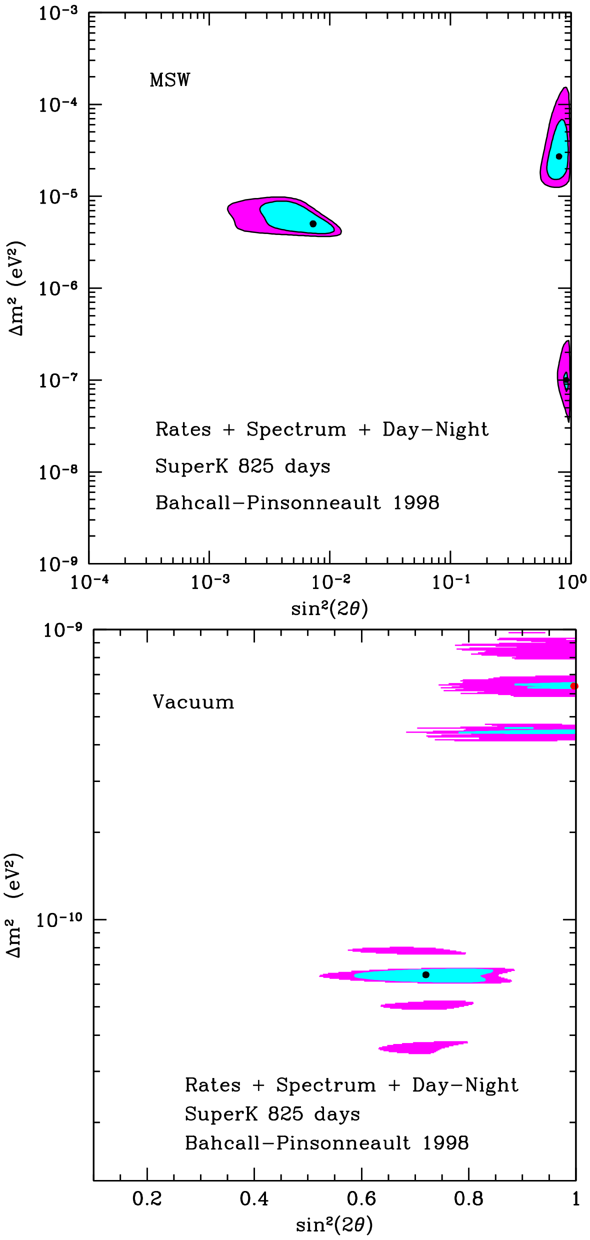

Figure 2.2: Global Fits to Solar Neutrino Oscillations. Taken from Bahcall *et. al.* [20]. These plots show the allowed regions (at 90% and 99% confidence limits) for solar neutrino oscillation parameters. The first plot shows MSW solutions; the second shows vacuum oscillation solutions. The three regions shown on the first plot are referred to as LMA, SMA, and LOW (respectively top left, top right, and bottom right).

solar neutrinos oscillate from ν_e to ν_{sterile}. (If a sterile neutrino is involved, SNO would see that the absolute NC rate would be low, which is another observable.) A ratio greater than unity would indicate that neutrinos are oscillating to other active flavors of neutrino (ν_μ or ν_τ).

Another important measurement that can be made by SNO is the energy spectrum of the ^{8}B neutrinos from the sun. (SNO is sensitive only to ^{8}B and hep neutrinos due to the Q-value of reaction (2) of 1.44 MeV. In addition to this, SNO has an experimental energy threshold of $\sim$ 5 MeV.) Interaction (2), the charged current interaction, has excellent energy response to the incoming neutrinos, because unlike interaction (1), the electron carries almost all of the energy of the incoming neutrino (since the deuterium recoil energy will be small). Experiments using H_2O as a medium (e.g. Super-Kamiokande) must rely on elastic scattering, which results in a spectrum that is highly distorted and therefor difficult to analyze with respect to small shape distortions. These spectra are shown in Figure 2.3.

Shape distortions are expected to arise because of the energy term in equation (2.4). Figure 2.4 shows how this spectrum will distort under the various oscillation scenarios shown earlier.

Figure 2.4 omits an important feature, however, that of the hep neutrinos. Hep neutrinos (originating in $^3\text{He} + p \rightarrow^4 \text{He} + e^+ + \nu_e$) have an endpoint that extends past the ^{8}B spectrum. A recent calculations [25] have given accurate predictions for

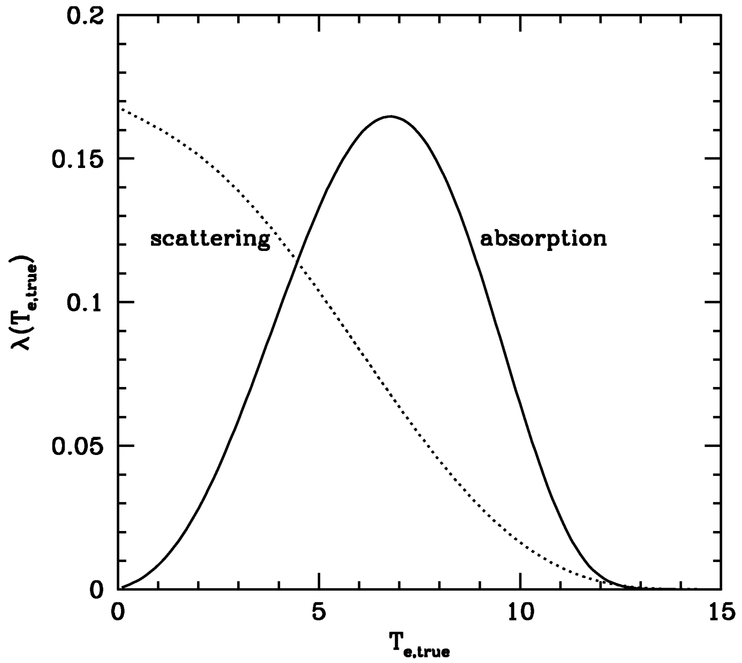

Figure 2.3: Charged Current Spectrum. Taken from Bahcall *et. al.* [20] The solid curve shows the measurable electron energy spectrum due to ^{8}B solar neutrinos on deuterium, measured using the charged-current interaction. The dashed curve shows the expected electron spectrum measured using the electron recoil energy in an elastic scattering experiment.

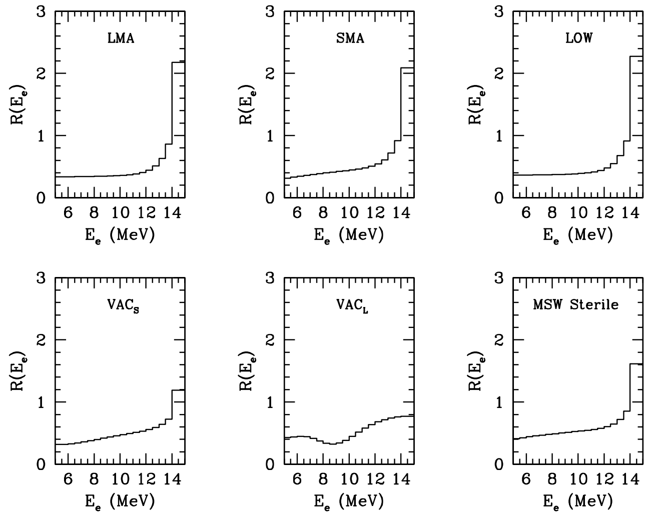

Figure 2.4: Relative Charged Current Spectra Under Oscillation. Taken from Bahcall *et. al.* [26]. Each plot shows the shape distortion of the charged current spectrum given a different oscillation scenario. A value of 1 on the ordinate corresponds to the flux as predicted by the SSM.

the hep rate, but this has not been tested experimentally. A large hep flux can create a distortion of the measured ^{8}B spectrum at the higher energies, which in turn can mimic the shape distortions shown in Figure 2.4. Understanding the detector energy scale in this region may help us to separate the hep spectrum from the.^{8}B spectrum.

It is instructive to look only at the first moment of the energy spectrum, which can be used as a simple measure of the shape distortions. The value of this measurable parameter can be used to distinguish between some of the different neutrino oscillation solutions, as is shown in Figure 2.5. It can be seen that in order to distinguish between the SMA and LMA models, systematic uncertainties in the measurement need careful attention.

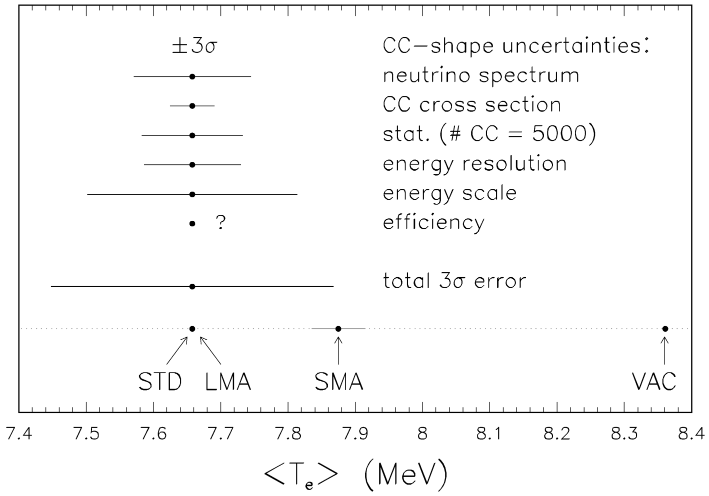

Figure 2.5: Discrimination of Neutrino Model by $\langle T_e \rangle_\nu$. Taken from Bahcall and Lisi [27]. It may be determined which of the possible oscillation scenarios (Large Mixing Angle, Small Mixing Angle, vacuum oscillations, and the standard solar model) is the correct one by measurement of the mean energy of the ^{8}B neutrino spectrum. Estimates of SNO's systematic and statistical errors are those of the Bahcall and Lisi, not SNO.

2.3 Motivation I: Energy Calibration and Shape Distortions

When looking for subtle shape distortions described in 2.2, the error budget for making the observation must be considered. Bahcall and Lisi [27] make such a computation. In this paper, the authors use $\langle T_e \rangle_\nu$, the first moment of the observed neutrino spectrum, as the observable quantity to be used to measure shape distortions. They compute an error budget for this observation as shown in Table 2.1. Two important systematics shown here are labelled 'neutrino spectrum' and 'absolute energy calibration'. The former refers to an intrinsic problem when attempting to predict the shape of the ^{8}B spectrum. The latter refers to the uncertainty in the exact energy scale of SNO.

Calibration sources are necessary to determine the precise energy scale and resolution of the SNO detector. ^{8}Li can be used for this purpose in several ways. The centroid or endpoint of the spectrum may be used as an energy calibration point. A more sophisticated analysis would compare Monte Carlo simulation(s) of the beta spectrum to the spectrum measured by the detector. Because the spectrum is a continuum, details of the detector energy response will be washed out. However, there exists the potential to use ^{8}Li in a more sophisticated way, because of the relationship between ^{8}B neutrinos and ^{8}Li electrons.

The decay scheme for A=8 atoms is shown in Figure 2.6. ^{8}B nuclei undergo β^+

Table 2.1: CC Shape Error Budget. Percentage 3σ error in $\langle T_e \rangle_\nu$ from Bahcall and Lisi [27] and $\langle T_e \rangle_\nu / \langle T_e \rangle_e$ from Jonkmans, Towner, and Sur [28]. Note that the total error in column 3 is claimed as "optimistic" by Jonkmans *et. al.*

Percent error in	$\langle T_e \rangle_\nu$	$\langle T_e \rangle_\nu / \langle T_e \rangle_e$
Statistics of 5000 CC events	0.98	0.98
CC cross section	0.43	0.43
Neutrino spectrum	1.14	0.15
Energy resolution	0.94	0.11
Absolute energy calibration	2.04	0.41
Total error	2.82	1.16

decay to the J=2^+ level of ^{8}Be, which itself is unstable. The ^{8}Be quickly breaks up into two alpha particles. The intermediate ^{8}Be nuclear state has a large width (about 1.5 MeV). The ^{8}B β-decays into this broad state, which makes the shape of the resulting neutrino spectrum differ substantially from the standard allowed shape. The final state distribution can be found only by an accurate measurement of the delayed alpha spectrum of ^{8}Be decay.

This is a difficult experiment to perform, however, as it requires a good absolute energy calibration of the alpha particles. Precise estimates of the energy loss of the alpha in the target material are necessary, including contribution for straggling tails. Thus, the predicted ^{8}B shape has the substantial systematic uncertainty shown above. Bahcall, *et. al.* [30] make use of several of such measurements to provide the shape and associated uncertainty. Ortiz [31] has made new measurements of the ^{8}Be alpha spectrum that reduces this uncertainty; these improvements are not accounted for in

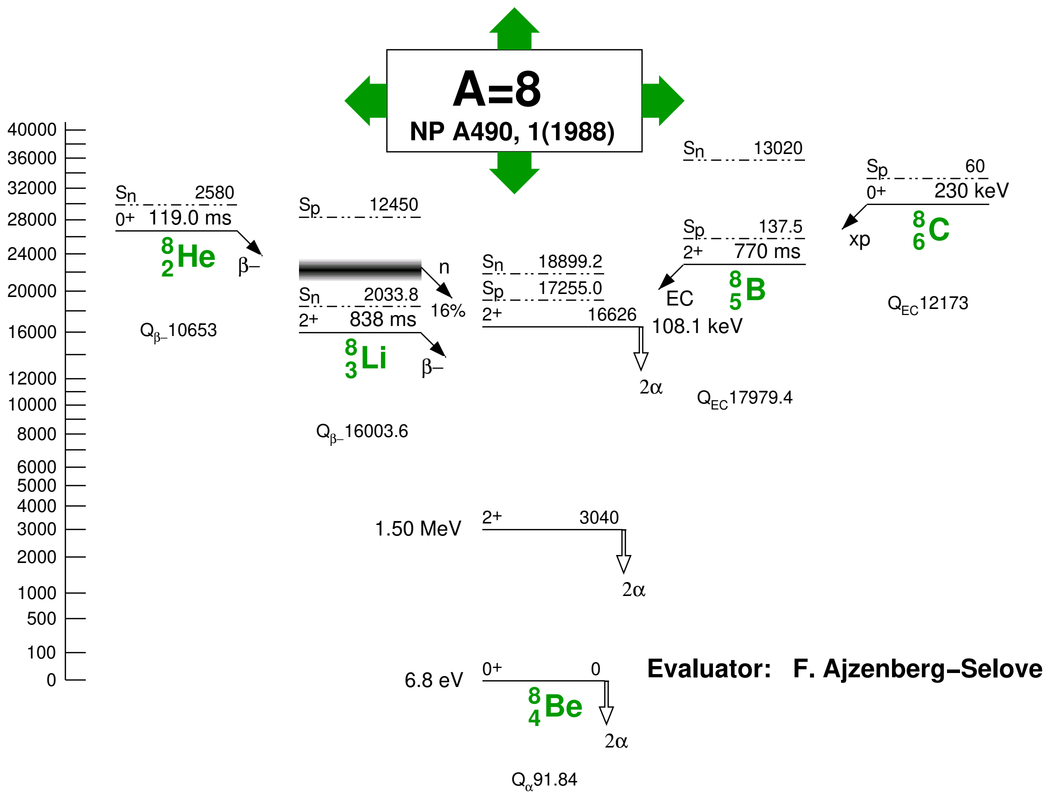

Figure 2.6: A=8 Decay Scheme. Taken from [29]. ^{8}Li and ^{8}B both beta-decay to the same ^{8}Be state of spin-parity 2^+ at 1.50 MeV.

this discussion (see below).

The use of an ^{8}Li calibration source has the potential to alleviate this source of uncertainty. As can be seen in Figure 2.6, ^{8}Li β^- decays into ^{8}Be as the isospin mirror of ^{8}B. If the ^{8}Li decays go to the same ^{8}Be states as do ^{8}B, the same shape distortions will apply to the ^{8}Li spectrum. Apart from a slightly smaller Q-value, the ^{8}B neutrino and the ^{8}Li electron should have very similar spectral shapes.

Jonkmans, Towner, and Sur [28] have demonstrated that if one distorts one's prediction of the ^{8}B ν shape by assuming that the delayed-alpha measurements are energy shifted ($E_\alpha \to E_\alpha + b$), the shapes of the ^{8}Li and ^{8}B spectra change in the same way. They demonstrate that radiative and recoil corrections are of minor importance with respect to measurement in SNO, and that these corrections are similar magnitude and the same sign in both cases.

With the deployment of a ^{8}Li source, a new measurement can be made: $\langle T_e \rangle_\nu / \langle T_e \rangle_e$, where the denominator is the mean electron energy measured from ^{8}Li decays. Since the uncertainty in the ^{8}B and ^{8}Li spectrums is highly correlated, dividing the two in this way removes most of the uncertainty. This is shown in Table 2.1.

With the improvements to understanding of the ^{8}B neutrino spectrum, this uncertainty becomes less important. But, since the ^{8}Li and ^{8}B signals are propagated through the same detector, the energy scale and energy resolution distortions for the two signals are nearly identical. Therefore, taking the ratio of these results should reduce the uncertainty of these important systematic factors.

The authors stress that their case is optimistic, however. The effect of a non-ideal ^{8}Li source is not properly dealt with, and simplistic representations are used for the detector resolution and energy scale. In the real SNO detector, for instance, the measured energy of an event (as measured by NHITS) is a function of position in the detector, so the energy resolution function will similarly be a function of position. Therefore, the whole-detector resolution function will not be a simple Gaussian distribution, as the authors use. These problems can be mitigated by using the Monte Carlo as a reference, by taking a ratio-of-ratios:

$$R = \frac{\langle T_e \rangle_\nu / \langle T_e^{MC} \rangle_\nu}{\langle T_e \rangle_e / \langle T_e^{MC} \rangle_e} \tag{2.5}$$

A new measurement of the ^{8}B neutrino spectrum made by Ortiz *et. al.* [31] does away with much of the uncertainty due to the ^{8}B neutrino shape. However, this new measurement has not been verified, and is not yet accepted as an 'industry standard'. New error budgets have not been composed based on Ortiz, but it is expected that this source of systematic uncertainty will no longer be a large contributor to the overall error budget. This measurement makes the spectrum comparison method somewhat redundant. However, uncertainty due to energy scale remains large and so use of the source as an energy calibration remains valid and useful.

The ^{8}Li source will be a useful energy calibration for SNO, because it explores the high-energy region in which neutrino signals are expected, up to about 10 MeV, which cannot be probed by other sources.

2.4 Motivation II: Vertex Reconstruction

Several calibration sources have been proposed and are being deployed in SNO, or developed for later deployment. These include the laser ball (optical photons), the ^{16}N source (a nearly mono-energetic 7 MeV gamma), the proportional counter source (a tagged low-energy radioactive source), the p-t source (20 MeV gamma source from a small proton-tritium accelerator), and various neutron sources. (A brief overview is listed in [1]. See also [4, 32, 33].) Apart from the proportional counter source, none of these sources are well-localized in space. The gamma and neutron sources both provide Cherenkov-light events that are widely distributed around the source. The laser-ball provides well-localized light, but does so isotropically and at a single wavelength at a time, which is qualitatively different from light from a Cherenkov particle. The PC source does provide localized Cherenkov light, but only up to a few MeV.

However, SNO requires a well-localized source of Cherenkov light in order to test reconstruction algorithms. SNO locates the position and direction of a neutrino event in the detector by looking at the positions and relative timing of phototubes that fire in a given event. Simply put, tubes closer to the event vertex will fire earlier than tubes further away. Direction information can be derived from the positions of fired tubes relative to the reconstructed position vertex. Several algorithms (e.g. [34, 35]) exist to reconstruct events, with various strategies to use these and other data available in a given event. These algorithms have been designed and tuned using Monte Carlo data. Without a calibration source we would be forced to rely on Monte Carlo as our sole measure of the position resolution of the detector, a dangerous method for doing analysis.

Position resolution in particular is important to SNO for several reasons. First, it may be necessary to introduce a particular fiducial volume cut when analyzing neutrino data. When finding absolute fluxes it is important to know how precisely this volume can be defined. Second, all of our reconstruction techniques have tails in their position residuals. (Figure 2.7). Thus, high-energy gammas from radiation in the external rock wall can penetrate into the SNO detector volume, and some proportion of these can mis-reconstruct into the detector fiducial volume. Estimation of these fitter tails is important to accurately measure this systematic. Third, the energy response of the detector is a fairly strong function of position within the detector, particularly at the edges of the D_2O region. (See Figure 2.8.) Optical calibration should be able to accurately determine the dependence, but not in such a way that it is convoluted with the reconstruction response function.

^{8}Li is fairly well suited to this task. Although the source is self-shadowing (betas are masked by the source container itself) it nonetheless remains an important source

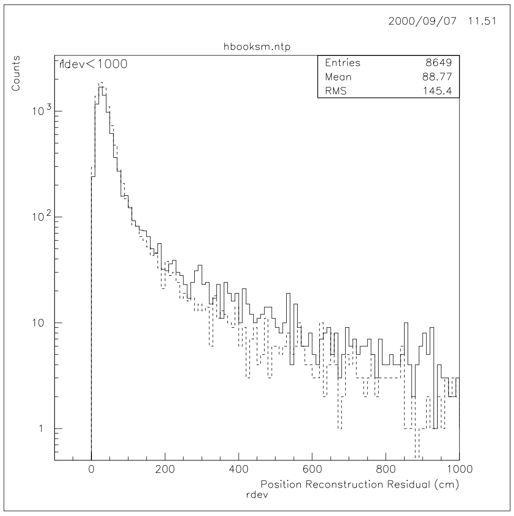

Figure 2.7: MC Reconstruction Residuals. 8 MeV electrons are scattered homogeneously through the detector in Monte Carlo simulation. The distance of the reconstructed position from the true position is shown for the time fitter (solid line) and the grid fitter (dashed line). Fitters are described in ref. [36].

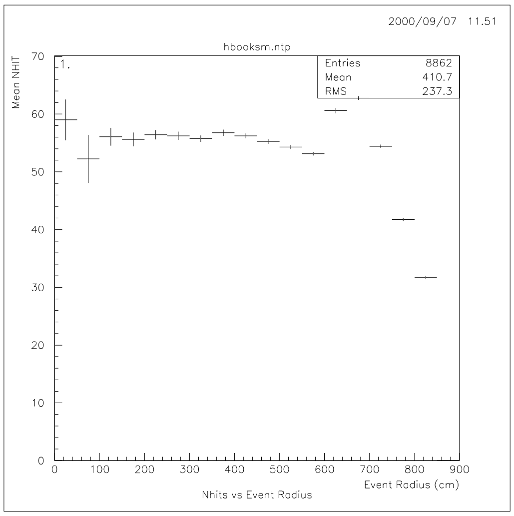

Figure 2.8: MC Energy Response. 8 MeV electrons are scattered homogeneously through the detector in Monte Carlo simulation. NHIT, the simplest energy measure, is plotted as a function of event position in the detector.

for checking these problems.

2.5 Motivation III: Data Cleaning Sacrifice

SNO has a certain number of intrinsic detector-related backgrounds that can potentially interfere with the measurements it can make. For instance, a dominant background, probably the most dangerous to solar neutrino measurements, consists of a set of events dubbed 'flashers'. These are events where light is generated by some electrical breakdown inside a PMT, which creates a large voltage spike at the tube's anode, with a corresponding wash of light across the far side of the detector. These events fall into roughly the same NHIT range as is expected for solar neutrinos, but occur much more often. In addition, there are several other backgrounds, such as light originating in the chimney, or 'neck events', and events due to pickup or crosstalk. Some of these phenomena occur in bursts (particularly during seismic activity in the mine) but are not limited to bursts.

The SNO collaboration has constructed a thorough set of low-level cuts designed to cut all of these obvious backgrounds, without removing real "physics" events [37]. This process is called 'data cleaning'. [3] There are two measures for the performance of a cut (or set of cuts), named *sacrifice* and *contamination*. Contamination is a measure of how many "non-physics" background events pollute the cleaned data set,

[3] This is distinct from a process of 'data reduction' in that only detector-related backgrounds are removed, rather than any uninteresting signal.

and is not discussed here.

Sacrifice is the measure of the number of true physics events are cut out of the data. It can be measured by applying the data cleaning cuts to a data set known to be consisting of valid events. This can be accomplished in two ways: either a high-rate source can be used, or a tagged source can be used. High-rate sources are relatively risky: some fraction of the events in a high-rate run will really be instrumental background (requiring a subtraction), and the high-rate data taking can itself generate new problems. (For instance, high data rates are known to cause artifacts due to DAQ polling of the front-end cards.) Furthermore, a high-rate source can not be used reliably to test dead-time or time-correlation cuts.

The ^{16}N source, a tagged gamma source, has already been used extensively for this application, and fulfills all the required properties to make a good source for data cleaning. This source, although extremely useful, has two important limitations. First, the ^{16}N source is nearly mono-energetic; it explores a limited range in NHIT. Ideally, one would want to test the relative and absolute sacrifice of a suite of cuts against both low- and high-NHIT data. Many of our cuts are known to be sensitive to this parameter, as they frequently look for crosstalk clusters in neighboring channels, or abnormal charges in specific tubes. Secondly, the ^{16}N source data was used to tune the cuts for minimum sacrifice in some cases. Measuring the sacrifice of a cut with the same data that was used to find the optimal cut parameters is potentially dangerous. If possible, an independent set of data should be used to do the testing.

Using a Monte Carlo simulation of the detector to test (or tune) the cuts is a possibility, but cannot be used for several very important cuts. Many of the detector characteristics used by the cuts are badly modeled by the Monte Carlo. These characteristics include such things as channel crosstalk, front-end electronics charge response, and the OWL and NECK tubes. These characteristics are heavily used by many of the cuts, rendering the Monte Carlo useless for this purpose.

^{8}Li is not an ideal source for the purpose of data cleaning, for the simple reason that the total radioactive yield is expected to be quite low (i.e. measured in fractions of counts per second), so statistics are limited. Moreover, energy losses in the source wall, combined with the low endpoint of the beta-decay, means that the source will not completely explore the complete range of energies expected of ^{8}B neutrinos. These are small drawbacks. The source is tagged, and can generate enough statistics to be comparable to the ^{8}B statistical sample. ^{8}Li has the advantage that the beta-spectrum shape is, apart from the lower energy, fairly representative of the ^{8}B neutrino spectrum. This source is expected to be very important for testing the data cleaning sacrifice.

3

Production and Delivery Systems

3.1 Overview

The gas transport system is responsible for delivering the short-lived ^{8}Li isotope to a decay chamber inside the SNO detector. One of the major limitations of the ^{8}Li source is the low event rate, so a thorough understanding of this system is necessary in order to achieve the best possible rate of ^{8}Li. This chapter serves as an overview of this system.

The ^{8}Li system was developed and prototyped by Sur *et. al.* [38, 39, 40]. Figure 3.1 shows an overview of the system, discussed below.

Helium gas from a conventional gas bottle is flowed at rates of ∼200 cc/s through a glass oven tube, filled with NaCl heated to a temperature of 600 C. This temperature is sufficient to sublimate the salt into aerosol, which is picked up by the helium gas. The salt-laden helium is flowed into a target chamber that is mounted around a deuterium-tritium accelerator. The accelerator emits 14 MeV neutrons at a rate

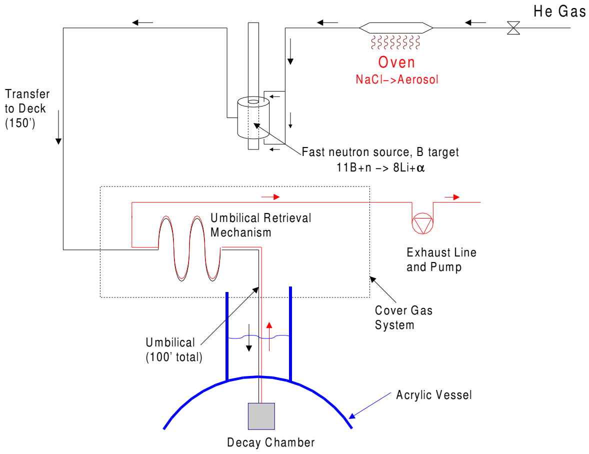

Figure 3.1: Diagram of Gas Transport System.

between 10^7 and 10^8 neutrons per second. [40].

The target is set into an annulus around the inside of a target chamber (see Figure 3.2) and consists of an enriched ^{11}B powder in a polyethylene matrix. The ^{8}Li isotope is produced by the reaction ^{11}B (n, α) ^{8}Li. The ^{8}Li recoils out of the target and into the gas stream, where it is swept up by the NaCl aerosol. After passing through the target chamber, the gas is carried through a conduit from the accelerator pit to the deck above the SNO detector.(See Figure 3.3.)

An umbilical carries the gas down to the decay chamber. (See Figure 3.4.) The total distance from the pit to the source chamber is about 76 meters for a full-length umbilical (sufficiently long to reach the bottom of the AV). The chamber then exhausts the gas through the umbilical. The umbilical input gas line is coaxially inside the exhaust line (for practical reasons of umbilical construction). Outside the return line are wrapped the power and signal cables used by the tagging system. The outer umbilical consists of a silicone potting gel and a silicon sheath to act as a radon barrier.

A the end of the umbilical is the decay chamber, which contains the gas for a brief period, allowing the isotope to decay. This chamber is described in detail in the next chapter; for purposes of analyzing gas flow it is a one litre volume with well-mixed gas.

The system can be configured to pump to the exhaust line to decrease the decay chamber pressure; otherwise, the stale gas is simply vented to room pressure (18 psi underground).

3.2 Gas Transport Physics

This section explores some of the basic physics of the gas transport system that can be used to help understand and optimize the system.

The short half life of ^{8}Li is the major design consideration: the radioactive product must be transported to the decay chamber before it can decay. The ideal method to transport short-lived isotopes is to push the carrier gas through the system at supersonic speeds. However, this solution has several problems in this application. Besides the high pressures the system must be designed for and large quantities of

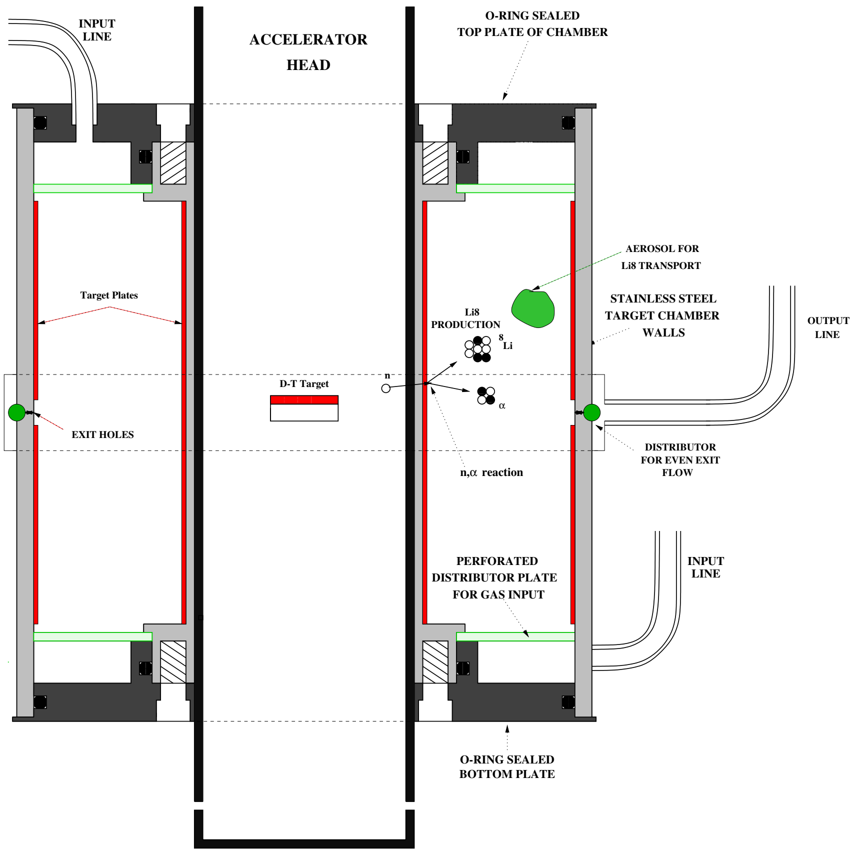

Figure 3.2: ^{8}Li Target Chamber. Target plates of ^{11}B are shown in red. There are two annuli of these targets, one inside and one outside. Gas is blown in from the top and bottom and dispersed through the can with perforated plates. Gas is drawn out through a series of holes distributed around the circumference of the chamber.

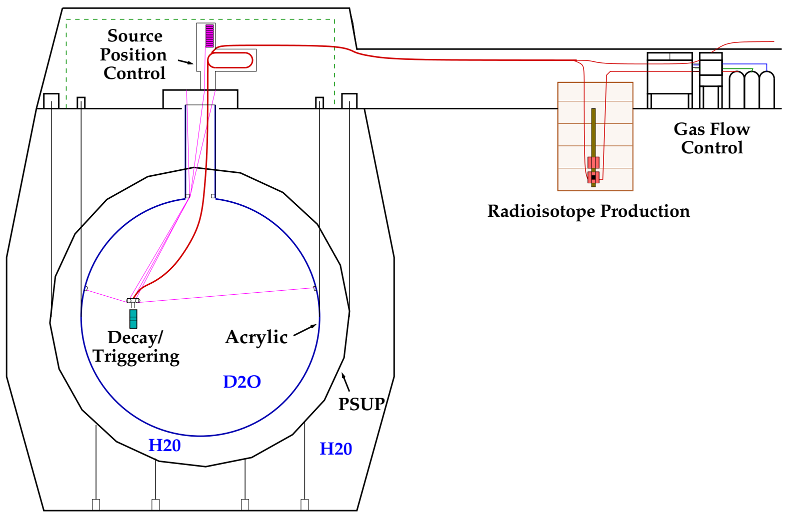

Figure 3.3: Cross Section of SNO Lab.

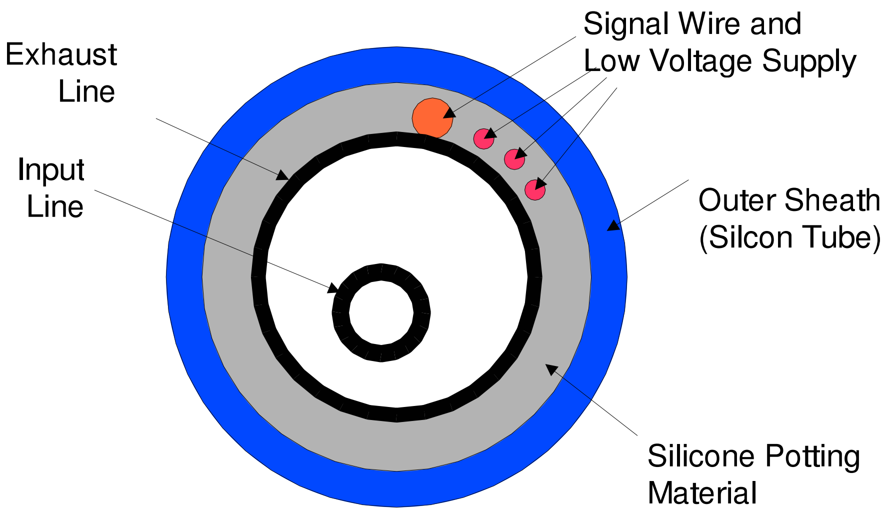

Figure 3.4: Schematic of Umbilical Cross-Section.

Table 3.1: Definition of terms.

Q	=	Mass flow rate (in atm cm^3/s)
η	=	gas viscosity
	=	18.6 μPa s = 1.8410^{-10} atm s (for He gas)
R_e	=	Reynold's number (dimensionless)
d	=	Tube diameter (cm)
A	=	Tube cross-sectional area (cm^2)
l	=	Tube length (cm)
$P_1 - P_2$	=	Pressure difference between the ends of a tube (atm)
P_d	=	Decay chamber (tag chamber) pressure (atm)
P_t	=	Target chamber pressure (atm)
τ	=	Radioactive mean life = 1.209 s for ^{8}Li
τ_l	=	Mean transport time down a tube of length l (s)
τ_t	=	Mean residence time in target chamber
τ_d	=	Mean residence time in decay chamber

gas required, such a design would deposit a very large quantity of salt into the decay chamber, which might cause problems when trying to tag the delayed alpha decay. The ^{8}Li system described here uses much more moderate rate of flow. Sub-turbulent gas velocities are used to minimize transport time.

The equations governing the transport of the gas through the tubing are Poiseuille's law (3.1) and the associated mean time for gas transport down a tube (3.2):

$$Q = \frac{\pi d^4 (P_1^2 - P_2^2)}{256 \eta l} \tag{3.1}$$

$$\tau_l = \frac{P_2 + P_1}{2} \frac{Al}{Q} \tag{3.2}$$

Note that Q here refers to mass flow rate, not volume flow rate. Equation (3.1) contains a factor of $(P_1 + P_2)/2$ to convert to mass flow. (An ideal gas is assumed, so that the mean pressure times the volume-flow rate is proportional to the mass flow rate.)

Helium was chosen as the carrier gas because of the relatively high gas velocity for a given rate of laminar flow. Laminar flow starts to degrade into turbulent flow when the Reynold's number gets above a threshold of 1000-2000. The Reynold's number is a dimensionless quality defined as:

$$R_e = \frac{4m}{\pi\eta kT}\frac{Q}{d} \lesssim 1000 \tag{3.3}$$

The decay chamber can be modeled by assuming perfect mixing of the gas in a volume of about 1000 cm^3. It simplifies understanding to consider what happens to a single atom injected into the ball at time t=0. The probability of the given atom to decay in time dt is λdt, and the probability of being flushed out of the ball is σdt, where σ is the fraction of the ball volume flushed in unit time. (i.e. $\sigma = Q/PV$). So, if N_0 atoms are introduced into the ball at time t, they disappear as

$$N(t) = N_0 e^{-(\sigma+\lambda)t} \tag{3.4}$$

where t is the time since this clump of atoms was injected into the ball. Therefore, the number of these that decay in the ball in time dt is

$$
\begin{aligned}
N_{decay}dt &= N(t)\lambda dt \\
N_{decay} &= \int_0^\infty dt\lambda N_0 e^{-(\lambda+\sigma)t} \\
&= \frac{1}{1+\sigma/\lambda} \\
&= \frac{1}{1+\tau/\tau_{chamber}}
\end{aligned}
\tag{3.5}
$$

Inside the target chamber, we can either use the complete mixing assumption of (3.5) or assume laminar flow through the chamber. Although it was designed for laminar flow, the optimum case, the flow patterns are not precisely known. Complete mixing is a simple worst-case solution.

The system is constrained by the size of the decay chamber, the size of the umbilical lines (which are physically limited by the requirements of the umbilical retrieval and manipulator systems in SNO), and the limit for turbulent flow (equation (3.3)). The decay chamber is approximately 1000 cm^3 in volume, and the total size of the umbilical is limited by the design of the SNO umbilical retrieval mechanism.

The size limit on the umbilical constrains on the width of the conduit that runs to the deck interface. A thinner line obviously has lower conductance. A conduit line thicker than the umbilical line also is inefficient. The majority of the pressure drop will be across the thinner segment, so the larger conduit is at high pressure and transit time. The gas accelerates as it moves through the tubes so by widening part of the line, one impedes this acceleration and therefore increases the total transit time.

One parameter that needs careful optimization is the size of the target chamber.

It is desirable to harvest as many ^{8}Li atoms as possible, and also to minimize the residence time of the gas in the chamber. A minimal residence time ensures that as little isotope as possible decays before it leaves the target chamber. The chamber was originally sized to allow the maximum recoil from the target to range out in the helium gas before hitting the far wall, but empirical measurements have shown that improvements in yield can be made by inserting a collar in the target to take up space and therefore decrease the residence time. The original design was overly conservative in this respect.

A related consideration is that the pressure at the target chamber must not be too high, or once again, the residence time is increased. This is part of the reason for running the system at the laminar flow limit rather than applying more pressure and running in a semi-turbulent regime.

Absolute production of ^{8}Li in the chamber can be estimated from the (n, α) cross section, but the efficiency for uptake of the isotope on salt is not well known. Therefore an empirical measurement is used to fix the yield of ^{8}Li produced per second in the target chamber. This is done using a short length of transit tube, i.e. a 10 meter log segment of 1/8" ID plastic tubing. Using the short transfer tube, the observed rate of ^{8}Li is roughly 5 Hz, and the predicted efficiency for this system is about 22%, (with the efficiency loss dominated by target chamber effects). The production rate is thus $A_0 \sim 20$ Hz.

The total yield delivered to the decay chamber (using the pessimistic model of complete mixing in the target chamber) is:

$$\text{Net Yield} = A_0 \times \epsilon_{target} \times \epsilon_{conduit} \times \epsilon_{decay} \quad (3.6)$$

$$= A_0 \times \frac{1}{1+\tau_t/\tau} \times \exp(-\tau_l/\tau) \times \frac{1}{1+\tau/\tau_d} \quad (3.7)$$

Figures 3.5 and 3.6 show the transfer times and efficiencies of the system for a fixed target chamber size (509 cm^3), for two different decay chamber pressures. Losses due to recoils in the target chamber hitting the walls are neglected; it is assumed that the this effect is constant over the pressures calculated. Note that there is a drop in yield when the umbilical is large; can be seen in equation (3.2). The turbulence limit sets $Q \propto d$, so $A/Q \propto d$. As diameter is increased, the head pressure in P_1 goes as $d^{-3/2}$ for $P_1 >> P_2$ (from 3.1). Therefore, at large head pressures, the transit time increases as $d^{-1/2}$. As the diameter increases above the optimum, more gas gets through the tube, but the mean transit time gets longer because the head pressure is so low.

Because of this tradeoff, an optimum tube diameter exists for a given decay chamber pressure. By contrasting the two figures, one can see that gains can be made by keeping the decay chamber pressure low.

There are several more optimizations that can be done, such as tailoring the size of the decay chamber to match your umbilical diameter for optimum performance. However, this requires a good knowledge of the atomic recoil kinematics, so predic-

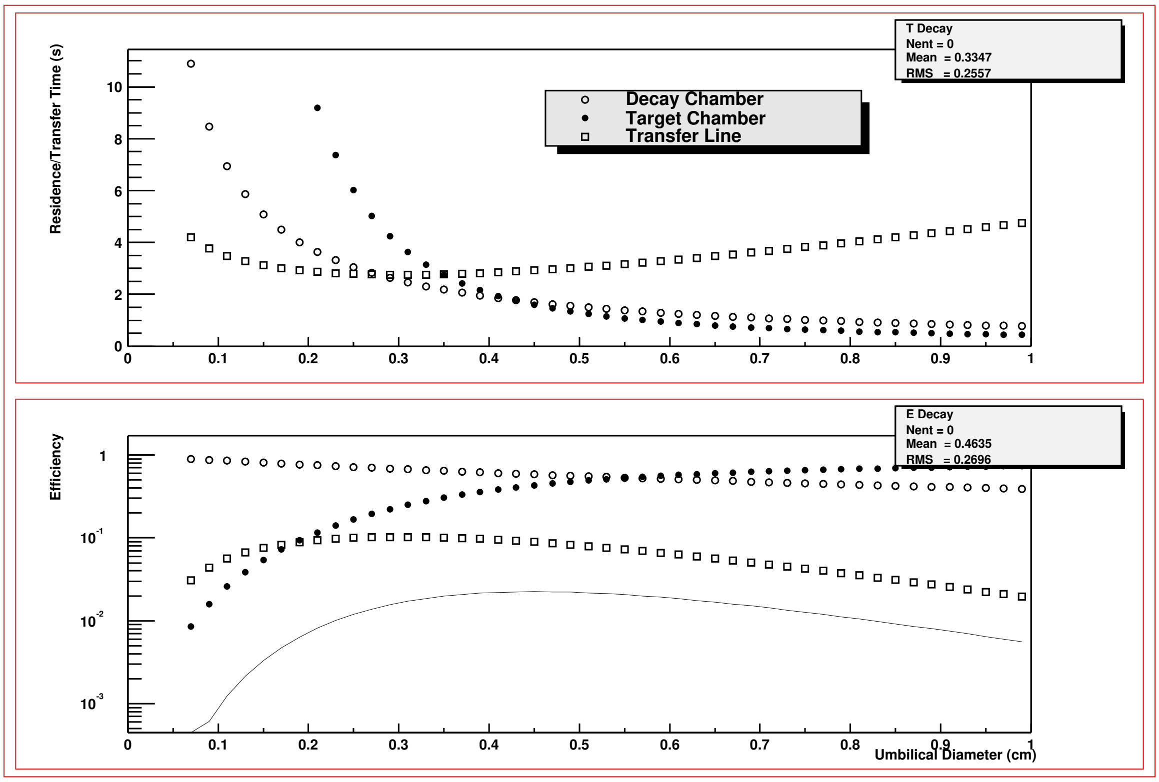

Figure 3.5: Calculated Efficiency at P_d=18 psi. The top plot shows the mean residence and transfer times as a function of tube diameter. The lower plot shows fractional efficiencies of the same components; the solid line is the total efficiency. Flow rate (Q) is assumed to be optimized to a Reynold's number of 1000. P_d is set at 18 psi, the atmospheric pressure underground. The maximum efficiency is 0.95% at a diameter of 0.34cm

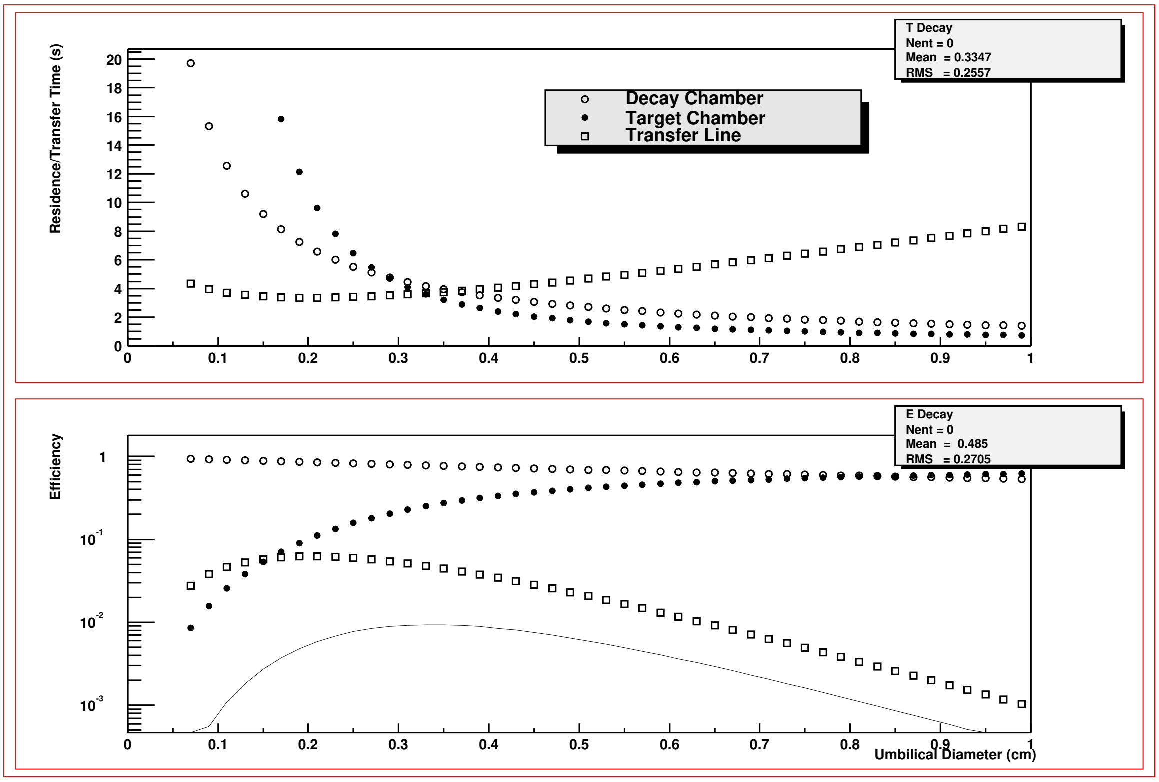

Figure 3.6: Calculated Efficiency at P_d=10 psi. The top plot shows the mean residence and transfer times as a function of tube diameter. The solid line is the total efficiency. Flow rate (Q) is assumed to be optimized to a Reynold's number of 1000. P_d is set at 10 psi, the atmospheric pressure underground. The maximum efficiency is 2.2% at a diameter of 0.45cm

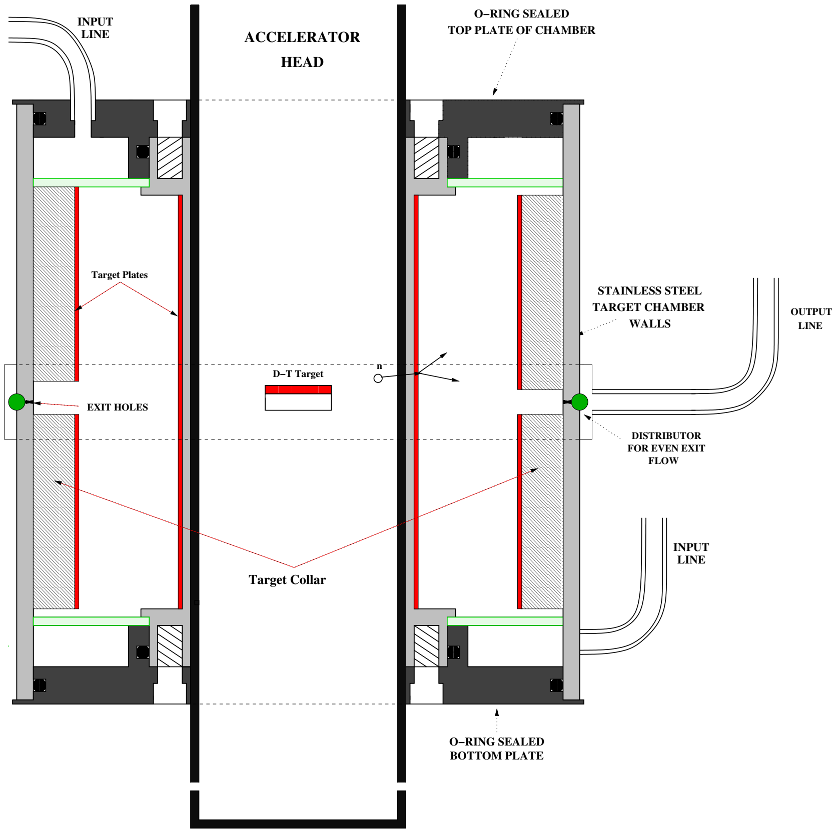

Figure 3.7: ^{8}**Li Target Chamber with Collar.** A teflon collar is inserted into the can to reduce the volume and therefore the residence time.

tions are of limited value. In practice, a single target chamber collar was tried, with an inner diameter of 3.25". (See figure 3.7.) Another parameter left to empirical testing is the inner diameter of the outer (return) line in the umbilical. This size must be large enough not only to accommodate the size of the input line, but also to have a large enough conductance to pump the decay chamber down to optimal pressure. Although calculations exist for viscous flow through annuli (see ref. [41]), empirical measurements were used as the primary tool for finding good candidates for umbilical materials. Finally, the choice of tubing itself was one that had to be made on the basis of experiment rather than modeling, because the value of the Reynold's number at the turbulence limit is a function of the material used; small gains were to be had by use of different materials.

The conclusions that can be drawn from these calculations is that the best umbilical consists of an input tube between 0.35 and 0.45 cm in diameter, and that the deck conduit should be the same diameter. Naturally, both of these lines should be as short as physically possible. It is desirable to have the option of pumping the decay chamber down to low pressures (less than 1 atmosphere). Empirical tests need to be done to establish that the materials we use allow for good Reynold's numbers, and the option of inserting a target collar also needs to be tested.

Although there are many parameters that can be adjusted in a given source run (head pressure, target chamber size, length of line, width of line, decay chamber pressure, etc) and that these parameters are all interdependent, there exist optimum relationships. These optima are not, as can be seen in Figures 3.5 and 3.6, are not sharp maxima, but allow a fair degree of play, so exact numerical modeling is not required to find good operating conditions.

4

^{8}Li Decay Chamber

4.1 Overview

There are several design constraints in constructing a decay chamber for ^{8}Li. The foremost of these is that the chamber must reliably tag ^{8}Li decays. Because of the short decay time of the isotope and long transport time of the gas, the number of decays per second in the D_2O will be quite small. Although the event rate will be orders of magnitude faster than the neutrino rate, the 'non-physics' background of the detector will contaminate the calibration data. Therefore, it is imperative that as many ^{8}Li decay events as possible are tagged as such in the SNO data.[1]

Secondly, the decay chamber must allow the escaping beta particle to give off Cherenkov light with little impediment. The chamber must be thin-walled, and block as little Cherenkov light as possible. (At the same time, it must not generate any

[1] A tagged source is not necessarily a triggered source as well. The former identifies events that come from the source; the latter is responsible for triggering the entire detector every time the source fires. A triggered source may also be useful in looking for systematic effects due to trigger thresholds, but is not of fundamental concern with ^{8}Li.

light of it's own, by scintillation or other mechanism.)

Third, the chamber must be large enough that the residence time of the gas be longer than the lifetime of the isotope. If the decay chamber is run at atmospheric pressure, a volume of 1/2 litre is sufficient (as was demonstrated in early test runs [42]. If lower pressures are used, a larger volume is necessary to keep the residence time sufficiently long. In addition to volume, the shape of the chamber should be such that most betas escape into the water.

Fourth, the chamber must satisfy some basic physical constraints: it must be clean (with respect to radon, uranium, or thorium contamination of the water), it must be able to withstand the shock of cold water, and the water pressure at 30 meters depth of D_2O, with suitable safety factors.

The initial prototype system, described in ref. [42], was a 1 meter-long proportional counter. The helium transport gas provided the gas gain, and a small amount of CO_2 was added as a quench gas. The α particles would be tagged by the counter. This system, although operable, suffered from several flaws, notably tag signal instability and poor event localization. These problems are described in detail in Chapter 8.

The current design relies upon gas scintillation rather than a proportional counter. The helium carrier gas acts as the scintillation medium, so alpha decays can be tagged by a PMT. This method has the advantages of simple operation, stable signal strength, and flexibility of decay chamber geometry.

A second prototype, also discussed in more detail in Chapter 8, was a spherical acrylic shell based on this concept. This source was put aside due to safety concerns, and was replaced.

The final design, discussed here, is a stainless-steel sphere which is mechanically much more rugged than the acrylic prototype. The relative merits of various designs and thoughts on future improvements are discussed in Chapter 8.

4.2 Design

Stainless steel was chosen as a good material to work with because of its mechanical strength and good cleanliness. Because the source has to withstand the pressure of being under $\sim$30 meters of water, it must be resistant to compressive forces, but a thin wall is desirable for reasons of doing good calibrations. A spherical shape is very good for satisfying these conditions. [2]

A diagram of the source[3] is shown in Figures 4.1. The basic shape and dimensions of the decay volume were chosen for a conservatively large decay volume of 1 litre. It consists of the round ball, a 'neck' above it tapering to flange, and a tall endcap

[2] The failure modes of a vessel under compression are described in terms of buckling, for which "classical" analytic solutions are available, as well as more sophisticated modern analyses[43]. A more practical guide to realistic safety limits on vessel design is to use the ASME Pressure Vessel Code [44], which is used as a guideline for certifying sources in SNO [45]. The wall thickness used for the source was based on such a calculation.

[3] The source was engineered by Ken MacFarlane and drawn by Peter Liimatainen.

covering the top.

The decay volume is a hollow sphere with 5" inner diameter. The ball was constructed from two spun stainless steel hemispheres, which were electron-beam welded together and to the tapered neck. The hemispheres were machined to a specified wall thickness of 0.020 to 0.025", corresponding to a $\sim$2 MeV beta particle energy loss. The wall thickness is somewhat better than the specified tolerance, as is shown by a set of measurements of the wall thickness were made. (See Table 4.1.) The ball is not completely spherical; the bottom of the sphere is slightly flattened out in a disk 1/2" across.

The conical neck piece joined onto the top of the ball contains the gas ports and the PMT, and ends in a flange that connects to the endcap. The PMT sits on an acrylic window (supported by a small ledge). Around the window is an O-ring gas seal which acts as a pressure boundary. The window held down in place with a collar and metal snap-ring. A cylindrical screw-in collar goes around the PMT to hold the base attachment.

The base attachment is an aluminum cylinder which holds the PMT base, and a DC low-voltage to DC high-voltage converter used to step up the voltage supplied through the umbilical (obviating the need for a bulky insulated wire). The attachment is potted with a silicone gel to protect the high-voltage elements from helium gas diffusing through the gas system seals.[4]

A large cylindrical endcap sits around the base attachment, gas lines, and wiring. This section has atop it the seal to the umbilical, made with a stack of three O-rings separated by plates used to compress them. On top of the endcap sits a 'lighthouse' attachment, used to attach the source to the weight and manipulator carriage, part of the SNO manipulator system.

Table 4.1: SS Ball Wall Thickness. Measurements [45] of wall thickness for the bottom hemisphere of the stainless steel ^{8}Li decay chamber. Measurements are in inches. Measurements were unavailable for the top hemisphere.

	Azimuthal Position			
Zenith Position	0°	90°	180°	270°
Near rim (top)	0.0224	0.0220	0.0222	0.0226
Middle	0.0222	0.0215	0.0221	0.0223
Near hub (bottom)	0.0224	0.0241	0.0250	0.0245
Hub (bottommost)	0.0300			

4.3 Tag Signal

The source is designed to tag ^{8}Li decays using scintillation light from delayed alpha decay. The physics of this process are discussed here.

4.3.1 Decay Geometry

The physical geometry of the delayed alpha decay is important. The alpha decay from ^{8}Li ejects the two alphas almost anti-parallel. (The maximum recoil momentum

[4] Helium has a low breakdown potential, so sparking across the high-voltage terminals is a danger.

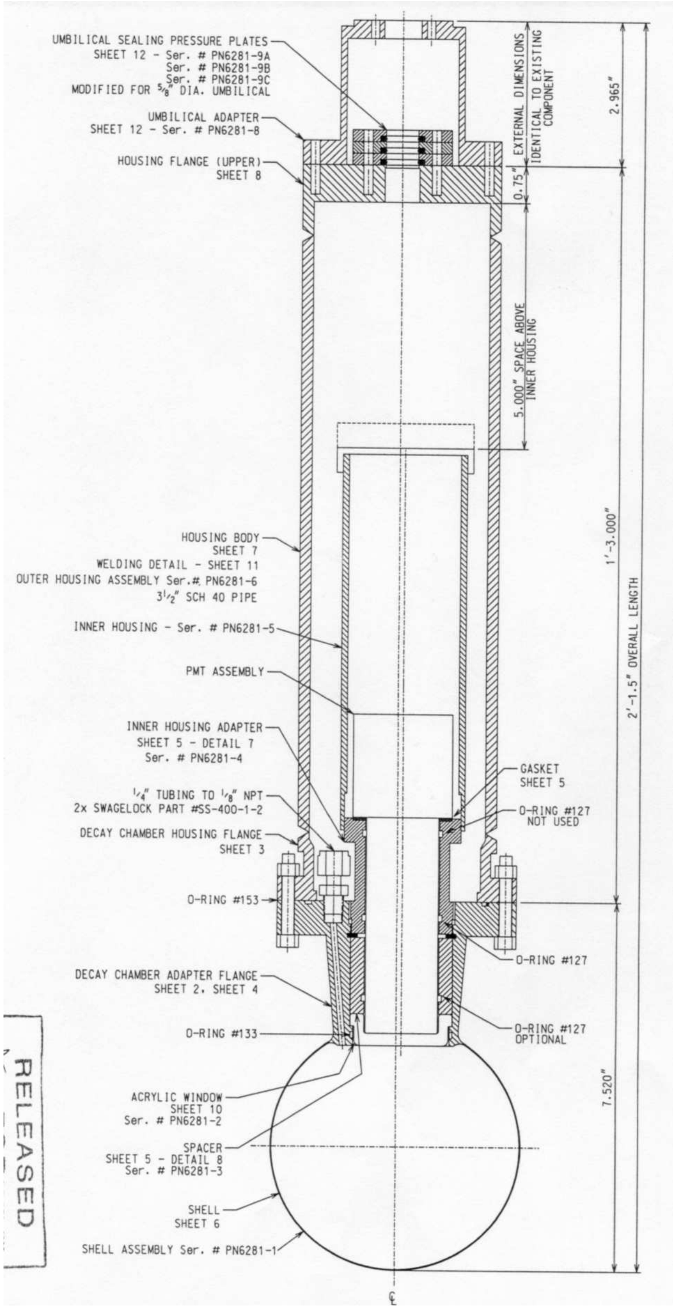

Figure 4.1: Stainless Steel Ball Drawing. The ball, neck, endcap, and "lighthouse" are shown.

Figure 4.2: Stainless Steel Ball Picture. The ball, neck, and flange are shown upside-down. Note the weld at the equator.

from the beta is about 13 MeV/c. whereas the momentum of each alpha from the ^{8}Be decay is about 150 MeV/c, so the alphas will be ejected at least 165°from each other.) A typical alpha particle has an energy of 1.6 MeV, and a range of about 4 cm in pure helium gas, so a sizable fraction of alpha particle per decay particles will hit the wall before depositing their energy in the gas. However, the back-to-back geometry means that one alpha will usually deposit all of its energy in the gas. The alpha particles have a range on order one micron in solids, so they cannot escape from the decay volume.

A simple Monte Carlo was performed to predict the light output of the alpha decay. Ionization was tracked using a simple Bethe-Bloch model as given in ref. [46]. Scattering was neglected, and the alpha particles were assumed to always be perfectly anti-parallel. The alpha energy spectrum was taken from Wilkinson and Alburger [47]. The simulation computed how much energy was lost to the gas before the alpha particles hit the wall of the chamber. The results are shown in Figure 4.3: the mean energy deposited in the gas is 2.6 MeV per ^{8}Li decay.

Pure helium is rarely used as a scintillation gas. (Birks, for example [48] refers mostly to argon and neon when discussing noble gas scintillation.) Pure helium is often used at many atmospheres of pressure in order to get sufficient target material to stop energetic particles [48]. To make a prediction for low-pressure scintillation studies, the Monte Carlo was again employed to look at what quantity of energy in ^{8}Be alphas would be deposited in the helium gas at various pressures. This is shown in Figure 4.4.

Knoll [49] notes that gas scintillation counters are quite fast, "typically a few nanoseconds or less", and that they also "tend to be unusually linear over a wide range of particle energy and dE/dx". The light yield from helium is poor at visible wavelengths; the light yield is given as 1100 photons for a 4.7 MeV particle in helium. However, a much larger fraction of light is given off in ultraviolet wavelengths.

A Hamamatsu R580 1.5-inch PMT is used for the tag signal. An acrylic window separates the tube from the gas volume to protect the tube from direct exposure to helium. This window was made of SNO acrylic, and so has a low wavelength ($\sim$320nm) cut-off, shown in Figure 4.5.

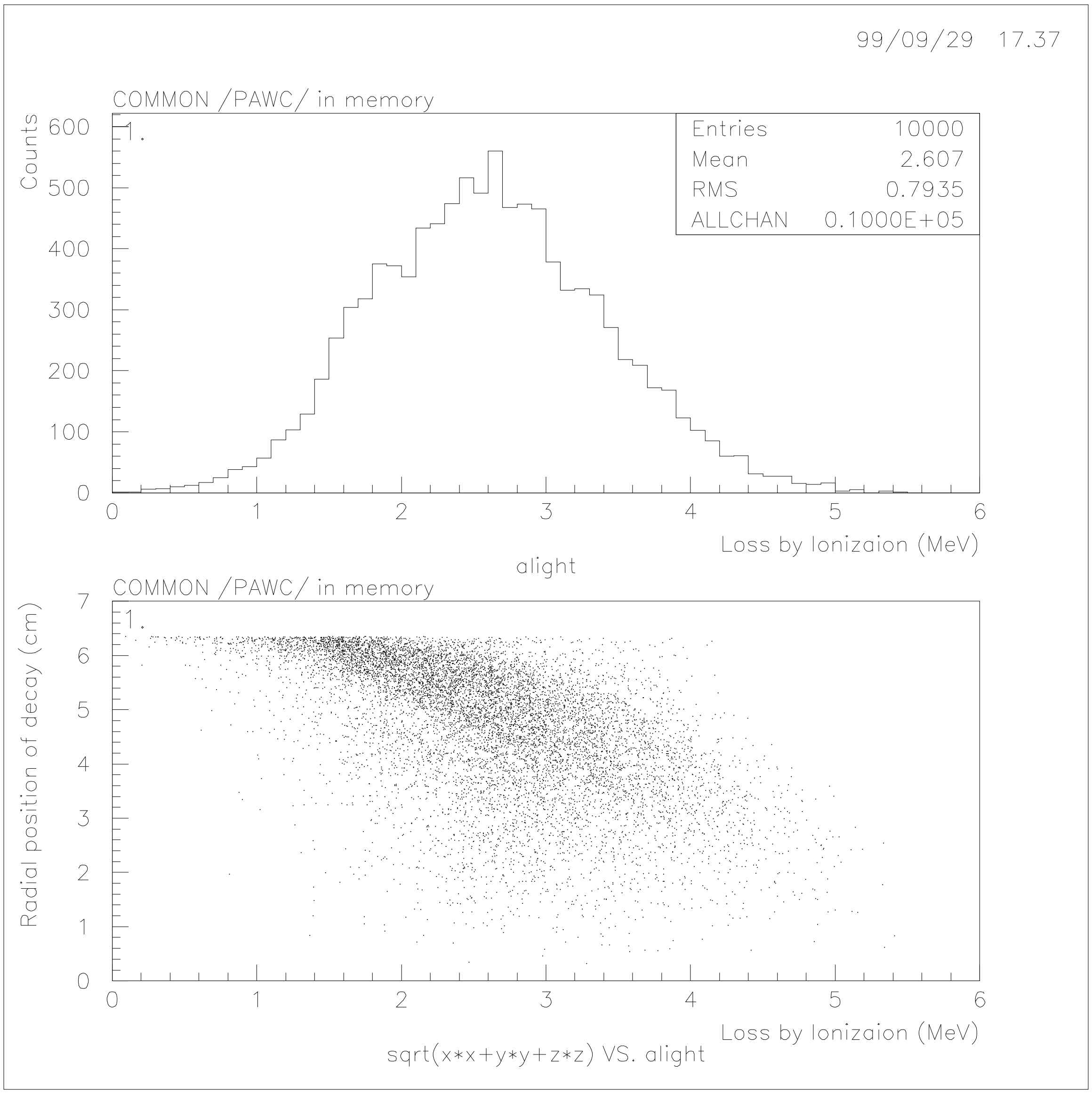

Figure 4.3: Alpha Particle Monte Carlo. The top plot shows the expected total energy loss by ionization of ^{8}Be alpha particles in one atmosphere pressure of helium in the ^{8}Li decay chamber geometry. The lower scatter plot shows this loss as a function of the radial position of the decay: decays near the wall are at the top of the plot and decays in the center at the bottom.

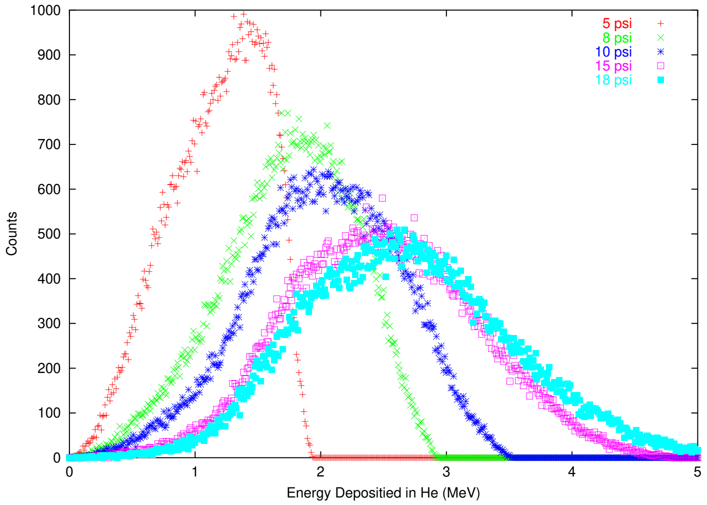

Figure 4.4: Alpha Energy Response Vs. Pressure. ^{8}Be alpha decays are modeled by Monte Carlo for different pressures of helium gas. Note that for all but the lowest pressures the total deposited energy is greater than 1 MeV.

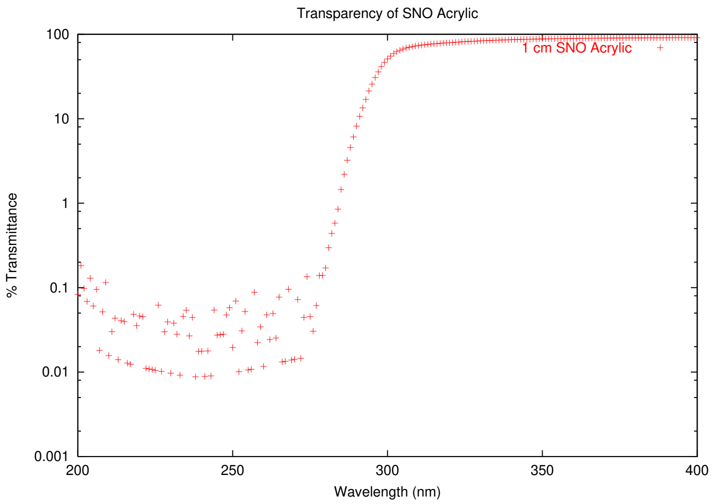

Figure 4.5: SNO Acrylic Light Transmission. The transmission curve was measured for a 9.9 mm thickness piece of SNO acrylic at Guelph, using a Beckman model DU-640 spectrophotometer at the University of Guelph. Other measurements are given in [50].

The PMT sees only about 3% of direct light in the decay volume, and the PMT has about 25% quantum efficiency, so a 1 MeV alpha has a gives a response of about 3 photoelectrons. This response was improved in several ways outlined below.

First, the inner walls of the chambers were painted with a titanium-oxide paint to enhance the light reaching the phototube by multiple reflection. A water-based white titanium-oxide paint (Bicron BC-620) was used, as this paint has good reflectivity for blue light (see Figure 4.6). Although this system worked acceptably with the acrylic-ball prototype, the signal was indistinguishable from thermionic dark current pulses (i.e. the response was about 1 p.e.). (The reason for this was believed to be because of the larger acrylic window in the acrylic ball. It is supposed that this window acted as a light-pipe to gather more light.) Tests done with the source (described in Chapter 5 showed that PMT pulses were coincident with decays in the ball, so the tag system worked in a minimal fashion.

Second, the decay volume was modified by application of a wavelength shifter to the inside wall of the ball, on top of the reflector paint. The wavelength shifter, tetraphenyl butadier (TPD) was applied in solution of toluene 2% polystyrene, and 1% TPD. The toluene was then allowed to evaporate, leaving a thin layer of polystyrene and TPD on the surface. The efficiency of the tagging system before and after this modification is measured in Chapter 5.

Despite difficulties, the scintillation technique works reliably, and allows for a

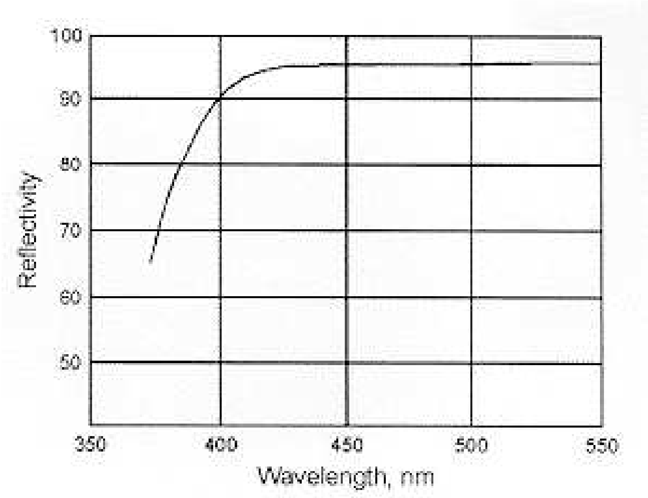

Figure 4.6: Reflectivity of BC-620 Paint. Taken from Bicron product specifications.

good flexibility of design. This flexibility allowed the construction of a spherical decay chamber with thin external walls, which allows for reasonably small energy loss of the beta particle as it leaves the walls. This design is somewhat conservative in physical aspects, possible improvements are discussed in Chapter 8.

5

Bench Test Results

Several aspects of the ^{8}Li system were tested extensively before preparing the source for introduction into the SNO detector. These tests had several purposes.

First, the ^{8}Li production system (DT generator, gas board, etc.) was tested *in situ* (in the underground laboratory) to ensure that ^{8}Li could be produced.

Second, the tag chamber (decay chamber) was tested to ensure that a signal could be reliably generated. The tagging efficiency was measured as a function of various flow parameters to ensure stability (particularly with regard to decay chamber pressure). These tests were done with the tag chamber both before and after application of the TPD wavelength shifter.

Third, the overall yield of ^{8}Li needed to be measured and the transport efficiency was tested so that materials could be chosen to maximize ^{8}Li yield. Optimization of the system was performed empirically.

Fourth, it was important to test if the gas system produced any non-^{8}Li contam-

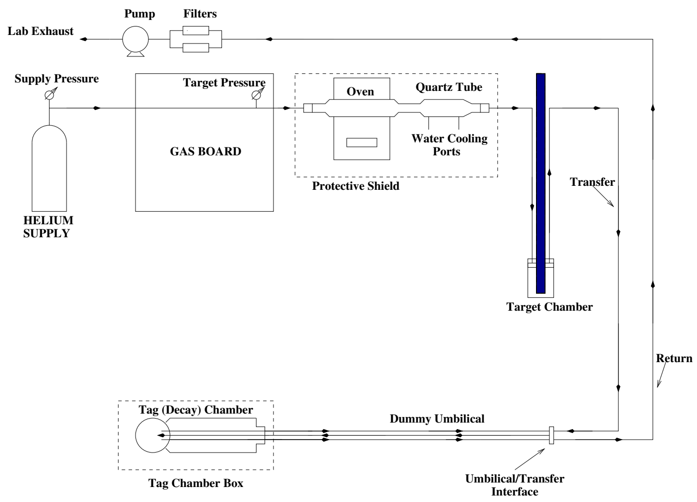

Figure 5.1: Diagram of Test ^{8}Li System..

ination, and the efficiency with which the tagging system rejected any such contamination.

These experiments were all performed underground at the SNO lab, with most of the equipment in the finalized form. The most important missing component was the umbilical transfer line, for which full-scale mock-ups were used (lacking outer jackets and potted signal lines).

5.1 Proof of Principle

The system was tested in a short-line configuration designed to maximize signal. A 33' long section of thick-walled, 1/8" ID teflon tubing provided the transfer line between the target chamber and decay chamber (rather than being separated by the full 250' of line needed to run in SNO). This ensured a high rate of ^{8}Li decays to observe.

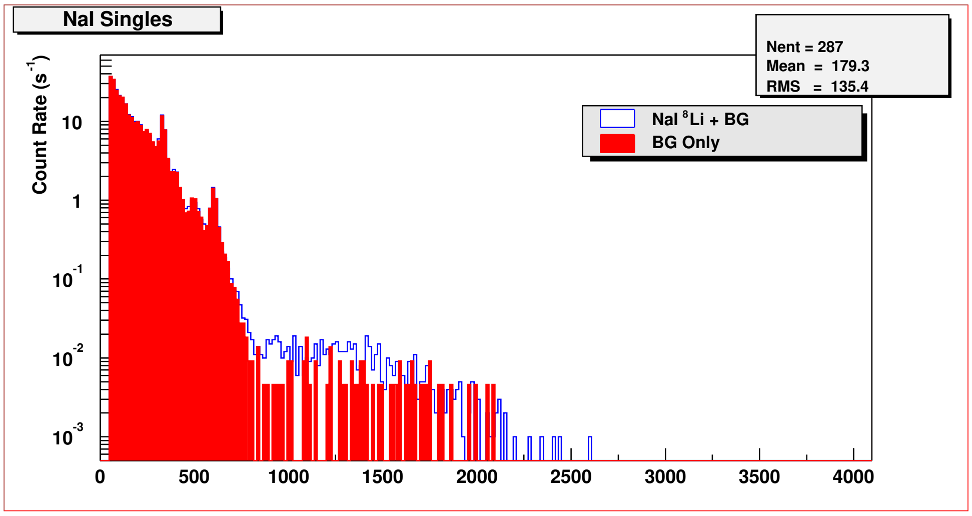

Figure 5.2: ^{8}Li β in NaI Detector. Note that the background falls off around channel 800, which corresponds to roughly 3.5 MeV of gamma energy.

A 5”x5” sodium iodide detector was placed next to the decay chamber. High energy events were seen in this detector if and only if helium gas was flowing through the system, the oven was above 600 C, and the DT generator was on. The observed spectrum is shown in Figure 5.2. This signal disappeared when either 1cm of aluminum or 5cm of acrylic was placed between the detector and the decay chamber, consistent with the detected particle being a high-energy beta.

It was observed that this signal could be seen in coincidence with PMT pulses from the tag chamber.

5.2 Tag Signal

The tag signal was tested to ensure that signal speed and amplitude were of sufficiently high quality to be useful and robust.

Before application of the wavelength shifter to the inside of the ball, the PMT response was quite poor, giving no more than a few photoelectrons per event, shown in Figure 5.3. These events were selecting using the 3-fold coincidence technique as described in Section 5.3.

Although this signal was of sufficiently large amplitude to successfully tag the alpha decays, the rise time was as long as 1μs, much too slow to be in time to tag an event in SNO (which has a valid time width per event of about 500 ns). Such a long rise time is consistent with values found in Birks [48].

After the application of TPD wavelength shifter, the pulse-height response of the tag chamber phototube was improved by roughly a factor of 4, with an associated reduction in the pulse rise time to $\sim$ 100 ns.

Based on research presented in Birks [48], nitrogen gas was employed as an additional wavelength shifter. It was found that a small admixture (2%) of N_2 gas further increased the output signal by a factor of 2. After these enhancements, the phototube signal was now quite sharp, with a rise time of approximately 50-100 ns and an amplitude of 100-300 mV on the anode. Figure 5.4 shows the signal pulse height using both wavelength shifters (TPD and N_2).

The same figure also shows how the system responds to activities other than alpha-decay. ^{16}N is a beta-gamma emitter with a branch to both high-energy gammas and to high-energy betas. The curve on Figure 5.4 shows how the decay chamber responds to ^{16}N decays using CO_2 as both the neutron target and the carrier gas. A small fraction of the beta particles will go upward through the acrylic window to create a small quantity of Cherenkov light directly in front of the PMT, generating a small but detectable signal. (This mechanism was confirmed by placing a piece of thin black plastic over the face of the acrylic window, for which case the signal persisted. This experiment demonstrated that the light originates from the window or PMT assembly, not from the decay volume.) Thus, it is possible for a beta-gamma decay to trigger the decay chamber. However, with the increased sensitivity made possible by the wavelength shifter a cut on pulse height can be made, allowing good rejection of this signal if it exists as a background. Background issues are discussed further in Section 5.4.

5.3 Efficiency

Two plastic scintillator paddles were used for the efficiency measurements. These paddles were approximately 1cm thick, 6" wide, and 12" long, with a 2" PMT at one end. Each paddle had reasonable detection efficiency to 1 MeV gammas (from ^{60}Co), but had very little energy discrimination. To run at an acceptable threshold meant

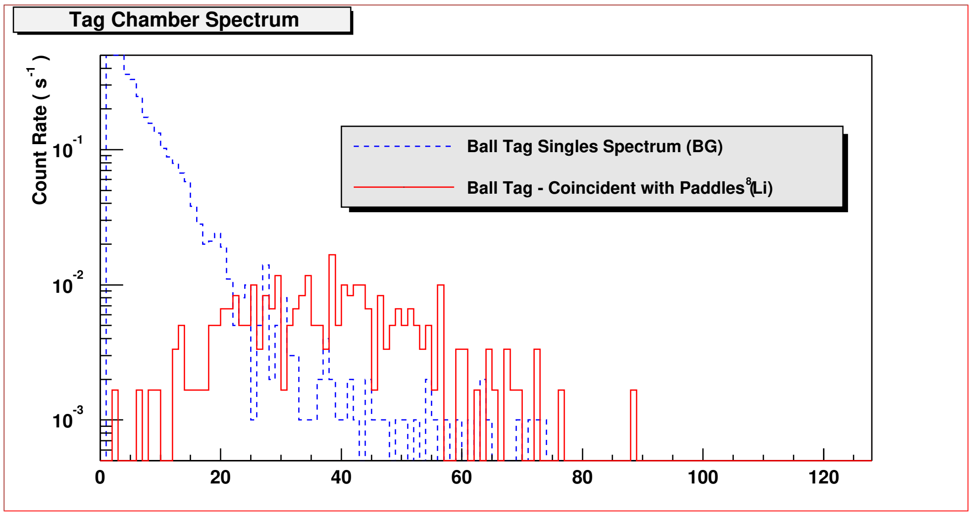

Figure 5.3: Ball Tag Signal Without Wavelength Shifter. Events were selected using the 2-3 coincidence technique described. The abscissa is in arbitrary units of pulse height.

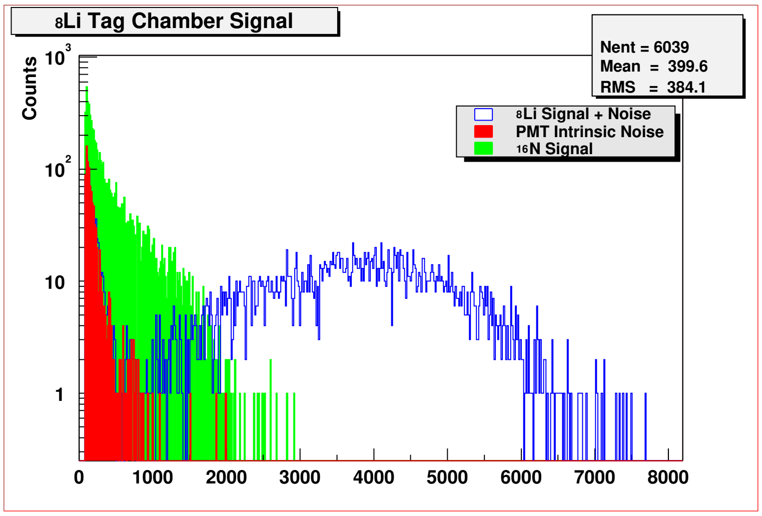

Figure 5.4: Ball Tag Signal With Wavelength Shifter and N_2 Gas. Ball PMT singles are shown for three cases: dark current, ^{8}Li signal, and ^{16}N signal. Note the horizontal scale is different from that in Figure 5.3.

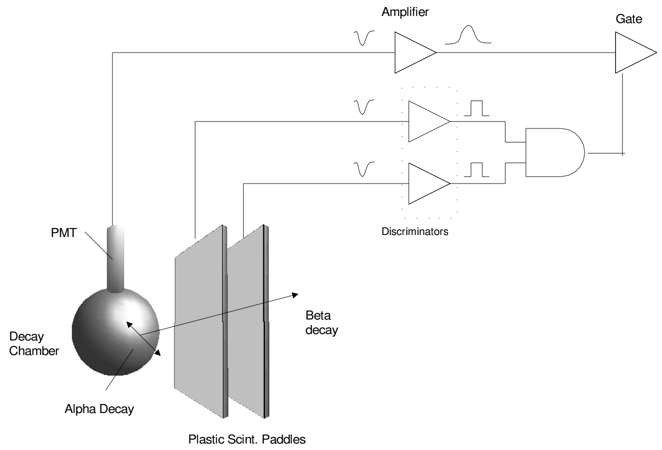

Figure 5.5: Schematic of 2-3 Coincidence System. Two paddles are placed next to the decay ball. Betas going through both paddles create a 2-fold coincidence. Successfully tagged events create a 3-fold coincidence. Both 2- and 3-fold coincidences were recorded. (Not shown.)

that each paddle counted at a rate of about 40 Hz under background conditions.

The paddles were arranged as shown in Figure 5.5, which allowed beta particles leaving the decay chamber to pass through both paddles.

The output signal from each paddle was fed to a shaping amplifier, then to a discriminator. A coincidence window was 5 μs was used to detect coincidences from both discriminators. The number of 2-fold coincidences was recorded.

The signal from the tag chamber was delayed, gated with the two-paddle coincidence (using a linear gate stretcher) and sent to an ADC, which recorded only tag-chamber pulses in coincidence with both paddles.

Background runs were taken periodically through the three days over which these experiments were conducted. Background runs were conducted by shutting off the gas flow to the tag chamber, but leaving the D-T generator on (since the generator creates a substantial gamma field when running). All background runs were consistent over this time to within statistical errors. The mean background rates were $120 \pm 4 \times 10^{-3}$ Hz for the two-paddle coincidence, and $0.81 \pm 0.33 \times 10^{-3}$ Hz for the two-paddle-plus-tag coincidence. (This latter number is possibly an overestimate due to spurious counting artifacts.) For the purposes of analysis, the triples background rate is taken as zero.

Because the system was run with double- and triple-coincidences recorded simultaneously, a count recorded as a triple coincidence was always counted as a double coincidence as well. This gives the analysis a slightly greater statistical power when looking at efficiencies, and much greater control of systematic problems.

Using the 2-3 coincidence technique, we ran under many different gas flow conditions. We concentrated our efforts on the short (33") transport line, and flow rates at 225, 250, and 275 cc/s of helium, with decay chamber pressures at or below 1 atmosphere. (Note that in the underground lab one atmosphere is equivalent to 18.1 psi absolute.)

We calculate the tagging efficiency by first presuming that there is no activity in or near the detection system that is not ^{8}Li (e.g. beta particles from another isotope in the carrier gas, or gamma rays from the environment) that can create a two-paddle coincidence. If this presumption is true, the ratio of double- to triple-coincidences (after background subtraction) measures the efficiency with which the ball tags ^{8}Be alpha decays. If it is untrue, (i.e. a background exists) the ratio is a lower limit on the ball tagging efficiency.

The formula used to calculate the efficiency is given in Equation (5.1):

$$\xi_\alpha = \frac{C_t}{C_d - R_d^{BG} \times t} \tag{5.1}$$

where C_t and C_d are the number of triple- and double-coincidence counts, respectively, R_d^{BG} is the rate of random double-coincidences, and t is the duration of the run. (Triple-coincidence background is negligibly small.) However, the uncertainty is not given by simple Gaussian statistics. We have two sources of uncertainty: the statistical variance on the number of triples measured, and the variance in the number of background events that are subtracted in the denominator.

The number of background events in time t is $C_d^{BG} = R_d^{BG} t$ and has a variance of

$$\mathrm{Var}(C_d^{BG}) = (\Delta R_d^{BG} t)^2 + (R_d^{BG} t) \tag{5.2}$$

The first term represents the uncertainty in the measured background rate; the second term represents the uncertainty in getting C_d^{BG} counts in time t, given a known rate.

The uncertainty on the efficiency is given by equation (5.3):

$$\left(\frac{\Delta\xi}{\xi}\right)^2 = \frac{1}{C_t} + \frac{(\Delta R_d^{BG} t)^2 + (R_d^{BG} t)}{(C_d - R_d^{BG} t)^2} \tag{5.3}$$

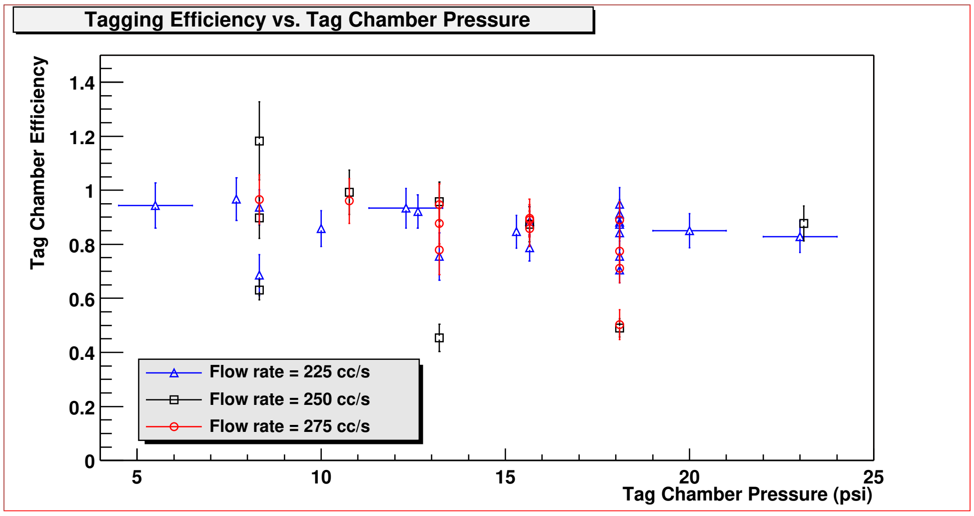

Figure 5.6: Tag Chamber Efficiency Vs. Tag Chamber Pressure. Points with horizontal error bars represent runs where pressure was measured at the gas board, and varied over the course of the run. Different flow modes are shown by different markers. Note that these runs were done without wavelength shifter or nitrogen gas.

It was predicted that the tagging efficiency of the decay chamber would be a strong function of pressure. One would expect a low decay chamber pressure to result in alpha particles depositing little energy in the gas (as shown in Figure 4.4). For low pressures, less light should reach the PMT, and therefore a smaller tagging efficiency should be measured. However, Figure 5.6 shows a very slight trend in the opposite direction, towards higher efficiency when the pressure is dropped.

The most likely explanation was that there was a beta-emitting background in the carrier gas that is creating false 2-fold coincidence counts. Lower decay chamber pressures result in lower decay chamber residence times, which would reduce the number of decays in the chamber for a (relatively) long-lived contamination isotope. This would decrease the number of 'false' 2-fold coincidences, thus making the system appear more efficient. This was the first evidence for a background in the detector; this data is used to put limits on the background in Section 5.4.1

Summing all runs together gives a mean tagging efficiency for the decay chamber of 86%. Several of the trials have results far away from this mean, but most are consistent with it. Although specific trials showed large variations in tag efficiency, this was largely uncorrelated to the gas flow conditions. Removing the worst outliers, 39 (out of 47) trials give a chi-squared of 67 for 38 degrees of freedom about this mean.

Note that all of the experiments described were done before the addition of wavelength shifter or nitrogen gas. A similar but shorter set of experiments were done after these modifications with similar results: an efficiency of approximately 0.92 ± 0.05 was measured at $P_d = 18$psi, and 0.97 ± 0.08 at $P_d = 8$psi. Again, the efficiencies were high, and increased slightly at lower pressures.

5.4 Backgrounds

Any calibration requires precise understanding of the signal introduced into the detector. The gas stream may be contaminated by radioactive isotopes other than ^{8}Li. Such a contamination is not of any concern unless it both generates tag chamber

PMT pulses and creates Cherenkov light in the water outside the chamber. A contamination generating no tag signal will simply be ignored in the analysis phase, and a contamination that generates no SNO detector trigger will not be recorded, so both of these conditions must be met for a contamination to impact calibration results in any substantial way.

A tagged background is undesirable in several ways. A background such as this is obviously of concern to measurements involving energy scale or charged current shape studies. If the contamination takes the form of a gamma (rather than beta) particle leaving the decay chamber it will artificially skew any estimates of reconstruction error, because a high-energy gamma ray will travel much further than a beta particle. However, data cleaning studies will be unaffected by such contamination, since they require only genuine 'physics' events, not beta particles in particular.

As was mentioned in Section 5.2, beta particles going through the acrylic window can create Cherenkov light seen by the PMT. This effect has been directly observed in this system by injecting a high rate of ^{16}N into the decay volume by running carbon dioxide rather than helium through the ^{8}Li system. The 5" x 5" NaI detector was used to find ^{16}N gammas. A coincidence was set up between this detector and the tag chamber. The efficiency with which the decay chamber tags betas was measured by:

$$\text{Efficiency}(\beta) = \frac{R_d - R_d^{BG}}{R_s - R_s^{BG}} = \frac{0.23\text{Hz} - 0.00\text{Hz}}{6.12\text{Hz} - 0.17\text{Hz}} = 3.9\% \tag{5.4}$$

Here R_d represents the counting rates of coincidences between the NaI and decay chamber, R_s represents the count rate of NaI singles. These rates were taken using counts above a threshold of about 3.5 MeV gamma energy, in ~25 minute runs. The measured coincidence requires a gamma ray, so the ^{16}N beta decays that were detected were not to the ground state but to the excited state. This demonstrates that beta particles of only a few MeV can trigger the chamber.

The ratio of the surface area in the decay volume exposed to the acrylic window, to the total surface area is 17.9 cm^2 / 506.7 cm^2 = 3.5%. This value agrees well with the result in Eq. (5.4), illustrating that this mechanism is fairly well understood.

Here we attempt to provide good estimates of this contamination here, but the ultimate measurement must be made by SNO itself, by looking for untagged events occurring near the decay chamber, which is shown in Chapter 7.

We assume that any tagged background must be a beta-gamma coincidence. There are basically two ways to look for such a contamination: attempting to identify excess betas coming from the source, or attempting to identify gammas associated with the source. Both of these techniques were attempted

5.4.1 Background Limits Using 2-3 Coincidences

This analysis attempts to find a excess of beta particles coming from the source, by employing the 2-3 coincidence technique used in Section 5.3. We use the assumption that the tag chamber is 100% efficient with respect to ^{8}Li decay, so that every event that was seen in the double-coincidence but not in triple-coincidence was due to a beta particle from a radioactive background in the gas.[1] For each run, we compute the number of double-coincidence events that are untagged by the trigger chamber:

$$\text{Events Untagged} = C_d - C_t - R_d^{BG} \times t \tag{5.5}$$

We plot in Figure 5.7 the rate of untagged events as a function of the estimated residence time in the trigger chamber, given by (5.6):

$$\tau_{res} = \frac{P_{\text{decay}}}{14.77\text{psi}} \times \frac{V_{\text{decay}}}{Q} \tag{5.6}$$

where P is the pressure, V is the volume, and Q is the mass flow rate (normalized to one atmosphere). If the gas is evenly mixed in the decay chamber volume, we would expect the event rate to go as described by (5.7):

$$\text{Measured Rate} = \text{Total Activity} \times \frac{1}{1 + \frac{\tau}{\tau_{res}}} \tag{5.7}$$

The untagged event rate follows a trend that implies that there is indeed a background with a half life of more than a second. (Fits to this trend are inconclusive as they tend to favor an unrealistically long half-lives.) Background runs show no long-lived background, so the maximum half-life is less than one minute. This is consistent with several different candidates for a background, including ^{11}Be and ^{16}N. It is unclear if there is a constant background due to untagged ^{8}Li events. We conclude

[1] This assumption is opposite to the one used to find tagging efficiency limits. This assumption is worst-case with respect to backgrounds, and the earlier assumption was worst-case with respect to trigger efficiency.

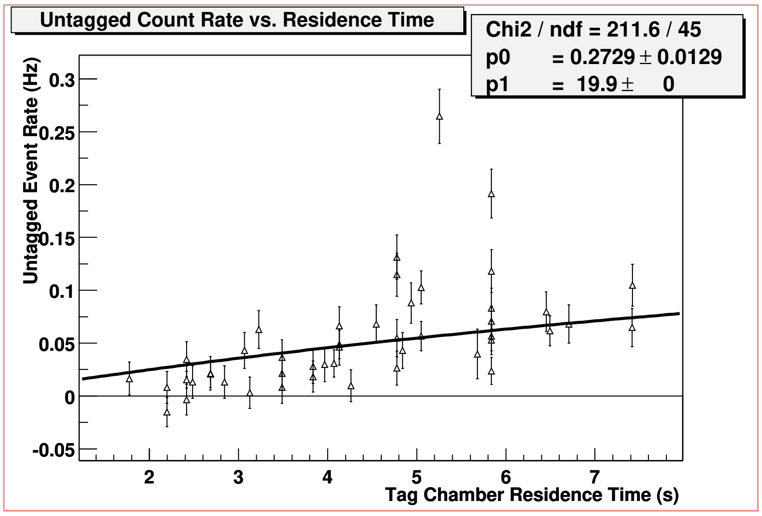

Figure 5.7: Untagged Events Vs. Decay Chamber Residence Time. The event rate is as seen in the paddles; multiply by 11.3 to get the total rate for the source. The solid line is the curve expected for 0.27 Hz of ^{11}Be, which has a 19.9s mean life.

that this evidence appears inconsistent with zero background, but does not give a useful lower limit.

At low residence times, the background rate in the paddles is less than 0.05 Hz. As will be shown in Section 5.5, the trigger efficiency of the paddles to betas is 8.8%, so this yields a total estimate of the beta rate as $\leq$ 0.57 Hz. Because this analysis depends upon the assumption that the ball is 100% efficient, it is only an upper limit on the possible contamination.

5.4.2 Background Measurements with NaI

The experiment described here attempts to look for an excess of gamma rays when the source was turned on, or to look for beta-tagged gamma rays.

These experiments employed a 5"x5" NaI detector in an attempt to observe any gamma-rays coming from the ^{8}Li decay chamber. (A germanium detector, although having superior power to discriminate the type of contamination, would simply have an efficiency too low to see activities at the low rates we are concerned with.) Two experimental setups were employed, the first using coincidences with the ball, and the second using the scintillator paddles.

5.4.2.1 NaI and Ball

An experiment was performed by measuring NaI counts as singles and counts in coincidence with the tag chamber. This test was done under conditions as close as possible to those we anticipated would be used during a real deployment (at a pressure of about 12 psi) but in the short (33') configuration at 220 cc/s helium flow. This test was done before application of the wavelength shifter, and without N_2 gas. The NaI detector was separated from the decay chamber by 5 cm of acrylic, which is sufficient to stop the highest-energy betas from the source from reaching the NaI.

We observed 1 coincidence with the ball in 1600 seconds, above an energy threshold of 3.5 MeV, compared to 0 events in the same duration with the gas flow off. An upper limit, to two sigma, is 0.0019 Hz of tagged $\beta - \gamma$ events. This is multiplied by our known efficiency for tagging betas with the decay chamber (3.9%) to arrive at a rate of 0.054 Hz total $\beta - \gamma$ events with $E_\gamma > 3.5$ MeV occurring in the ball.

Taking no energy threshold, we measured a total of 51 counts with gas on, and

41 counts with gas off. This corresponds to an upper limit on tagged events of 0.018 Hz, or 0.46 Hz of total activity, each to two sigma.

Both of the coincidence results are statistically consistent with zero background to within a 68% confidence limit.

Looking only at NaI singles events taken in the same run with energies greater than 3.5 MeV (to minimize background), we saw 292 events with the gas flowing, compared to 267 events in the background run, so these 25 extraneous counts come to 0.0156 ± 0.0148 Hz of γ events caught in the NaI detector. This measurement of 25 counts roughly agrees with 1 count in coincidence, given a 3.9% beta-detection efficiency by the tag chamber.

We can estimate that the total efficiency of the NaI detector to gammas, including solid angle, is approximately 3%, so these measurements put a rough upper limit on tagged $\beta - \gamma$ background (above 3.5 MeV) as about 1.5 Hz. The best-fit number is one third of this, and the rate is consistent with zero to within one sigma.

5.4.2.2 NaI and Paddles

After application of the wavelength shifter, we again sought to perform a background measurement, this time done under slightly better conditions. For this experiment, we intentionally ran the system with a slightly low flow rate (200 cc/s He), included an admixture of $\sim$5% of N_2 gas, and ran the decay chamber at 23 psi (absolute) pressure. This had the effect of increasing the residence time of the gas in the decay chamber from 2.5 seconds (in the previous experiment) to 8 seconds. By this we hoped to enhance any contamination signal. This configuration was run for approximately 90 minutes. Two simultaneous measurements were performed, each using a gamma energy threshold of $E_\gamma > 3.6$ MeV.

The first measurement was to look at NaI singles, but with a scintillator paddle inserted between the ball and the NaI to veto ^{8}Li betas. This allowed us to use the NaI detector close to the decay volume, slightly increasing the gamma detection efficiency.

Using the active shielding technique, an excess of 0.053 ± 0.021 Hz of activity in the NaI was observed. Figure 5.8 shows the resulting spectrum.

The second measurement looked at NaI pulses that were in coincidence with a paddle on the far side of the decay ball. This arrangement was designed to detect escaping high-energy betas with the paddle, rather than using the tag chamber PMT. A short ^{16}N run was performed to evaluate the efficiency to detect a beta in the paddle. This resulted in an excess rate of 0.034 +- 0.006 Hz of activity in the NaI, after correcting for the paddle efficiency. This result is shown in Figure 5.9.

These two measurements are in agreement to within statistical uncertainty.

A GEANT simulation of the geometry [51] was performed for 6 MeV gamma particles in our geometry. It indicated that the NaI detector had an efficiency of 2.7% if a deposited energy threshold of 3.6 MeV was applied. This efficiency allows us to

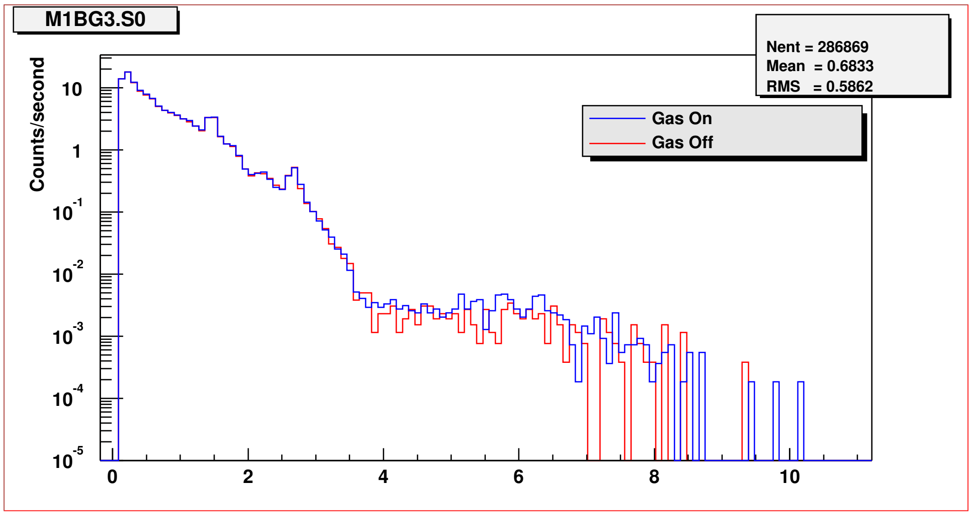

Figure 5.8: NaI Singles, BG Studies. Events (vetoed by active shield) counted in NaI detector are shown.

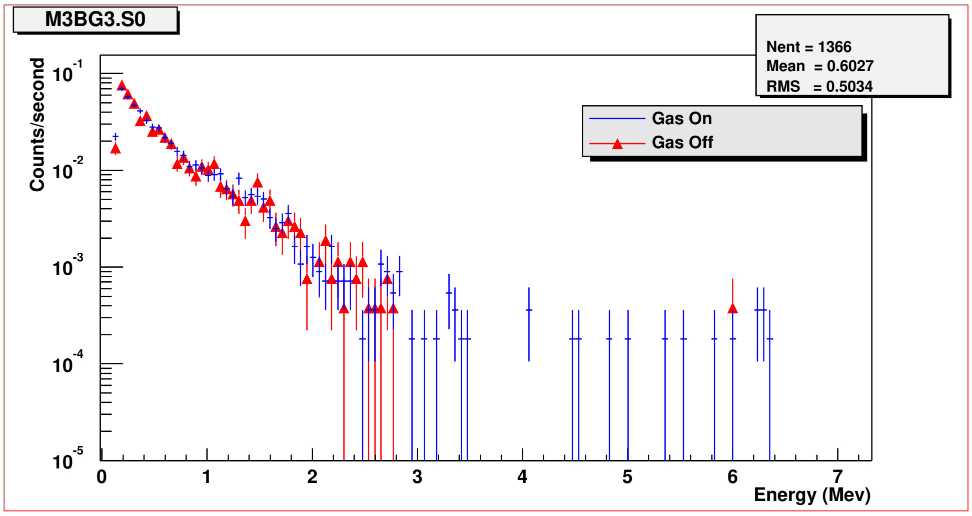

Figure 5.9: NaI Coincidences, BG Studies. Events seen in coincidence with a scintillator paddle are shown.

estimate our total background rate as approximately 1-2 Hz of high-energy gammas coming from the ball into 4π solid angle.

Because this run had a long residence time, the background signal is enhanced. For an isotope with a half-life of 7 seconds, this enhancement is roughly a factor of 2, so our predicted rate of background events (greater than 3.6 MeV) is 0.5-1 Hz into 4π.

However, only about 4% of the these decays will successfully be tagged. Further, a modest cut on PMT anode pulse height will reduce the tagged event rate by another factor of 10, so we can expect an upper limit of activity in SNO of about 0.004 Hz, compared to an expected yield of ^{8}Li on the order of 0.2 Hz.

5.4.3 Possible Contaminants

Identification of the contaminant allows for better prediction of what signals to expect when running the source in the SNO detector. There are two likely candidates for high-energy[2] radioactive contamination of the gas stream. Both are sufficiently long-lived to survive the gas transport process.

Two possible beta-gamma decays appear to be likely contaminants. In previous tests at Chalk River[38] the most important contaminant was found to be ^{11}Be, produced by ^{11}B (n,p) ^{11}Be. After this discovery, ^{11}Be contamination was suppressed

[2] Radioactive backgrounds must have decay energies in excess of ~2 MeV to trigger SNO even under ideal conditions, but must also have lifetimes on order of one second or more. These two criteria are moderately restrictive.

by reconstructing the boron target, which is now set in a polyethylene matrix. This arrangement tends to stop ^{11}Be in the target, since it has a lower average recoil energy than does ^{8}Li.

^{11}Be has only a $\sim$10% branching ratio to high-energy gammas. If we do have a 1 Hz contamination of gammas above 3.5 MeV, we would expect to see 3 Hz of 2.1 MeV gammas, (see Figure 5.10), or 0.1 Hz excess in the detected gamma rate at this energy. Figure 5.8 shows no detectable excess there, although it should be just within the limit of sensitivity. This is suggestive that ^{11}Be is not responsible for the contamination.

The second likely contaminant is ^{16}N, which can be produced in a number of ways. (See, for example experiments done with target materials by Hamer [4].) If a small quantity of O_2 or CO_2 were introduced into the gas stream, for instance, a sizable quantity of ^{16}N could be created by ^{16}O (n,p) ^{16}N. Other possibilities include activation and recoil from materials in or near the target chamber, such as teflon or G-10 (^{19}F (n,α)) or phenolic ((n,p) on oxygen in C_6H_5OH).

5.5 Yield

The total yield of ^{8}Li decays in the chamber was measured in several different configurations. As discussed in Chapter 3, the yield must be found by empirical measurement, and the optimal operating conditions can only be estimated by gas transport

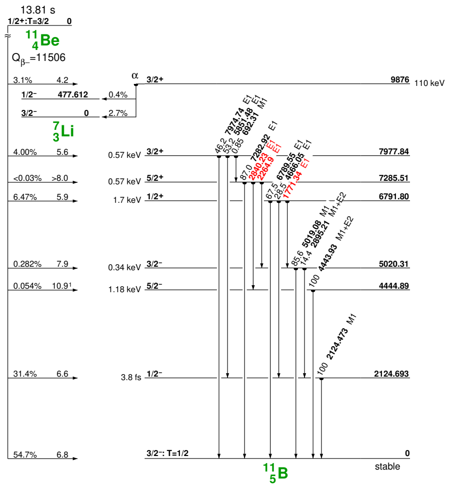

Figure 5.10: ^{11}Be Decay Scheme.

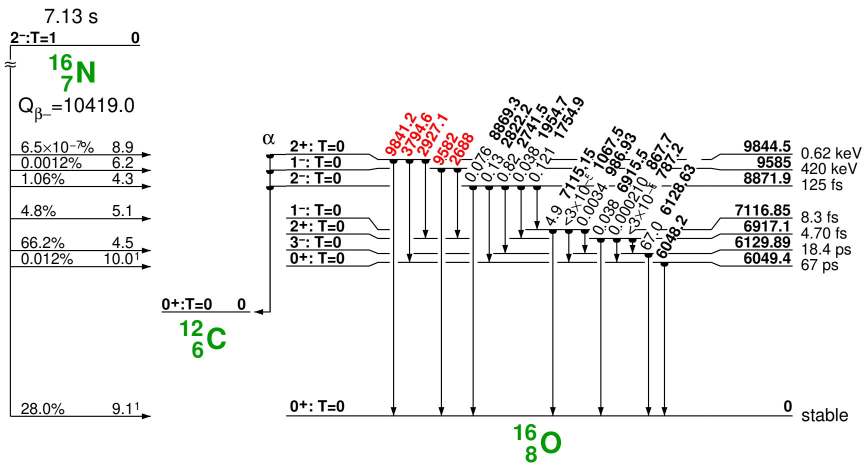

Figure 5.11: ^{16}N Decay Scheme.

models. In these measurements, 'yield' refers to the rate of tagged ^{8}Li.

5.5.1 Preliminary Tests Using 2-3 Coincidence Technique

Before application of the wavelength shifter, the 2-3 coincidence method was required to estimate yield, because the signal strength was so low that the signal could not be differentiated from the dark current. A subtraction of the dark-current background was possible, but led to substantial statistical errors if the ^{8}Li rate was low.

In order to estimate total yield, we assume that the energy deposited in the ball is independent of the probability of the event being tagged in the paddles. We further assume that every triple coincidence is due to ^{8}Li (which should be a good approximation even if a small background exists). We then take two successive high-rate ^{8}Li runs in which we measure the rate of tag chamber singles, then tag chamber and paddle triple-coincidence events. We further assume that the ^{8}Li total event rate did not vary between these runs, which were done in immediate sequence under the same gas conditions. Above a software threshold (13 channels), we measured a rate of 6.52 ± 0.10 Hz in tag chamber singles over a background of 3.095 ± 0.056 Hz, compared to 0.303 ± 0.022 Hz in triples. This gives a total efficiency for the double-paddle coincidence of $8.84\% \pm 0.71\%$.

The double-paddle coincidence measurement allows us to use the 2-3 coincidence data to measure yield. Figures 5.12 and 5.13 show the event rate measured by double- and triple- coincidence respectively. In these plots, the lengths referred to are 33, 150,

Name	Inner Capillary			Outer Capillary		
	Material	ID	OD	Material	ID	OD
'^{16}N Umbilical'	Teflon	0.241	0.301	Polyethylene	0.432	0.635
Small **O**uter **D**iameter	PTFE	0.389	0.414	Silicon	0.600	0.800
Large **O**uter **D**iameter	PTFE	0.389	0.414	Silicon	0.800	1.000

Table 5.1: Umbilical Prototypes. All measurements are in cm. See Figures 3.5 and 3.6 for notes on calculated efficiencies.

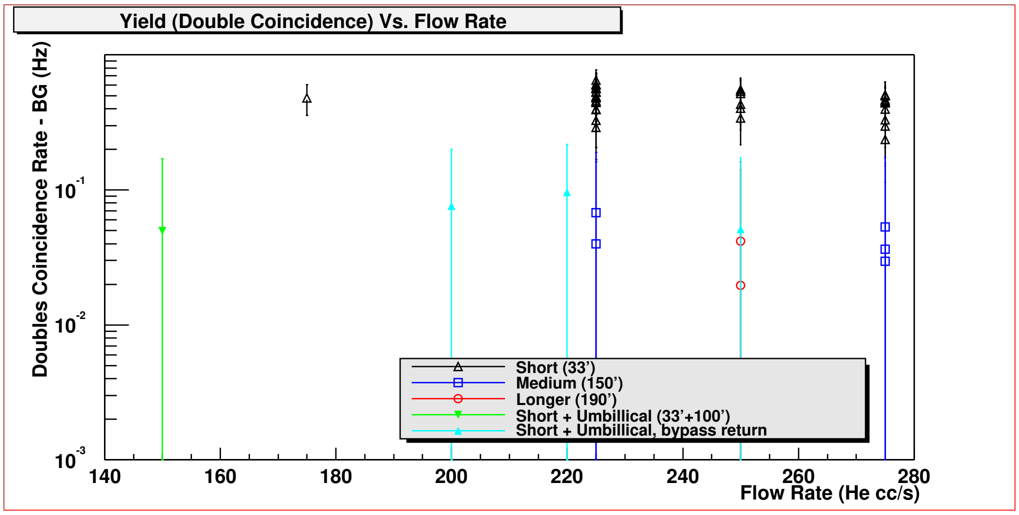

Figure 5.12: Double Coincidence Rate Vs. Flow Conditions. The ordinate shows measured rate using coincidence techniques; multiply by 11.3 to get total yield.

or 190 feet of thick-walled 1/8" ID, 1/4" O.D. teflon line. The 'umbilical' referred to is the "^{16}N umbilical" which is the prototype for this system. (See Table 5.1.)

The maximum rate of ^{8}Li seen in the 33" configuration is about 5.5 Hz. This was high enough to estimate that our goals were achievable. We realized, however, that the prototype umbilical system (originally used for the ^{16}N source) would not work, since we saw practically no activity when the umbilical was used. The reason for this was clear: the conductance of the coaxial return line was too low, which made the

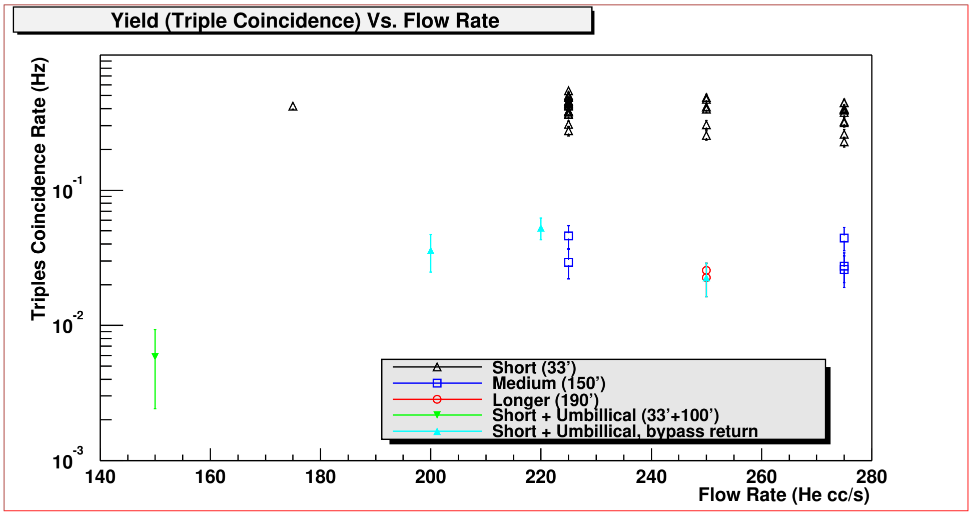

Figure 5.13: Triple Coincidence Rate Vs. Flow Conditions. The ordinate shows measured rate using coincidence techniques; multiply by 11.3 to get total yield.

decay chamber pressure too high. A vacuum pump was used on the return line, but was unable to draw enough flow to keep the decay chamber at low pressure. The pressure differential across the input capillary was small and the resulting transport time was high.

To prove this hypothesis, we ran the system with the same inner (input) capillary, but by-passed the coaxial return line to gain large exhaust conductance. This allowed us to increase the flow rate and also keep the pressure in the decay chamber low, so the gas could accelerate quickly down the input line. Doing this, we achieved approximately 0.2 Hz total yield. This is similar to the result achieved when a uniform 190' line of 1/8" ID line was used, instead of the ^{16}N-style capillary.

5.5.2 Final Tests

Subsequent tests used the TPD wavelength shifter and nitrogen injection. In these tests, the ^{8}Li tag signal was well enough distinguished from the phototube dark pulses that no coincidence technique was required. (Tagged background, if existent, is known to be a small contribution to the total tagged signal.) Yield was taken as being equal to the number of counts above a software threshold for the tube. This threshold was chosen to minimize dark counts while cutting few signal counts. (The 2-3 coincidence technique was used to estimate that the sacrifice of ^{8}Li events with this cut is $\lesssim 5\%$.)

No measurable difference in yield was observed with the introduction of nitrogen gas, when measured at short transfer lengths. This indicates that there will be no large yield decrease when using nitrogen gas to enhance the tag signal, despite the heavier gas mixture.

Two new umbilicals were tested, denoted the 'LOD' and 'SOD', described in Table 5.1. The SOD is a slight enlargement on the '^{16}N umbilical', in an attempt to modify existing technology to work with the new system. It uses a thin-walled inner (input) line, and an exhaust line that could be potted in the standard 1/2" umbilical. The LOD has a much larger return line, and requires a 5/8" umbilical, which in turn requires a redesign of the umbilical retrieval mechanism (URM). Results are shown in Table 5.2. Several different flow conditions (target chamber pressure, flow rate) were applied. Decay chamber pressures below one atmosphere (18 psi underground) were achieved by applying a vacuum pump the exhaust line.

As expected, the LOD umbilical gives substantially better yields than the SOD umbilical. Both gave the best results with a flow rate of 275 cc/s of helium gas. The LOD results give slightly better results with low decay chamber pressures. Although different pressures and flow rates were applied, no clear trends exist due to the dispersion of the results (due to low statistics). Precise tuning will require long running times, but the first line of Table 5.2 provides good default running conditions for the source, with a net yield of somewhere between 0.15 and 0.20 Hz.

The SOD umbilical was tried with two variations. One variation (marked 'bypass' in Table 5.2) was to bypass the return line. This experiment was done to prove that the input line was of sufficient size and quality to get a good yield, but that the exhaust line was the limiting factor in getting a good yield. Yields were improved when a better exhaust conductance was allowed. This explains why the LOD gave better yields than the SOD. The second experiment (marked 'reverse' in Table 5.2) reversed the input and output connections, so that the input gas flowed around outside of the coaxial line and the exhaust returned through the small inner line. This experiment showed that the umbilical would not work in such a configuration.

Several system modifications were tried with the LOD umbilical. Most notable is introduction of a collar inside the target chamber, which restricts the volume, decreasing residence time (τ_t) in an attempt to increase yield. No substantial yield gain is in evidence, however. This may be evidence that the laminar flow through the target chamber renders the complete-mixing model irrelevant.

The effects of shortening the umbilical is shown. The shorter length is chosen to be just barely long enough to deploy the source to the center of the SNO detector, with increased yield as a result. This had the expected effect, increasing the yield by 30%.

Lastly, the fitting coupling the umbilical to the ball was modified with a short piece of narrow capillary to see if the flow patterns in the decay chamber could be improved. This did appear to improve the yield by as much as 40%.

5.6 Conclusions

The most important result was proof that the ^{8}Li system does generate an acceptably high yield, and that the isotope produced was a high-energy beta with an alpha that is tagged in the decay chamber. Further gains may be possible with optimization of the gas lines and the target chamber, but we predict a delivery rate of $\sim$0.2 Hz of tagged ^{8}Li to SNO, using the LOD umbilical.

We have demonstrated that the tagging system can be made to work reliably. Wavelength shifter and nitrogen gas injection help enormously in amplifying the signal and decreasing the rise time. The tagging efficiency has a lower limit of approximately 90%. The tagging efficiency varies only slightly with pressure, with a trend toward

Run Configuration	Q(He) (cc/s)	$Q(N_2)$ (arb.)	P_d (psi)	Yield (Hz)
LOD	275	5	10.1	0.198 ± 0.022
LOD	275	5	10.1	0.158 ± 0.020
LOD	275	5	21.1	0.126 ± 0.018
LOD	275	5	13.1	0.188 ± 0.021
LOD	276	5	10.1	0.164 ± 0.022
LOD	276	5	21.1	0.112 ± 0.020
LOD	290	2	10.1	0.169 ± 0.008
LOD	300	5	10.6	0.054 ± 0.014
LOD new target	290	2	20.5	0.154 ± 0.011
LOD new target	290	2	10.6	0.197 ± 0.013
LOD new target	290	2	10.1	0.173 ± 0.010
LOD new target, Short	290	2	10.1	0.271 ± 0.017
LOD new target, Short	290	2	20.5	0.235 ± 0.012
LOD new target, Short, Insert	259	2	20.5	0.283 ± 0.021
LOD new target, Short, Insert	291	2	15.5	0.314 ± 0.030
LOD new target, Short, Insert	291	2	10.1	0.336 ± 0.030
LOD new target, Short, Insert	291	2	20.5	0.320 ± 0.025
LOD new target, Short, Insert	291	2	13.1	0.366 ± 0.031
SOD	200	4	19.1	0.096 ± 0.017
SOD	250	5	22.1	0.102 ± 0.017
SOD	250	5	28.1	0.114 ± 0.018
SOD	275	5	23.1	0.150 ± 0.020
SOD	290	2	14	0.098 ± 0.007
SOD	300	6	24.1	0.126 ± 0.019
SOD	350	7	25.5	0.084 ± 0.016
SOD bypass	275	5	13.1	0.226 ± 0.023
SOD bypass	275	5	8.2	0.188 ± 0.022
SOD reverse	275	5	19.1	0.070 ± 0.015

Table 5.2: Umbilical Yield Tests. Yield is measured for various umbilical configurations, as given in Table 5.1. $Q(N_2)$ is in arbitrary units (roughly cc/s within a factor of 2). 'New Target' runs have the extra target collar installed, see text. 'Short' runs have the conduit shortened from 150 to 135 feet, and a the umbilical shortened from 100 feet to 75 feet. 'Insert' runs have modification to the decay chamber interface. 'Bypass' runs do not use the umbilical exhaust line. The 'reverse' run inverts the input and output lines in the coax.

higher efficiencies at lower pressure, which may be evidence of contamination.

There is a substantial body of evidence to suggest that there is a β-γ contaminating isotope in the gas stream. Two candidates are ^{11}Be and ^{16}N, with total β rates of $\sim$1 Hz in the decay chamber. Of the two ^{11}Be is disfavored by the evidence. At the observed rate, ^{16}N is the more dangerous of the two, since it has a larger branching ratio to high-energy gammas. This background is expected to give approximately 0.03 Hz of tagged events, and 0.003 Hz of tagged events above a conservative software threshold, so the fraction of data taken due to contamination will be about 1% of the ^{8}Li signal, multiplied by the branching ratio of the isotope to high-energy gammas.

It is worth reiterating that this contamination can be accurately determined *in situ*, by looking for the untagged events reconstructing near the decay chamber during a source run in the SNO detector, described in Chapter 7.

6

Monte Carlo Predictions

These analyses are based on Monte Carlo data produced by a customized version of SNOMAN (the Sudbury Neutrino Observatory Monte carlo and ANalysis program) version 3.02. None of these simulations include the umbilical, carriage, manipulator weight, or manipulator ropes. In each case, the source was positioned at the center of the detector; no effort was made to look at the source systematics as a function of radial position. Events were generated from a ^{8}Li beta-spectrum. The source in each case was assumed to be only tagged, not triggered, so there is a simulated hardware trigger threshold of NHIT ≥ 20. Each run consists of $\sim$ 50k events.

6.1 Source Description

6.1.1 Stainless Steel Ball

The stainless steel ball is not modeled completely, but has the basic components that exist in the source. It has the following components:

Decay Volume The decay volume is modeled as a perfectly uniform shell of stainless steel, 0.05 cm thick and 6.41 cm in outer radius.

Reflector Paint. A thin (0.1 cm) layer of paint coats the inside of the sphere. In real life, this paint is a suspension of titanium dioxide, but in the simulation has the material characteristics of 'dark' acrylic, i.e. acrylic with short absorption lengths. (The coat of wavelength shifter is negligibly thick.)

Carrier Gas. For these simulations, the gas volume is treated as vacuum. The energy loss of a high energy beta through several centimeters of low-pressure helium gas is negligible.

Neck. The neck is modeled incorrectly as being a cylinder of stainless steel 11.4 cm in diameter, with a flange above it of 15.3 cm. (These measurements are the same as those used in the acrylic ball prototype described in Chapter 8) The true source has a tapered neck closer to 7.2 cm across, with a flange that is 12.4 cm across. These larger dimensions will distort upward-going events in the simulation, so Monte Carlo results may be distorted for upward-going events.

PMT. The PMT is not modeled; this region is solid metal.

Window. Attached to the end of the neck is a 1/4" (6.35mm) acrylic window, which serves to protect the PMT and act as a light pipe to for the gas scintillation light.

Endcap. The endcap sits atop the thorax, a stainless steel cylinder just over one foot long, in rough approximation to the true piece, which is slightly longer. This piece is made of solid stainless steel in the model, whereas the real hardware is hollow, with only a 1 cm thick wall.

6.1.2 'Blank' Source

The ideal source is one with no walls. This case has no components existing in the D_2O. Events are generated on a thin shell of radius 6.35 cm, with isotropic direction.

6.1.3 'Shadowed' Source

One attempt to reconcile the ideal case to the practical case is to generate events in a thin shell just outside the real source. Beta particles created in this way lose no energy in going through the wall of the source (unless they backscatter into it), but do have their Cherenkov light shadowed by the source in a similar way.

6.2 Energy Response

6.2.1 Nominal Response and Correlation with Direction

The first question to be asked of any design is how well the measured Cherenkov light (measured by NHIT) is representative of the beta energy. Betas can lose energy in the wall of the source, and light can be shadowed by the source.

The basic NHIT response of the SS ball is shown in figure 6.1. However, it can be seen from figure 6.2, the mean NHIT of the ball source is strongly dependent upon the

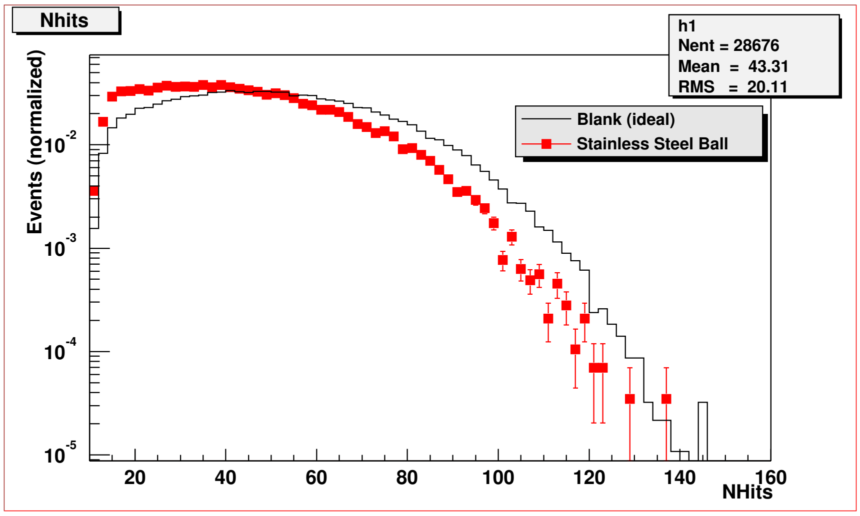

Figure 6.1: SS Ball: NHIT. Statistical errors are shown with error bars. Each run is normalized to the same number of detected events.

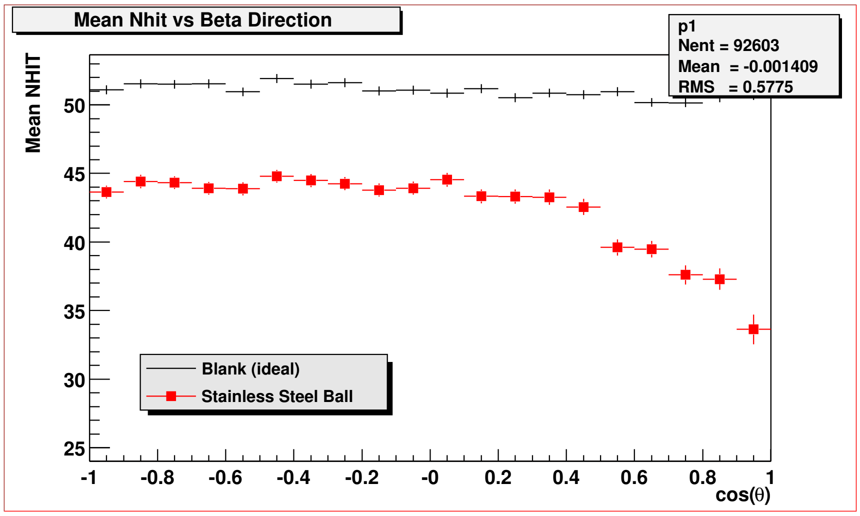

Figure 6.2: SS Ball: NHIT as a Function of Theta. Statistical errors are shown with error bars. Upward-going betas get much more light absorbed than downward-going ones

direction of the beta. This is unsurprising given that all of the optical complications of the ball source are on the top, namely the neck piece, neck flange and endcap.

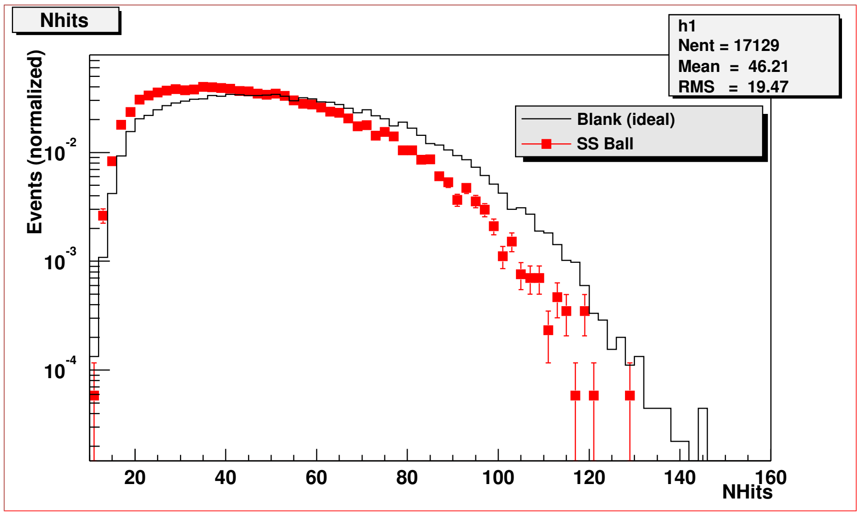

Figure 6.3: NHIT for SS Ball With Cut on Direction. Each spectra is cut so that $\cos\Theta_{fit} < 0$, using the reconstructed direction from the time fitter (FTT). Statistical errors are shown with error bars. Each run is normalized to the same number of detected events.

If we take a cut such that we demand that events are reconstructed to be going downwards (i.e. $\cos\Theta_{fit} < 0$), then the source gives an NHIT spectra as shown in figure 6.3. It can be seen from this plot that the source creates substantial distortion of the spectra shape.

In order to de-convolve this picture with the smear of the ^{8}Li spectrum, one can look at the mean number of hits generated by a beta of particular energy. This is shown in figure 6.4 for both the cut and the un-cut data. It can be seen from this figure that above about 8 MeV, there is a loss of about 1.5 detected photons per MeV of beta energy.

The 'blank' source is shown in each of the energy response plots in Figures 6.4

through 6.6. This response falls off at low energy, due to the relatively high stopping power of the water at low energy. One feature to disregard is the apparent up-turn in Nhit/MeV at the lowest energy bin (e.g. the 2 MeV bin in Figure 6.4.) This is due to the simulated hardware trigger threshold of $\sim$15 Nhits; a few low-energy betas make large-nhit signals that pass this threshold, artificially skewing the Nhit/MeV ratio. This bin is shown in these plots to illustrate what is essentially energy straggling at low beta energies.

The energy loss in the source wall is approximately 1.5 NHIT per MeV, corresponding to roughly 2 MeV of measured energy.

6.2.2 Source Shadowing

We can find out which mechanisms are responsible for the energy loss. The beta loses energy as it passes through the source wall. Some of the light created by the beta is shadowed by the source itself. Figure 6.5 shows what happens if we inject the simulated ^{8}Li betas into the water just outside the source container. This illustrates the reduction in detected photons for the case where no energy is lost in the wall (unless the beta backscatters into it) but where backwards-going light will be absorbed by the source container. It can be seen that (unsurprisingly) the shadowing effects account for a substantial fraction of the lost light, the remaining portion being due to energy loss as the electron moves through the steel.

This also illustrates the need for a full Monte Carlo simulation of the source

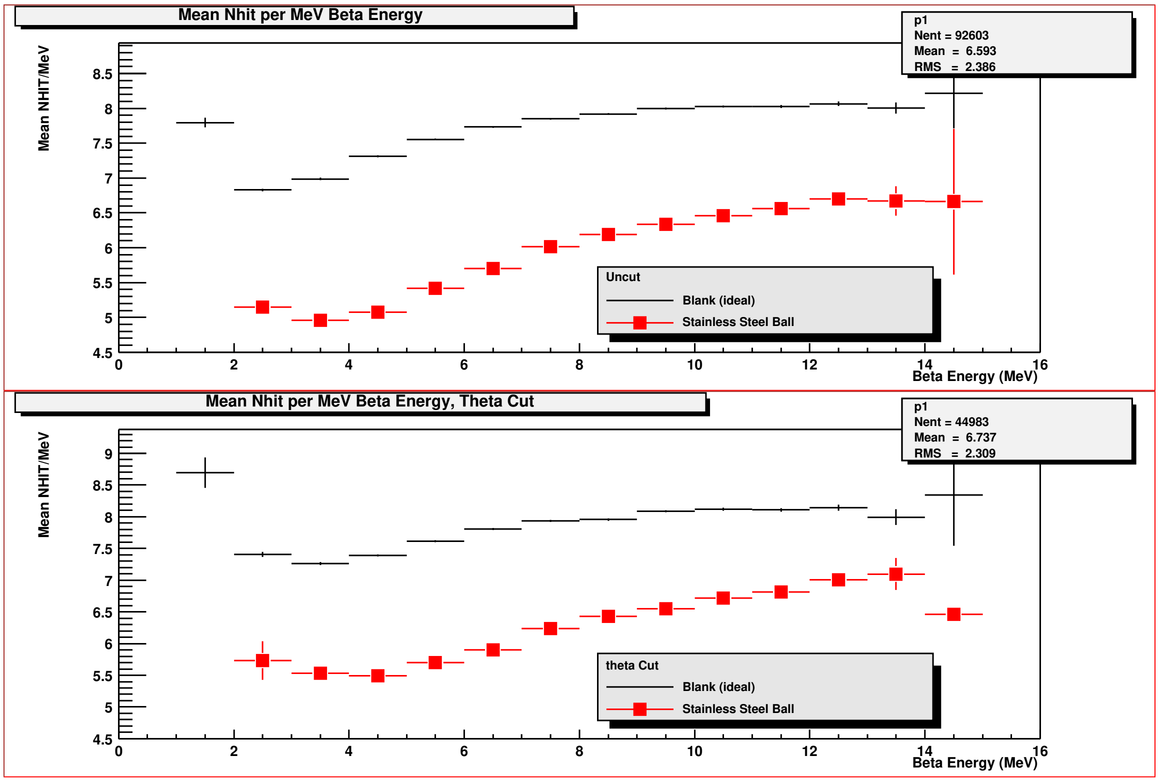

Figure 6.4: Nhits Per MeV For SS Ball. These plots show the mean Nhit/E_{gen} per event binned in 1 MeV bins of E_{gen}. (Note that the vertical scale is offset.) Error bars represent the error on the mean. The top plot shows the uncut spectrum; the lower plot is cut on reconstructed direction from the time fitter (FTT) such that $\cos\Theta_{fit} < 0$.

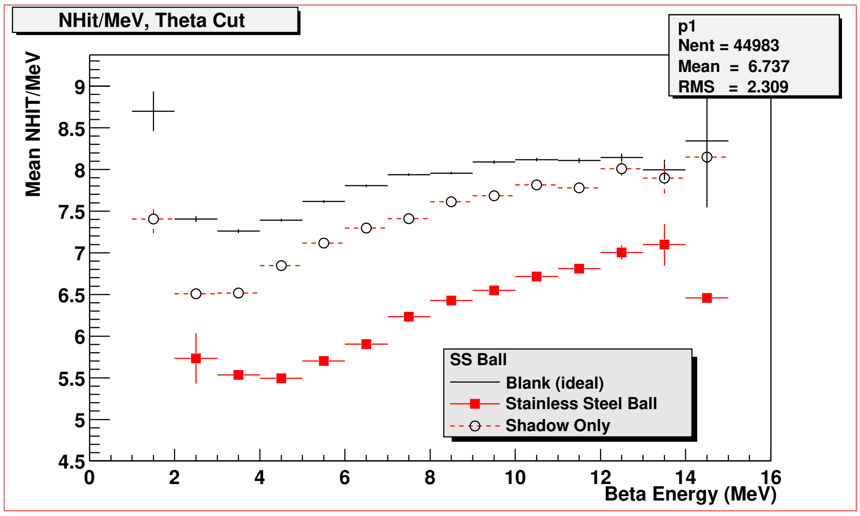

Figure 6.5: NHits Per MeV for Full Simulation and Shadow Only. **The 'shadow only' case refers to simulations where ^{8}Li events are injected into the water in a thin shell just outside the source container wall. Cuts are made to ensure that the beta is going radially outward (i.e. $\vec{r} \cdot \vec{v} > 0$ and all events are chosen so that $\cos\Theta < 0$.**

chamber in the SNO detector, since a calculation of the beta energy loss in the wall will not account for all the source-related systematic losses in energy response.

6.2.3 Systematic Uncertainties

Of particular interest are systematic uncertainties associated with the energy loss. One that can be simply analyzed is the thickness of the decay chamber wall. Figure 6.6 shows the effect of gross changes in the SS ball wall thickness. The wall thickness was varied by ± 50% of the nominal value. The actual machining tolerances were ± 0.0025" (0.65 mm, or 12%) for the stainless steel ball. (The measurements in Table 4.1 show that the wall thickness was in fact greater than 0.022" nominally, and

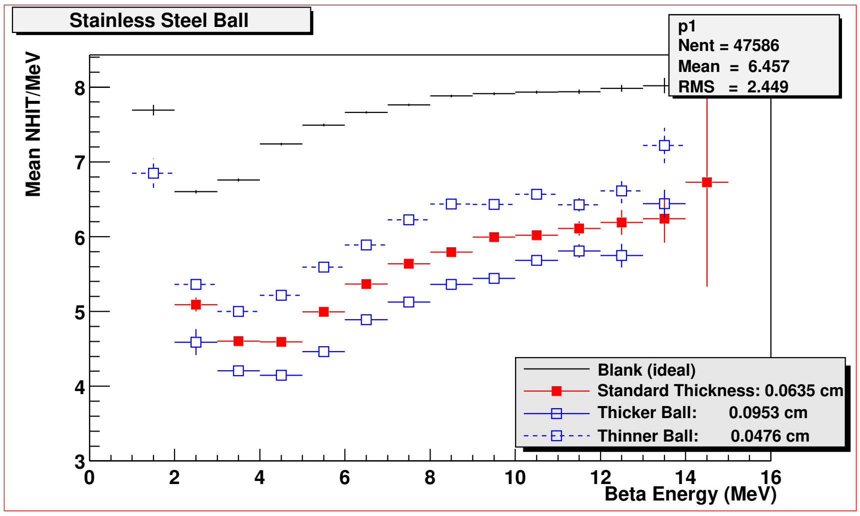

Figure 6.6: Energy Response vs Stainless Steel Ball Thickness. The energy response (NHIT/MeV) is shown for differing thickness of decay chamber wall. Events were cut so that $\cos\Theta < 0$.

varied up to 0.03”.) The relatively large variation applied to the wall thickness in this study was used to get a quantitative result without requiring the enormous number of events needed to overcome statistical variation.

The variation in energy response is about ± 0.5 NHIT per MeV when the wall thickness is varied by $\mp 50\%$. This gives a systematic error on the energy response of about $\pm 9\%$ for the exaggerated case. The tolerance on the ball thickness is one quarter this variation, for a net systematic uncertainty (for the realistic case) of about $\pm 2\%$.

6.3 Position Reconstruction

The real source will give a different ensemble of reconstructed event positions that will an ideal source. We can examine these differences to some degree with Monte Carlo.

A perfect source for use in attempting to understand vertex reconstruction would be a point source. If SNO had perfect position reconstruction, the ^{8}Li source would look like a source of betas being emitted radially from a thin-walled sphere. Without perfect resolution, however, the 8Li decay chamber is probably small enough to be used like point source. The argument, put simply, is that SNO reconstruction has a resolution substantially larger than the physical size of the source.

Some definitions:

$\vec{x}_{event}$ is the true position of the decay.

$\vec{x}_{exit}$ is the (true) position at which the beta exited the decay chamber wall and entered the water.

$\vec{x}_{fit}$ is the reconstructed position.

$\vec{R}_{dev}$ is the displacement from the real starting position of the beta ($\vec{x}_{exit}$ or $\vec{x}_{event}$ for the 'blank' source) to the position reconstructed by the fitter.

$\vec{R}_{fit}$ is the distance from the center of the AV of the position of the reconstructed vertex. For the case presented here, this is identical to the distance from the center of the spherical decay chamber to the reconstructed vertex.

$\vec{v}$ is the true direction of the beta (before any scattering).

$\vec{v}_{fit}$ is the direction found by the fitter after reconstruction.

Figure 6.7 shows a histogram of the value of $|\vec{R}_{fit}| - |\vec{R}_{dev}|$ for a case where events are introduced to the detector on a thin shell of radius 6.35 (i.e. the 'blank' source as described in section 6.1). This corresponds to the systematic error introduced when one naively treats a source with finite extent as a point source centered at the same location. The mean of this histogram is not too far from center, as one would expect (since events are evenly distributed across the sphere), and is peaked in the forward direction (i.e. events tend to fit on the same side of the sphere as they were created.)

This distribution has a mean of 1.5 cm and RMS value of about 3.5 cm. This means that if one takes a distribution of R_{fit} values (fit residual from the source location), it will look very much like the R_{dev} (fit residual from the *event* location), except systematically smeared.

As can be seen from Figure 6.8, the mean values on R_{dev} are about 35 cm. Since these residuals are uncorrelated to event geometry, using R_{fit} in the place of R_{dev} increases the mean residual by about 2 cm, or 5%. In other words, treating the source container as a point source will create position resolution plots that give residuals

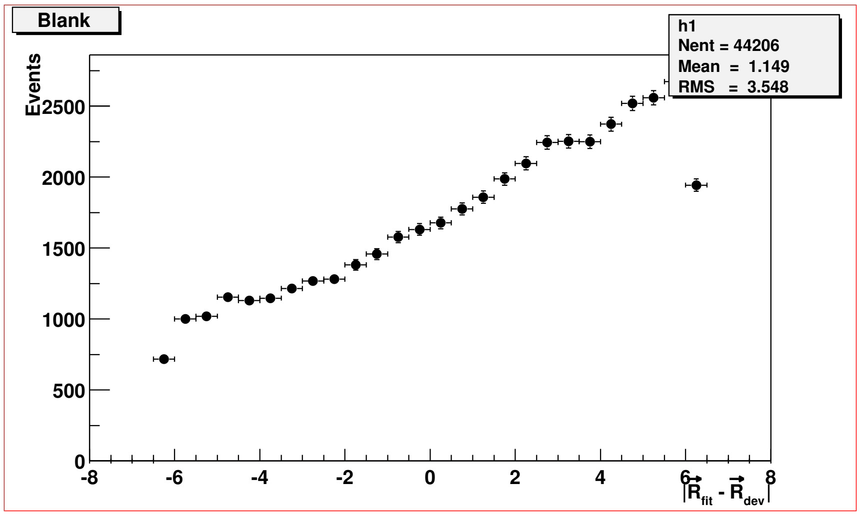

Figure 6.7: $|\vec{R}_{fit}| - |\vec{R}_{dev}|$ **for Blank Source. Events are created on a thin shell at radius 6.35cm, and cut so that only outward-going events are taken (i.e. $\vec{x} \cdot \vec{v} > 0$). Positive numbers indicate fits that reconstruct to the correct side of the chamber, negative numbers the opposite side.**

correct to better than 5%.

Figure 6.9(b) shows that this is not a perfect approximation, but the shapes of the two curves have similar properties. The first and second moments of the distributions agree to within 10%, which gives an estimate on the accuracy with which we this method can determine the true moments of the fitter resolutions.

Figures 6.10 and 6.11 illustrate the basic response of the fitters as a function of NHIT. As can be seen from the contour graphs, this dependence must be taken into account when using a distribution of electron energies.

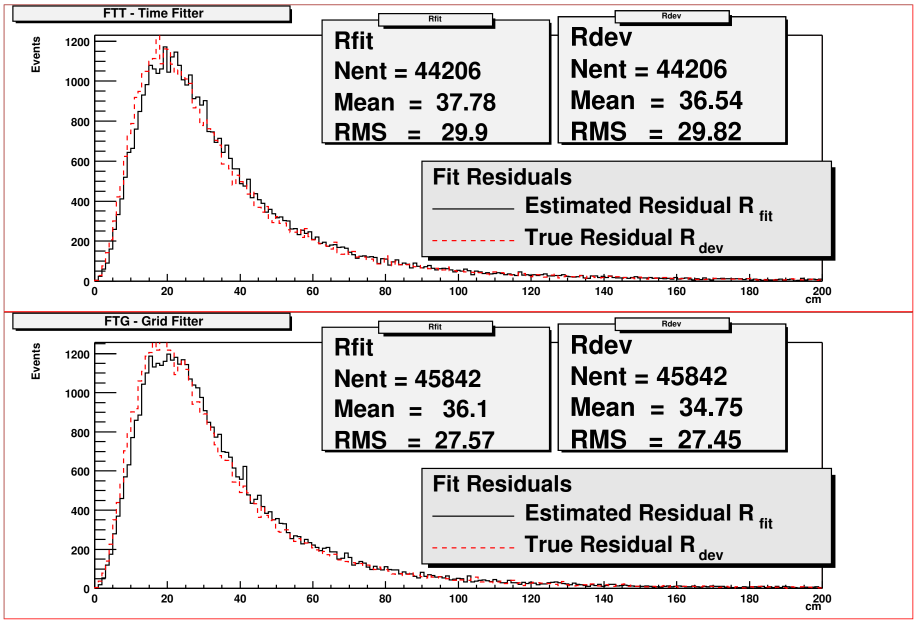

Figure 6.8: R_{fit} and R_{dev} Reconstruction Errors on the Blank Source. The position reconstruction residuals are shown for outward-going events created by the 'blank' source. (Note that R_{dev} and R_{fit} distributions are very similar.) The upper plot shows the fitter residual using the Time fitter, the lower using the Grid fitter.

6.4 Direction Reconstruction

Another measure of how much a practical source will differ from the ideal is how the fitters reconstruct the direction of a given track. If source shadowing interferes with direction reconstruction, this is evidence that the source is not good for testing the fitters.

The reconstruction of direction by the FTT and FTG fitters is based on a very simple algorithm, once position has been reconstructed. They simply average over all the normalized (unit) vectors from the source position to the hit PMTs.

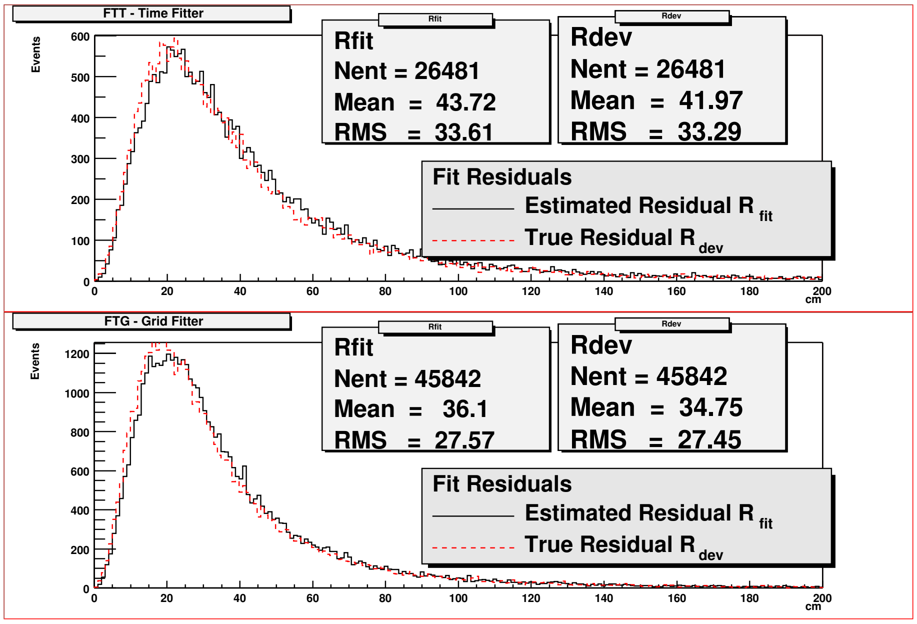

Figure 6.9: R_{fit} and R_{dev} Reconstruction Errors on the SS Ball Source. The position reconstruction residuals are shown for events created in the stainless steel ball source. The upper plot shows the fitter residual using the Time fitter, the lower using the Grid fitter. R_{dev} in this case is $|\vec{x}_{fit} - \vec{x}_{exit}|$

The accuracy of this technique is thus both a function of the accuracy of the fitted position of the given event, and a function of the NHIT. The direction fit residuals with respect to these variables are shown respectively in Figures 6.12 and 6.13.

Figure 6.12 shows essentially no structure; the direction fit is fairly insensitive to fitted position unless it fits quite badly (outside 200 cm). In Figure 6.13, it can be seen that the fit improves with NHIT, as would be expected. The wall-less sources (shadowed and blank) do markedly worse than the realistic sources because of the NHIT effect (not removed in the latter plot).

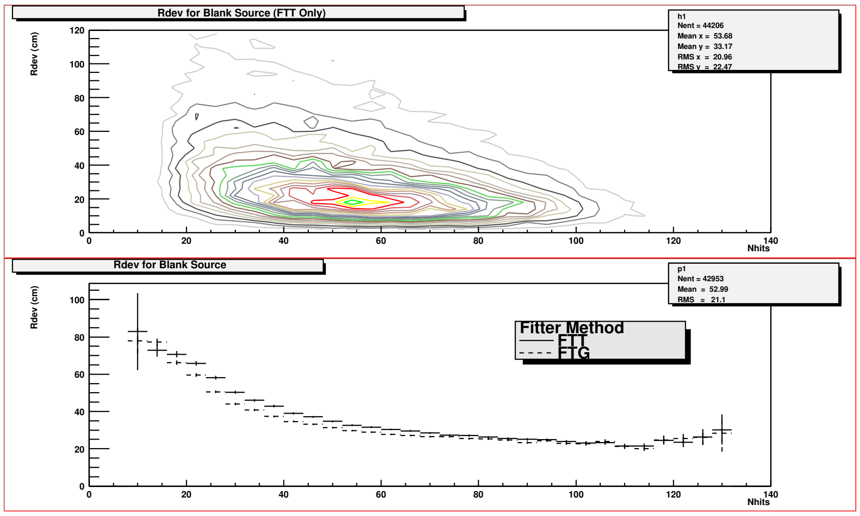

Figure 6.10: R_{dev} **vs NHITs for Blank Source.** The top plot shows the various contours of fitter position residual (from the FTT fitter) and NHITs. The bottom plot shows the mean R_{dev} on the same scale for both FTT and FTG.

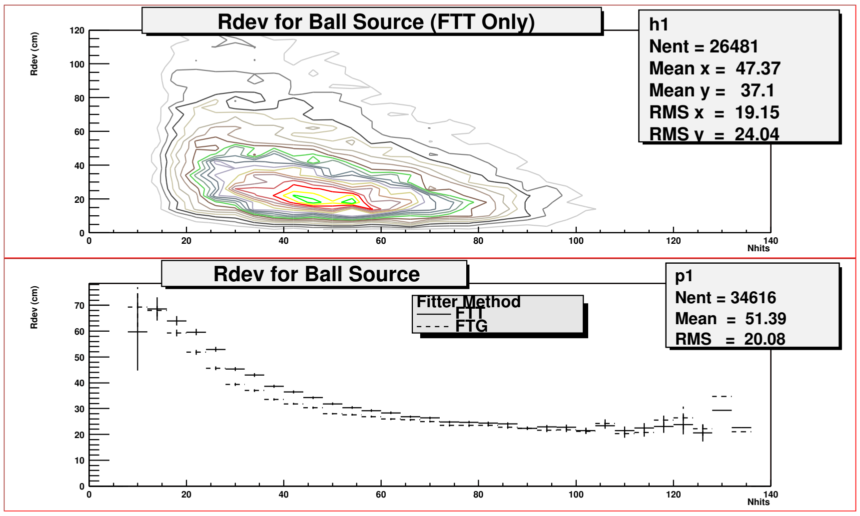

Figure 6.11: R_{dev} **vs NHITs for Acrylic Ball.** The top plot shows the various contours of fitter position residual (from the FTT fitter) and NHITs. The bottom plot shows the mean R_{dev} on the same scale for both FTT and FTG.

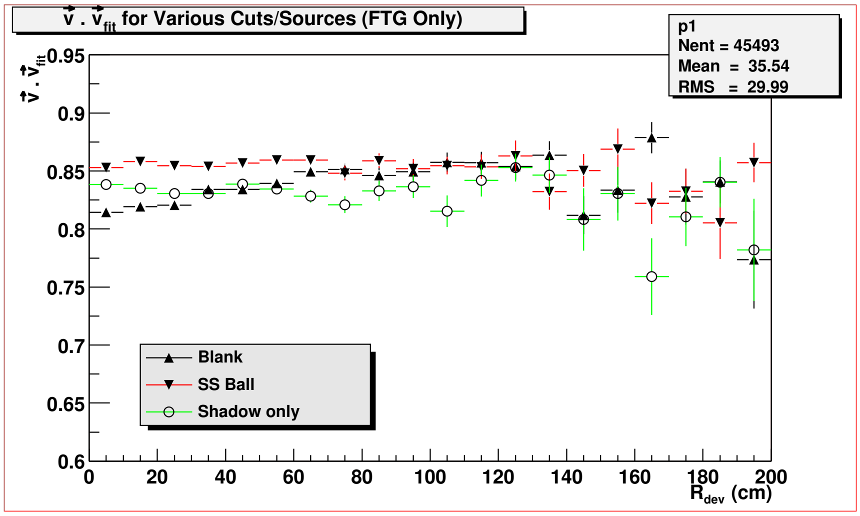

Figure 6.12: v_{dev} **for SS Ball as a Function of** R_{dev}**.** The grid fitter FTG is used to fit events from each data set. R_{dev} is the same as shown in Figure 8.5. $\vec{v}$ is similarly computed, using either initial beta direction $\vec{v}$, or the direction the beta had when it left the source wall $\vec{v}_{exit}$. Only events with $R_{dev} < 250$cm are used.

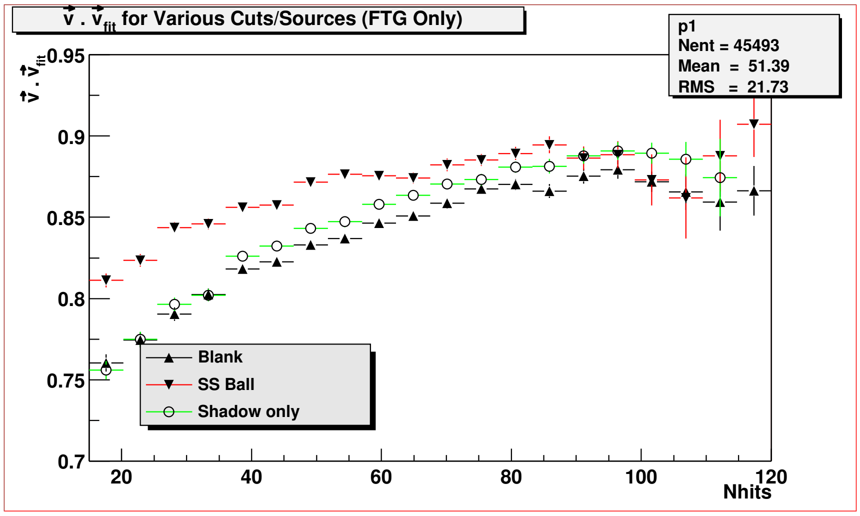

Figure 6.13: v_{dev} **for SS Ball as a Function of NHIT.** The grid fitter FTG is used to fit several different source configurations. Direction fit is the same as Figure 6.12

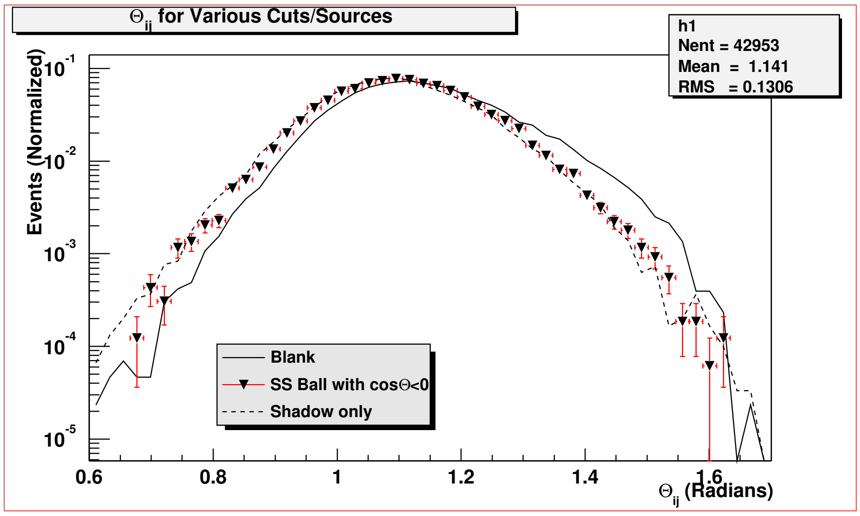

Figure 6.14: Θ_{ij} Distributions For SS Ball. These histograms are normalized. Vertex position is as ascertained by FTT.

6.5 Event Topology

Figure 6.14 shows the Θ_{ij} distribution for the source. Theta-ij (Θ_{ij}) is the mean angle between every pair of hits in an event, and is thus a fair statistic of the topology of the event. (This parameter is one that might be used by classifiers attempting to distinguish between neutral current and charged-current events, for instance.)

The response of the stainless steel ball closely follows that of the 'shadow only' source, which indicates that the effect seen is not due to any interaction the beta has in the wall, but is simply an unavoidable consequence of having a real source chamber. Large Θ_{ij} values are suppressed due to shadowing, while small values are enhanced due to reflection of backward-going light.

6.6 Conclusions

The stainless steel ball is probably not a good design to do energy studies. The energy lost by the beta as it passes through the chamber wall is about 2 MeV, which is a significant shift. The ^{8}B neutrino spectrum will have a centroid about 20 NHIT higher than the measured centroid of this ^{8}Li source. Therefore, the two spectra cannot be treated as having the same shape, so a comparison of the ^{8}B to ^{8}Li energy centroids, discussed in Chapter 2 is too simple and analysis. Energy measurements with this source are not impossible, but to be done well a different choice of materials and chamber design may be required. This is discussed in Chapter 8.

It appears that we can understand reconstruction distributions at the level of ±5 cm without resorting to sophisticated comparisons to Monte Carlo. Instead, we may simply use the residual between the source chamber position and the reconstructed position to determine the fitter error. This is important, because an ideal analysis is insensitive to specific Monte Carlo parameters The most important measurement is an estimation of the tail of the distribution at large distances from the source, and an accurate measure of this is possible.

Error on reconstructed direction is of lesser concern, but again it appears that there are no serious disagreements between ideal, wall-less sources and the simulated sources, on the order of 5° variations from the ideal. This variation does indicate that there are qualitative differences in the two types of event (from an idealized source or a realistic one), and so use of this parameter in analyzing the source data should be done with caution. For instance, if the source is deployed off-center in the detector, the direction anisotropy may be slightly different than for neutrinos that interact at the same position.

Simulations show that the realistic source distorts event topology, measured by Θ_{ij} because of self-shadowing. This is an unavoidable consequence of having a source container, and the effect can only be reduced by changing the size or shape of that container. The distortion is not extreme, however, so it cannot be said that events from the source will be greatly dissimilar to those created by neutrinos.

7

Experimental Results Using the SNO Detector

The ^{8}Li source was successfully run in the SNO detector, giving a good first data sample. A preliminary analysis of this sample is presented here as a demonstration of the utility of the source.

The ^{8}Li source was deployed in the SNO detector from December 18, 2000 through December 21, 2000, for a total run time of about 30 hours of running time.

The system configuration included a shortened conduit to the deck, and a short umbilical (70 m), based on the LOD test configuration, that was just sufficient to get to the center of the detector. The gas system was run with 260 cc/s helium flow, plus a 5% mixture of nitrogen gas. The exhaust was not pumped; rather, the system was run with the exhaust line at atmosphere.

Little work was done to optimize this system, due in part to the expense of valuable detector live time and in part because the system worked much better than

Source coordinates (cm)	^{8}Li Events Recorded
(-16.0, 23.5, 0.08)	20376
(-16.0, 23.5, 450.05)	13269
(-16.0, 23.5, 249.38)	3507
(-16.0, 23.5, 550.04)	2750

Table 7.1: Source Deployment Statistics. The position of the source, in detector (x,y,z) coordinates is shown along with the number of tagged ^{8}Li events (in coincidence with a detector trigger). Events were tagged using the software charge threshold discussed in the Section 7.1.

expectations.

The measured rate of ^{8}Li decays was approximately 0.5 Hz after the system had reached equilibrium. This process took approximately two hours after system start-up, and is assumed to be due temperature equilibration in the salt oven.

This unexpectedly high rate allowed the collection of good statistics at two detector positions (near the detector center, and at 450 cm above the center), as well as two other positions (z=+250 cm and z=+550 cm) with somewhat worse statistics. Due to manufacturing errors in the manipulator carriage construction, we were unable to move the source off the vertical axis.

7.1 Tag Signal

The tag chamber PMT was fed into a spare SNO front-end channel (FECD) and the time and charge of the phototube pulses were recorded in coincidence with the detector. The detector was not triggered on the source, but rather operated in the normal (neutrino run) mode, using a 100 ns, 20 NHIT coincidence trigger.

The tag chamber PMT pulses were extended in time, so of the three FEC integrators, the high-gain, long-integration-time digitization (QHL) was used to measure pulse height.

In order to test the trigger, CO_2 gas containing the ^{16}N isotope was flushed through the decay chamber. The tag signal for ^{16}N can then be compared to the signal generated by ^{8}Li. The integrated charge measured in the tagging phototube is shown in Figures 7.1 and 7.2. These figures illustrate that the ^{8}Li is well separated from beta-gamma backgrounds. (These plots can be contrasted with the bench test shown in Figure 5.4.)

Figure 7.2 shows that the background triggers come considerably earlier in the event than do triggers from the ^{8}Li events. Cherenkov light from the acrylic window should be very prompt, so the difference in mean time between these distributions shows the latency of the PMT pulses triggering on scintillation light. This latency is about 20 ns, which is quite acceptable. (If desired, this source could probably be operated in a triggered mode.)

7.2 Backgrounds

Roughly 8 Hz of high-NHIT background was seen in the SNO detector in addition to the $\sim$0.5 Hz ^{8}Li signal. There is good evidence that this background consists of ^{16}N.

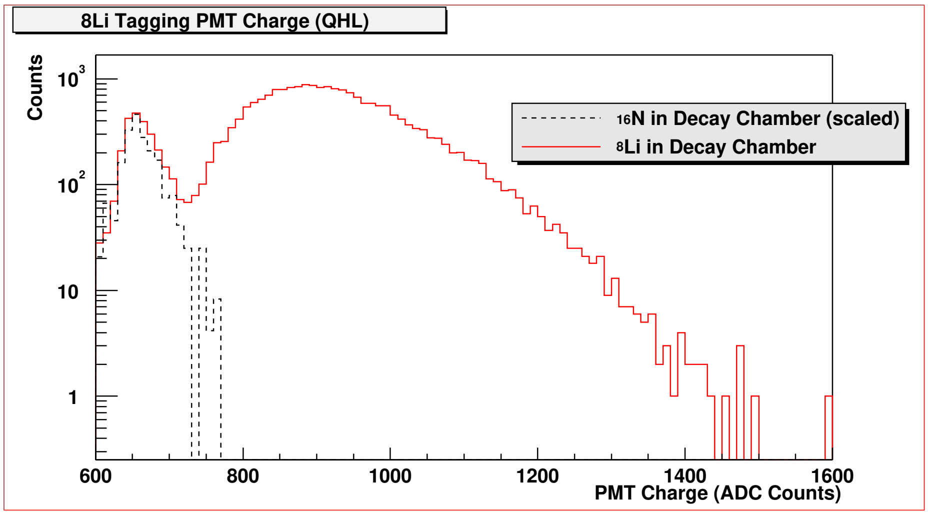

Figure 7.1: Tag PMT Integrated Charge. The integrated charge measured on the tag chamber PMT is shown in raw ADC counts for the case of ^{16}N and ^{8}Li isotopes, measured in coincidence with the SNO NHIT trigger. Typical pedestal charge on the front end cards is 600 counts.

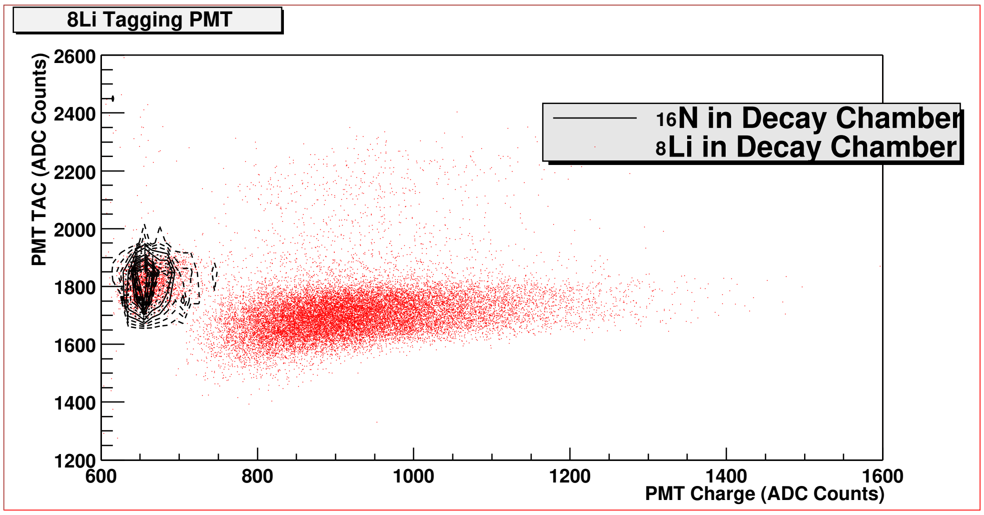

Figure 7.2: Tag PMT Integrated Charge vs. Time. The time shown on the vertical scale is measured in raw ADC counts. High values indicate early times; 10 ADC counts roughly corresponds to 1 ns of time. The horizontal scale is as in Figure 7.1. Contours indicate tag signals from ^{16}N runs, while dots indicate tags from ^{8}Li runs.

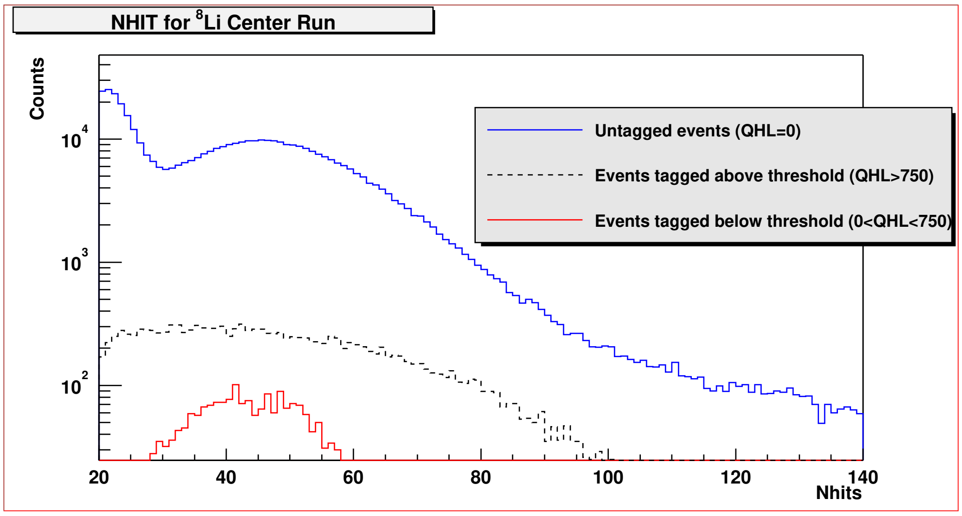

Figure 7.3: NHIT Spectra For Signals in ^{8}Li Running. The NHIT spectra are shown for the ^{8}Li source near the center of the detector. The top curve shows untagged events, the middle curve events with large tag signals (^{8}Li), and the bottom curve shows events tagged with low threshold (background isotope).

The ^{8}Li run data can be separated into three distributions: untagged events (events in which the PMT pulse did not pass threshold), events that were tagged but with small PMT charge (QHL<750 ADC counts), and events that were tagged with large PMT charge (QHL>750). The NHIT spectra of these three signals are shown in Figure 7.3. The bottommost curve in this figure shows the tagged background. This is believed to be ^{16}N for two reasons.

First, the NHIT spectrum of the background is nearly identical to that of ^{16}N gammas recorded by the ^{16}N source (with data taken several weeks earlier), as is shown in Figure 7.4. This plot shows an excess of events in the ^{8}Li data in the low and high NHIT tails. These events appear to be due to pickup by the FECD channel.

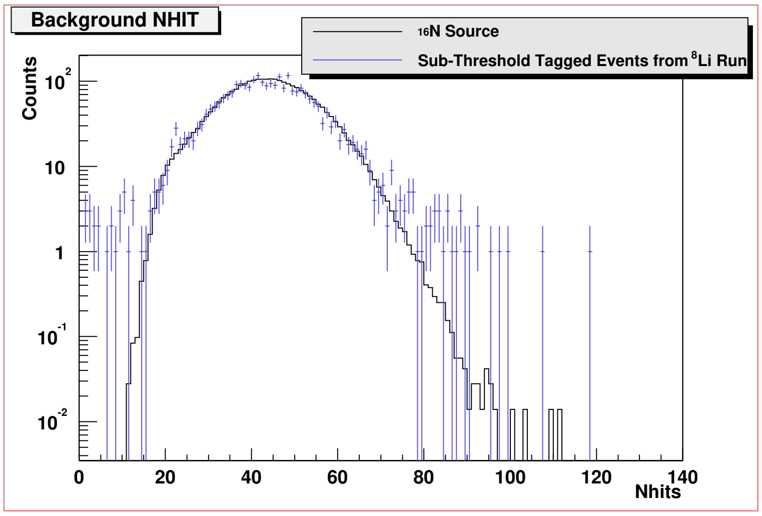

Figure 7.4: NHIT Spectra for ^{8}Li Background and for ^{16}N Gammas. The solid line shows the scaled NHIT spectrum for a long ^{16}N run done in the center of SNO with the ^{16}N source [4]. The ^{8}Li background (i.e. low-charge tagged events) is shown with error bars.

(The low NHIT events are 'sharkfin' events; the high-NHIT events are due to flashers, muons, or other high-charge, high-NHIT activity).

Second, we performed an explicit test by running ^{16}N gas through the ^{8}Li chamber, and achieved similar effects. The number of events in each tag distribution is shown in Table 7.2. For both runs, the data taken by the detector (between 30 and 140 NHITS) is dominated by the untagged events from the source. For both runs, the ratio of small-charge tags to untagged events is $\sim$0.6%. This gives us confidence that the same mechanism is acting in both runs.

Table 7.2 can also be used to estimate the contamination of the ^{8}Li sample. Two events out of 73k events in the pure ^{16}N run passed the high-charge threshold, giving

Run Mode	Tag condition	Events
^{16}N in chamber:		
	Untagged	73109
	Tagged (small charge)	437
	Tagged (high charge)	2
^{8}Li in chamber:		
	Untagged	376005
	Tagged (small charge)	2400
	Tagged (high charge)	16106

Table 7.2: Number of Events Vs Tag Signal. "^{16}N run" refers in this case to running ^{16}N isotope through the ^{8}Li decay chamber.

a contamination estimate of 0.003% ± 0.002%. We make the assumption that all the untagged events in the ^{8}Li run are due to background. (This is a worst-case estimate, since we know that some small fraction of these events will be due to decays in the umbilical.) Doing this, we get an estimated contamination of 11.3 ± 7.5 events due to ^{16}N in the ^{8}Li event sample, less than 0.1% of the ^{8}Li sample.

(This contamination can be reduced further by increasing the charge threshold in software, should a cleaner data sample be required for analysis. However, this comes at the price of sacrificing valuable ^{8}Li decays.)

The total rate of background is considerably higher that than predicted in the bench tests, which estimated the contamination at approximately 1 to 2 Hz. However, the statistical errors on those measurements were large, and they were made under slightly different conditions from those ultimately adopted for SNO detector

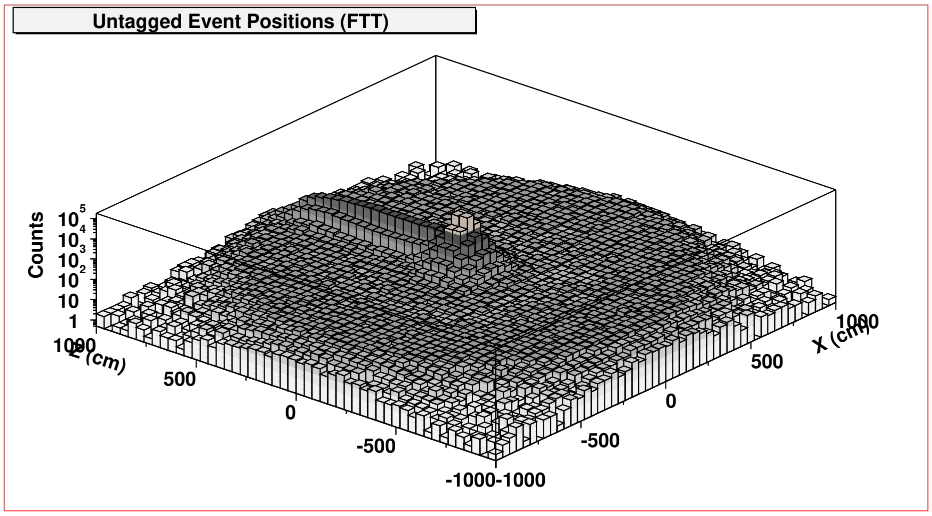

Figure 7.5: Event Positions of Untagged Events. The reconstructed positions (using the FTT fitter) of events in ^{8}Li runs (source near the origin) are projected onto the x-z plane. The umbilical can clearly be seen stretching up to the top of the detector.

conditions: the new setup uses a much shorter conduit and umbilical length (which improves both ^{8}Li and ^{16}N transport efficiencies) and we did not pump on the exhaust line, so the decay chamber was being run at relatively high residence times, further exacerbating the rate. Finally, we are measuring not just ^{16}N decays from the chamber, but also from the entire length of umbilical seen by the SNO detector (see Figure 7.5, which can add up to a considerable total rate. With these factors in mind, the bench tests results are not unreasonable in comparison to the SNO detector data.

7.3 Results I: Energy Scale

Usage of the ^{8}Li source to determine or check the SNO energy scale is a difficult analysis, and one that cannot be exhaustively discussed here.

The use of the ratio-of-ratios technique described in Chapter 2 is beyond the scope of this work; it requires a statistically significant spectrum of ^{8}B neutrinos interacting in the detector via the charged-current reaction. Extraction of this signal is a non-trivial process. Such an analysis is further complicated by the position dependence of the detector energy response, which needs careful measurement.

A preliminary analysis is performed here. The measured NHIT response is analyzed for ^{8}Li data taken with the source near the center of the detector. In this simple analysis, we generate a PDF function for the expected NHIT of the source, using a Monte Carlo simulation (which includes a wall thickness of 0.022" and a reasonable choice of detector optical parameters [52]). We then scale this PDF by a constant factor until it matches the data.

$$N_{hit} -> a \times N_{hit} \tag{7.1}$$

We first perform this analysis for ^{16}N source data taken two weeks previous to the deployment of the ^{8}Li source (to ensure identical detector conditions). The result is shown in Figure 7.6, where a Monte Carlo of the ^{16}N source is compared to data. The Monte Carlo needs to be scaled up by approximately 1% in NHIT to match the

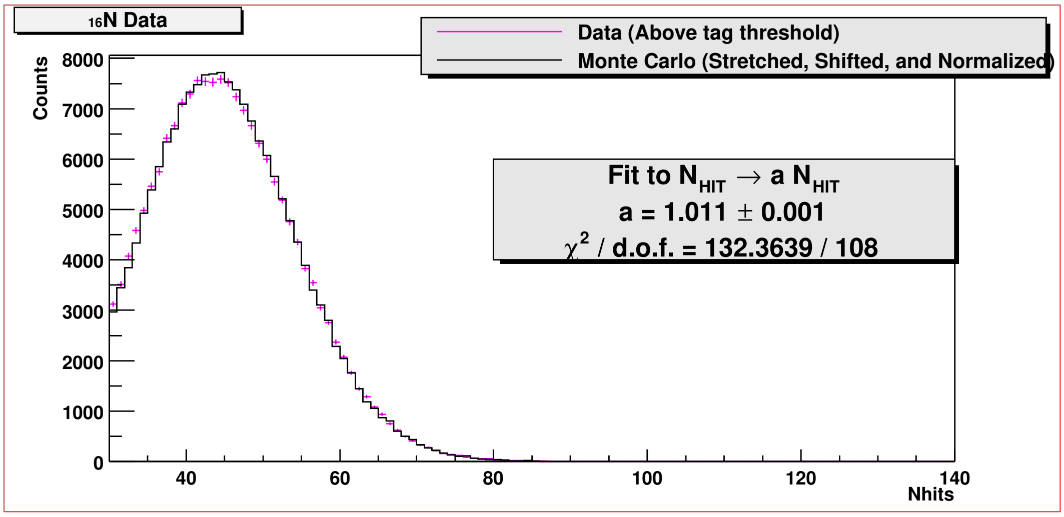

Figure 7.6: ^{16}**N Fit to Data. The NHIT spectrum of Monte Carlo data is scaled to match data taken with the** ^{16}**N source deployed at the center of the detector.**

data. A very good chi-squared value is obtained.

The ^{8}Li runs near center were analyzed in a similar fashion to get the resulting fit shown in Figure 7.7. The same scaling is needed to get good agreement with the data. Note that uncertainties due to wall thickness and to source optics are not taken into account; wall thickness uncertainty alone creates a 3% systematic uncertainty in the scaling factor. Again, an excellent chi-squared value is found.

This result is very encouraging; the sources seem to agree very well on the energy scale of the detector, despite having very different energy spectra. This is very important to SNO, since ^{8}Li is the first source deployed with an energy above that of ^{16}N.

The 3% uncertainty in NHIT due to wall thickness renders the result too inaccu-

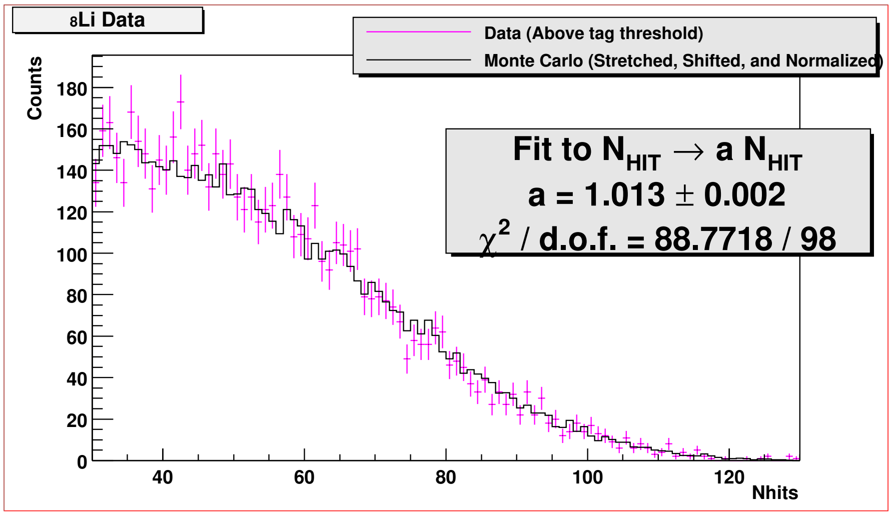

Figure 7.7: ^{8}Li Fit to Data. The NHIT spectrum of Monte Carlo data is scaled to match data taken with the ^{8}Li source deployed at the center of the detector.

rate to trust as a precision calibration point (for the purposes of absolute calibration).

This analysis may be used as a starting point for more studies. Although unsuitable for precise absolute energy calibration, relative calibrations between different source positions are possible. Another subject requiring full investigation is the choice of measurement to be used in estimating energy; NHIT is the simplest but not the only one. (For instance, an energy estimator could use only prompt light, or event topology, or phototube anode charge.) In addition, careful thought must be applied to understanding position resolution as it relates to energy estimation because of the position dependence of the detector response.

7.4 Results II: Vertex Reconstruction

Fitters used for reconstruction of neutrinos in the SNO detector are still under development. However, FTT (the time fitter), is used in nearly every analysis performed by SNO collaborators, because it is computationally fast. FTT can be compared to FTG (the grid fitter), which is somewhat slower but more robust and accurate. These fitters are evaluated here as benchmarks for future study.

Figure 7.8 shows the acceptance of the FTT and FTG fitters to ^{8}Li events (i.e. events with high tag charge) for the source deployed at the center of the detector. An event is marked as rejected if the fitter fails (i.e. cannot find a minimum) or if it reconstructs to a radius greater than 12 meters from the source. The FTG fitter is superior in that it rejects no events.

The resolution of the fitters is shown for three axes in Figures 7.9 and 7.10. The fit residuals are defined as the difference between the position of the center of the ball and the position of the event reconstruction. The mean values agree fairly well with the position of the source. Note that the RMS values include the $\sim$3 cm resolution smearing due to the finite source size, discussed in Chapter 6.

Figure 7.9(d) shows the correlation between the reconstructed time of the event and the time the tag PMT fired. The latter is shown as the raw TAC value: low numbers indicate early times and *vice versa*. Ten TAC counts roughly correspond to 1 ns, indicating that the time resolution of the source tag is approximately $\pm$10 ns.

This resolution can be compared to that of the low-charge tags, due to background (believed to be ^{16}N). The fitter residual for these events (shown in Figure 7.11) gives a larger RMS position due to the finite scattering length of the gamma ray. The correlation between tag phototube time and reconstructed time shows a smaller offset, as expected by the faster rise time of the PMT pulse for background events).

Figure 7.12 shows the overall fitter position accuracy, by measuring distance from the source to the reconstructed position. This can be compared to the Monte Carlo distributions shown in Chapter 6 (i.e. Figure 6.9). The mean and RMS displacements are better than predicted by the Monte Carlo, which was unexpected and bears further research.

Fitter	Value	Data	MC
FTT	Mean R_{fit}	40.9 cm	43.7 cm
	RMS R_{fit}	29.3 cm	33.6 cm
FTG	Mean R_{fit}	38.1 cm	42.0 cm
	RMS R_{fit}	26.3 cm	31.9 cm

Table 7.3: Fitter Residuals vs Monte Carlo. The first and second moments of fitter position residuals is given for the ^{8}Li data and for Monte Carlo. The source is near the center of the detector in both cases.

7.5 Results III: Data Cleaning

A thorough documentation of data cleaning sacrifice studies in progress; only the most preliminary data can be presented here. Using the data cleaning mask (i.e. set of cuts) currently being used for development work, the sacrifice of ^{8}Li data at the

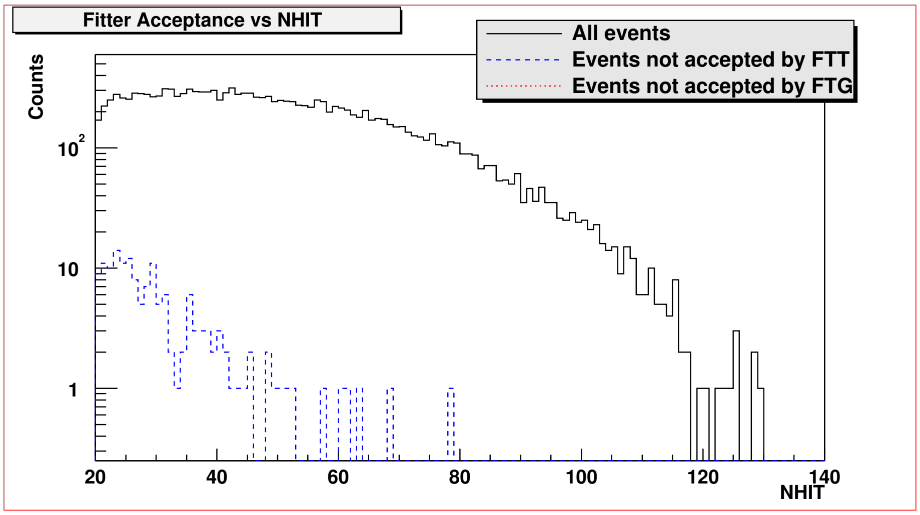

Figure 7.8: Fitter Acceptance. The NHIT distribution of all tagged ^{8}Li events is compared to that of events that did not survive the fitter (i.e. the fit radius was undefined or greater than 12 meters). The FTT fitter is shown; the FTG fitter accepted all events.

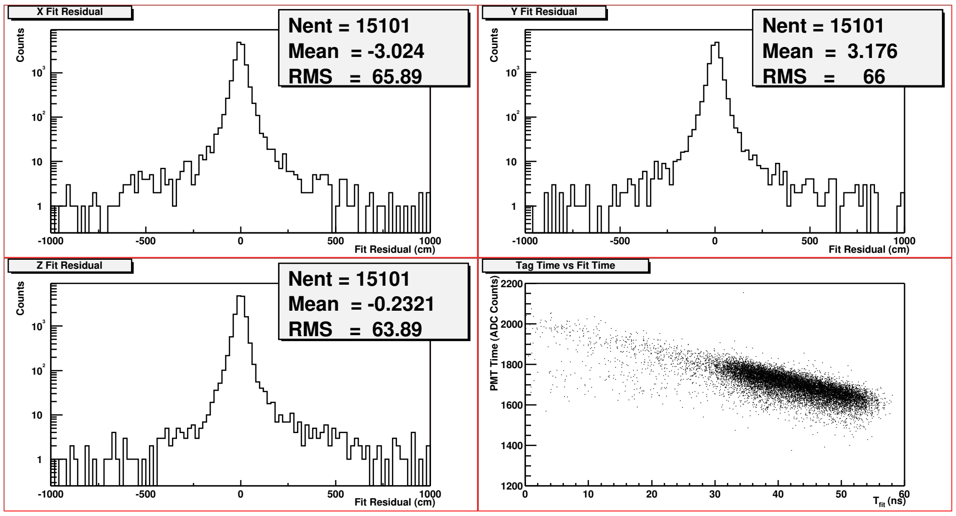

Figure 7.9: FTT Reconstruction Residuals for ^{8}Li Events. The x-, y-, and z-axis residuals are for ^{8}Li events. The fourth plot shows the correlation between the TAC value of the tag PMT against t_{fit} given by the fitter.

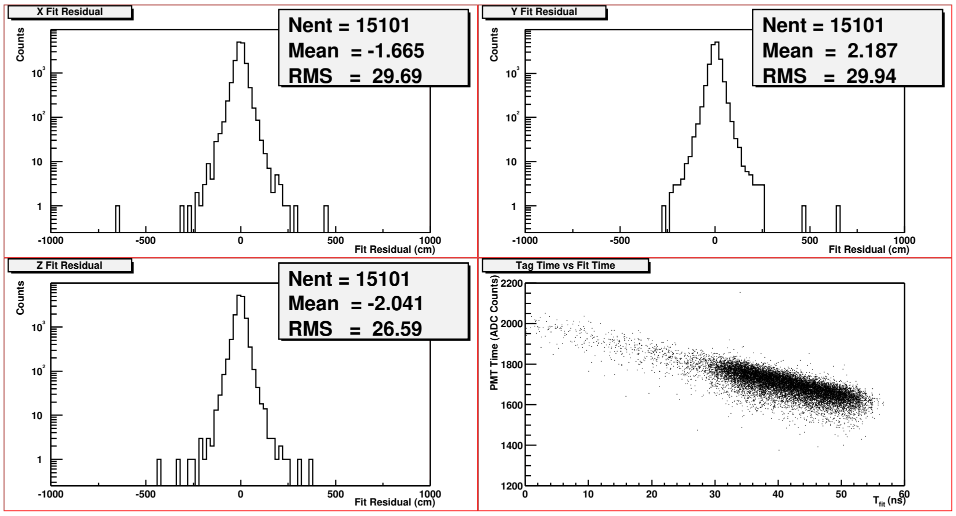

Figure 7.10: FTG Reconstruction Residuals for ^{8}Li Events. The x-, y-, and z-axis residuals are for ^{8}Li events. The fourth plot shows the correlation between the TAC value of the tag PMT against t_{fit} given by the fitter.

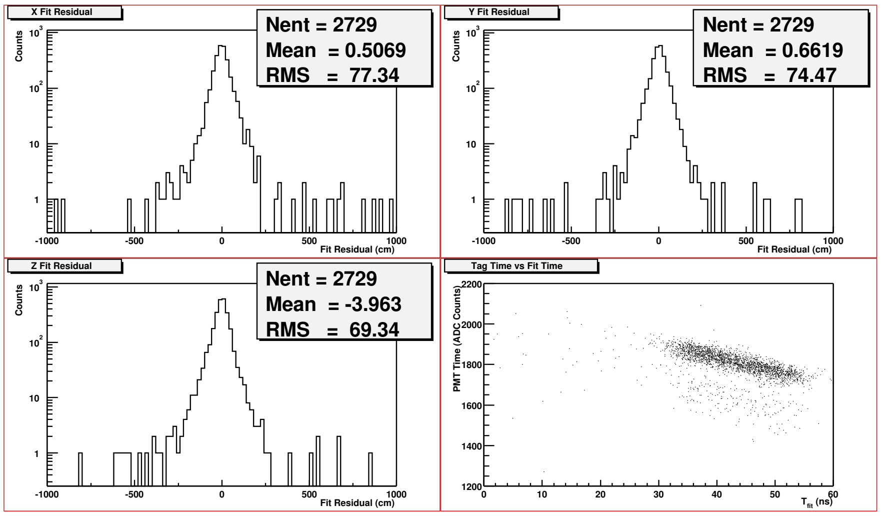

Figure 7.11: FTT Reconstruction Residuals for Background Events. The x-, y-, and z-axis residuals are for tagged background (i.e. events with low charge in the tag PMT). The fourth plot shows the correlation between the TAC value of the tag PMT against t_{fit} given by the fitter.

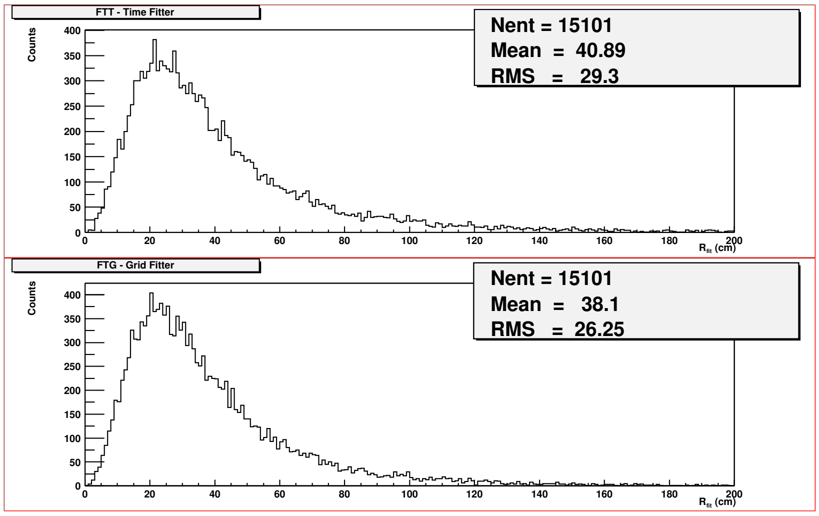

Figure 7.12: Radial Position Residual for ^{8}Li Events. The distance from the source center to the reconstructed position is shown for FTT (top) and FTG (bottom). This figure can be compared to Figure 6.9 in Chapter 6.

center of the detector was approximately 0.6%, which is in good agreement with the sacrifice found by using the ^{16}N source. The data cleaning sacrifice is shown as a function of NHIT in Figure 7.13.

7.6 Discussion

The analysis presented here represents only a fraction of the uses that the source data will be put to in the next few months. The data cleaning group is committed to digesting this data as soon as possible to finalize their sacrifice estimates. Authors of individual fitters will be using this data to test (and possibly even tune) their favorite algorithms to get the best possible reconstruction of events in the detector.

Most difficult will be the understanding of the energy scale by the ^{8}Li data. Of

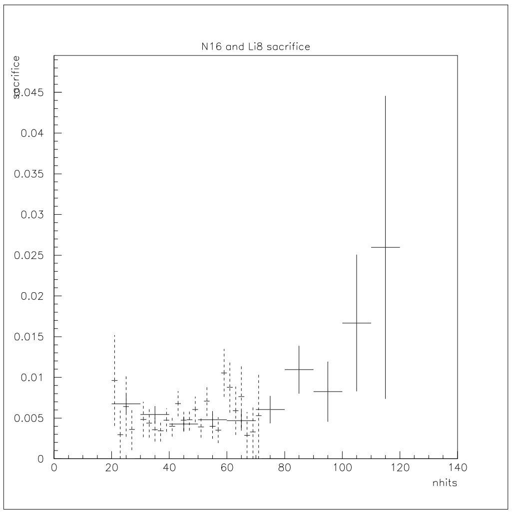

Figure 7.13: Data Cleaning Sacrifice vs. NHIT. Provided by McCauley [53]. The fraction of ^{8}Li events identified as instrumental detector background (sacrificed) by the default cuts is shown as a function of the NHIT of the event. The dotted points shows the same measurement as made by the ^{16}N data.

particular difficulty is the estimation of source related systematic uncertainties. For instance, although the energy loss of the electron in the wall should have uncertainties easy to estimate, the effect of diffuse reflection by the unpolished stainless steel is harder to understand.

One possibility I would like to suggest is to delay such analysis until the neutrino shape analysis has been attempted, then to use the ^{8}Li data as a check on that analysis. This 'blind' analysis is a technique gaining favor amongst experimenters, and should be considered for this data.

8

Alternate Designs and Future Work

The ^{8}Li source that was described in Chapter 4 and evaluated in Chapter 6 is not ideal. This chapter deals with some of the history of this final design, contrasting it with other designs, either existing prototypes or hypothetical designs. Future ^{8}Li deployment schemes should use these ideas to improve the quality of the calibration signal that can be given to SNO.

8.1 The Proportional Counter System

The original design of the ^{8}Li decay chamber was a long, cylindrical chamber described in ref. [42]. It is approximately 100 cm long and 2.5 cm in diameter. A thin wire running down the center of the tube allowed it to be used as a proportional counter, with the helium acting as the interaction medium. The cylindrical design allowed for thin metal walls to be used in the preliminary design, on approximately the same thickness as the stainless steel source.

The biggest problem with this source was maintaining stability. Helium gas, used as a proportional counter medium, requires a quench gas. The most straightforward solution was to include a 5% mixture of CO_2 in the helium stream.[1] Very precise control had to be maintained over the mix ratio, because the CO_2, even in such small relative quantities, accounted for about half the density of the counter gas. This meant that a small change in the partial pressure (even with total pressure constant) could mean a big change in the dE/dx of the alpha particles, which typically travel about 4 cm in pure helium. Because the cylinder was only a few centimeters diameter, the number of alpha particles that ranged out in the gas could change dramatically with a small variation in gas admixture. In addition, a changing admixture could substantially change the gas gain, and the pulse rise-time.

The overall rise-time of the pulse was another major concern. Proportional counters of this type have $\sim 1\ \mu s$ timing constants. This creates a tag signal that does not arrive in time to be included in the 400 ns time window of a SNO event, and laborious analysis processes must be used to back-correlate the tags with the events that caused them. Fast differentiation may be possible, but implementation may be difficult. Problems of this type have been noted when deploying a similar source in SNO. [54].

[1] The proportional counter had to work in flow-through mode, so these mixtures had to be controlled during the run of the source. This is also true of the N_2 gas used in the current version of the source, but the scintillation mechanism is far less sensitive to changes in gas mixture than the proportional counter.

The use of a long cylinder means that the decay position is not accurately known, unless it can be measured by the source itself. This was attempted using one-end and two-end charge division, with limited success. There is no reason why this technique could not, in principle, be realized, but it is unlikely that position resolutions better than 10 cm could be achieved.

If the position of an event along the length of the wire could be found, the PC source would have superior power in testing the reconstruction of the SNO detector, because the source position would be well localized on an event-by-event basis.

Another strong reason for going to a source of this design is that the event topology resulting from the source is quite good. The distribution of the Θ_{ij} parameter (for a PC ^{8}Li source deployed at the center) appears to be very similar to a blank source when computed by Monte Carlo. This result is shown in Figure 8.6. This improvement over the spherical design(s) is due to the source being very narrow, so it presents a smaller shadow.

8.2 Source Size

The tests done in Section 5.3 show that decreased decay chamber pressure does not result in severe problems with tagging efficiency. This would indicate that only a small amount of helium is necessary as target material to create enough scintillation light as a tag. If true, this means that the stainless steel sphere is larger than necessary to get a good tagging efficiency. Further testing remains to be done to prove that the yield will not suffer, but if it does not, a smaller chamber size can mean substantial improvements.

The source wall can be thinner for a smaller source, which is probably the most important improvement. Both cylindrical and spherical source shapes have critical buckling pressures that scale with the ratio of d/t, where d is the diameter and t is the thickness of the wall. Decreasing the linear size of the chamber allows one to decrease the wall thickness by the same factor, which directly impacts on the energy loss of the escaping beta particle.

The smaller shadow cast by the source means a more representative topology, and more accurate fitter response.

8.3 Volume Constrained Source

A possible, if difficult, modification to the source container is to insert a balloon or other thin-walled membrane inside one of the spherical source designs. This has the effect of reducing the decay volume, but restricting 8Li decays to small radii inside the source. The beta particles would impact the source wall at more angles of incidence close to the normal, which would result in shorter path length in the wall material and thus smaller energy loss, and less energy straggling.

Both stainless steel and acrylic source containers can benefit from this modification by roughly 0.3 NHIT/MeV (about 5% more light). However, it is not obvious that the yield will stay at sufficiently high rate under such a constraint.

8.4 The Acrylic Ball Source

Acrylic was used to build a prototype ^{8}Li source that was roughly the same shape as the stainless steel. Acrylic is a good choice of material for several reasons. First, acrylic already exists in SNO in large quantities, and so has many well-understood properties (both optical and mechanical). It is radiochemically very pure, and can be formed into any shape.

Most important, acrylic is transparent to Cherenkov light to a large degree. Beta particles escaping through an acrylic wall will generate Cherenkov light as they go through it in a fashion exactly analogous to water. Therefore, the light collected from such a source could be very similar to the ideal, wall-less source. Light attenuation in the acrylic should not substantially reduce the light output, because the thickness of the source wall should be small compared to the thickness of the SNO acrylic vessel which contains the D_2O.

8.4.1 Design

The basic design of the acrylic chamber is shown in Figure 8.1.[2] The decay chamber consists of a spherical acrylic ball, 5" in (inner) diameter, with a 0.2" thick wall. The

[2] The acrylic source was designed with the help of Tom Riddolls, who also performed the difficult work of machining the entire chamber.

top of the ball is extended into a neck piece that mates with the aluminum 'thorax' by the use of bolts along the middle flange. The inside of this ball is painted white (see below). This piece is machined out of a piece of SNO acrylic, the same stock the was used for building the SNO AV.

The thorax holds a PMT which extends down into this neck. It also holds the gas connections. Helium gas is injected down the neck on one side of the PMT, into the 'head' and is exhausted up a channel on the other side. If necessary, the acrylic window covering the PMT can be replaced by a distribution plate.

The top of the source looks much like the stainless steel version, with and endcap (abdomen) PMT base and HV assembly, umbilical connection, etc.

The acrylic 'head' was machined out of two pieces of SNO acrylic, and cemented together. The two pieces of the head were first machined on the inside, while the outside remained cylindrical. The two pieces were mated along a join running around the midpoint of the sphere in a horizontal plane. The pieces were bonded by using a solvent cement, methylene chloride. The outside of the head was then machined into the ball-and-neck form. After this, the ball was re-annealed to remove bonding and machining stresses The bond remained translucent but not completely transparent, (See figure 8.2) but was very thin. Because of the difficulty in getting tools into the neck, the inside bond remained somewhat rough. This bonding process came under criticism from SNO collaborators for being an untested process. Considerable

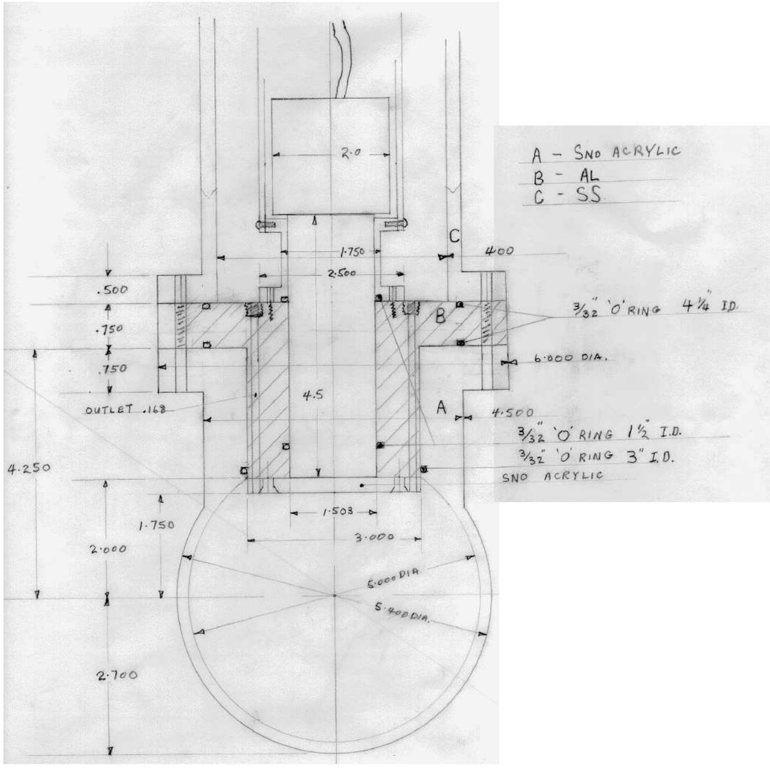

Figure 8.1: ^{8}**Li Chamber Sketch.** For the purposes of reference, the top stainless steel shell is named the 'abdomen' (C), the middle aluminum stage and flange is called the 'thorax' (B), and the acrylic sphere the 'head' (A).

development work would be necessary to prove that this method is a safe one for building a source for SNO.

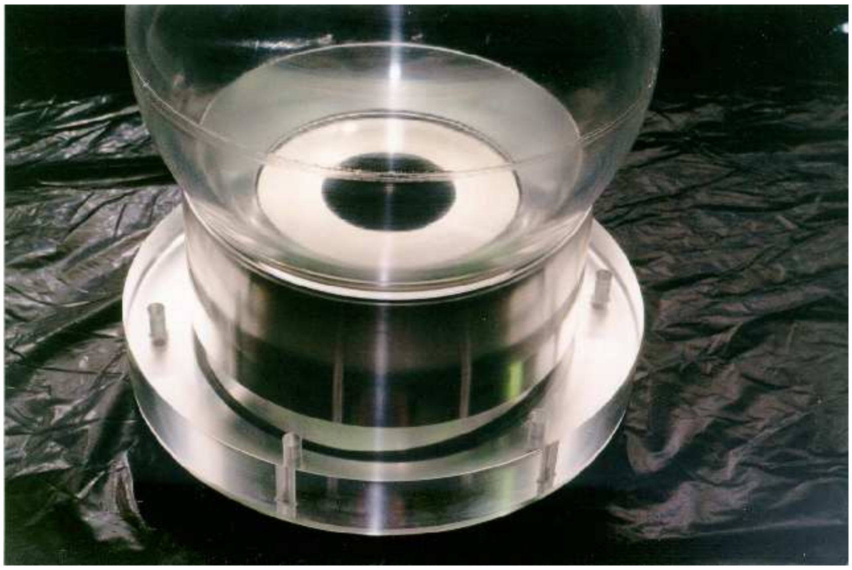

Figure 8.2: Acrylic Ball 'Head'.. Photograph taken before sanding and painting.

In the case of the acrylic ball, the inside of the ball needed to be painted, in order to ensure that alpha scintillation light would not leak into the SNO detector, corrupting the Cherenkov light signal.

The construction of the acrylic source was useful for several reasons. First, it gave us a prototype system to test the tagging mechanism. Second, we demonstrated that such a device could be machined with good optical properties, and with a precise wall thickness.

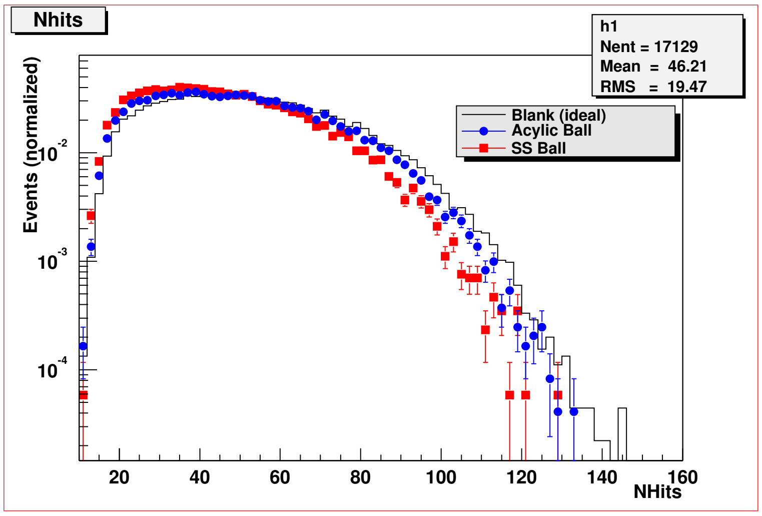

Figure 8.3: NHIT for SS and Acrylic Balls With Cut on Direction. Each spectra is cut so that $\cos\Theta_{fit} < 0$, using the reconstructed direction from the time fitter (FTT). Statistical errors are shown with error bars. Each run is normalized to the same number of detected events.

8.4.2 Monte Carlo Results

The acrylic source was modeled by Monte Carlo in a way analogous to that done in Chapter 6. The acrylic wall, paint, acrylic window, and aluminum thorax were all included in the model.

8.4.2.1 Energy

The acrylic source generates significantly more light than the SS source, because the beta can produce Cherenkov light in the acrylic as it passes through the wall. This creates a source much better approximation to a wall-less source than the stainless steel vessel does, as is shown in Figure 8.3.

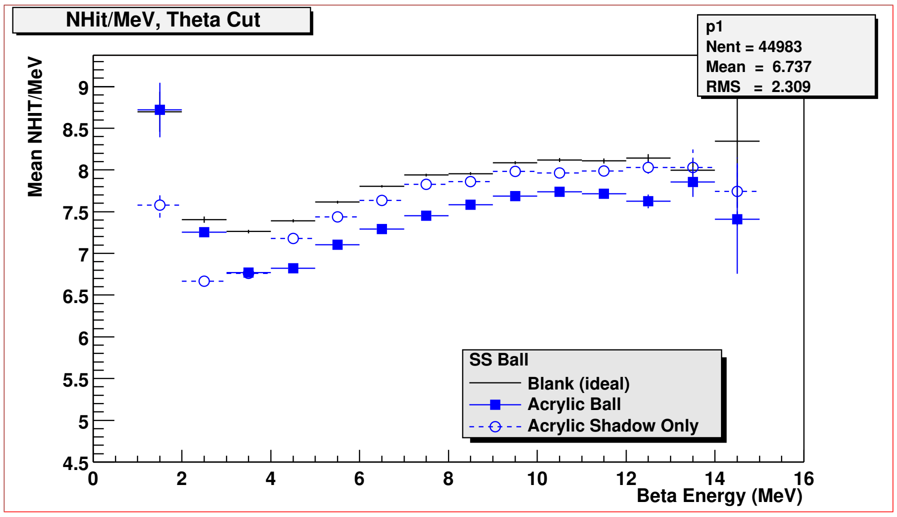

Figure 8.4: NHits Per MeV for Acrylic Ball and Shadow Only. **The 'shadow only' case refers to simulations where ^{8}Li events are injected into the water in a thin shell just outside the source container wall. Cuts are made to ensure that the beta is going radially outward (i.e. $\vec{r} \cdot \vec{v} > 0$ and all events are chosen so that $\cos\Theta < 0$.**

Figure 8.4 shows that this gain in energy response is due to two effects. First, the energy loss in the wall (although about the same ΔE on the beta) creates far less light loss than for the stainless steel wall. In addition, the 'shadow only' plot shows less light loss by shadowing: the optical surface of the acrylic allows back-scattered light to reflect off of (or refract around) the ball.

The systematic error on wall thickness for this source is significantly smaller than for the stainless steel source. Because the machining tolerances for plastic are somewhat better (since the piece is cut rather than shaped or cast) and since the piece is much thicker in absolute dimension (by about a factor of 8), the maximum deviation in energy loss is much smaller. The systematic error on the energy loss in the wall becomes only 0.5%, a factor of 5 better than for the stainless steel.

However, these improvements come with significant complexity. For instance, a possible systematic in the acrylic source has to do with the reflectivity of the paint. Darkening the paint (making it black) decreases the energy response of the source slightly, on the order of 0.1 NHIT/MeV, or about 2%. The refractive index and geometry of the acrylic must also be very well modeled. Small changes in the optical properties of the acrylic could potentially lead to large swings in light output. These challenges are not insurmountable, but do pose difficulty for analyzing a source of this type.

8.4.2.2 Fitter Resolution

Figure 8.5 shows the fitter resolution for several different source configurations. The acrylic source fits slightly better than the stainless steel version, even better than a wall-less source. This may be due to light being refracted around the acrylic sphere, providing more backward-going light to fix the position of the event. However, these small deviations from the ideal would not be very significant in practice.

The direction fit is nearly identical to that already shown for the stainless steel source.

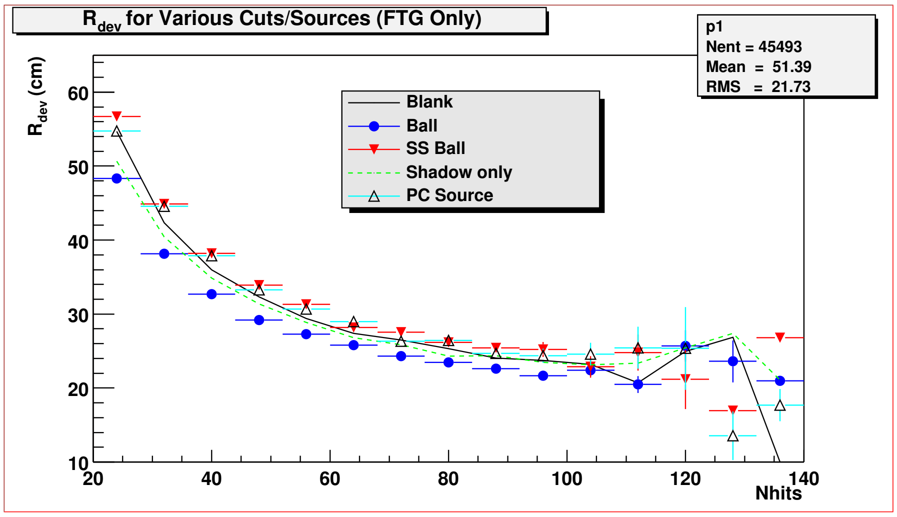

Figure 8.5: R_{dev} **for Various Sources. The grid fitter FTG is used to fit several different source configurations.** R_{dev} **is taken as distance from** $\vec{x}_{fit}$ **to** $\vec{x}$ **(blank and shadow sources) or** $\vec{x}_{exit}$ **(ball sources).**

8.4.2.3 Event Topology

The theta-ij distribution is shown for the acrylic ball in Figure 8.6. The acrylic ball pushes the distribution in the opposite direction as the stainless steel ball. Again, this is due to extra refraction in the acrylic. The magnitude of this effect is slightly larger than for the SS ball.

8.5 Discussion

The PC source has several useful characteristics, but probably the best of these is the narrow shape. The tagging system can probably be made to work, but after much effort I abandoned the system as simply being to unstable and having insufficient

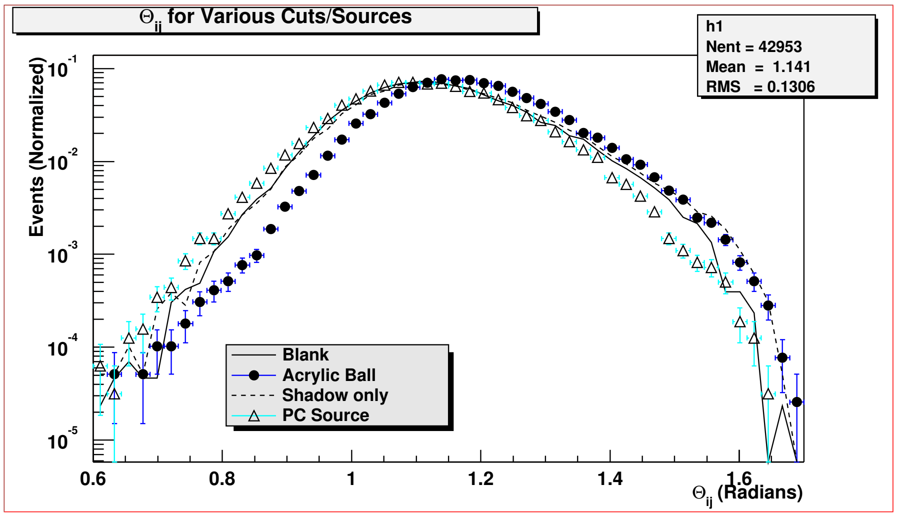

Figure 8.6: Θ_{ij} Distributions For Acrylic Ball and PC sources. These histograms are normalized. Vertex position is as ascertained by FTT.

position resolution to be useful.

The acrylic source is certainly better than stainless steel, at least in terms of being able to do good energy calibrations. The energy response is much closer to the ideal, and the transparency of the source means that it casts little shadow. However, it is at the same time much more difficult to analyze, because these optical effects must be carefully modeled and understood.

I now believe that the best source that could be constructed is a hybrid of all three sources. This proposed design would be a small sphere, less than 1/2 litre in volume, with a radius of 4 to 5 cm. The gas-scintillation technique could be used to tag this source, using either a 1/2" PMT, or perhaps an array of avalanche photo-diodes attached to the inside of the sphere. (These would have the advantage of being small, and requiring no high-voltage supply. However, they have limited size, requiring a large light signal to trigger.)

The chamber wall would best be made of an opaque plastic, such as polyethylene, or perhaps a dyed polycarbon. The reason for this choice is that, unlike the stainless steel, it allows for a very accurate measure of $\Delta t/t$, the fractional tolerance on the wall thickness. The same quantity of material (about 1 g/cm^2, or 1-2 MeV) is needed to make a strong wall no matter whether stainless steel or plastic, but the tolerance on the thicker plastic is fractionally much better, resulting in a small systematic uncertainty on the energy loss of the particle. I suggest that a transparent acrylic wall is probably counter-productive, because of the complexities in analyzing such a source. An opaque plastic wall gives simplicity as well as well-understood systematics. In addition, light sealing the inner volume is not an issue.

Physical construction of such a source container is non-trivial. It would ideally be machined or cast in one piece, and if photodiodes were used rather than photomultipliers, careful testing would have to be done to ensure that the signal was of sufficient reliability. The small size of the source makes gas and electrical connections more awkward, since the need to attach to a much smaller neck.

The currently existing ^{8}Li source is a compromise between practical solutions to physical problems and good science, but I believe that given time and effort, a better bargain may be struck.

Part II

Muons

9

Introduction

9.1 Cosmic Rays

Cosmic rays are ionized nuclei, mainly protons, that hit the earth's atmosphere with a rate of about 1 kHz per square meter. They follow a power-law energy spectrum [55] roughly of the form:

$$\frac{dN(E)}{dE} = N_0 E^{-\gamma-1}, \gamma \simeq 1.7 \tag{9.1}$$

This power law holds up to very high energies. Above about 1 PeV, the spectrum steepens. (This is commonly referred to as the "knee" of the cosmic ray spectrum.) Cosmic ray primaries have been observed with energies as high as several joules per nucleon. Particle accelerators cannot reach energies nearly so high as the spectrum extends to, and so cosmic rays have historically been of enormous value in particle physics.

The dominant theory[55] for cosmic ray genesis is that they are created in supernovae, which are a source known to generate power on the right order of magnitude. The cosmic rays are then accelerated by interaction with shock waves, and then diffused in propagation by galactic magnetic fields. These mechanisms can explain most of the phenomena associated with the lower energy cosmic rays (up to 10^5 GeV), but higher energy cosmic rays are not so well modeled.

The composition of cosmic rays at low energies is fairly well understood from work with direct experiments. About 79% of all cosmic ray nucleons are in the form of protons, about 15% are in helium nuclei, and the rest are in heaver nuclei, up to Z values as high as that of nickel.[56]. The composition of the primaries is quite suggestive of their origin. For instance, usually rare elements like boron are quite abundant compared to elements created by stellar nucleosynthesis.[55] It is understood that the 'secondary' nuclei are created by spallation of the 'primary' nuclei in propagation between the source and the Earth. However, direct measurements have difficulty measuring composition at high energies (i.e. above the knee) and so indirect measurements, such as muon multiplicity, become interesting.

There are essentially three classes of experiment for looking at cosmic rays: direct measurements (such as balloon-carried spectrometers), air-shower measurements, and underground muon detectors. SNO can obviously be employed as the latter.

9.2 Cosmic Ray Muons

Cosmic rays create particle showers when they hit Earth's atmosphere. Besides creating electromagnetic showers (which can be seen by the air-shower experiments by either observing Cherenkov radiation in the atmosphere, or scintillation light from ionized nitrogen), there are hadronic showers for all but the lowest-energy cosmic rays.

$$p + \text{air} \rightarrow N, \pi, K, ... \tag{9.2}$$

The pions and kaons produced in these reactions can, in turn, decay into muons and the associated neutrinos. Calculating the muon flux means solving cascade equations that relate particle fluxes as a function of energy and atmospheric depth between primaries and secondaries in the shower. Gaisser [55] solves these cascade equations to calculate the muon flux at the bottom of the atmosphere for low and high energy limits:

$$\frac{dN_\mu}{dE_\mu} = N_0(E_\mu)\left\{A_\pi \xi_\pi(E_\mu) I_\pi(E_\mu) + A_K \xi_K(E_\mu) I_K(E_\mu)\right\} \tag{9.3}$$

where

$$\xi_i(E_\mu) = \frac{m_i}{E_\mu \cos\theta} \tag{9.4}$$

The functions $I_i(E_\mu)$ have solutions at the limits of very high and very low energy:

$$I_i(E_\mu) \rightarrow \begin{cases} B_i & \mathrm{High} E_\mu \\ \\ C_i/\xi_i(E_\mu) & \mathrm{Low} E_\mu \end{cases} \tag{9.5}$$

Here the subscript i refers to pion or kaon decay, as appropriate, and the two terms in flux refer to these decays respectively. Combining these equations and substituting for the cross-sections and the like, Gaisser arrives at equation (9.6).

$$\frac{dN_\mu}{dE_\mu} = \frac{0.14 E_\mu^{-\gamma_\mu}}{\mathrm{cm}^2 \text{ s sr GeV}} \left\{ \frac{1}{1 + \frac{1.1 E_\mu \cos\theta}{115 GeV}} + \frac{0.054}{1 + \frac{1.1 E_\mu \cos\theta}{850 GeV}} \right\} \tag{9.6}$$

Here γ_μ represents the steepness of the muon spectrum.

The high energy limit includes a $\cos\theta$ term, which refers to the zenith angle of the direction of the cosmic ray. (High energy secondaries tend to be very closely parallel to the direction of the incident primary, so $\cos\theta$ also indicates the muon direction.) In this case, the pion (or kaon) has two competing modes for extinction: decay in flight, or interaction with the earth. At zenith angles near the vertical the meson will hit the ground before it can decay more often than it will for showers coming from the horizon..

Muons with sufficient energy can survive to be detected in deep underground detectors. Equation (9.6) shows that the high-energy muons follow an approximate power-law spectrum of $E^{-\gamma_m u - 1}$, so the slope of the muon spectrum can be used to infer the primary cosmic ray index. By looking at the intensity of the muon flux through different slant depths of rock, one may use knowledge of muon survival probabilities to calculate the parameters (γ_μ in particular) of the muon spectrum at the surface, and therefore the primary spectrum.

9.2.1 Prompt Muon Flux

A rare but accessible channel to create muons in the cosmic ray shower is by charm meson decay. However, the cross sections for this are not well understood, and theoretical models conflict as to the expected rate by as much as 2 orders of magnitude [57].

The muons created by charm meson decay are referred to as "prompt" because of the short lifetime of the meson, even in the laboratory inertial frame. Because of this short lifetime, the mesons will always decay in the atmosphere before hitting the earth's surface. An approximation to this situation is the low-energy solution of equations 9.3 and 9.5, but with different normalization. This parameterization then gives a total combined muon flux at the surface:

$$\frac{dN_\mu}{dE_\mu} = \frac{0.14 E_\mu^{-\gamma_\mu}}{\mathrm{cm}^2 \text{ s sr GeV}} \left\{ \frac{1}{1 + \frac{1.1 E_\mu \cos\theta}{115 GeV}} + \frac{0.054}{1 + \frac{1.1 E_\mu \cos\theta}{850 GeV}} + R_c \right\} \tag{9.7}$$

R_c is the charm flux contribution relative to the pion contribution. More sophisticated functions can be derived from various models, but this simple form can serve to determine whether or not a prompt muon signal can be observed at all. LVD [57] has recently used this parameterization to find a limit of $R_c < 2 \times 10^{-3}$.

The SNO detector, which samples similar rock depths, should be able to make a such measurement.

9.3 Atmospheric Neutrinos

The creation of mesons in the atmosphere by cosmic rays creates a flux of high-energy neutrinos by the process:

$$\pi^+ \rightarrow \mu^+ + \nu_\mu \tag{9.8}$$

$$\mu^+ \rightarrow e^+ + \bar{\nu}_\mu + \nu_e \tag{9.9}$$

The similar process by kaon decay also occurs, as do the same processes under charge conjugation.

Because these processes are the dominant decay modes for the mesons, each meson makes, on average, two muon neutrinos and one electron neutrinos. This ratio of 2:1 is very robust across different models (e.g. [58]) and so serves as a good measurement to make.

The overall flux of neutrinos is not so easily calculated, since it depends on the specific cross-sections of these processes at high energies convoluted into a Monte Carlo that accounts for mesons and leptons being stopped at the surface. Thus, the overall flux is model-dependent and can be calculated to only about 20% [58]. In addition, the primary flux and spectrum has to be well measured; this is accomplished by airborne or surface measurements of the muon spectrum, for which precision experiments are required. [58, 59]

Atmospheric neutrinos are typically greater than 200 MeV, with the fluxes falling off at high energy. Calculation of fluxes at low energy is complicated by the geomagnetic field of the earth causing incoming cosmic rays to be deflected away from the earth's surface, creating anisotropic zenith and azimuthal angle distributions in an underground detector. New generations of three-dimensional Monte Carlo programs [60, 61, 62] are in development to account for this complexity. Above a few GeV of neutrino energy, these effects are largely negligible (due to the magnetic rigidity of the high-energy cosmic ray primary).

Underground neutrino detectors can observe atmospheric neutrinos in three modes: fully contained events, partially contained events, and through-going muons. Fully contained events are typically a few GeV or less, depending on the size of the detector. Neutrinos interact inside the detector, creating a detectable lepton. Partially contained events are of sufficient energy to escape the detector, so their energy cannot be measured, but have a measurable lower bound. Finally, a neutrino may interact in the rock outside the detector and create a high-energy muon which can penetrate through hundreds of meters of rock and then the detector. This allows measurement of a small flux over a large volume of interaction medium.

Fully contained events allow a detector to perform discrimination of electron-like and muon-like events, allowing measurement of the ν_μ/ν_e ratio. Through-going muons allow measurement of the higher-energy part of the flux and angular distributions, but only for muons (since electrons are not penetrating).

9.3.1 Atmospheric Neutrino Oscillations: Recent Results

The best atmospheric neutrino data to date is from Super-Kamiokande [63, 64]. This detector is a 50 kiloton water Cherenkov detector. The Super-Kamiokande collaboration has reported[65] a ratio-of-ratios that compares the electron and muon neutrino rates:

$$
\begin{aligned}
R &= \frac{\Big(N(\mu-\text{like})/N(e-\text{like})\Big)_{\text{observed}}}{\Big(N(\mu-\text{like})/N(e-\text{like})\Big)_{\text{expected}}} \\
R_{subGeV} &= 0.652^{+0.019}_{0.018}(stat) \pm 0.051(syst) \\
R_{multiGeV} &= 0.661^{+0.035}_{0.033}(stat) \pm 0.079(syst)
\end{aligned}
$$

This data provides some of the best evidence to date of neutrino oscillations. These oscillations are posited in much the same way as in the case of solar neutrinos, except now a deficit of muon neutrinos is seen. Moreover, this deficit is zenith-angle dependent (see Figure 9.1), which is strong evidence for a neutrino oscillation solution: the observed flux varies between short neutrino path lengths from down-going to the horizon (minimal oscillation) to long path lengths for upward-going events (maximal oscillation). (Actual oscillation over path length is washed out in the integration over energies.)

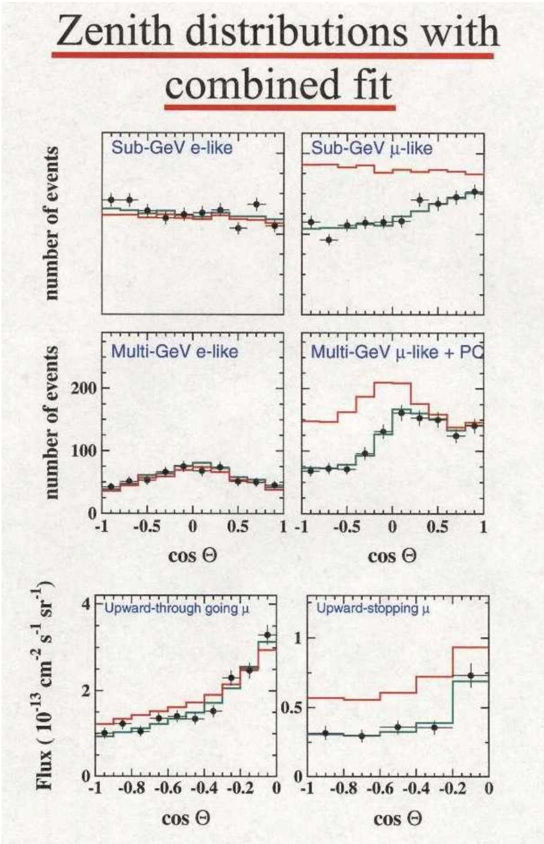

Figure 9.1: Super-Kamiokande Atmospheric Neutrino Results. **Taken from Sobel [65]. The solid curves show the expected fluxes for the cases of no oscillation and best oscillation fit ($\nu_\mu \rightarrow \nu_\tau$).**

Super-Kamiokande [65], along with the MACRO [66] and Soudan 2 [67] experiments, claim that the atmospheric neutrino data disallow $\nu_\mu \to \nu_e$ oscillations. This is independently confirmed by the CHOOZ [68] and Palo Verde [69] reactor experiments, which showed no ν_e disappearance. Super-K's global fits [65], as well as the MACRO results [66] highly favor $\nu_\mu \to \nu_\tau$ rather than $\nu_\mu \to \nu_{sterile}$. The arguments made by the Super-Kamiokande collaboration [70] are particularly convincing that sterile neutrinos do not participate in atmospheric neutrino oscillations.

However, LSND [71, 72] has observed neutrino oscillations conforming to a Δm^2 much larger than those reported for the solar neutrino or atmospheric neutrino cases. Thus, there are three different Δm's, and so there must exist *four* neutrino flavors. This fourth neutrino is dubbed 'sterile' since it does not constitute an allowed decay mode for Z^0 decay, which accounts for only three neutrino species. The sterile neutrino does not participate in weak interactions, only neutrino oscillations. Global fits [24, 22] confirm that this is the simplest method by which the data can be unified. This requires, however, that the $\nu_{sterile}$ be involved in the solar neutrino mixing, atmospheric neutrino mixing, or both.

This controversy may be resolved in part by SNO solar neutrino data, but independent checks on these results must also be accomplished. Therefore it is important to establish and verify, in atmospheric neutrino experiments, the oscillation mode for the ν_μ neutrinos to either active or sterile. .

In this work we examine the upward through-going muon signal in SNO. SNO will be sensitive to low energy atmospheric neutrinos as well (including a potential measurement of the $\nu/\bar{\nu}$ ratio), but with limited statistics. Such a discussion is out of the scope of this work.

9.3.2 "Upward" Through-Going Muons

Although upward-going muons do not give the clean 'smoking gun' signal of the ν_μ/ν_e ratio, they are useful in several other respects. Assuming a neutrino oscillation hypothesis, high-energy neutrinos are more sensitive to matter effects.

It is possible to determine which solution (active or sterile) is correct because the sterile neutrino will not encounter matter effects. Matter effects exhibit themselves in $\nu_\mu \rightarrow \nu_{sterile}$ oscillations as the neutrino passes through the Earth because the ν_μ and ν_τ feel neutral-current interactions with nuclei, whereas the $\nu_{sterile}$ does not. Following a form analogous to vacuum oscillations, we can determine the probability for a neutrino created in one position to be detected as the same flavor a distance L away.

For $\nu_\mu \rightarrow \nu_\tau$ oscillations, both neutrino flavors will undergo the same coherent forward scattering, so the oscillation probability can be written [70]:

$$P_{\nu_\mu \rightarrow \nu_\tau} = \sin^2 2\theta_V \sin^2 \left(\pi \frac{L}{l}\right) \tag{9.10}$$

where, in a vacuum, the oscillation length l is $4\pi E_\nu/\Delta m^2$.

For $\nu_\mu \to \nu_{sterile}$ oscillations, the sterile neutrino does not participate in the same process, so the oscillation probability becomes:

$$P_{\nu_\mu \to \nu_s} = \sin^2 2\theta_m \sin^2\left(\pi \frac{L}{l_m}\right) \tag{9.11}$$

$$\sin^2(2\theta_m) = \frac{\sin^2 2\theta_V}{(\zeta - \cos 2\theta_V)^2 + \sin^2 2\theta_V} \tag{9.12}$$

$$l_m = \frac{l_V}{\sqrt{(\zeta - \cos 2\theta_V)^2 + \sin^2 2\theta_V}} \tag{9.13}$$

Here the parameter ζ is given by $-\sqrt{2}E_\nu G_F N_n/\Delta m^2$ for neutrinos and $+\sqrt{2}E_\nu G_F N_n/\Delta m^2$ for antineutrinos, where N_n is the neutron density in the matter traversed. It is because of this term that matter effects become important for high-energy neutrinos. If the Δm^2 of $3 \times 10^{-3}\mathrm{eV}^2$ that Super-Kamiokande measures is correct, the ζ parameter goes to unity for a neutrino energy of 15 GeV [70]. A muon created by a charged-current interaction with a 15 GeV neutrino is too high energy to observe as a fully-contained event in any contemporary neutrino detector. Measurement of neutrinos by neutral-current interactions is one method of getting at this high-energy regime; looking at upward through-going muons is another.

It is also possible that mechanisms other than oscillations are creating a change of flavor. Paolo Lipari describes these succinctly:

> These studies [of high-energy neutrinos] are of great importance for the discrimination of the oscillation hypotheses from alternative mechanisms that are characterized by transition probabilities with different energy

dependences. The transition probability has the form $P = F(LE_\nu^{-1})$ for standard oscillations, $P = F(XE_\nu^0)$ (X is the column density) for models with flavor changing neutral currents, and $P = F(LE_\nu^{+1})$ for models with violations of the equivalence principle. To discriminate between these models it is useful to study a broad range of E_ν. [59]

The Super-Kamiokande collaboration have investigated [65] this question by fitting their observed neutrino oscillations to a function form involving a freely-floating power of the neutrino energy ($sin\beta LE^n$) and have found a best fit for function forms of $sinL/E$, strongly suggesting that these more exotic oscillation models are incorrect.

Upward-through-going muons have the basic problem that one cannot look at the ratio of e-like and μ-like events in ratio, so one is forced to compare the zenith angle distributions to model-dependent calculations of the ν_μ flux from cosmic rays. This flux, in absence of oscillations, should be identical for upward-going and downward-going neutrinos. The ratio (up/down) is again a robust way of looking for an oscillation signal, but cannot be done because the neutrino signal cannot be distinguished from the downward-going cosmic-ray muon signal.

Other neutrino experiments (MACRO, Super-Kamiokande, Baksan, IMB) looking for upward-going muons make a cut at the horizon ($\cos\theta < 0$) in order to eliminate this signal, so oscillations will show up as a zenith-angle dependent divergence from a modeled neutrino flux. SNO, however, enjoys the distinction that it is not built under a mountain but rather under an extremely deep, flat overburden of rock. This means that the atmospheric muon background becomes negligible at zenith angles as great as $\cos\theta \sim 0.4$. (See Figure 12.15 in Chapter 12.) This allows one to check at least part of the zenith angle distribution in absence of neutrino oscillations (i.e. at very short baseline distances).

Although the statistical errors on measurements at SNO are large (due to the relatively small detector size and as-yet limited live time), this measurement of the downward-going neutrino-induced muon flux will be an important check. It will allow the absolute flux of high-energy neutrinos to be fixed without a model-dependent shape correction, since the downward-going neutrinos will be undistorted by oscillations. This provides an excellent check on the neutrino oscillation hypothesis, equivalent to looking at the up/down ratio of lower-energy atmospheric neutrinos.

9.4 SNO Detector Response to Through-Going Muons

Muons are observed in SNO only by their Cherenkov light, seen in inward-looking and outward-looking phototubes. Both light intensity and timing can be measured; Figures 9.2 and 9.3 show a picture of a fairly typical through-going muon event. Besides the distinctive timing and hit-pattern, muon events exhibit a high-charge region near the position they leave the inner detector (dubbed the "exit wound").

Outward looking tubes can in principle be used to identify and reconstruct muon

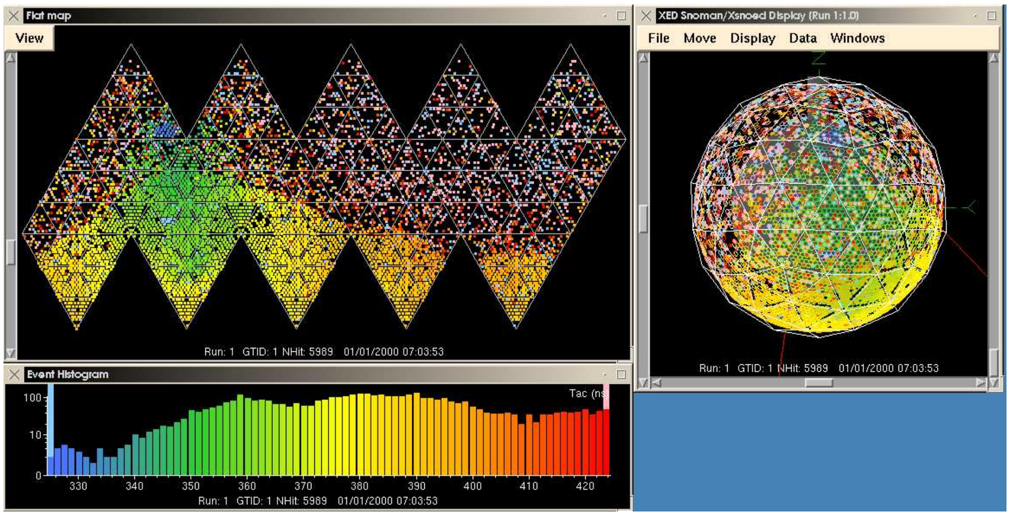

Figure 9.2: Typical Muon Event (Time). A muon with impact parameter 600 cm is simulated by SNOMAN and viewed by xsnoed [73]. Tube color corresponds to relative tube timing.

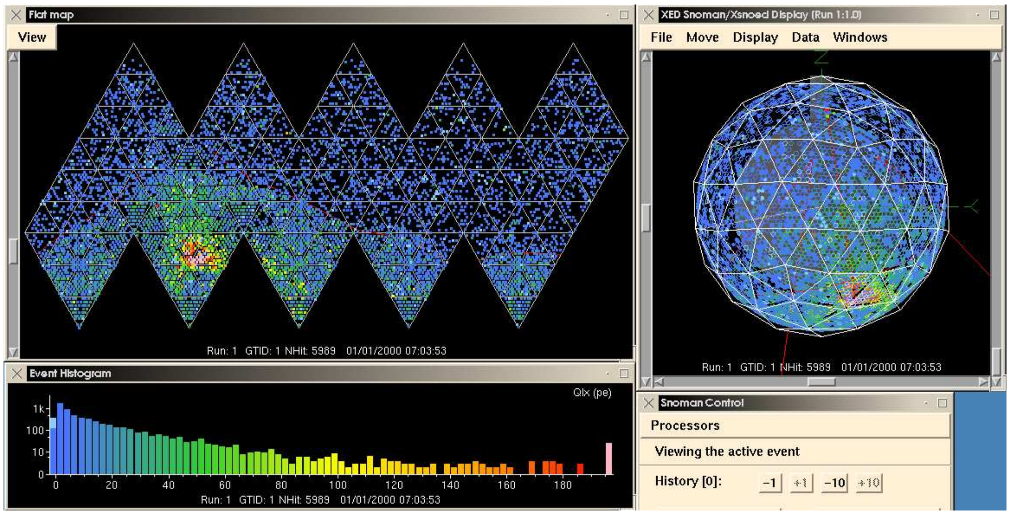

Figure 9.3: Typical Muon Event (Charge). The same muon event as shown in Figure 9.2. Tube color corresponds to anode charge in photoelectrons (QLX).

events, but in practice are not very helpful.[1] OWL tubes cannot be calibrated by the laserball system, so the time-zeros and charge-walk characteristics of these tubes are not calibrated. More importantly, the PMT cables form a dense wall in the outer detector, which can block substantial amounts of light, and the outer cavity walls are not easily modeled optically. Therefore, no Monte Carlo simulation exists for this outer detector. Because of these problems, this work does not employ the outer detector. (Results of this analysis, however, can be used to test the effectiveness of the outer detector as a muon tagging system for use with solar neutrino studies, which is discussed in ref. [75])

Because of spherical symmetry of the SNO detector design, the effective cross-sectional area for through-going muons is constant over all angles. Detector response to a given track geometry is simply a function of the track 'impact parameter', or distance from the center of the detector to the closest approach of the track. The length of track in the inner detector is given by

$$l = 2\sqrt{R^2 - P^2} \tag{9.14}$$

where R is the effective radius of the detector, and P is the impact parameter for the event. R is taken as 840 cm, which corresponds to the mean distance from the center of the detector to the front-face of all the inward-looking PMTs.

[1] This can be contrasted with the example of Super-Kamiokande, which is able to use the outer detector as part of the event identification system. [74].

Muons with large impact parameters are known as ’clipping’ muons. The response of the detector to these muons changes slightly as the angular cutoff for the reflector buckets becomes important for the event topology. Removing these events is equivalent to reducing the effective area of the detector.

If such a cut is made at an impact parameter of 750 cm, this corresponds to an effective detector area of 1 767 000 cm^2, a minimum track length of 757 cm, and a mean track length of 1020 cm. This corresponds to a minimum muon energy of approximately 2.2 GeV (using the dE/dx tables of Lohmann [76]).

Multiple muons made in the same cosmic-ray shower will sometimes be detected (simultaneously) in a deep-underground detector. (A simple argument [77] can be made that the multiplicity of observed events is correlated to the composition of the primary cosmic rays that created them.) Multiple muon tracks, if close together, cannot be resolved by SNO; the two timing signals will simply smear together, and the exit wounds will be indistinguishable. At distances greater than 1 or 2 meters, they can in principle be separated.

10

Data Collection

Raw data from SNO was first selected by run type, then passed through two stages of data reduction. The resulting summary data was reconstructed, and judged by the reconstruction goodness-of-fit. The data selection and reduction cuts are described here.

10.1 Data Selection

Data was taken only from SNO 'neutrino' runs. The criteria for these runs are that the detector is taking data at low rates (less than 30 Hz), that there is no calibration source active, that the trigger is set to NHIT-triggered data with low threshold, and that the individual channel settings are in a well known configuration.

In addition, runs were chosen from the same run list as the official neutrino analysis which has several more criteria [78]: There was no lab activity, software error or hardware breakdown during the run, no crate of electronics was turned off, nor were more than a total of 960 channels. Only official 'production' data (started November, 1999) were used to ensure stability of the data and the associated calibration databases. (However, pre-production data was used during early stages of analysis, to test the data reduction and reconstruction algorithms.)

It was judged best to be slightly conservative with these criteria, despite the fact that high data quality is not strictly necessary for finding high-energy phenomena such as through-going muons. However, the largest problem with muon analysis is the rejection of detector-related backgrounds in the detector, such as flashers, pickup, neck light, and breakdown (which are discussed in the next section). It is policy of the detector operations group, for instance, to change the run mode of the detector to 'supernova' mode when one of these backgrounds is (or is in danger of) swamping the detector with high-rate noise. Data taken under these more noisy conditions may be mostly good to use, but for simplicity and safety, this analysis works from the best data available.

Another danger that is avoided by this selection is detector anisotropies. Usually if more than a few tubes are turned off, there exists a dead region of tubes. Muons with exit positions in such a dead area have higher odds of mis-reconstructing. Therefore, the upper limit on dead tubes works to avoid this circumstance.

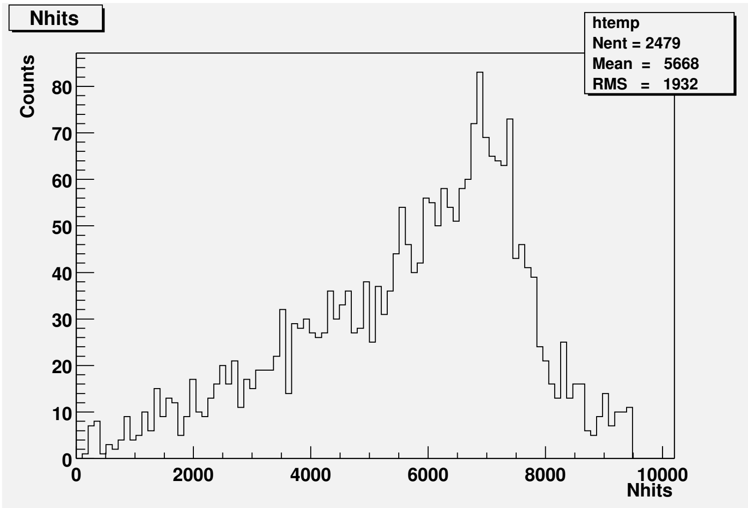

Figure 10.1: NHIT spectrum for Monte Carlo Muons. Muons generated at the surface with a spectrum of $\gamma_\mu = 2.7$ are propagated to detector depth via Monte Carlo code of Lipari and Stanev [79] and simulated with SNOMAN.

10.2 Data Cuts

The primary data selection cut is NHIT, which serves as a basic method of finding the energy deposited in the detector. Muons typically fire more than 1000 phototubes. A Monte Carlo spectrum of NHIT is shown in Figure 10.1. A cut of 150 NHIT (which corresponds roughly to a contained electron with energy 16 MeV) is used as a conservative lower limit.

There are several detector-related ("non-physics") backgrounds that are of concern above this NHIT threshold:

- Flashers
- Neck light

- Electronic pickup
- High-voltage breakdown
- Flat-TAC
- Retriggers
- DAQ artifacts

Flashers were described in Section 2.5. Flashers can occasionally generate events of several hundred NHIT. (See Figure 10.2.) In addition to creating a large quantity of light, the flashing tube will generate a large anode pulse, which creates pickup clusters on neighboring channels. Because of this, a flasher can occasionally have the same NHIT and charge structures as a clipping muon. A large fraction of the tubes in SNO are known to flash, so they cannot simply be cut out of the data. The time spread of flashers tends to be much broader than that of a real event, and the event topology is different, so they can be removed by reconstruction.

Because flashers of great concern to solar neutrino studies, there is a large number of cuts employed by SNO to remove flasher events (see data cleaning results in ^{8}Li section Chapter 7.) but most of these rely on looking for the high-charge pickup cluster, large trigger charge, or some sort of NHIT-biased clustering. This makes use of these algorithms dangerous for events with high NHIT or high charge per tube so they are not used.

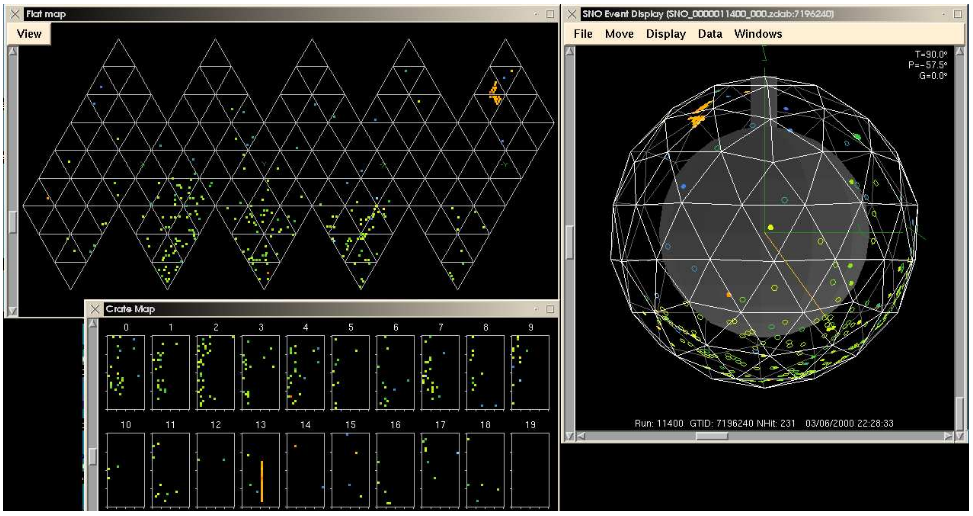

Figure 10.2: Typical Flasher Event. The small patch of tubes at the top of the PSUP (and shown in crate 13) is a pickup cluster fired due to the anode spike of the flashing tube. Light is thrown across to the bottom of the detector in an oblong shape.

Neck light is apparently created through several mechanisms. For instance, the calibration source manipulator is known to generate small amounts of in-time light, thought to be created by static discharge of the source umbilicals against the manipulator take-up pulleys.[1] Neck light creates events with many tubes hit at the bottom center of the detector. The PSUP shadows this light so that the hit pattern is similar to that of a centered, vertically downward muon. Although the timing pattern of tubes is different from a muon, this is nonetheless the most dangerous of the backgrounds in that the morphology and charge distribution of the events is close to that of muons. Two phototubes are installed high up in the neck, and these are used to

[1] This variety of light has been dubbed “manipulight” by the SNO collaboration zoologists.

cut neck events, using the algorithm described in ref. [80]. This algorithm uses the timing of these tubes to cut neck events with reasonable efficiency.

Electronic pickup is not terribly dangerous except in that it has large NHIT. These events tend to have zero (i.e. pedestal) charge in the vast majority of channels, and completely unphysical time structure.

High voltage breakdown is a case of electronic pickup that deserves some comment. The high-voltage connector on SNO PMTs is known to break down when immersed in degassed water. Although the H_2O in SNO is now re-gassed with N_2 gas in the recirculation/chiller loop, some connectors are prone to breakdown following the earlier stress. This breakdown is usually exhibited by bursts of very high charge seen in the front-end electronics, combined with detector-wide pickup.

Flat-TAC events are so named because they have a time structure that is not event-like but resembles DC light. These will never reconstruct like a muon event, but are convenient to remove.

Retrigger events are slightly more serious. If a phototube fires with many p.e., it will create a trigger pulse extended in time. This will in turn cause the front-end electronics to generate multiple trigger pulses, which can add up in the global sum to create a second trigger immediately following the first, after the lockout time has expired. The result is that a second event can follow a first 480-540 ns later. The hit pattern of the tubes will tend to mirror the first event, so this can and should be removed with a time cut following the first.

Last, there are several artifacts created by the data acquisition system, such as 'orphan' events. These are events where data from one or more front-end cards fails to be included in the rebuilt event, and so creates a spurious event as the amputated data is left 'orphaned' in the data stream. This background is easily removed.

Here are the cut algorithms used.

- $150 < N_{hit} < 10000$ Basic energy cut.
- Retrigger cut. Cuts any event for which follows the previous one by less than 5 μs.
- Junk cut. Cuts orphans and other DAQ oddities.
- Q/NHIT. Cuts events with little or no total anode charge.
- Neck tube cut with dead time. Cuts events in which the neck tubes fire, and all events preceding or following by less than 5s.
- t_{RMS} cut. Removes events in which the second moment of the phototube time distribution is greater than 70 ns.

The NHIT cut is explained above. It is quite conservative, since very few through-going muons will have NHIT less than 150. Those muons that do have such low NHIT will tend to be muons that are just inside the PSUP (i.e. 'clipping' muons) and so will tend to be removed by a radial cut anyway. (See chapter 11.)

The Q/NHIT cut computes a parameter related to the mean charge per tube,

$$\frac{\sum_{i=1}^{N_{HIT}-100} q_i}{N_{HIT} - 100} \tag{10.1}$$

The unused 100 tubes are the highest charge tubes in the event. Van de Water [81] claims that this cut parameter corresponds roughly to 1/4 p.e. per tube. It should be noted that this cut is quite safe, since there is a charge cut already implicit in the fitter algorithm. (See Section 11.2.)

The neck tube dead time cut uses the identification algorithm by McCauley [80] to identify neck tubes. However, although this cut is a very good one (since the cut is based on an external (veto) detector, so introduces no bias) it is known that the neck tubes are not 100% efficient. This is most important during a burst of such events, when the neck tube channels may experience dead times.

Neck events do tend to occur in bursts, as is evidenced by Figure 10.3. (Neck events were identified using the neck tube cut for a subset of neutrino runs, 10000 - 10173 inclusive. Only events with NHIT > 30 are shown.) In the case of solar neutrino analysis, these bursts are removed with a simple burst cut, but such a cut will also tend to remove muon events, particularly those that are followed by spallation decays or neutrons in the D_2O. It is obvious that creating a dead time around each (tagged) neck event will have good efficiency for removing untagged neck events.

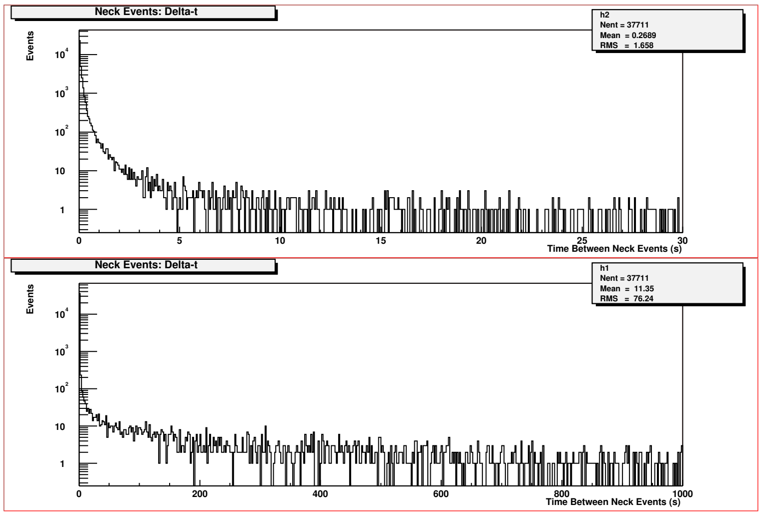

Figure 10.3: Time Structure of Neck Events. The time between successive neck events is plotted for 346 hours of data. The top plot is an expanded view of the bottom, showing the distribution for delta-t less than 30s.

A dead time of 10 seconds is used, so that any event up to 5 s before or after a neck event is cut. From this sample set, the dead time for this cut will be approximately 1.2%. Number of events per burst are shown in Figure 10.4.

The t_{RMS} cut removes all events where the RMS statistic on all inward-looking tubes is greater than 70 ns. It is known that pickup events and flat-TAC events generate events with large time spreads. Muons tend to generate events quite limited in time spread, as is shown in Monte Carlo data in Figure 10.5. The largest values seen in Monte Carlo are about 40ns, so 70ns represents a conservative cut on the data.

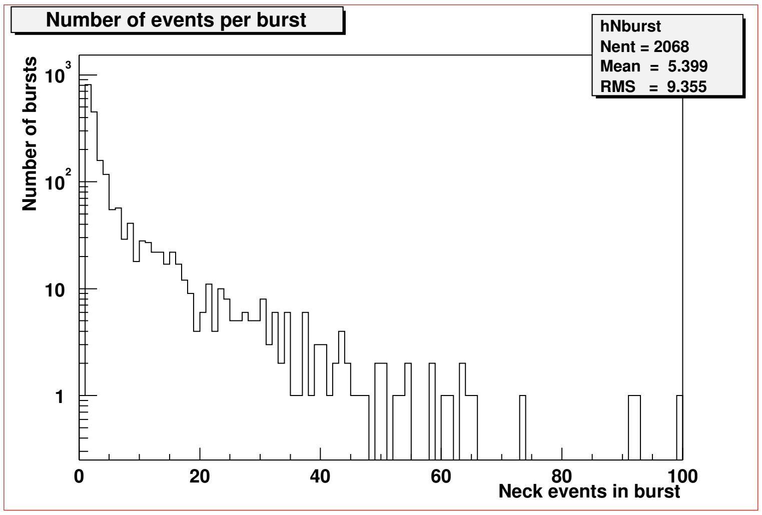

Figure 10.4: Neck Events Per Burst. A burst is here defined as any sequence of neck event in which each event follows its predecessor by less than 5 seconds.

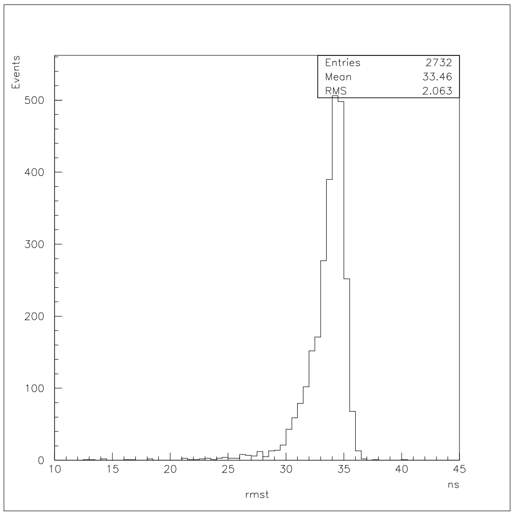

Figure 10.5: RMS Time for MC Muons. The RMS of the individual phototube times per muon event is shown, in nanoseconds. Events are from SNOMAN Monte-Carlo.

10.3 Contamination and Sacrifice

The cuts described in this chapter are intended to cut most of the recorded events without cutting the muon signal. There are two systematic measures associated with this procedure: *sacrifice*, the number of events of interest (in this case, muons) cut during the data reduction, and *contamination*, the number of background events remaining in the data set afterwards that are not signal. Measures of sacrifice cannot be directly determined in the absence of a calibration source (as is done in the case of solar neutrinos), so must be evaluated with Monte Carlo or other means. Contamination is very difficult to measure in any analysis.

In this analysis, the data used in the reconstruction stage has a large contamination; a rough estimate gives the ratio of background events to muon events as about 6:1. Nearly all of these background events are flashers, (which do not reconstruct and so are removed by the fitter in the next stage of the analysis). Neck events constitute a much more dangerous background that could contaminate the reconstruction data.

McCauley [82] estimates the contamination left by the neck tube cut as 4×10^{-4}, which will allow approximately 20 neck events to contaminate the data. The burst analysis shows that approximately 98% of all neck events occur in bursts. Therefore, the final contamination of neck events in the reduced data sample (before reconstruction) should be on order 0.5 events.

The sacrifice is better understood than the contamination. The retrigger and dead-time cut have sacrifices that are substantial, but exactly known. In the case of the retrigger cut, we are cutting approximately 5 microseconds per event, with a raw trigger rate in SNO of about 20 Hz, which results in a dead-time loss of 0.01%, which is negligible compared to other corrections. In the case of the neck tube dead-time cut, the dead time is tracked exactly and summed; the overall dead time on the data sample is 0.55% of the live time. The only danger with such a cut is that the neck tube tag is in itself biased to tag through-going muons; this concern is dealt with in an analysis described in Section 13.1.2; These sacrifices are folded into the live-time calculation.

The t_{rms} cut cannot be evaluated except by Monte Carlo, for which it cuts no events in a data sample of 2732 events, which gives an upper limit on the sacrifice of about 0.03%. The same holds true of the raw NHIT cut, giving the same upper limit. The Q/NHIT and junk cuts should sacrifice no events, but this cannot be directly tested.

The Q/NHIT depends on detector charge response, which is not well simulated in Monte Carlo. Similarly, the junk cut response cannot be estimated because the full DAQ system is not simulated.

Therefore, a reasonable upper limit on the sacrifice is about 0.1%, after dead time corrections. It is not expected that this sacrifice should be biased in muon direction, since the important difference between different muon track geometries is in impact parameter, as is discussed in Chapter 11.

10.4 Live Time

Data used for analysis was taken between November, 1999 and June, 2000, corresponding to runs 10000 through 12168 (inclusive), for a total of 595 sub-runs.

A total of 5M events (with NHIT > 30) were processed, resulting in a reduced data set of 84k events used for fitting. The live times are shown in the table below. The error on total run time is the upper limit of 0.2% quoted by the data selection committee; they find this error by comparing the 50 MHz and 10 MHz clocks. [83].

Table 10.1: Live Time Calculation.

Total run time	3577.03 h $\pm$ 7.15 h
Neck tube dead time	27.29 h
Estimated retrigger dead time	0.50 h
Total live time	3549.24 $\pm$ 7.15 h

11

Reconstruction Techniques

11.1 Basics

The muon fitter minimizes a goodness-of-fit function that is a simple chi-squared in PMT timing as compared to a model:

$$\text{GOF} = \frac{\chi^2}{\text{N}_{\text{good}}} = \sum_{i=1}^{\text{N}_{\text{good}}} \frac{(t_i - t_i^{fit})^2}{(1.6\ \text{ns})^2} \tag{11.1}$$

The model assumes that every tube fires from light that is direct Cherenkov light from a muon that follows a straight line through the detector. This ignores effects of scattering, which are small for typical through-going muon energies, and also presumes that any phototube in the event was not fired by reflected, refracted, or scattered light, and that there is no pre-pulsing or late-pulsing of the signal. More specifically, t_i^{fit}, the time a particular phototube was supposed to fire, is given by equation (11.2). (See Figure 11.1.)

Table 11.1: Definition of Symbols.

d	Radius of PSUP, 840 cm. (i.e. Size of spherical detector.)
GOF	Goodness of fit
t_i	Time that PMT i fired
t_i^{fit}	Time that PMT i should have fired given the current hypothesis
q_i	Charge measured on anode of PMT i
N_{hit}	Number of well-calibrated tubes hit in event
N_{good}	Number of tubes after cuts
$\hat{v}$	Muon direction vector
η	Muon direction vector zenith angle (0=upgoing)
ψ	Muon direction vector azimuthal angle
$\vec{x_0}$	Muon position as it enters the PSUP
$\vec{x_f}$	Muon position as it exits the PSUP
θ	Muon exit position in polar coordinates, zenith angle
ϕ	Muon exit position in polar coordinates, azimuthal angle
p	Track impact parameter; radius of closest approach to center of the detector
n	Index of refraction of water
θ_c	Cherenkov angle

Note that superscript 'fit' always implies fitted quantity, where no superscript implies the true quantity.

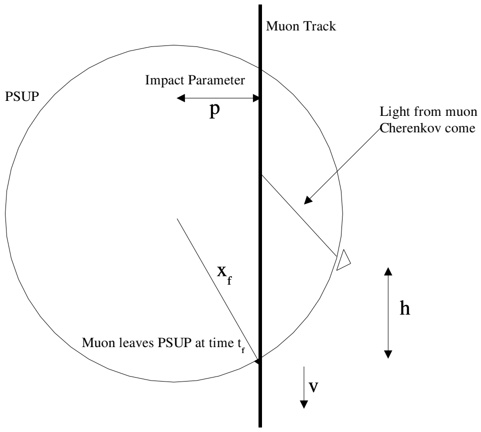

Figure 11.1: Muon Fitter Geometry.

$$t_{i,fit} = t_f + \frac{1}{c}[|\vec{r}_p|\sqrt{n^2-1} - h] \tag{11.2}$$

where

$$h = \hat{v}\dot{(}\vec{x}_f - \vec{x}_i) \tag{11.3}$$

$$\vec{r}_p = |\vec{x}_f - \vec{x}_i + h\hat{v}| \tag{11.4}$$

$$\sqrt{n^2-1} = \tan\theta_c \tag{11.5}$$

Note that the refractive index, n, enters in two places: the Cherenkov angle, and the speed of the resulting light in the water. An implicit assumption is that there is only one effective index of refraction in the detector; differences between media (acrylic, D_2O, H_2O) are ignored. Wavelength dependence is also ignored. These small differences are largely washed out statistically in the large amount of light shed by a muon.

This model neglects the shadowing of light in the detector. Light in the real world cannot physically travel from outside the PSUP to the inside, and the real phototubes accept light only from the forward direction. This simplification in the model is addressed in the fit evaluation stage.

11.2 Algorithm

The fitter follows this procedure:

(1) Compute raw tube statistics: N_{hit} and $\langle q \rangle$ (the mean charge per phototube). Charge is calibrated QHL (i.e. high-gain, long integration time.).

(2) Throw out badly calibrated tubes and throw out all low-charge tubes. Tubes with high charge are more likely to have been hit by direct Cherenkov light, so are more likely to satisfy the model. The charge cut is given by: $q_i \geq (\langle q \rangle \times 1.2)$

(3) Find the exit wound. A cluster of high-charge tubes is chosen as the exit point. The cluster is defined by a set of less than 10 tubes inside 80 cm radius of a given trial tube. The center tube is not used in the charge sum. The exit time is estimated from the centroid time of the cluster.

(4) Search $\hat{v}, \vec{x_f}$ on a grid. Seven points at and around the exit wound, and 300

directions are each independently evaluated by Equation (11.1). Chi-squared is calculated using only tubes where $|t - t^{fit}| < 10$ ns. Each trial is a fit to one parameter, the muon exit time. Directions are chosen from a pre-calculated ensemble of (η, ψ) co-ordinates. [1]

(5) The best trial is chosen, and all tubes outside the time window $|t - t^{fit}| < 10$ ns are thrown out.

(6) A full minimization is done on all track parameters (two direction, two position, one time) with equation (11.1), using the *Numerical Recipes* code MRQMIN. [84].

(7) The tube with the worst chi-squared contribution is thrown out, and the function is fit again. This is iterated until a small total chi-squared is achieved, or until 30 tubes have been thrown out. The fitter always keeps at least 50 tubes at any stage.

(8) Evaluate the fit with the F_{should} and p.d.f. parameters. (See Section 11.3.)

The core of the algorithm is in step(6), which is a maximum-gradient technique used in 5 dimensions. Gradients are calculated for each trial point, using analytical expressions for $\sum_i \frac{dt_i^{fit}}{d\theta}$, etc.

[1] The first 20 points are (θ, ϕ) coordinates of the vertices of an isocohedron. Successive points are chosen by bisecting the faces of the polyhedron and projecting the centers of bisection onto the unit sphere. The result is a set of unit vectors such that $\hat{v}_i \cdot \hat{v}_j$ is very similar for all nearest neighbors. Thanks to Dr. Bernie Nickel for help with this procedure.

This method depends on having a good subset of tubes as inputs because the simple model described in the previous section does not account for optical complications of the detector. The acrylic vessel, PMT reflector petals, and even the PMTs themselves all act as optical surfaces that reflect the Cherenkov light from the muon to other PMTs, so many of the tubes in an event can fire due to reflected rather than direct light. (See Figure 11.3.) This introduces a large number of tubes with systematically late times that must be suppressed as much as possible.

Tube selection is accomplished in step (2), where a charge cut is made. Reflected light tends to be greatly attenuated, so tubes hit only by reflected light (i.e. the tubes with late times) will tend to have systematically lower charge than tubes hit by direct light This cut is made relative to the mean charge per tube, because the overall quantity of light tends to vary from event to event. Muons will produce high energy knock-on electrons (delta-rays) stochastically, and each delta-ray accompanying the muon creates a share of the total Cherenkov light. Using mean charge guarantees that no *a priori* assumptions are made about the total quantity of the light produced by a given muon.

Step (2) also serves as a reasonable data cleaning cut, since it requires that the anode charge distribution in the event be fairly broad: at least 50 tubes have to be greater than 1.2 times the mean charge. This tends to eliminate events in which all tubes are hit by single p.e. or less.

Steps (5) and (7) throw out tubes that do not agree well in time with the current track parameters. This is done for similar reasons as the cut in step (2), in that it removes tubes that are likely to be reflections. However, this is now being done in a way based on the tube timings themselves, and thus biases the data in favor of a good muon fit, throwing out all tubes that disagree and generating a good chi-squared no matter what the true event is. Therefore, the chi-squared parameter being minimized is not a good parameter with which to test the hypothesis that the fit is a good one.

Step (4) (the grid search) is necessary to ensure that we have correctly sampled the global parameter space before settling down into our a specific local minimum. Maps made of the global parameter space indicate that it tends to be well-behaved for selected events, but this search ensures a global minimum is found if this is not the case.

This grid search is not in all 5 parameters, but rather concentrates on getting the direction correct, and searches only locally for the best exit position. It is therefore important that step (3) correctly finds the exit position of the muon. Several different algorithms were employed on Monte Carlo data, of which this was the best. (Other methods included, for instance, finding the first moments of the positions of all the hit tubes, weighted by anode charge, then projected onto the PSUP.) Simply looking for the largest charge is dangerous as a badly calibrated tube could falsify this signal.

Naively, one would expect that the entrance position of the muon could be found in an analogous way, by looking for tubes hit quite early in the event. Super-Kamiokande, for instance, uses this method by looking in its outer detector. [74]. SNO has no good outer detector (as the OWL tubes have an unknown response). Muons shed very little isotropic light, so a muon entering the detector does not shine much light on the tubes near the entrance point, but rather throws its first light across to the far side of the detector. Therefore, the first tubes hit are not necessarily very close to this entrance position. Moreover, beta-gamma background or random tube noise in near coincidence with a given event will generate 1-2 early tube hits on average which could fool an algorithm looking for early hits. Last, an effect known as pre-pulsing has been observed in SNO, causing a very small fraction of tube hits to appear systematically early in the event. These practical considerations mean that the entrance wound of the muon track is easy to find reliably.

Together, these elements of the algorithm tend to make for good reconstruction, without a huge burden of processor time. On modern processors, the algorithm can process events at a rate of about 5-10 seconds per event.

11.3 Evaluation of the Fit

The numerous cuts on phototubes, along with an aggressive algorithm for finding the minimum creates a situation in which the goodness-of-fit parameter in Equation 11.1

is not a good criterion to determine the quality of the fit. Therefore, independent tests must be used to test the fitter's hypothesis, which is that the event was a through-going muon with track parameters $(t_f, \theta, \phi, \eta, \psi)$. Two criteria are used for this evaluation: the 'F_{should}' and 'PDF' parameters.

The first of these uses the topology of the event, i.e. the pattern of tube hits on the PSUP. For the fitted track, each live tube in the detector is assessed to determine whether or not it could have been hit by direct light from the muon. The muon must have been inside the PSUP when it generated light that would hit the PMT, and the light must be inside the acceptance cone of the PMT bucket and reflector assembly. For the set of PMTs satisfying these conditions, the fraction that actually went off is defined as F_{should}.

$$F_{should} = \frac{\text{Number of PMTs that should have fired and did fire}}{\text{Number of PMTs that should have fired}} \tag{11.6}$$

The correlation between fit accuracy and this parameter, for Monte Carlo data, is shown in Figure 11.2. A cut of $F_{should} > 0.8$ allows one to remove nearly all the bad fits. Note that most of the fits removed by this cut are at high impact parameter (i.e. "clippers"). This effect will be discussed later.

The second goodness-of-fit criterion uses the tube timings for all tubes hit in the event. Unlike the actual fitting procedure, this function uses *all* the hit phototubes, and weights them according to a probability density function, rather than chi-squared. The probability density function used is shown in figure 11.3. It was generated by

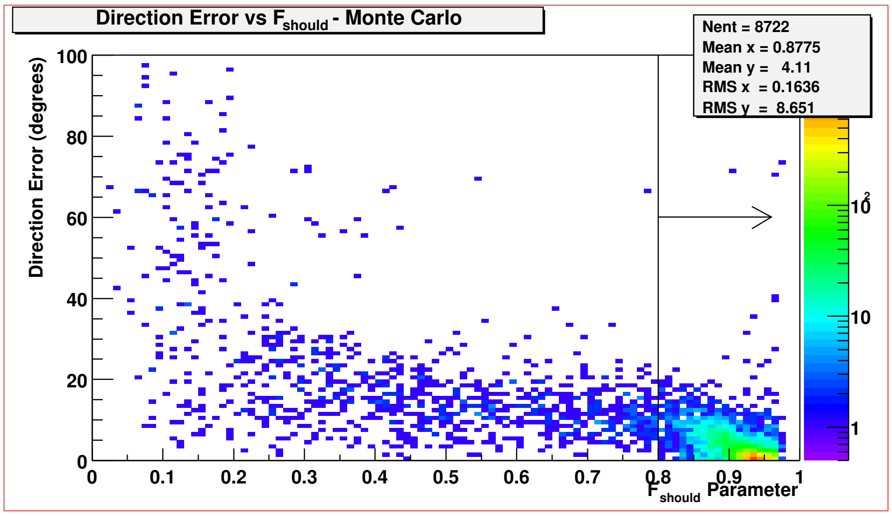

Figure 11.2: F_{should} **Parameter Vs. Direction Fit Error. The cut used to distinguish 'good' fits from 'bad' is shown as the vertical line. Color indicates number of counts per bin, indexed on the right.**

injecting approximately 100 muons, by Monte-Carlo, into the detector, choosing from realistic energy, direction, and position distributions. The Monte Carlo information is used to generate a 'perfect' fit and the resulting tube time residual is summed over all tubes in all events.

This function is applied to each tube in an event to generate a probability. The value used to evaluate fits is:

$$\sum \frac{-\log(\mathrm{pdf}(t - t^{fit}))}{N_{HIT}} \tag{11.7}$$

The correlation between this function and the direction error (on Monte Carlo data) is shown in figure 11.4. As can be seen from the plot, many poor fits can be

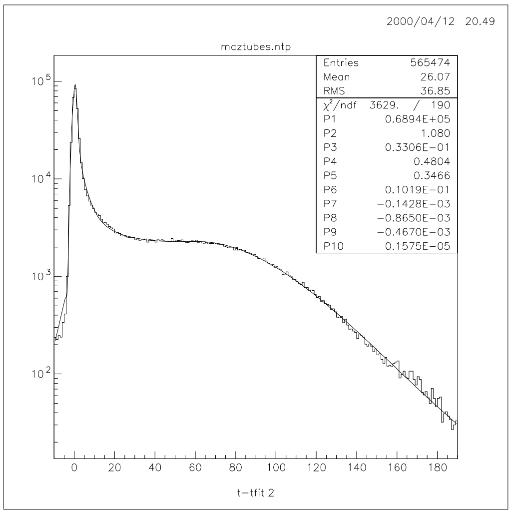

Figure 11.3: Sum of PMT Time Residuals From 'Perfect' Fits. This distribution is used to generate the 'pdf' function used to evaluate fits. The curved line indicates the parameterization of the distribution used in the algorithm.

eliminated by cutting on this parameter. This cut ensures that the fit has not found a false minimum arrived at from throwing out the wrong tubes. Although the initial charge cut on the tubes is good at picking out a subset of tubes that are mostly fired by in-time light, it does not pick out a majority of these tubes. Thus, this PDF function uses much more information than the actual fit.

Note that this technique could be further refined in future by taking a probability density function that is itself a function of fit impact parameter (or of NHIT) but this complexity is not used here.

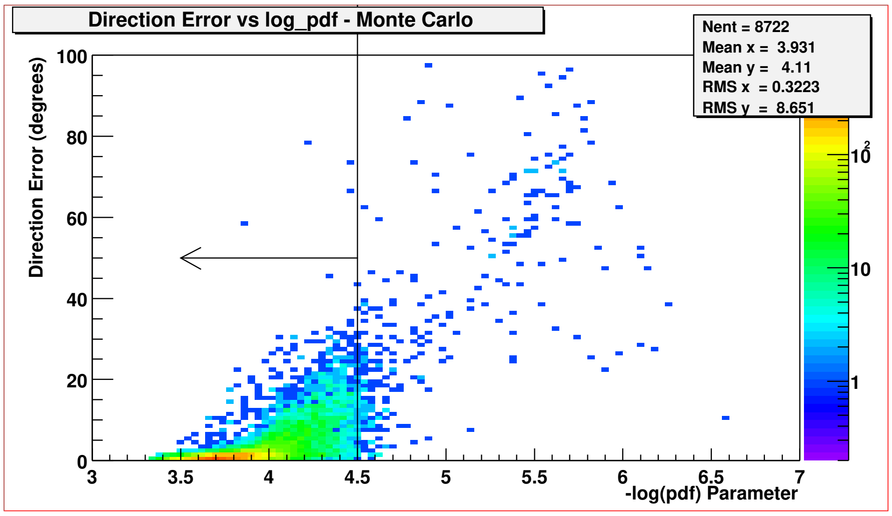

Figure 11.4: Direction Error Vs. PDF Goodness-of-Fit. **The cut used to distinguish 'good' fits from 'bad' is shown as the vertical line. The number of counts per bin is indicated by color (indexed on the right).**

11.4 Fitter Performance

11.4.1 Position Error

The error on the position in the detector is shown in figure 11.5. Again, note that muons going through the center of the detector fit much better than those that go through only the light water. This plot shows a consistent "pull" of the fitter towards the PSUP, so that fits that are at true impact parameter p reconstruct at impact parameter $p^{fit} = p + \Delta p$.

This 'pull' is exhibited in nearly all of the SNO reconstruction algorithms. For a clipping muon, nearly all PMT hits are on one side of the track. Therefore there is no penalty for the fitter to adjust the time of the track systematically earlier and

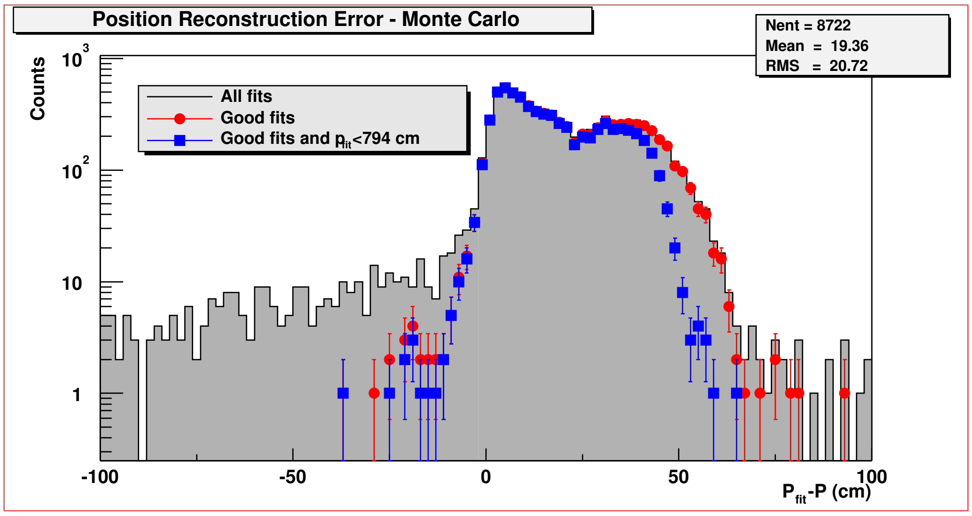

Figure 11.5: Impact Parameter Reconstruction Error. Positive values indicate that the fit track of the muon is too far from the center of the detector, which is the dominant "fitter pull" for the muon fitter. The tail at negative numbers is due to mis-reconstructing clipping muons as through-going ones, an effect which is mostly removed by the goodness-of-fit cuts.

move the track closer to the wall. All fitters used in SNO tend to pull outward.

Because this is a systematic (not random) effect, it can be corrected. Figure 11.6 shows the pull as a function of event position, and the correction found with Monte Carlo data, which is a piecemeal polynomial. This correction is a maximum of about 40 cm at the edge of the detector. (Note that there is a distortion at the radius of the AV, and a change in slope at this point.) The detector position resolution after correction is shown in Figure 11.7.

The impact parameter is used to make a radial cut on the data. Good reconstruction of muon direction requires a sufficiently long 'lever arm' of track length inside

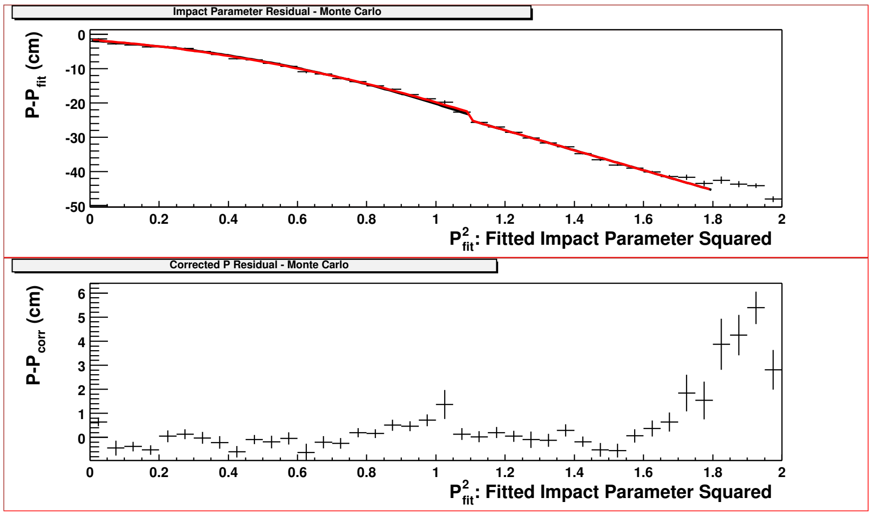

Figure 11.6: Fitter Pull Correction. The abscissa in both plots is the reconstructed impact parameter squared, $(P_{fit}/600cm)^2$. In these units the AV is at 1 and the PSUP is at approximately 2. (Each bin has the same cross-sectional area.) The top plot shows the fitter residual and the systematic correction. The bottom plot shows the fitter residual after the correction.

the detector. A track length of ∼7 meters measured with a time resolution of about ∼1 ns gives a direction resolution of about 2 degrees, which is acceptable resolution. Thus, a choice was made to select for analysis only events within $P_{corrected} < 750\ cm$, or $P_{fit} < 794.4\ cm$. This gives a minimum track length of approximately 7.6 m.

11.4.2 Direction Error

The direction reconstruction error is given in Figure 11.8, as derived from comparing the fit direction to that given by the Monte Carlo. The fit gets better for muons that go through the center of the detector. Note that there are few fits at high residual angle after the goodness-of-fit evaluation.

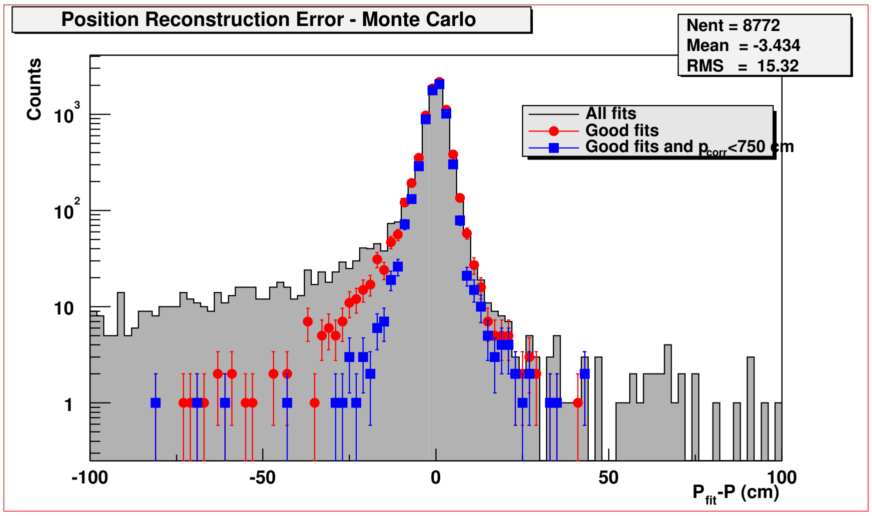

Figure 11.7: Corrected Impact Parameter Error. The error on impact parameter (after correction) is shown. "Good fits" have -log(pdf)<4.5 and F_{should} >0.8

Table 11.2: Reconstruction Direction Error. Angles are in degrees. The 90 and 99% labels refer to the angles which contain 90 or 99% of Monte Carlo events.

	Mean Error	RMS	90%	99%
All fits	3.4	5.3	10.8	40.0
Good fits	2.1	2.6	5.2	12.8
Good fits w/ radial cut	1.4	1.5	2.8	7.8

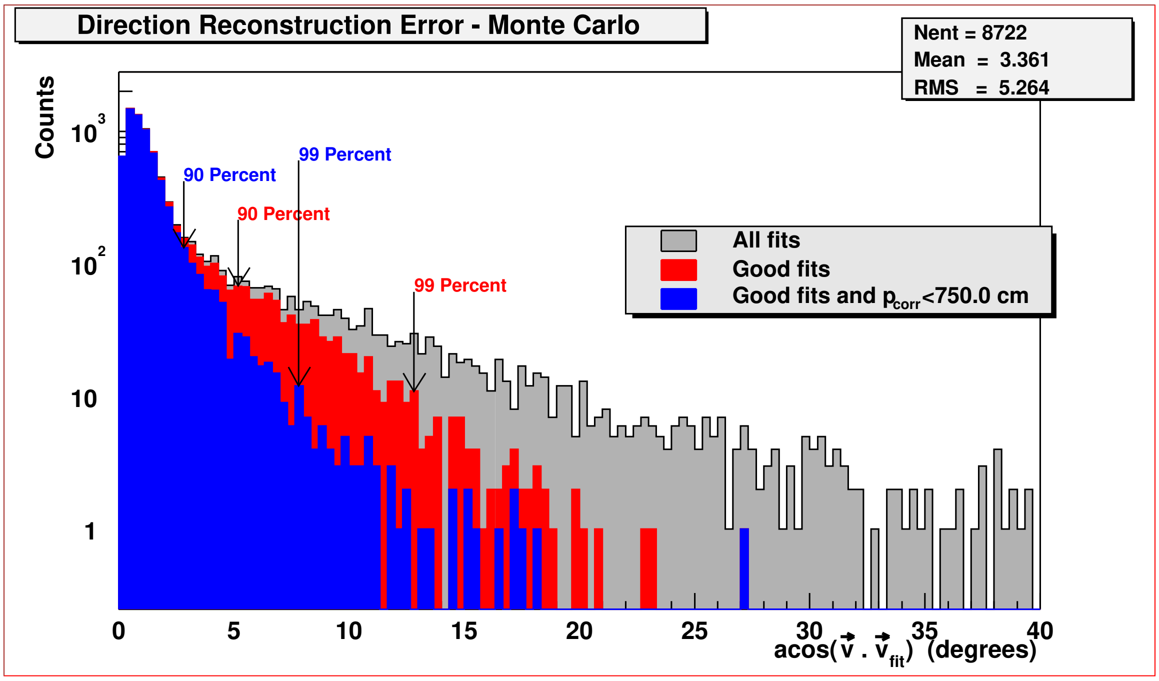

Figure 11.8: Direction Reconstruction Error. "Good Fits" are those where $F_{should} > 0.8$ and -log(pdf) < 4.5. p_{corr} refers to the (corrected) reconstructed impact parameter.

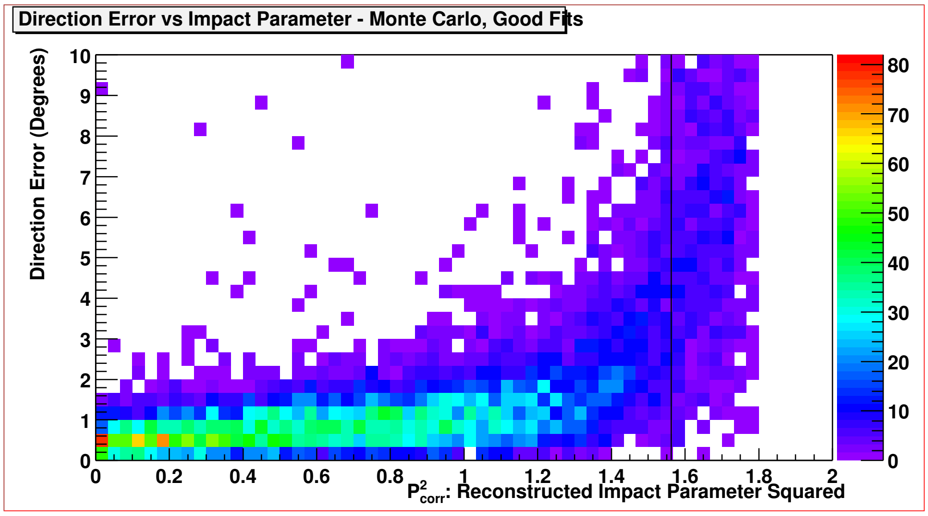

Figure 11.9: Direction Error Vs. Impact Parameter. The horizontal axis is given by $(P_fit/600cm)^2$. Only fits passing both the F_{should} and log(pdf) cuts are shown. Fits tend to get poorer the further out they are. The radial cut removes events to the right of 750 cm on the horizontal axis.

Because SNO detector is to a good approximation spherically symmetric, the impact parameter of the muon is the only geometric parameter that is substantially different between muon events. The fit residuals are plotted as functions of the (fitted) impact parameter in Figure 11.9.

The primary measurement made with the fitter will be a measurement of zenith angle. Convolution of the fitter resolution with a zenith angle spectrum is a non-trivial integration. For instance, events coming from near the zenith will be smeared (in zenith angle) much less than events near the horizon.

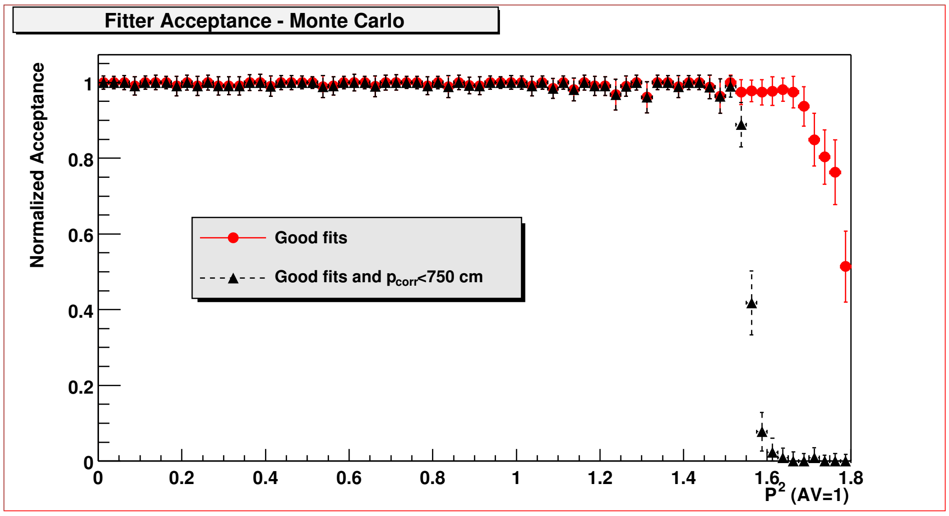

Figure 11.10: Fitter Acceptance, Based on Monte Carlo. Each bin shows the ratio of the number fits accepted (in a given radial bin) to the number of muons simulated at that radius. Error bars account for Monte Carlo Statistics. Each bin represents equal detector area, with the abscissa normalized to the area of the acrylic vessel.

11.4.3 Fitter Acceptance

Figure 11.10 shows how many events reconstruct properly and give acceptable goodness-of-fit values used in the evaluation stage. If the radial cut is not applied, the F_{should} parameter rejects clipping muon events at $P^2 \sim 1.7$ (i.e. $p_{fit} > 780$ cm). Note that the cut on fitted impact parameter gives a fairly clean cut-off with respect to the true impact parameter

The complete set of cuts applied to the data is:

$$
\begin{aligned}
F_{should} &> 0.8 \\
-\log(p.d.f.)/n.d.f. &< 4.5 \\
p_{corrected} &< 750cm \qquad (p_{fit} < 794.4)
\end{aligned}
\tag{11.8}
$$

Total detector acceptance is found by integrating the acceptance for each radial bin of Figure 11.10 from $P = 0$ to $P = 805cm$, weighting each term by area. This integration gives an all-detector fitter acceptance of 86.2% $\pm$ 2.7%. This corresponds to an effective area of 175.5 m^2 $\pm$ 5.4 m^2. (If the reconstruction was perfect with a cut at 750 cm, the effective area would be $\pi r^2 = 176.7m^2$.) Yet another way this result can be quoted is that the detector has an effective radius of 747 cm $\pm$ 12 cm.

The uncertainty on fitter acceptance is the dominant systematic uncertainty on rate measurements (as will be shown in Chapter 13). The quoted uncertainty is simply the calculated error due to Monte Carlo statistics. This error could of course be improved by further Monte Carlo run time. (Approximately one month of processor time would be required to reduce the uncertainty by a factor of 2.) However, the true systematic uncertainty remains very difficult to calculate. It is believed that this error is much less than the statistical error quoted, and so is neglected in this analysis.

In order to understand the error on the acceptance, it is necessary to understand the ways in which events fail the acceptance test. There are two ways in which this happens: events fail the radial cut, or are inside the radial cut by fail the GOF cuts.

The uncertainty in events failing the radial cut is created by uncertainty in the position resolution of the fitter, and the uncertainty on fitter pull effects. These in turn are functions of how well the Monte Carlo models tube timing characteristics, and possibly tube charge measurement characteristics. However, these uncertainties are known to be small, by looking at low-energy calibration sources, which are vulnerable to the same problems. As shown in Chapter 7, the Monte Carlo appears to reproduce the position reconstruction characteristics of the low energy fitter algorithms (FTT and FTG) at the level of $\sim$1 cm. Low-energy events will be much more sensitive to these effects than muon events will be. (Single events contain fewer tubes in the low-energy case, so the fit will be more sensitive to individual tube variations.) These measurements give us confidence that uncertainties on the radial cut should be small.

Occasionally, events with small impact parameters can fail the GOF tests. These events are typically mis-reconstructed. This can happen either because the tube timings do not conform well to the model, or because the fitter is seeded with a bad exit wound guess position. The frequency of these conditions occurring is again a function of tube time characteristics and of tube charge characteristics. Again, these are believed to be well-modeled, based on comparison to calibration sources.

11.4.4 Response to Stopping Muons

A small Monte Carlo set was generated to estimate the fitter's response to stopping muons. Muons with energies between 0.5 and 3 GeV were injected into the detector volume. Events were selected in which the muon stop vertex was inside 840 cm, and NHIT was greater than 150.

Because the muon does not exit the PSUP, it leaves no charge wound, nor does it fill in the Cherenkov cone completely. For these reasons, the F_{should} parameter is sensitive to stopping muons:

Table 11.3: Stopping Muon Acceptance.

Total events	161
Events $F_{should} > 0.9$	0
Events $F_{should} > 0.8$	9

.

The log(pdf) parameter gave very little discrimination either way. This result shows the fitter rejects stopping muon events with an estimated efficiency of 94% $\pm$ 2% (statistical).

Goodness-of-fit cuts aside, approximately 30 of the 161 events were fit to approximately the correct track coordinates; the rest failed. This is evidence that the muon track fitter is not an acceptable algorithm to use for stopping muons.

11.4.5 Response to Multiple Muons

Multiple muon tracks will also fit poorly, due to the timing patterns being inconsistent with a single track. Multiple muons were simulated by Monte Carlo with distances of several meters separation, and entering the detector at the same time. Of 331 simulated events, 196 passed the $F_{should} > 0.8$ and log(pdf)< 4.5 cuts, so the fitter efficiency for multiple muons is on order 1/2. Because the true decoherence function was not simulated (i.e. the mean separation of muons was much larger than would be expected in genuine data), this efficiency is not well estimated by this experiment. Therefore, the muon sample being described is neither 'all muon' nor 'single muon', but a combination of the two.

12

Expected Muon Flux

12.1 Muon Propagation

Energy loss by muons traveling through matter is a fairly well-understood process. It is discussed by Gaisser [55, 85] with an eye towards analytic approximation, which is discussed here. Another good reference for muon energy loss includes the standard tables provided by Lohmann [76]. Muons lose energy in rock by several mechanisms: ionization, bremsstrahlung, direct pair production, and hadroproduction.

Ionization occurs continuously as the muon travels through rock, with an energy loss that is almost constant with energy:

$$\frac{dE}{dX} = -\alpha \simeq 2 \text{ MeV } / \text{ (g cm}^2) \tag{12.1}$$

(X here is measured in g/cm^2) In fact, alpha rises logarithmically with energy, and is described with the well-known Bethe-Bloch equation. (See, for instance, [46] for a general discussion.)

Bremsstrahlung, although suppressed by a mass-squared factor relative to the electron, is still an important contributor, and acts as a discrete rather than continuous energy loss mechanism. Two other mechanisms act as discrete losses:

$$\begin{aligned} \mu + Z &\rightarrow \mu + \text{hadrons} && \text{(hadroproduction)} \\ \mu + Z &\rightarrow \mu + e^+ + e^- + Z && \text{(direct pair production)} \end{aligned} \tag{12.2}$$

The total energy loss is usually represented by this representation:

$$-\frac{dE}{dX} = \alpha + E\beta \tag{12.3}$$

where β (which is weakly dependent on E) is the sum of the fractional energy losses due to discrete processes. A critical energy is defined at $\epsilon = \alpha/\beta$, the energy at which continuous and discrete processes are equal. Gaisser [55] estimates this energy as about 500 GeV for muons in rock.

Because discrete processes are so important in the energy loss of high-energy muons, analytic solutions to equation (12.3) are not sufficiently accurate to calculate the probability of a muon surviving to detector depth. Because energy straggling is so important, a Monte Carlo algorithm is the best approach for computing survival probabilities. Lipari and Stanev [79] have created one such Monte Carlo, `PROP_MU`, and Bissino *et. al.* [86]. Antonioli *et. al.* [87] have created a newer 3D transport code named MUSIC. Although `PROP_MU` has been used to provide input to SNOMAN simulations in order to prototype reconstruction, MUSIC was used for the full analysis. This choice was made because V. Kudryavtsev [88] kindly provided customized cross sections for the SNO rock. (See Section 12.2.) The authors of MUSIC have extensively checked their algorithm against `PROP_MU`, showing that the calculations are equivalent. [87]

12.2 Magnetic and Geological Environment Around SNO

The SNO detector is situated at 46.5°N (57.2°relative to magnetic north). This is further north than most underground detectors. Because of this, geomagnetic cutoffs for protons have been calculated to be lower than 40 GeV/c. [61] The flux of muons above ~ 4 TeV will be unaffected by anisotropy due to earth's magnetic field.

SNO is a situated under an overburden that is roughly flat. Surface features above the detector are typical for the Canadian Shield: low hills and shallow lakes, with surface height variations of about ± 6 meters. The surface elevation is about 300 meters above sea level.

The Creighton mine extends diagonally down an interface between a hanging wall of norite (a low-grade nickel ore) and a footwall consisting mostly of granite (70-80%) with a patchy mix of gabbro. Down the interface runs a seam of nickel ore, the largest part of which has been mined out and backfilled. The interface slopes at approximately 25°from the vertical.

SNO is located about 70 meters from the interface, in the hanging-wall (norite) side. The rock interface runs roughly east-west, and is south of the detector. The top of the SNO cavity is 2072 meters below the surface, or 5996 meters water equivalent (m.w.e.). There is an air gap between the ceiling and the deck of 6 meters, and then light water above the inner detector. The center of the detector thus has an overburden of 6010 m.w.e., or about 6002 m.w.e. just above the PSUP.

The properties of various materials in the overburden are given in Table 12.2.

To a first approximation, the environment can be seen as a flat overburden of uniform norite rock but there are several known or suspected deviations from this. The footwall has a lower density, which should theoretically increase the muon rate coming from the south side of the detector. The ore body and rock interface create smaller regions of rock with densities that are not easily estimated. Some evidence exists that there are local pockets in the hanging wall with densities as high as 3.0 g/cm^3, although a systematic series of measurements of norite near the detector[90] show density variations only as large as 1%. Finally, there is a large hole on the surface, roughly 500m across and 100m deep, and 2km southeast of the detector, but

Table 12.1: Properties of SNO Overburden. Footwall properties assume a 75% (25%) mixture of granite (gabbro).[89]

Location	Hanging Wall	Footwall		Ore Body	
Material	Norite	Granite	Gabbro	Ore	Backfill (Sand)
Density	2.894	2.65	2.95	4-5	1.8
Z/A	0.491	0.495			
Z^2/A	6.01	5.84			

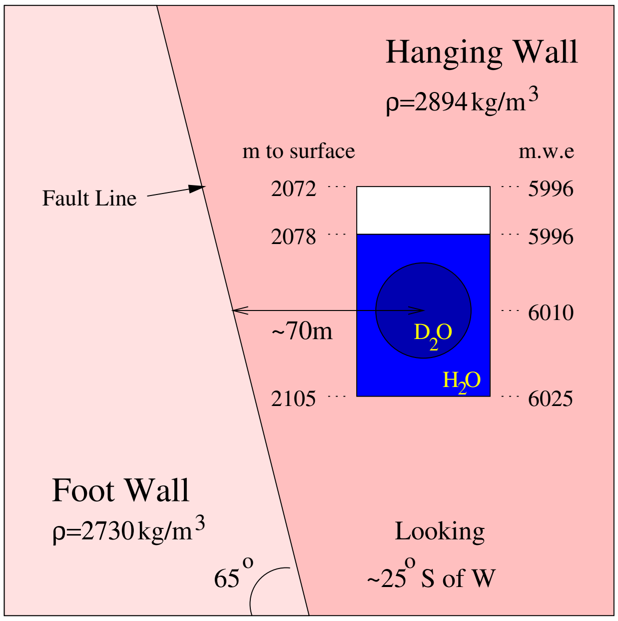

Figure 12.1: Diagram of SNO Geological Environment. Provided by C. Waltham. Note that this picture of the fault line is greatly simplified.

this is at the angular limit of cosmic ray muons observed in SNO.

These complications are not easily accounted for without more detailed measurement. The analysis presented here starts with the simple model of the uniform overburden of norite.

12.3 Downward-Going Muon Flux

12.3.1 Theoretical Calculations

The muon flux at surface is calculated using equation (9.6), for given values of γ_μ, A, and R_c. Computation of the underground flux was done by pre-calculating muon survival probabilities and then integrating over all initial muon energies.

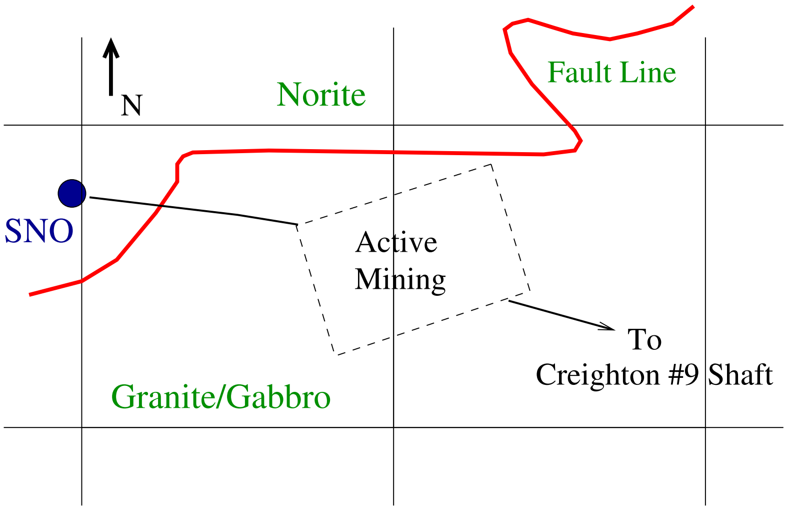

Figure 12.2: Overhead Map of SNO Geological Region. The horizontal line shows the location of the headwall/footwall interface.

Using the MUSIC Monte Carlo program, a table of survival probabilities in SNO rock was calculated for 64 muon energies logarithmically spaced between 1 and 1000 TeV, and binned in depth between 1 and 6 km. These probabilities are labelled $\mathcal{P}(E_i, d_i)$, where the energies E_i refer to the starting muon energy (i.e. energy at surface). A sample of these probabilities is shown in Figure 12.3.

These probabilities are multiplied by eq. (9.6) to get the differential flux underground:

$$\frac{\Phi(E_\mu, \theta)}{dE_\mu} = \frac{dN(E_\mu, \theta)}{dE_\mu} \times \mathcal{P}(E_\mu, d_\theta) \tag{12.4}$$

$$d_\theta = 6002 m.w.e./\cos\theta \tag{12.5}$$

This distribution is illustrated in Figure 12.4. It can be seen in this figure that the

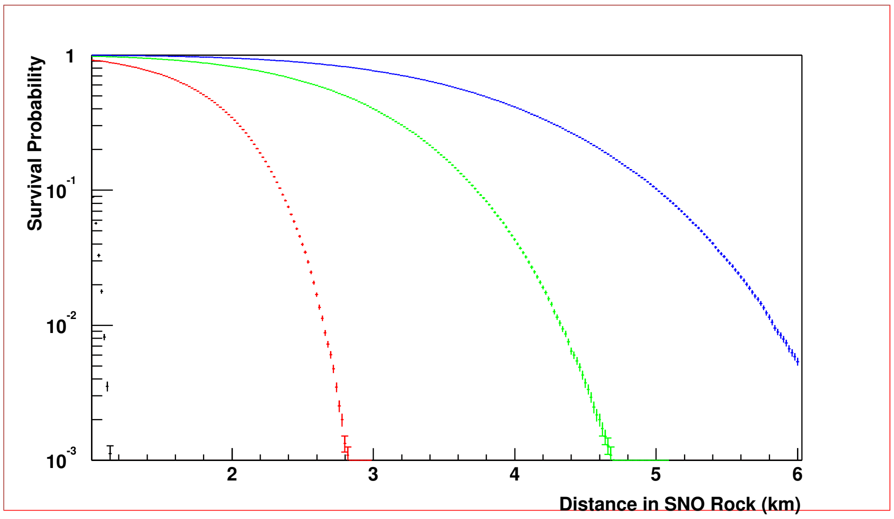

Figure 12.3: Muon Survival in SNO Rock. The survival probability (calculated by MUSIC [87]) for a muon to penetrate through a given distance of SNO rock is shown for muons of several initial energies. Error bars are statistical.

bulk of muons reaching the SNO detector depth will have surface energies between 3 and 300 TeV, corresponding roughly to primary cosmic ray energies between 30 and 3000 TeV.

The measurable zenith angle distribution can then be computed:

$$\begin{aligned}
\Phi(\theta) &= \int_0^\infty dE_\mu \frac{dN(E_\mu,\theta)}{dE_\mu}\mathcal{P}(E_\mu, d_\theta) && (12.6)\\
&\simeq \sum_i \Delta E_i a_i \frac{dN(E_i,\theta)}{dE_i}\mathcal{P}(E_i, d_\theta) && (12.7)
\end{aligned}$$

where a_i are the coefficients for the "alternative extended Simpson's rule" for integrating a function at known discrete intervals [91]. Because the E_i's are logarithmically spaced, we define:

$$\Delta E_i = E_i \log\left(\frac{E_{i+1}}{E_i}\right) \tag{12.8}$$

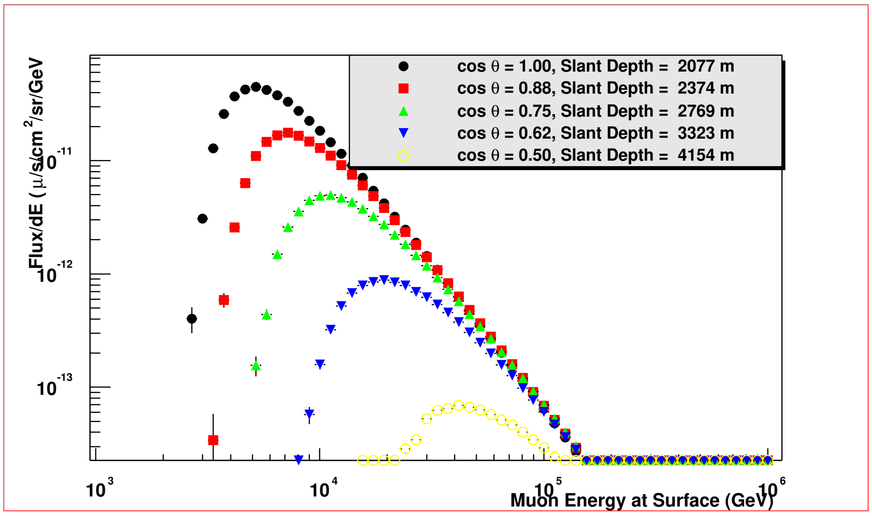

Figure 12.4: Energy of Muons Surviving to Detector Depth. The flux of muons that survive to detector depth are shown as a function of energy at the surface. Each curve is for a given zenith angle, given a flat 6002 m.w.e. overburden. Error bars show statistical errors from the Monte Carlo.

The resulting zenith distribution is quickly computed for different models of the surface muon flux. This distribution is shown in Figure 12.5 for parameters from references [55, 57]. The 'LVD+Prompt' distribution adds prompt muons at the maximum limit quoted by the authors. The integral of these fluxes is given in Table 12.2.

Table 12.2: Integrated Down-going Muon Fluxes. Muon fluxes in Figure 12.5 are integrated to give total fluxes at detector depth.

Gaisser [55]	3.29551e-10 mu/s/cm^2
LVD [57]	3.21216e-10 mu/s/cm^2
LVD [57], with R_c=0.002	3.63109e-10 mu/s/cm^2

Multiple scattering of muons is small compared to fitter direction resolution; MU-

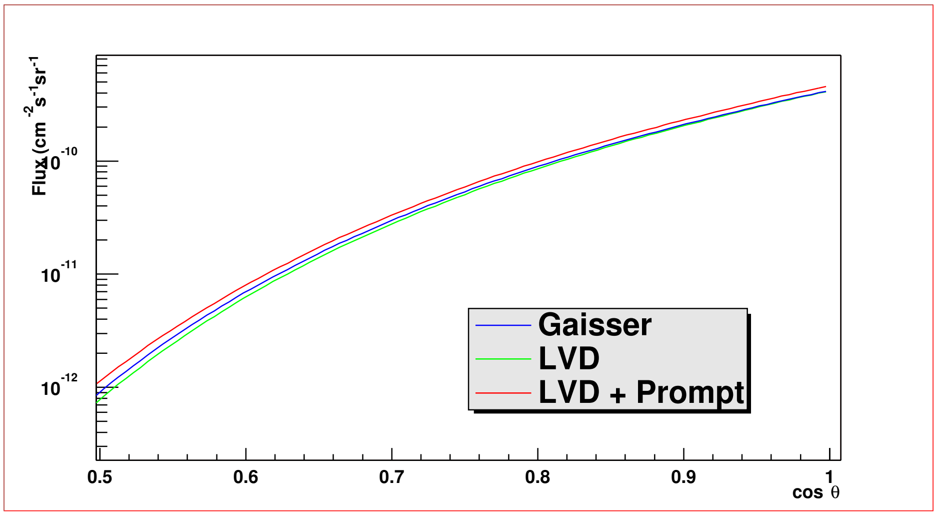

Figure 12.5: Predicted Zenith Angle Distribution in SNO. The predicted flux of atmospheric muons through SNO is shown for three models: $\gamma_\mu = 2.7$ ('Gaisser'), $\gamma_\mu = 2.77$ ('LVD'), and $\gamma_\mu = 2.77, R_c = 0.002$ ('LVD+Prompt').

SIC predicts that the mean scattering angle will be 0.55°for muons reaching the SNO detector, and that 90% of muons will scatter less than 1.05°. The fitter resolution is approximately 3 times this (shown in Table 11.2). Multiple scattering is not accounted for in the zenith angle distributions.

12.3.2 Fitter Resolution Effects

The effects of finite angular resolution will distort the measured distribution of cosmic-ray muons. The general effect of this smearing will be to flatten the steep angular distribution shown in Figure 12.5.

Because the impact parameter of an event dominates the quality of fit, and because the impact parameter of the event is independent of the direction angle, the angular

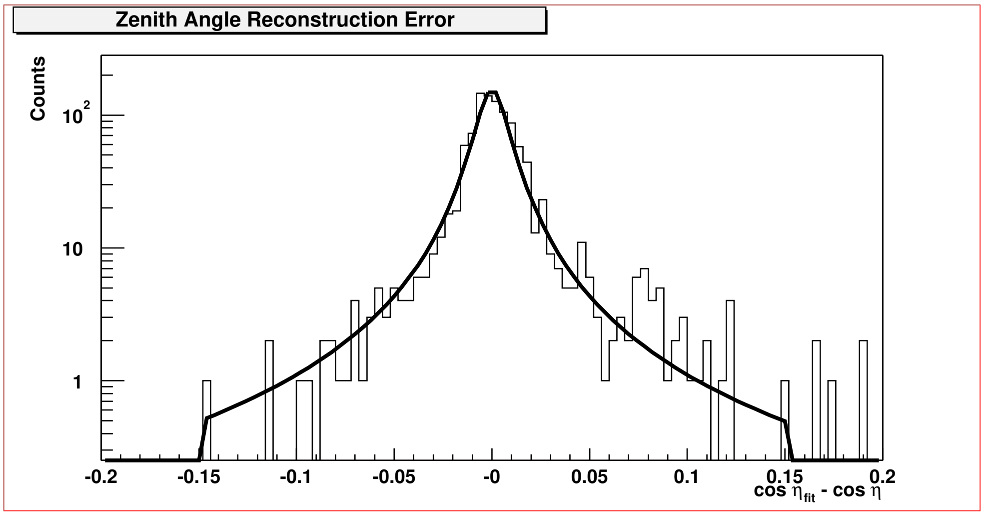

Figure 12.6: Reconstruction Error in Zenith Angle. The zenith angle residual is shown for a sample of Monte Carlo events injected into SNOMAN with $\gamma = 2.7$. The residual has tails that fit well to a truncated Lorentzian with a width of 0.08 in $\cos\theta$.

resolution of the fitter is independent of direction. The angular resolution of the detector is shown in Figure 11.8, and can be written as $R(\zeta)$, where ζ is the angle between the true and reconstructed muon direction vectors (i.e. $\cos\zeta = \vec{V} \cdot \vec{V}_f it$).

A simple measure of this resolution smearing can be found by simulating a realistic angular distribution in Monte Carlo, and then comparing the zenith angles before and after reconstruction. This is shown in Figure 12.6. Overall, 76% of all events reconstruct so that $|\cos\theta - \cos\theta^{fit}|$ is less than 0.01, with tails on the distribution. Note that this resolution function is not independent of zenith angle, however, so it is misleading use it as a simple detector resolution.

However, this function incorrectly models the zenith-angle dependence of the an-

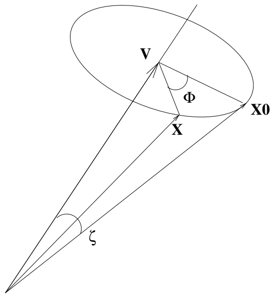

Figure 12.7: Illustration of Angular Smearing.

gular resolution, which due to phase space considerations is better at $\cos\theta = 1$ than it is at $\cos\theta = 0$. A more complete angular resolution convolution can be computed as follows.

A muon has a true direction $\vec{V}$, given in polar coordinates as (θ, ϕ). We set $\phi = 0$ without loss of generality. If the opening angle between the muon and the mis-reconstructed direction is ζ, as shown in Figure 12.7, the muon can mis-reconstruct into any vector $\vec{X}$ such that

$$\vec{X} = \vec{X}_0 \cos\psi + \vec{V}(\vec{V} \cdot \vec{X}_0)[1 - \cos\psi] + (\vec{X}_0 \times \vec{V}) \sin\psi \tag{12.9}$$

where ψ is an arbitrary rotation angle, and $\vec{X}_0$ is a specific solution for mis-reconstruction. We choose $\vec{X}_0 = (\theta + \zeta, 0)$ for convenience.

We may then calculate the zenith angle of the mis-reconstructed muon as

$$\theta_x = cos^{-1}\left(\cos\psi \sin\theta \sin\zeta + \cos\theta \cos\zeta\right) \tag{12.10}$$

Therefore, the probability that the muon will mis-reconstruct between the zenith angles θ' and $\theta' + \Delta\theta$ (for a given value of ζ) is given by:

$$T(\zeta, \theta, \theta') = \frac{1}{\pi} [\psi(\zeta, \theta, \theta' + \Delta\theta) - \psi(\zeta, \theta, \theta')] \tag{12.11}$$

where

$$\cos[\psi(\zeta, \theta, x)] = \begin{cases} -1 & \text{if x} > |\theta - \zeta| \\ \left(\frac{\cos(x) - \cos(\theta)\cos(\zeta)}{\sin(\theta)\sin(\zeta)}\right) & \text{if } |\theta - \zeta| < \text{x} < \theta - \zeta \\ -1 & \text{if x} < \theta + \zeta \end{cases} \tag{12.12}$$

Finally, we integrate over all values of ζ to arrive at our smearing function:

$$P(\theta, \theta') = \int_{\zeta=0}^{\pi} R(\zeta) T(\zeta, \theta, \theta') d\zeta \tag{12.13}$$

This function is used to modify the theoretical angular distribution by convolution:

$$\Phi_{\text{smeared}}(\theta') = \int_{theta=0}^{1} d\theta P(\theta, \theta') \tag{12.14}$$

The function $R(\zeta)$ is applied numerically, using the histogram in Figure 11.8.

Figure 12.8 shows the effect that these smearing functions have on the theoretical angular distribution, by taking $\Phi_{\text{smeared}}/\Phi$. It can be seen that the effect of fitter resolution smearing will distort the angular distribution, making it slightly less steep.

It can also be seen from Figure 12.8 that the magnitude of the effect is similar to a reducing the primary cosmic ray power index by about 0.04. This allows for an estimate of the systematic uncertainty on γ introduced by angular resolution smearing, as is discussed in Chapter 13.

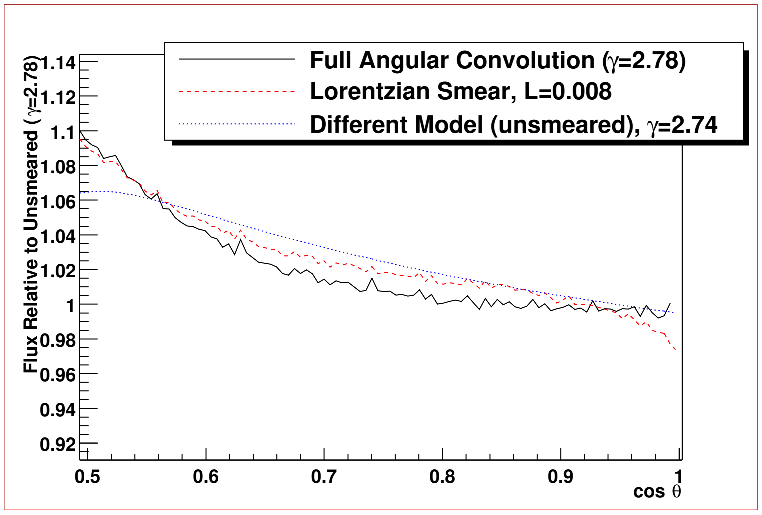

Figure 12.8: Angular Resolution Effects. The flux after angular resolution smearing is compared to the undistorted flux (with $\gamma = 2.78$) as a function of zenith angle. A full convolution model and a truncated Lorentzian resolution are both applied. (Scatter on points is illustrates Monte Carlo statistical fluctuation in the underlying theoretical calculation of survival probabilities) Also shown for comparison is the ratio obtained using a different, un-smeared angular resolution, with $\gamma = 2.74$.

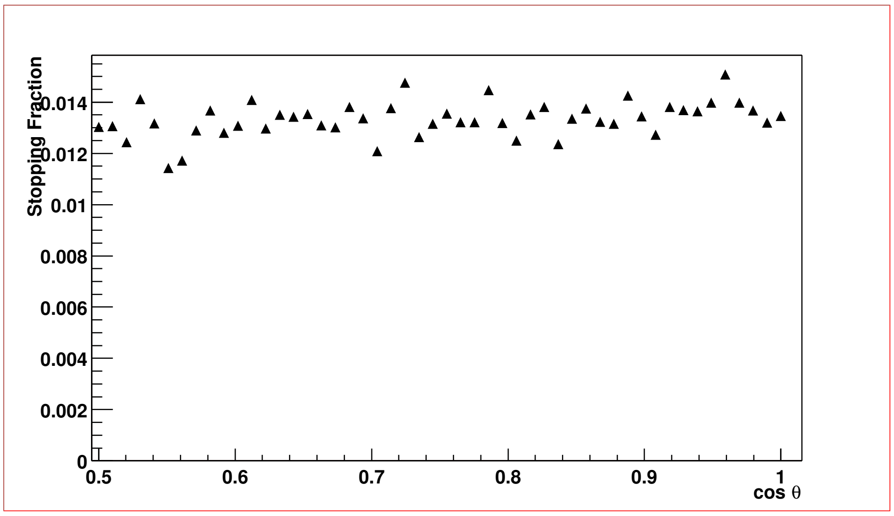

Figure 12.9: Stopping Muon Fraction By Zenith Angle. The fraction of muons surviving to detector depth that stop within 4 meters of rock (~12 m.w.e.) deeper than the top of the detector. The scatter on the points is due to Monte Carlo statistical errors.

12.3.3 Stopping Muons

Not all muons that reach SNO will be seen as through-going tracks. 1-2% of muons will stop in the detector. Figure 12.9 shows the fraction of muons surviving to detector depth that will stop close to detector depth. This calculation assumes $\gamma_\mu = 2.7$, and gives the probability of stopping in 4 meters of norite which corresponds to 12 meters water equivalent, close to the mean path length in the inner SNO detector. This fraction is fairly insensitive to the energy distribution. It is dependent primarily on the thickness of the detector.

12.3.4 Multiple Muons

Another characteristic of the down-going muon sample is that a fraction of the muon events observed will be due to multiple muon bundles. The parameterization of Forti *et. al.* [92] was employed to calculate the multiple muon fraction. The primary cosmic ray composition employed for this calculation was taken from the MACRO multiple-muon results [93]. This estimation indicates that approximately 3% of all muon events will be due to multiple-muon bundles at SNO depth. (Of these, 90% will be double muons.) No calculation was made of the detector acceptance to the multiple muon bundle, although it can be noted that the Fréjus experiment, which resides at an overburden nearly as deep as SNO, observed a muon decoherence function that was roughly exponential, with a mean of 1 m. [94]. This would indicate that the estimate of 3% is a conservative upper limit on the observable double muon fraction.

12.3.5 'Depth-Vertical Intensity' Relation

It is usual to express muon flux in a simple empirical form, known as the 'depth-vertical intensity' relation. This form can be written as:

$$I_\mu(vert) = A_v * \left(\frac{x_0}{x}\right)^\alpha \exp\left(-\frac{x}{x_0}\right) \tag{12.15}$$

Here, x is the slant depth of rock, and x_0 is the scale height, both measured in hg/cm^2 (i.e. m.w.e.). Often, x is measured not as true slant depth, but equivalent depth for standard rock.

The 'vertical intensity' can be defined as the intensity at a given slant depth, corrected for the $\sec\theta$ angular distribution for high-energy muons at the surface.

$$I_{\theta=0} = \Phi_{\mu}(\theta, x_{\theta,\phi}) \times \cos\theta \tag{12.16}$$

Various experiments have measured this distribution. For instance, the LVD [95] and Fréjus [94] give the values listed in Table 12.3.

Table 12.3: Empirical Fit Solutions from Other Experiments.

A_v [10^{-6} cm^{-2}s^{-1}sr^{-1}]	x_0 [hg/cm^2]	α	Source
(2.15 ± 0.08)	1155^{+60}_{-60}	$1.93^{+0.2}_{-0.12}$	LVD [95]
(1.96 ± 0.09)	1184 ± 10	2	Fréjus [94][a]

[a] Reported systematic and statistical errors on x_0 have been added in quadrature for comparison.

The MUSIC Monte Carlo was used to generate an expected vertical intensity for standard rock at SNO depth (6011 meters water equivalent), using a primary power index of $\gamma = 2.7$:

$$I^{\text{Std Rock}}_{\theta=0}(\text{Calculated}) = (4.94 \pm 0.07) \times 10^{-10} \mu/cm^2/sr/s \tag{12.17}$$

This calculation compares well with the empirical measurements:

$$\begin{aligned} I^{\text{Std Rock}}_{\theta=0}(\text{Measured, LVD}) &= (4.89 \pm 0.18) \times 10^{-10} \mu/cm^2/sr/s \\ I^{\text{Std Rock}}_{\theta=0}(\text{Measured, Frejus}) &= (4.74 \pm 0.21) \times 10^{-10} \mu/cm^2/sr/s \end{aligned} \tag{12.18}$$

This comparison validates that we may use the MUSIC code to generate an expected vertical intensity for SNO rock:

$$I_{\theta=0}^{\text{Norite}}(\text{Calculated}) = (4.13 \pm 0.08) \times 10^{-10} \mu/\text{cm}^2/\text{s} \tag{12.19}$$

Errors are due only to Monte Carlo statistics.

12.4 Neutrino-Induced Muon Flux

Calculation of neutrino-induced muon fluxes has four components: neutrino flux, neutrino oscillation, neutrino-rock interaction, and muon propagation through rock.

12.4.1 Neutrino Fluxes

Neutrino fluxes are taken from the Bartol model [96], which gives neutrino fluxes as a function of energy, zenith angle, and species. Calculations were done for solar maximum.

SNO is unlike many other detectors in that it is buried under a flat overburden, rather than a mountain. There is a considerable difference in the slant depth of atmosphere at the horizon relative to the slant depth at the surface. This leads to a small suppression of the excess flux seen at the horizon.[1] This is illustrated in Figure 12.10 For a zenith angle θ in SNO detector coordinates, the flux of neutrinos

[1] A helpful example to visualize this is to imagine a detector at the center of the earth, for which all neutrinos will have gone through exactly the same length of atmosphere, so no zenith dependence can be seen.

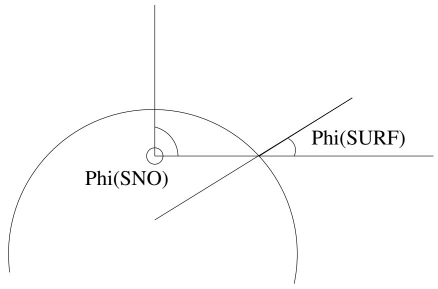

Figure 12.10: Zenith Angle Conversion. An exaggerated case is shown in which a neutrino hits the underground detector at an apparent zenith angle that is much greater than the angle at which the muon would intersect a surface detector.

is calculated as:

$$\Phi_\nu^{SNO}(\theta) = \Phi_\nu^{Surface}(\theta') \qquad (12.20)$$

$$\text{where} \quad \sin\theta' = (1 - d/r)\sin\theta \qquad (12.21)$$

The corrected angle θ' is given to the Bartol code `SNO_NUS` to find the flux at θ.

The absolute neutrino flux is known only to within 20% [74, 58, 96]. This is partly due to model dependencies, but has a large uncertainty due to the cosmic-ray shower measurements that the calculations are based upon. The angular dependence of the flux is known to much better accuracy.

12.4.2 Neutrino Oscillations

Neutrino oscillations are computed for the cases $\nu_\mu \rightarrow \nu_\tau$ and $\nu_\mu \rightarrow \nu_{sterile}$ using equations (9.10) and (9.11) respectively. The distance from source to detector was calculated by (12.22), with R as the earth's radius, and d as the detector depth

(2070m).

$$L = -(R-d)\cos\theta + \sqrt{(R-d)^2\cos^2\theta + d(2R-d)} \tag{12.22}$$

For the case of sterile neutrinos, the density of the earth was computed along the track, using an electron density profile given in reference [97]. The neutron density was taken as equal to electron density, which is low by 10% for the earth's core.

12.4.3 Neutrino-Rock and Muon-Rock Interactions

The neutrino-rock cross sections are approximations calculated by Gaisser and Stanev [85]. These cross sections are not the most up-to-date (e.g. [74]), but have the virtue of being straightforward to calculate. The spectrum of neutrino-induced muons in rock is given as:

$$\frac{dN_\mu}{dE_\mu} = \int_{E_\mu}^{\infty}\left[\int_0^{\infty} dX \int_{E_\mu}^{E_\nu} dE'_\mu g(X, E_\mu, E'_\mu) \times S(E_\nu, E'_\mu, \theta)\right] dE_\nu; \tag{12.23}$$

In this notation, a neutrino of energy E_ν interacts with the rock to produce a muon of energy E'_μ, which then travels through X distance of rock to reach the detector with final energy E_μ. The function $g(X, E_\mu, E'_\mu)dE'_\mu$ represents the probability of a muon with initial energy E'_μ to reach the detector with final energy E_μ.

The function $S(E_\nu, E'_\mu, \theta)$ represents the luminosity of muon-induced neutrinos in the earth. $\int SdE_\nu$ is in units of muons/(g s sr GeV). This luminosity is given by the authors as:

$$S(E_\nu, E'_\mu, \theta) = N_A\sigma(R)\frac{dN}{dE_\nu}\left[1 + A(R)\left[\frac{E'_\mu}{E_\nu}\right]^2\right] \tag{12.24}$$

where R is the $\nu/\bar{\nu}$ ratio, and the functions $\sigma(R)$ and $A(R)$ are approximate numerical expressions. The neutrino flux $\frac{dN}{dE_\nu}$ is the total for both neutrinos and anti-neutrinos. It is implicit that the muons and neutrinos are collinear to a good approximation.

This work is concerned only with through-going muons. We are not interested in the muon energy spectrum given by (12.23), but rather by the integral of this spectrum.

$$N_\mu(\theta) = \int_{E_0}^{E'_\mu} \left(\frac{dN_\mu}{dE_\mu}\right) dE_\mu \tag{12.25}$$

We define E_0 to be the minimum energy required for a muon to transit the detector. The upper limit is the kinematic constraint that the final muon energy always be less than the initial muon energy.

We combine (12.23) and (12.25) and change the order of integration:

$$\begin{aligned} N(\theta) &= \textstyle\int_{E_0}^{E'_\mu} dE_\mu \int_{E_\mu}^{\infty} dE_\nu \int_0^\infty dX \int_{E_\mu}^{E_\nu} dE'_\mu \Big(g(X, E_\mu, E'_\mu) \times S(E_\nu, E'_\mu, \theta)\Big) \\ &= \textstyle\int_{E_0}^{E'_\mu} dE_\mu \int_{E_\mu}^{\infty} dE_\nu \int_{E_\mu}^{E_\nu} dE'_\mu \Big(S(E_\nu, E'_\mu, \theta) \times \left[\int_0^\infty dX g(X, E_\mu, E'_\mu)\right] \Big) \\ &= \textstyle\int_0^\infty dE_\nu \int_{E_0}^{E_\nu} dE_\mu \int_{E_\mu}^{E_\nu} dE'_\mu \Big(S(E_\nu, E'_\mu, \theta) \left[\int_0^\infty dX g(X, E_\mu, E'_\mu)\right] \Big) \\ &= \textstyle\int_0^\infty dE_\nu \int_{E_0}^{E_\nu} dE'_\mu \ \Big(S(E_\nu, E'_\mu, \theta) \Big[\int_{E_0}^{E'_\mu} dE_\mu \int_0^\infty dX g(X, E_\mu, E'_\mu)\Big] \Big) \end{aligned} \tag{12.26}$$

In this last line, the quantity in the square brackets represents a quantity straightforward to calculate. The expression $\int g dX$ is the mean distance in rock that is required for a muon with initial energy E'_μ to fall to energy E_μ. The innermost two

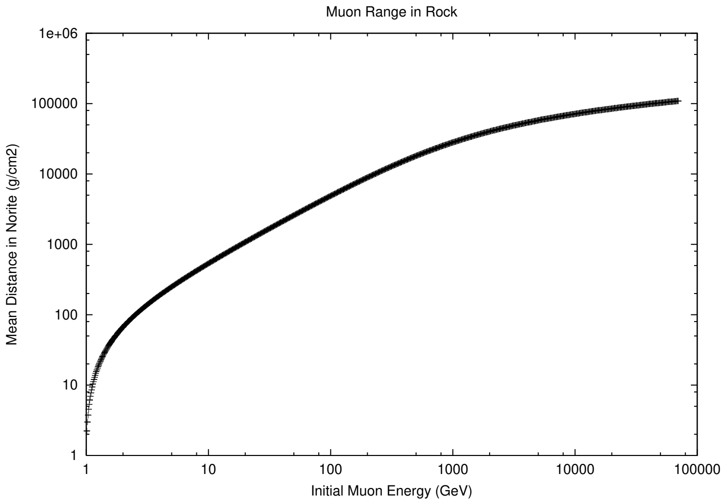

Figure 12.11: Mean Range of Muons in Rock. Calculated by MUSIC for SNO norite rock. Errors are statistical.

integration steps may thus be calculated:

$$\left[\int_0^\infty dX \int_{E_0}^{E'_\mu} dE_\mu g(X, E_\mu, E'_\mu)\right] = \langle X \rangle_{E'_\mu} - \langle X \rangle_{E_0} \tag{12.27}$$

where we have defined $\langle X \rangle_\epsilon$ as the mean distance for a muon of energy ϵ to travel before stopping in the rock. $\langle X \rangle_{E_0}$ is the thickness of the detector in g/cm^2.

Again, the MUSIC Monte Carlo is employed, this time to build a table of $\langle X \rangle_\epsilon$ for 1000 energies between 1 GeV and 70 TeV (with logarithmic spacing). For each energy, approximately 9000 trials were made to average the distance the muon traveled before stopping. The results are shown in Figure 12.11; statistical error on $\langle X \rangle$ varies from 0.1 to 0.3%.

12.4.4 Integrated Results

After accounting for the muon survival probabilities, there exist two remaining integrations, which are performed numerically. The integration over E'_μ is done in a way analogous to (12.7):

$$
\begin{aligned}
N(\theta) &= \int_0^\infty dE_\nu \int_{E_0}^{E_\nu} dE'_\mu \left(S(E_\nu, E'_\mu, \theta) \left[\langle X \rangle_{E'_\mu} - \langle X \rangle_{E_0} \right] \right) && (12.28) \\
&= \int_0^\infty dE_\nu \left\{ \sum_{i, E'_i > E_0}^{E'_i < E_\nu} dE'_i \left[\langle X \rangle_{E'_i} - \langle X \rangle_{E_0} \right] E'_i \log \left(\frac{E'_{i+1}}{E'_i} \right) \right\} && (12.29)
\end{aligned}
$$

The spectrum of weighted neutrino energies going into the neutrino-induced muon spectrum is given in Figure 12.12. This corresponds to the function of E_ν inside the curly braces of equation 12.29. The integration over neutrino energies is done numerically using the *Numerical Recipes* [91] routine TRAPZD to obtain the final result.

This calculation results in an angular distribution of neutrino-induced muons. For the case of the Super-Kamiokande oscillation parameters [65], this distribution is shown in Figure 12.13.

The angular flux distribution is weakly dependent upon detector depth, as is shown in figure 12.14. The distortion to the angular distribution is a maximum of about 2% in muon flux near the horizon.

The angular distribution is also plotted together with the expected atmospheric muon contribution in Figure 12.15. This figure shows that the downward-going muon

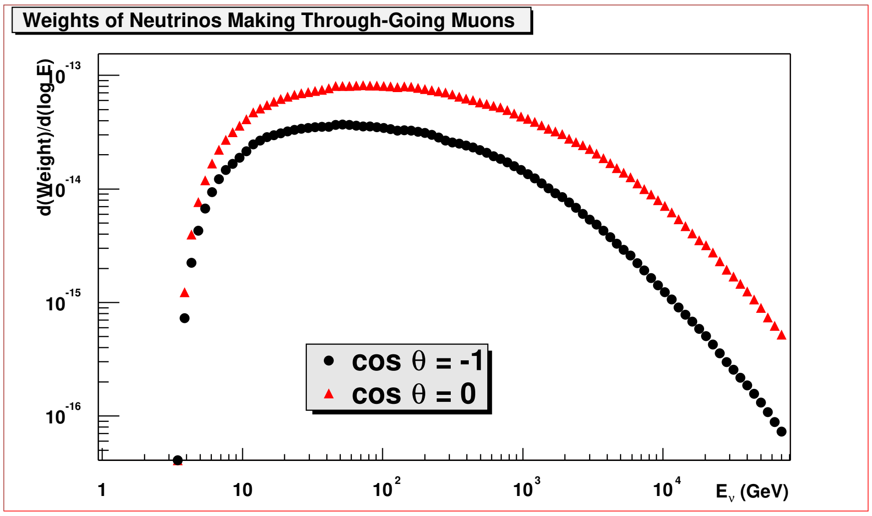

Figure 12.12: Neutrino Energies Contributing to Through-Going Muons. The weighted spectrum of neutrinos creating observable muons is shown. No oscillations are applied. The upper and lower bounds correspond to the limits of available neutrino fluxes given in [96].

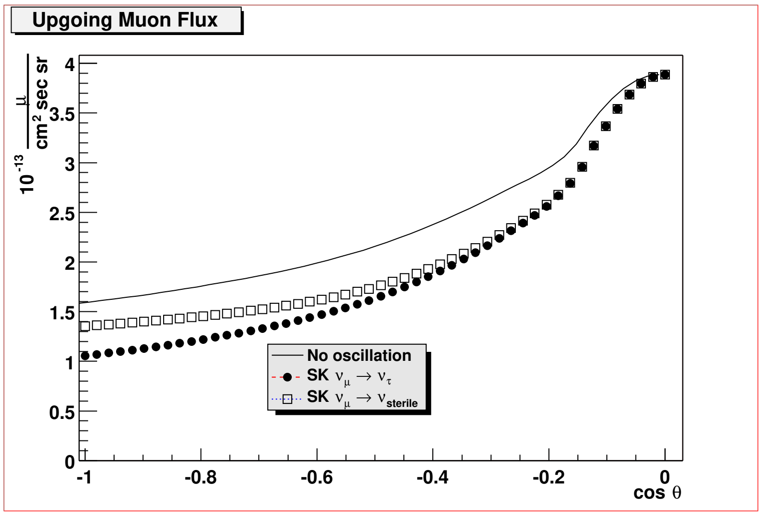

Figure 12.13: Expected Upgoing Muon Signal: SK Oscillations. The zenith-angle distribution for neutrino-induced through-going muons is shown for SNO, for the oscillation parameters $\sin^2 2\theta = 1.0$ and $\Delta m^2 = 3 \times 10^{-3}$.

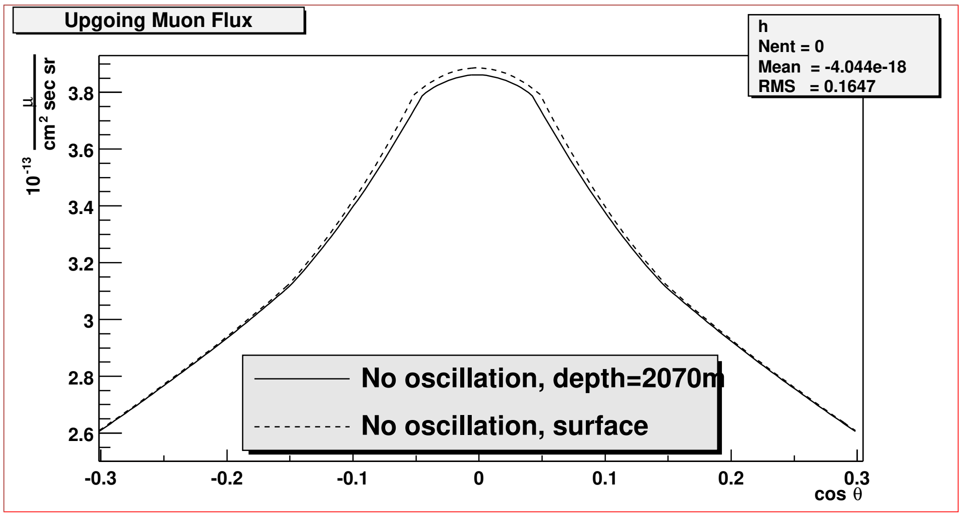

Figure 12.14: Expected Upgoing Muon Signal: Detector at Surface vs Detector at SNO Depth. The solid line shows the suppression of muon flux at the horizon due the SNO detector depth. A similar suppression is produced for oscillated neutrinos.

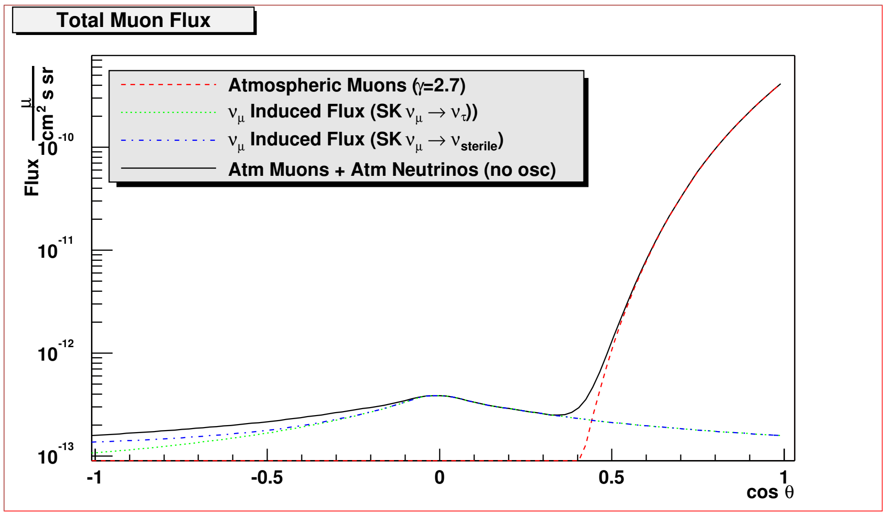

Figure 12.15: Expected Muon Flux At All Angles. Flux for both down-going atmospheric neutrinos and neutrino-induced through-going muons is shown. Possible oscillation solutions ($\sin\theta_V = 1.0, \Delta m^2 = 3 \times 10^{-3} eV^2$) are also shown.

spectrum becomes negligible at $\cos\theta < 0.4$.

The integrated neutrino-induced muon flux with $-1 < \cos\theta < 0.4$ is expected to be $2.52\times10^{-13}cm^{-2}s^{-1}sr^{-1}$ for the case of no oscillations, and $2.23\times10^{-13}cm^{-2}s^{-1}sr^{-1}$ for the best-fit case found by Super-Kamiokande ($\nu_\mu \to \nu_\tau, \sin^2 2\theta \simeq 1.0, \Delta m^2 \simeq 0.003$). Dominating these calculations is the 20% uncertainty in absolute neutrino flux.

The flux of upward-going muons coming from below the horizon (i.e. $-1 < \cos\theta < 0$) is calculated as $2.33\times10^{-13}cm^{-2}s^{-1}sr^{-1}$ for no oscillations. This calculation can be compared to the flux predicted by Super-Kamiokande collaboration for their detector [98]: $1.97 \times 10^{-13}cm^{-2}s^{-1}sr^{-1}$, which is about 15% smaller. The difference in these two rates is mainly attributable to the different sizes and shapes of the detector. SNO, being smaller, has a lower energy threshold for through-going muons. (For instance, the flux predicted for Kamiokande-II and -III made by Hatekyama [74] is approximately 25% higher than that for Super-Kamiokande.)

13

Muon Results

13.1 Downward-Going Muons

The downward-going muon sample is important for several reasons. First, measurements of the slope of the primary cosmic ray spectrum, and limits on prompt muon component are of interest. Second, downward-going muon analysis gives us an opportunity to exercise the analysis mechanisms to be applied to upward-going muons, giving us confidence that the techniques are reliable.

The analysis of the downward going muon sample is described in detail in this section. Many analysis issues are in common with the upward-going sample.

13.1.1 Event Selection

The data from the reduced sample (described in Chapter 10) was reconstructed, and events were selected using the goodness-of-fit and radial cut criteria summarized in (11.8). These cuts distilled the 'reduced' data set by roughly a factor of ten, for a

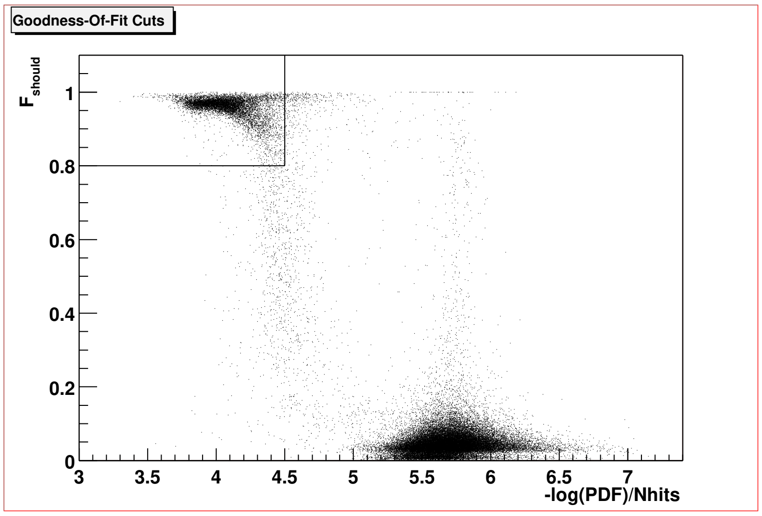

Figure 13.1: Goodness-of-fit Cuts Applied to Data. Each point represents an event in the data sample. The lines enclose the region accepted by the cuts.

final total of 7464 through-going muon events.

Figure 13.1 shows the data cut by the goodness-of-fit cuts. The non-muon data is well separated from the selected region, ensuring a clean data set. This is also shown in Figure 13.2, which illustrates that the low-Nhit flasher contamination is well removed by the goodness of fit cuts.

13.1.2 Neck Cut Contamination and Sacrifice

Sufficient computer time was available to independently process every event (greater than 30 NHITs) for which the neck tube cut had been flagged in an attempt to determine the possible contamination and sacrifice for this cut.

After fitting each of $\sim$ 23k events, only 4 events passed the F_{should} cut, only 3

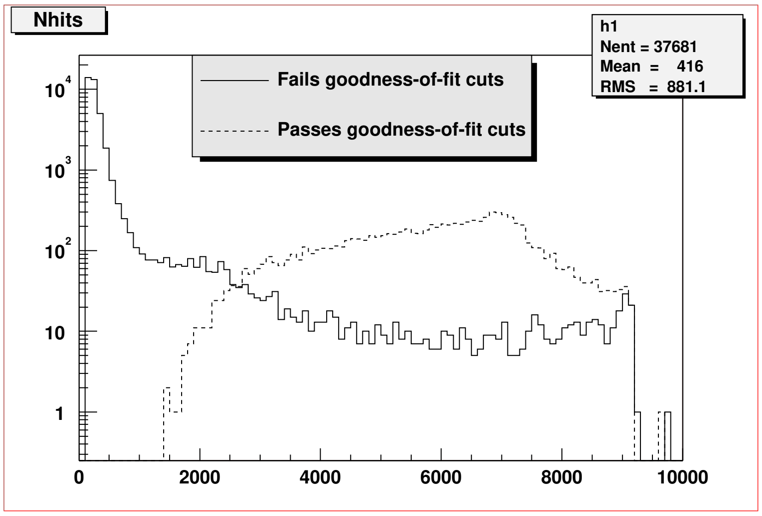

Figure 13.2: Nhits of 'Good' vs. 'Bad' Events. The solid line shows the low-Nhit flasher contamination of the data sample, which is removed by the goodness of fit cuts. In addition, there is a high-Nhit tail, consisting mostly of clipping muons which reconstructed poorly, as well as stopping muons and multiple muons.

passed the combined F_{should} and PDF cuts, and only 1 event passed the radial cut in addition to these. The events were apparently in the tail of a long distribution. The vast majority of events reconstructed (poorly) as downward-going muons. This indicates that any neck events surviving the neck tube cut have very little probability of reconstructing as a through-going muon. Since the neck tube cut has a contamination of less than 1 percent, the possible contamination of the data sample by neck events is on order 10^{-6} events.

There were no candidates for upward-going muons in this comprehensive data sample. This fact is important for the discussion in section 13.2. This analysis

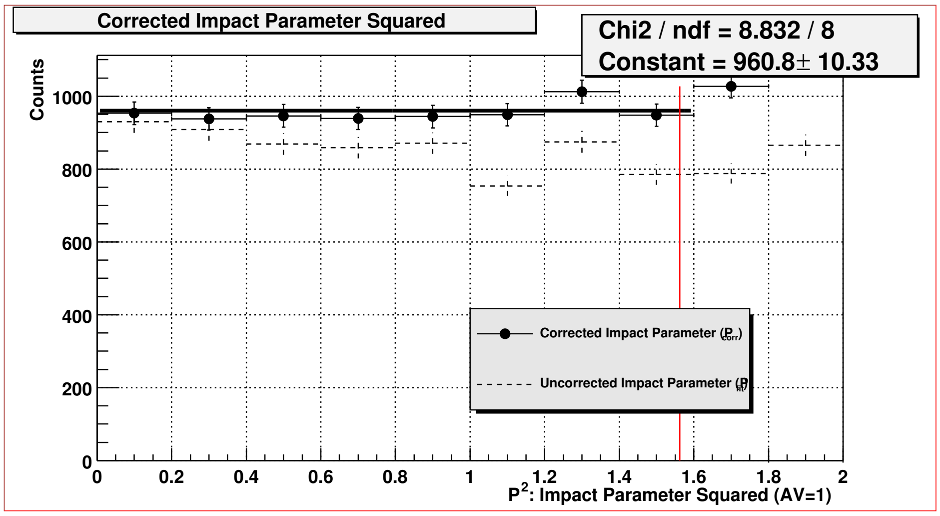

Figure 13.3: Impact Parameter Distribution. The squared impact parameter is plotted for the reconstructed data set. If the corrected impact parameter is used, this agrees well with a flat distribution (with the chi-squared value shown). The vertical line shows the radial cut of $p_{corr} < 750cm$.

effectively eliminates the possibility that otherwise good events were (falsely) tagged by the neck cut and thus sacrificed from the sample.

13.1.3 Radial and Energy Distributions

Distributions independent of zenith angle can be used to ensure that the final sample is a good one. The most important of these is the radial distribution (the distribution of impact parameter). Figure 13.3 shows that this corrected[1] impact parameter distribution is quite flat, as is expected.

Figures 13.4 and 13.5 show the energy response of the detector to through-going

[1] The correction impact parameter, described in Chapter 11 is based on Monte Carlo, not an *ad hoc* correction to the observed data.

muons. The distributions are strongly peaked at 4 NHITs/cm and 25 p.e./cm respectively, which demonstrates that the energy loss straggling is not severe, and most muons lose energy at a rate close to the mean. A larger NHIT response can be seen in the real data as compared to the Monte Carlo; this is indicative of the fact that the Monte Carlo used is not correctly tuned to the true PMT absolute efficiency; it is known through ^{16}N studies that the Monte Carlo is approximately 10% too low in this parameter.

Figure 13.5 shows a sharp downturn in the light collection outside 7 meters radius; this is expected because the phototube collection efficiency drops dramatically due to the shadowing effect of the PMT reflector buckets. The NHIT parameter is less sensitive to this because it is dominated by the quantity of reflected light, rather than direct light.

13.1.4 Event Rate and Time Distribution

The total rate of through-going muons in the detector can be found in one of two ways. The obvious method is to calculate counts divided by live time. The second is to calculate the time between events (Δt) and fit to an exponential distribution. As can be seen in Figure 13.6, these two methods give good agreement for the event rate. The slightly high chi-squared value on this plot can be attributable to finite run length, which suppresses event pairs with long time separations. Agreement between these measurements is an important check, since it allows one to compare information

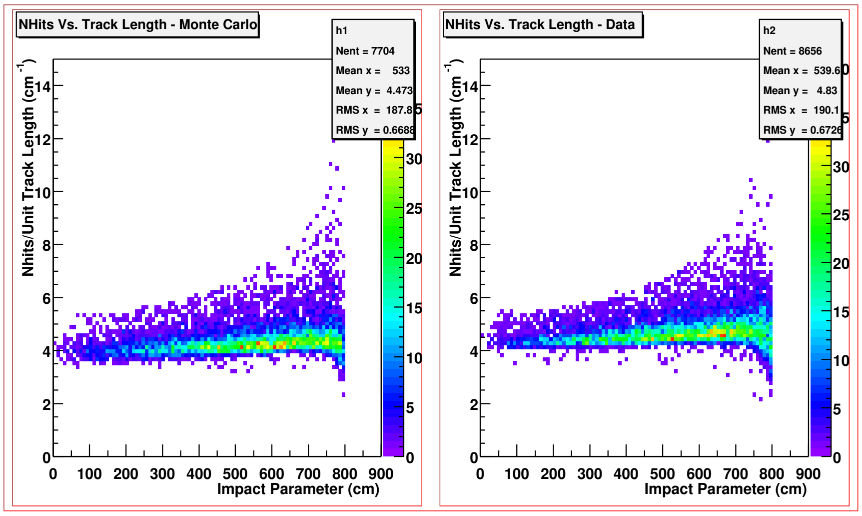

Figure 13.4: Energy Loss: Nhits Per Unit Track Length. The number of PMTs hit per centimeter track length is shown for Monte Carlo (left) and real data (right). Colors represent bin contents.

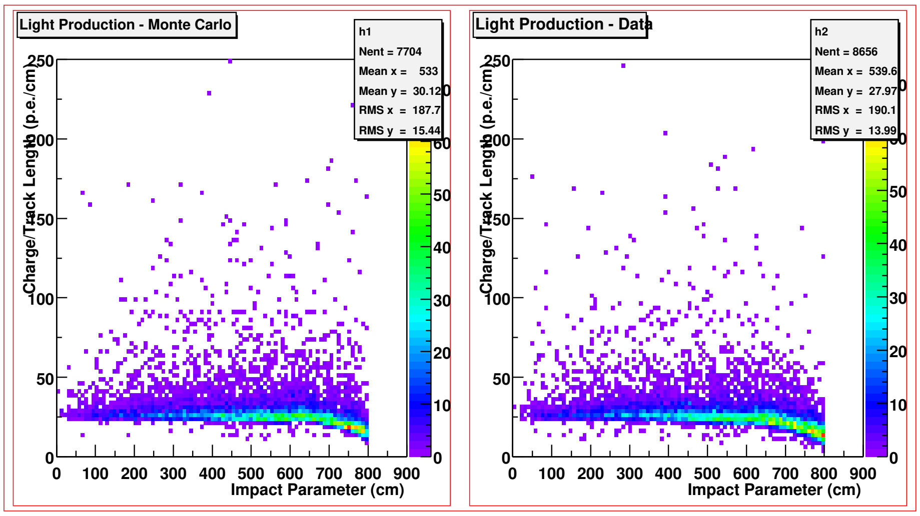

Figure 13.5: Energy Loss: Photoelectrons per cm. The vertical axes plot the total light count (in photoelectrons) divided by the reconstructed track length, for Monte Carlo (left) and real data (right). Colors represent bin contents.

from the data stream (event timing) with livetime calculations.

The measured rate for through-going single muons in SNO, inside the effective area of 175.5 m^2 is:

$$R = 50.14 \pm 0.7(\text{stat.})\mu/\text{day} \tag{13.1}$$

(This can be immediately extrapolated to give two numbers useful for SNO neutrino backgrounds: 32.3 muons per day through the D_2O region, and 64.6 muons per day through the region bounded by the PSUP.)

Systematic corrections and systematic uncertainties for finding the integrated flux are listed in Table 13.1. These errors are dominated by the uncertainty in fitter acceptance (i.e. effective area). The total flux of muons through the detector (with $\cos\theta > 0.5$):

$$\Phi_{\text{through-going}} = 3.30 \pm 0.04(\text{stat.}) \pm 0.09(\text{sys.}) \times 10^{-10}\ \mu\ \text{s}^{-1}\ \text{cm}^{-2} \tag{13.2}$$

$$\Phi_{\text{all-muon}} = 3.39 \pm 0.06(\text{stat.}) \pm 0.10(\text{sys.}) \times 10^{-10}\ \mu\ \text{s}^{-1}\ \text{cm}^{-2} \tag{13.3}$$

The first of these two rates is for the single, through-going muons. The second extrapolates to the all-muon sample, which includes both multiple and stopping muons.

The calculations of total rate done in Chapter 12 was for a flat overburden of pure Norite. We know (from knowledge of the geology of the area) that the footwall to the south of the detector has a lower density, so will enhance the rate slightly. If we look only at muons with reconstructed directions coming from the north half of the

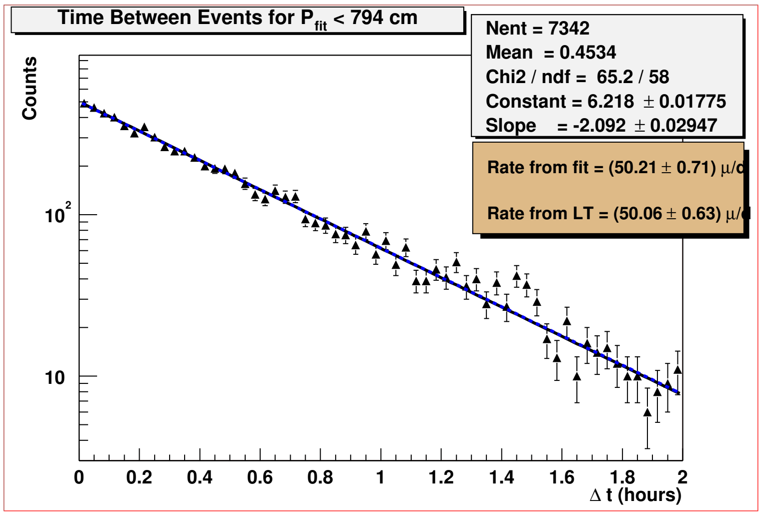

Figure 13.6: Through-Going Muon Event Rate in SNO. The time between events is histogramed and fit to an exponential. Pairs of events that span runs are removed. Superimposed is the exponential derived from the counts/time method, (indistinguishable on this scale).

sky, we get slightly lower rates:

$$\Phi^{North}_{\mathrm{through-going}} = 3.21 \pm 0.05(\mathrm{stat.}) \pm 0.09(\mathrm{sys.}) \times 10^{-10}\ \mu\ \mathrm{s}^{-1}\ \mathrm{cm}^{-2} \quad (13.4)$$

$$\Phi^{North}_{\mathrm{all-muon}} = 3.30 \pm 0.06(\mathrm{stat.}) \pm 0.10(\mathrm{sys.}) \times 10^{-10}\ \mu\ \mathrm{s}^{-1}\ \mathrm{cm}^{-2} \quad (13.5)$$

The all-muon rates agree well to the estimates calculated in Chapter 12, which were between 3.2 and $3.3 \times 10^{-10} \mu\ \mathrm{s}^{-1}\ \mathrm{cm}^{-2}$.

13.1.5 Azimuthal Distribution

The geological environment of the SNO detector is easily modeled over the greater part of the solid angle in which we expect to see atmospheric muons, but the footwall, interface, and ore bodies are not well understood.

Table 13.1: Systematic Errors in Absolute Rate. The stopping- and multiple-muon corrections apply only when calculating the 'all muon' rate.

Source	Value	Error	Contribution to total error
Live time	3549.24 h	7.15 h	0.20 %
Data sacrifice[a]	0 %	0.1%	0.10 %
Contamination[b]	0.006%	Neg.	Neg.
Effective area	175.5 m^2	5.4 m^2	2.65 %
Stopping muons[c]	-1.26 %	0.02 %	0.02 %
Multiple muons[d]	-1.5%	1.5 %	1.5 %
Total Error			3.05 %

[a] The data reduction stage is designed to cut zero muon events, but has an estimated uncertainty of 0.1%.

[b] There is expected to be approximately 0.5 neck events contaminating the muon sample before reconstruction; this leads to a negligible systematic error.

[c] 1.34 % of all downward-going muons will stop in the detector. Of these, 94±2% will be rejected.

[d] Approximately 3% of all downward-going will be observable as multiple-muon bundles. No good information exists on the rejection efficiency, although it is estimated at one half.

The azimuthal distribution of events is shown in Figure 13.7. The distribution shows large variations particularly in the region $0.85 > \cos\theta > 0.95$, or between 18°and 32°, roughly the region occupied by the hanging wall / footwall interface. A sharp distortion can be seen to the southeast, where the majority of the nickel ore and mine (open or backfilled) activity exists. A naive interpretation of the spike at 250°is that this is the major line that has been mined out and backfilled, whereas smaller pockets to the sides have not been so throughly excavated.

The azimuthal distribution of muons in the northern hemisphere is fairly flat.

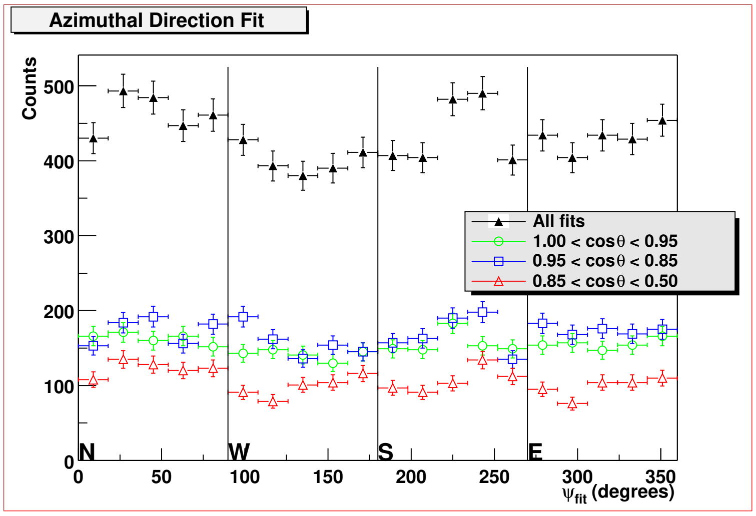

Figure 13.7: Azimuthal Distribution of Down-Going Muons. Different zenith angle bins are as marked. Vertical error bars are statistical. Horizontal error bars indicate bin width only; detector resolution is not accounted for.

This is as expected, since the majority of geological complications are in the south. Therefore, muons coming from the north are used as the 'golden' data sample, with data from other regions used as a check.

A complete map of the extrapolated positions muons passed through the surface is shown in figure 13.8. Note that there exist irregular spikes of muon flux near the center of these maps; these are not accounted for in our understanding of the geology of the area, and may be due to underground features in the rock.

13.1.6 Zenith Angle Distribution

The zenith angle distribution of downward going muons was binned in $\cos\theta$ between 0.5 and 1.0, in bins of 0.1. This gives a bin size that is slightly larger than the fitter

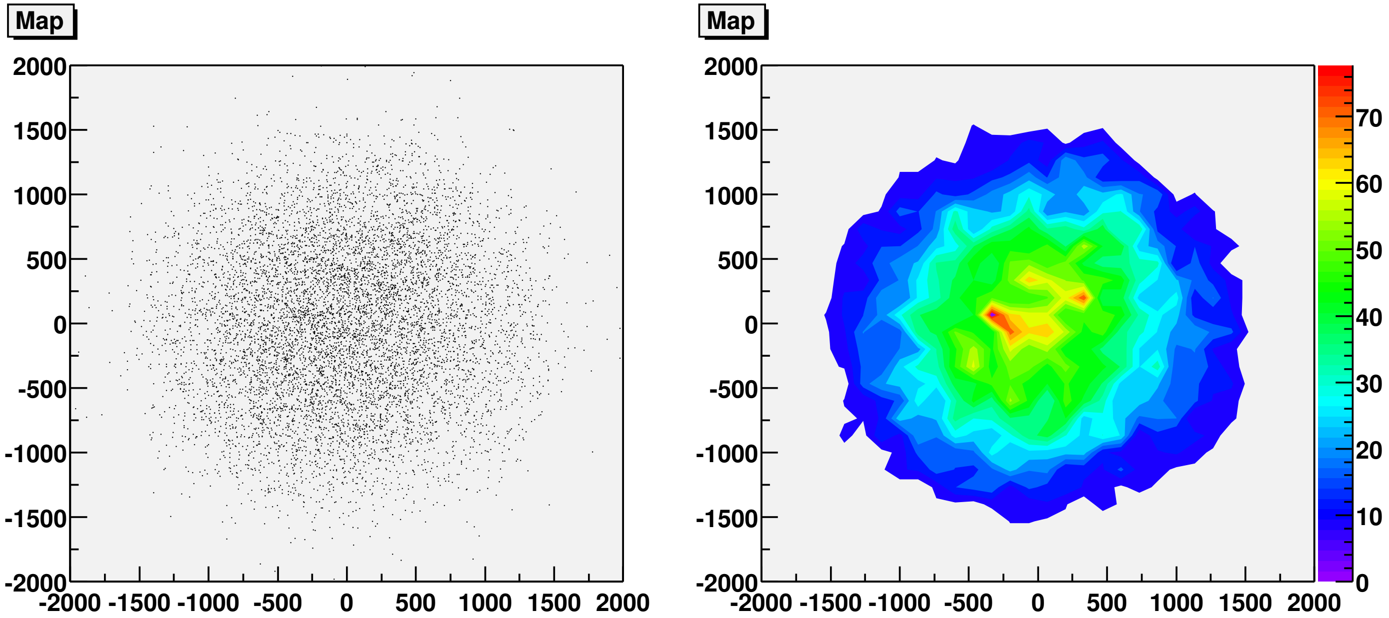

Figure 13.8: Surface Positions of Measured Muons. Axes are in meters, with the SNO location at (0,0). The +y axis corresponds to true north. The left figure shows positions of individual muon events; the figure on the right shows a contour plot of these positions.

resolution.

The data are looked at with different cuts applied in zenith and azimuthal angles. Cuts denoted 'north' refers to muons coming only from a northerly direction; 'south' implies events from the south, and 'all sky' takes both hemispheres together.

13.1.7 Fits to the 'Depth-Intensity' Relation

The data was binned in $\cos\theta$, then redrawn as a 'vertical intensity-depth' plot, shown in Figure 13.9. This plot was fit to the depth-vertical intensity empirical formula of (12.15). Only events coming from the north half of the sky were used. Three fits were made, with the alpha parameter set to 1.93, set to 2, and allowed to vary freely. These fits are shown in Table 13.2

With alpha fixed, the fits give good chi-squared values, with a x_0 parameter of 1090 hg/cm^2. This parameter is given in depth of SNO rock (i.e. norite), not standard rock. Freeing the alpha parameter to vary results in a fit with parameters wildly different from the first two, with a goodness-of-fit only slightly better. Moreover, MINUIT reports errors with the development of the error matrix, so this fit cannot be well trusted.

Ignoring the free-parameter fit, either of the two parameterizations gives reasonable results. In particular, both give a vertical flux of $(4.26 \pm 0.87(\text{stat.}) \pm 0.15(\text{sys.})) \times 10^{-10}$ s^{-1}cm^{-2}sr^{-1}. Here the statistical uncertainty is estimated from the fractional uncertainty in A_v, and the systematic uncertainty comes from the sources detailed in

Table 13.1.

This value is in very good agreement with the value predicted in equation (12.19). This indicates that the rock overburden has been correctly accounted for. As can be calculated from the empirical formulae of Section 12.3.5, a small error in the detector depth (or, equivalently, rock density) by 1% will change the measured vertical intensity by approximately 8%. The agreement between our measured and predicted rates demonstrates that the gross features of the rock overburden are correctly modeled (independent of structure in zenith angle).

Fit	A_v $[10^{-10}s^{-1}cm^{-2}sr^{-1}]$	x_0 [hg/cm^2]	α	χ^2/d.o.f.	$I_\mu(\theta = 0)$ $[10^{-10}s^{-1}cm^{-2}sr^{-1}]$
1	3030±630	1081±27	1.93±0	43.46/46	4.26±0.88
2	3180±660	1092±28	2±0	43.35/46	4.26±0.88
3	2830±4570	1928±845	4.97±2.78	40.43/45	4.41±7.15

Table 13.2: Fits to Empirical Depth-Vertical Intensity Relation. Fit 1 corresponds to the LVD value of α, fit 2 corresponds to the Fréjus value.

13.1.7.1 Fits to Muon Gamma

Several fits were done to find the γ_μ parameter. The distribution model described in Chapter 12 was calculated for trial parameters and a χ^2 value was computed.. Curve-fitting is done using the CERNLIB package MINUIT [99] (accessed through the ROOT libraries [100]). Errors on parameters are as reported by the MIGRAD or (where possible) MINOS routines.

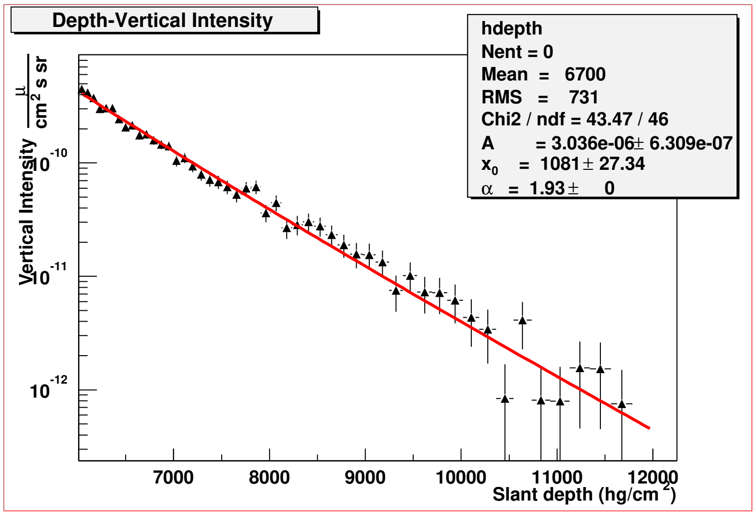

Figure 13.9: "Depth-Vertical Intensity Plot". Data shown corresponds to all muons from the 'northerly' set. The solid line corresponds to a fit to the depth-vertical intensity relation, with α set to 1.93, as per the LVD fit.

Global fits to the data are shown in Table 13.3. The first three fits (no. 1-3) involve only the free parameters A (normalization) and γ_μ. They agree to within one sigma statistical errors. The 'all-sky' fit has the highest statistics, but the goodness-of-fit is poor but believable, with a p-value of 0.21 (i.e. inside a 90% confidence interval). The north-sky and all-sky fits are shown in Figures 13.11 and 13.12.

It was noted that the biggest contributions to the chi-squared value came from the bins with highest $\cos\theta$. In order to understand this, fits were repeated with these bins removed from the data (fits no. 4-6). These data sets gave much better goodness-of-fit; fit number 6 in particular improved over fit number 3 (the all-sky data). The improved chi-squared is insufficient reason to reject these bins from the analysis, but

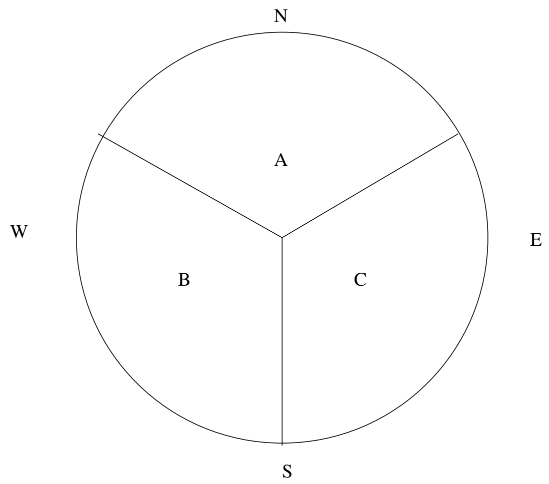

Figure 13.10: Azimuthal 'Wedge' Bins. The data are binned into three azimuthal angles: 60°W of N to 60°E of N (Wedge A), 60°W of N to S (Wedge B), and S to 60°E of N (Wedge C).

it is useful to show these fits as a measure of systematic errors: even when these important bins are removed, the fits give consistent values for the γ_μ parameter.

As an additional check on the azimuthal dependence of the fit, the sky was split into three 'wedges' (fits no 7-9), which splits the azimuthal data into three bins (shown in Figure 13.10). These fits generally agree with those above, to within two standard deviations.

In each of these fits, the chi-squared contour was well-behaved, as is shown in Figures 13.13 and 13.14. As was observed by the LVD group [95], the A and γ_μ parameters are highly correlated. Similarly, the errors on the two parameters are highly correlated; a singular value of γ_μ gives a well defined A. The correlation

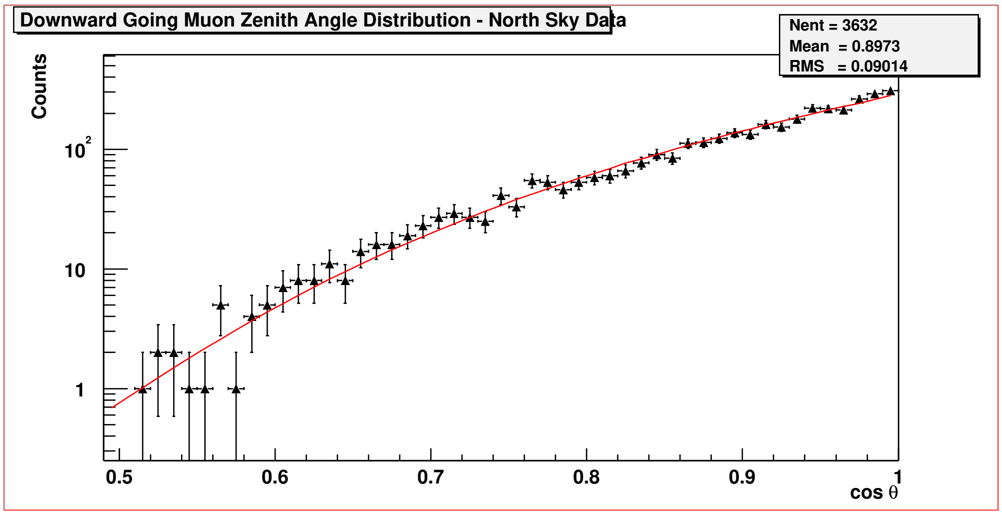

Figure 13.11: Fit To Zenith Angle - North Sky. The zenith angle distribution is shown for muons coming from the north hemisphere. (i.e. $\phi \in (270°,90°)$ east of north). The line shows the best fit, with $\gamma_\mu = 2.81,\ A = 2.6$.

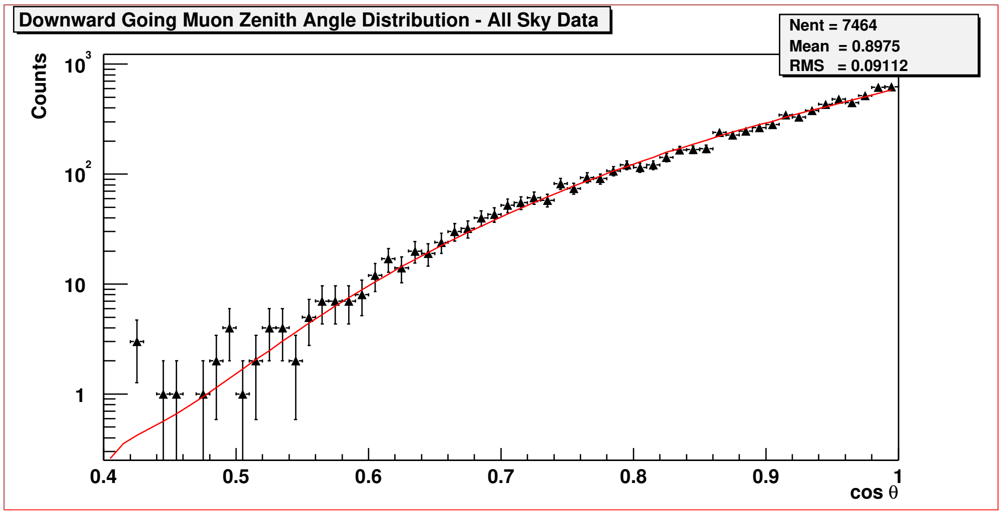

Figure 13.12: Fit To Zenith Angle - All Sky. The zenith angle distribution is shown for muons coming from any direction. The line shows the best fit, with $\gamma_\mu = 2.81,\ A = 2.6$.

No.	Azimuth Cut	Zenith Cut	Chisq/d.o.f.	Prob	A	γ_μ	Rc
1	North Sky	none	43.98/48	0.64	2.6±1.5	2.81±0.07	
2	South Sky	none	45.13/48	0.59	4.2±2.5	2.85±0.07	
3	All Sky	none	55.66/48	0.21	2.4±0.9	2.80±0.04	
4	North Sky	$\cos\theta < 0.98$	38.54/46	0.77	1.4±0.8	2.74±0.06	
5	South Sky	$\cos\theta < 0.98$	37.90/46	0.80	2.3±1.4	2.79±0.07	
6	All Sky	$\cos\theta < 0.98$	42.41/46	0.62	1.3±0.5	2.73±0.04	
7	Wedge A Sky	none	50.52/48	0.38	2.8±1.7	2.81±0.07	
8	Wedge B Sky	none	37.02/48	0.87	9.1±5.5	2.94±0.07	
9	Wedge C Sky	none	41.12/48	0.75	2.7±2.1	2.82±0.09	
10	North Sky	none	42.59/47	0.66	46.0±37.6	3.26±0.28	0.0425 ± 0.1025
11	South Sky	none	42.85/47	0.64	58.6±77.0	3.25±0.23	0.0283 ± 0.0485
12	All Sky	none	50.91/47	0.33	35.9±26.9	3.20±0.17	0.0290 ± 0.0371

Table 13.3: Downgoing muons: Global Fits. Various subsets of the down-going muon zenith angle distribution are fit. Unless stated otherwise, fits had R_c locked at zero. 'Prob' refers to the p-value of the given chi-squared.

between A and γ_μ is shown better in Figure 13.15.

There exist two important systematic uncertainties with these fits. The first is due to uncertainties in fitter resolution; the second is due to uncertainties in the geological environment. The parameter of interest is γ_μ.

The uncertainty due to fitter resolution smearing can be found by considering alternate cases. For instance, in data set no. 1 (north-sky data only) if no correction to the fitter resolution is made the value of γ_μ drops from 2.81 to 2.78. Therefore, the maximum uncertainty associated with fitter resolution gives an uncertainty on the order of 0.03 in γ_μ. A more accurate estimate would give a smaller uncertainty[2], but this effect is seen as small in comparison to geological environment.

A calculation of the uncertainty due to geological environment is more difficult to make due to the paucity of information. However, we may make a rough pessimistic estimate of uncertainties by comparing different data sets. Because the southerly and northerly data sets agree quite well to within statistical errors (fits no. 1 and 2), we may use fit number 3, the all-sky set as our final result. However, we are uncertain as to whether the two downward-going bins contain some sort of geological anomaly. Comparing fits number 3 and 6 gives a change in γ_μ of ± 0.07, which we use as our uncertainty estimate.

[2] A good estimation method would be to compare the effect of smearing functions based on different radial cuts. For instance, a radial cut of 760 cm would give a different angular smearing than the nominal 750 cm.

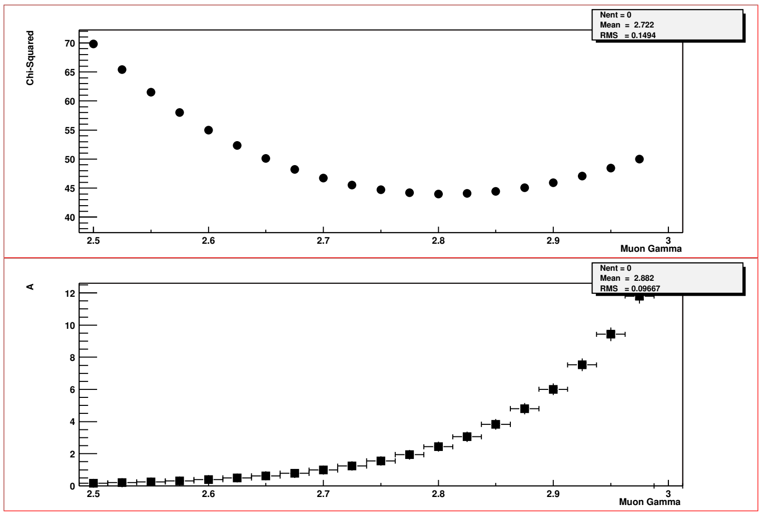

Figure 13.13: Chi-squared Contour in γ_μ, 'North' Data Set. **For each value of γ_μ the abscissa, a fit is done to the A parameter, which is shown in the lower plot. The one-sigma parametric errors for A are shown (mostly smaller than the points). The top plot shows the value of the χ^2 (for 48 degrees of freedom). Only events reconstructing as northerly are used.**

Because the systematic uncertainties due to fitter resolution and geological environment are entirely independent, we may add them in quadrature, for a net systematic uncertainty of ± 0.08.

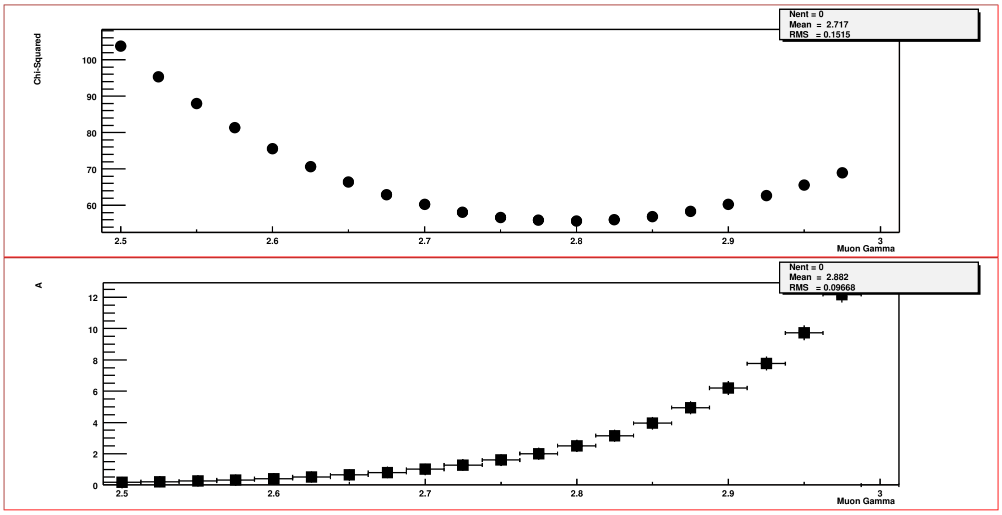

Figure 13.14: Chi-squared Contour in γ_μ, 'All Sky' Data Set. As in Figure 13.13, but for all data.

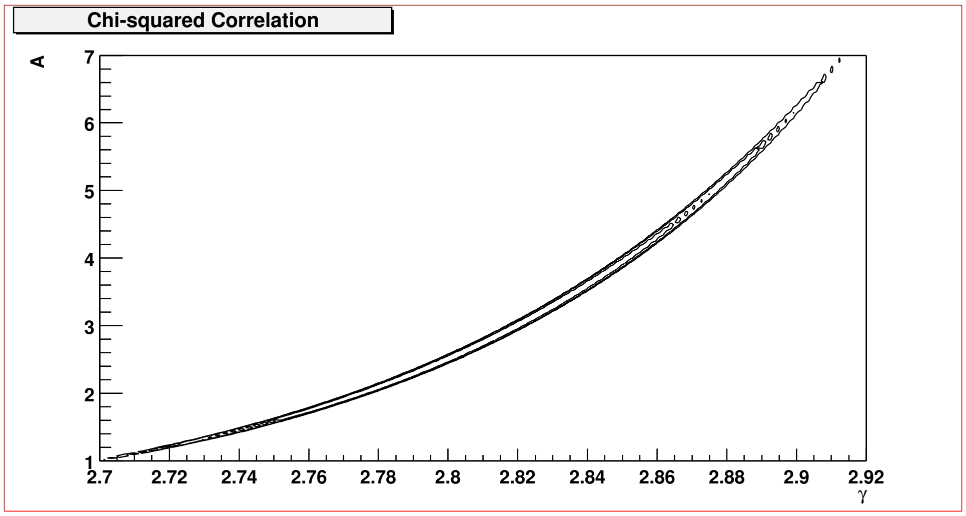

Figure 13.15: Contour Plot of Allowed Region in A,γ_μ. The allowed fit region for the downward going muon fit, using all-sky data, is shown for a fit to A and γ_μ. Contours are drawn for $\chi^2_{min} + 2.79$, $\chi^2_{min} + 4.61$, and $\chi^2_{min} + 5.99$ The best fit position is at $A = 2.40$, $\gamma_\mu = 2.80$.

13.1.7.2 Prompt Muon Fits

A fit to a prompt muon component was attempted. The A, γ_μ, and R_c parameters were all allowed to vary freely, although A and R_c were bounded to be greater than zero. This resulted in the best-fit parameters given in entries 10-12 in Table 13.3.

However, these global fits are not believed to be truly representative of the physical parameters. Rather, the algorithm is following a very shallow drop in χ^2 and to a non-physical minimum: the fit tends to pull towards unphysically large values of γ_μ. This is illustrated in Figures 13.16 and 13.17. It can be seen that if both γ_μ and R_c are left variable, then they are highly correlated. Moreover, the final goodness-of-fit values for these are only marginally better than the best fits with zero prompt component (fits 1,4, and 3 respectively).

For the SNO data, therefore, we must accept a value or range of values for the muon gamma before we can estimate limits on the prompt muon component. Reasonable limits on this from other experiments give γ_μ in the range between 2.7 and 2.8. The upper bounds for R_c are given by the fits at the upper end of a physically significant region.

For the 'all-sky' data set, the fits for γ_μ between 2.7 and 2.9 give one sigma bounds on R_c, listed in Table 13.4. These bounds are based on statistical measures only. If we bound $\gamma_\mu < 2.9$ (a very conservative upper bound), we may put an upper limit on the prompt muon component: $R_c < 5 \times 10^{-3}$.

γ_μ	χ^2 (48 d.o.f.)	R_c Min.	R_c Max
2.70	58.45	-0.0016	-0.00018
2.75	56.77	-0.0009	0.00072
2.80	55.39	-0.0001	0.00184
2.85	54.25	0.0009	0.00324
2.90	53.32	0.0021	0.00502

Table 13.4: Limits on Prompt Muon Component. The limits on R_c to one sigma are given for different hypothetical values of γ_μ. Data is from the 'all sky' data set. Errors (68% C.L.) are statistical only.

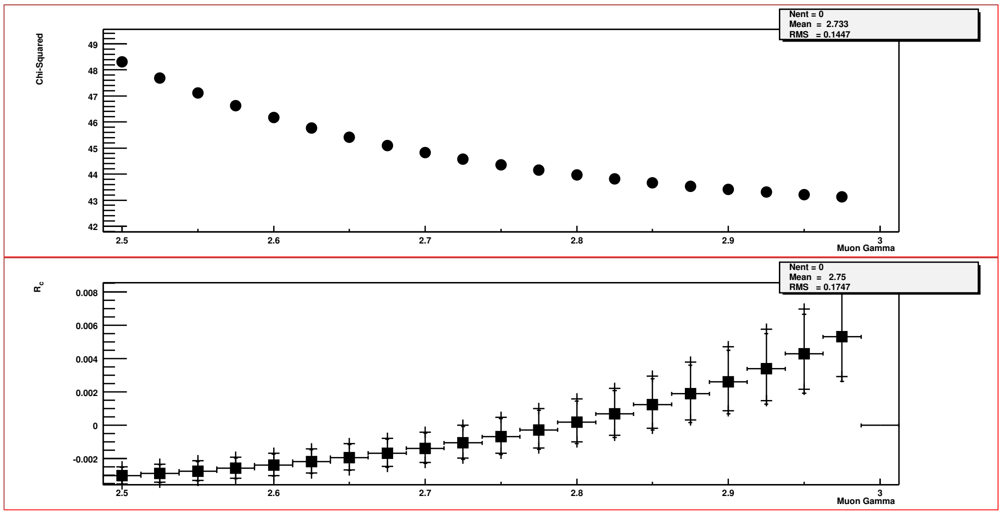

Figure 13.16: χ^2 Contour in γ_μ with Prompt Component, 'North' Data Set. The top plot shows the χ^2 value of the fit(to 47 degrees of freedom) for each value of γ_μ. The lower plot shows the fit value of R_c at each point, with one-sigma parametric errors. Data set is northerly events only.

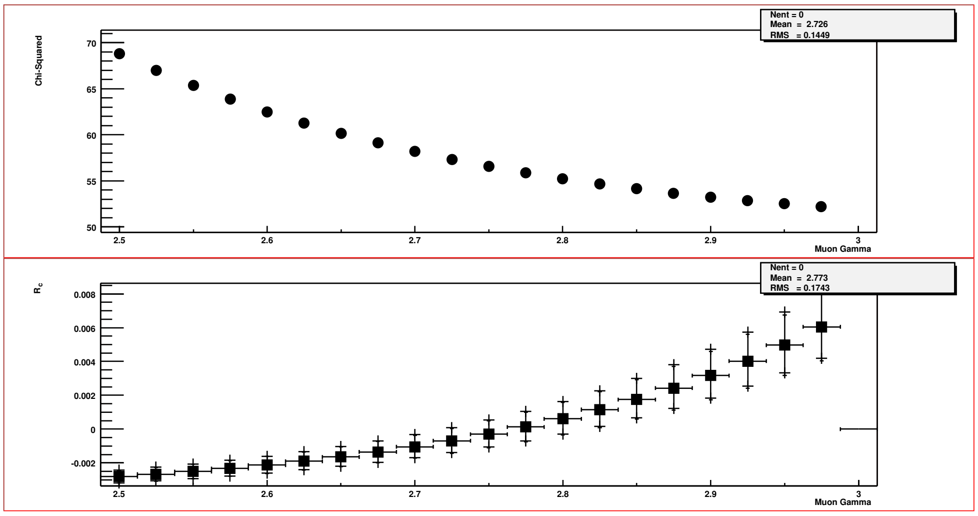

Figure 13.17: χ^2 Contour in γ_μ with Prompt Component, 'All Sky' Data Set. As in Figure 13.16, but all data is used.

13.1.8 Discussion

The total flux of through-going muons at SNO is estimated to be $3.39 \pm 0.05(\text{stat.}) \pm 0.12(\text{sys.}) \times 10^{-10}$ $\mu/\text{s}/\text{cm}^2$. The total flux of all muons, including stopping muons and multiple muons is estimated to be $3.48\mu/\text{s}/\text{cm}^2$, although the calculation of the multiple muon rate is based upon an old model, and the understanding of the acceptance is poor.

Despite apparent problems with our understanding of the geological region around SNO, reasonable fits to the data can be made that support a surface muon flux with $\gamma_\mu = 2.80 \pm 0.04(\text{stat.}) \pm 0.08(\text{sys.})$ and $A = 2.4 \pm 0.9(\text{stat.})$. The systematic errors are dominated by the uncertainties in geological environment, but also include fitter resolution effects. The error on A is due almost entirely to uncertainty in γ_μ, since the overall rate is constrained to the measurement above.

This result agrees well with the result published by LVD [95, 57] and MACRO [93]. With better understanding of the systematics and more statistics, SNO may in future be able to improve upon this measurement.

The prompt muon contribution cannot be fit simultaneously with the muon gamma, so constraints external to the SNO data must be imposed. I believe this is due to the fact that, for SNO, the slant depth and zenith angle for a given angular bin have one-to-one correspondence. (This would not be true of detectors under asymmetric overburdens). This might mean that the γ_μ and R_c parameters both serve to drive the size of the tail of the distribution (i.e. at large slant depth). However, if a reasonable constraint on the muon gamma is made as $\gamma_\mu < 2.9$, then we find a limit on R_c of 5.0×10^{-3} (to within a 68% confidence interval).

This figure is again in agreement with results from LVD [57], and promises to improve with better statistics. However, this figure must be taken cautiously, as no good systematic check exists. Moreover, this limit requires external validation of the gamma parameter, which is unsatisfying at best. The LVD collaboration makes no statement about the correlations between γ_μ and R_c, so it is unknown if they fit the two parameters independently or not.

Future work on the downward-going muon sample should concentrate on a better understanding of the geological environment of SNO, should such information be obtainable. [3]

Another major area for improvement is a complete study of multiple muons. Preliminary work in this area looks promising but technically difficult. Muon multiplicity at large depths is thought by many to be an interesting quantity to measure in order to obtain primary cosmic ray compositions (as done by MACRO [93]). SNO will have a very poor resolution for discerning multiple muons because it does not have segmented detector regions, but is larger in area than previously existing deep experiments such as KGF [7]. This allows a complimentary measurement to be made: rather than a small detector with high resolution like KGF, SNO can measure large separations, but with low resolution.

13.2 Neutrino-Induced Muon Flux

13.2.1 Rate and Systematics

A good sample of neutrino-induced muons can be clearly separated in angle from downward-going atmospheric muons. This is shown in Figure 13.18, which shows all muons surviving the goodness-of-fit and radial cuts. A cut is made at a zenith angle of $\cos\theta < 0.4$, which allows for good separation of downward going atmospheric muons and "upward-going" neutrino-induced muons.

The only sizable systematic error for the measurement of through-going neutrino-

[3] Because muon analysis is a low scientific priority for SNO, and because INCO (the mining company running the Creighton mine) has little interest in any geological region besides the ore body, such information is difficult to glean.

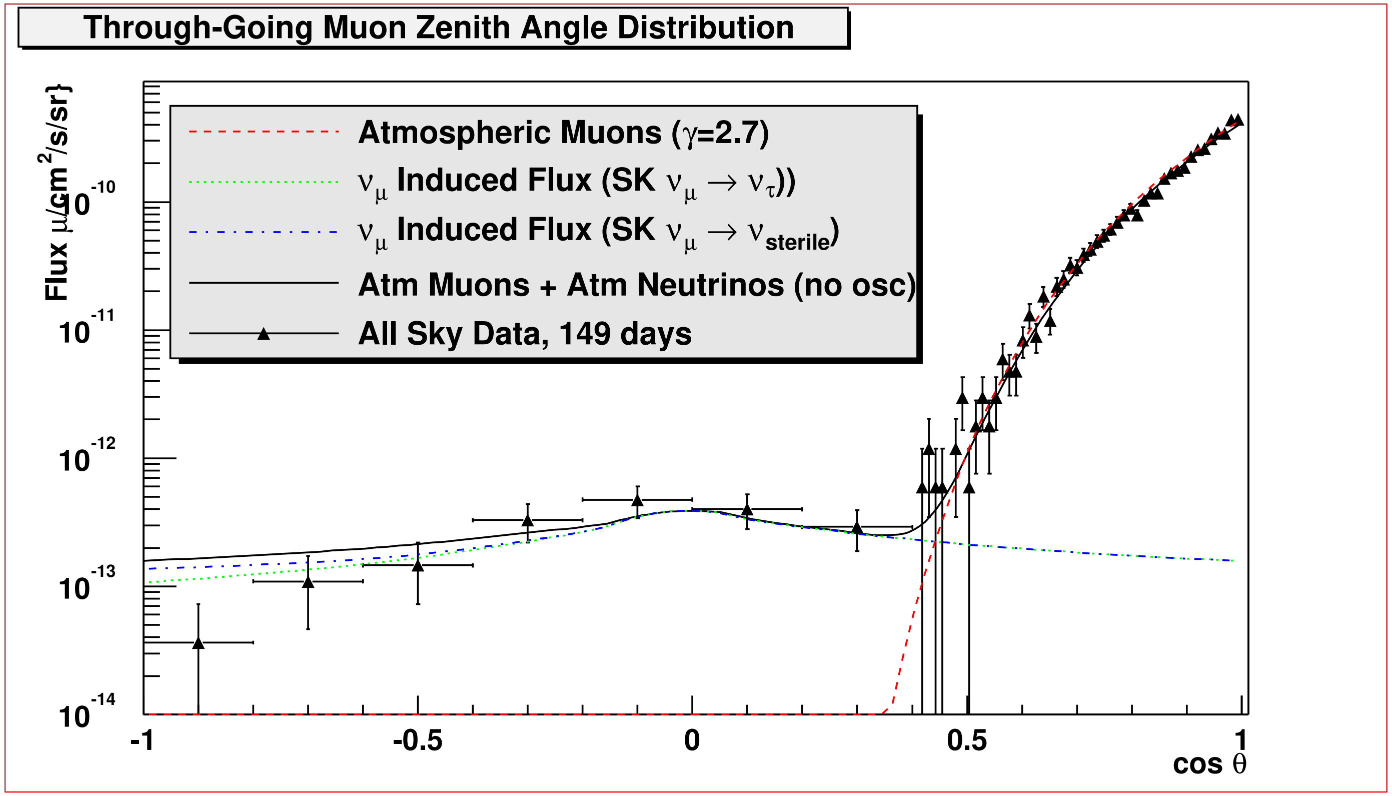

Figure 13.18: Zenith Angle Distribution of All Through-Going Muons. The theoretical curves shown are the same as in Figure 12.15. Data is the all-sky sample, normalized for livetime and effective area of the detector.

induced muons is fitter mis-reconstruction of downward-going muons (be they through-going, multiple, or stopping). The contribution of mis-reconstructed through-going muons coming from zenith angles with $\cos\theta$ between 0.5 and 1.0 is estimated to contaminate the "upward-going" muon sample with 0.12 events. Mis-reconstruction from the angular region between 0.4 and 0.5 in $\cos\theta$ is expected to give another 0.18 events, but this quantity is expected to be balanced by a similar sacrifice due to mis-reconstruction out of the region of interest. Through-going and stopping muons are largely rejected by the fitter and tend to reconstruct as downward-going events; special cases of event topology that could fool the fitter have not been investigated in detail, but the ratio of event rates of downward going to upward going muons is not so extreme that rare events are a concern. Therefore, shape distortions due to downward-going muon contamination may be safely neglected.

A large bin size (0.1 in $\cos\theta$) was chosen to give reasonable statistics per bin. Direction error on reconstruction is much less than bin width, so shape distortions due to fitter resolution can be neglected.

As mentioned in Section 13.1.2, no candidates for upward going muons were found in events tagged by the neck-tube cut, and no other cut contained any acceptance bias in detector coordinates.

Absolute rate of through-going muons in the sample range was found to be 49 muons into 175.5 square meters in 3549 hours live-time, plus or minus 2.7 percent (as in Table 13.1, for a total flux of $(2.18 \pm 0.31(stat) \pm 0.07(sys)) \times 10^{-13} cm^{-2} s^{-1} sr^{-1}$. This is in agreement with the fluxes predicted in Chapter 12, for both oscillation and no-oscillation models.

The rate of muons coming from below the horizon ($\cos\theta < 0$)is found to be $(2.13 \pm 0.39(stat) \pm 0.06(sys)) \times 10^{-13} cm^{-2} s^{-1} sr^{-1}$. This can be compared to the flux seen by Super-Kamiokande measurement [98] of $(1.74 \pm 0.07(stat) \pm 0.02(sys)) \times 10^{-13} cm^{-2} s^{-1} sr^{-1}$, about 18% lower than the flux for SNO. This agrees quite well with the comparison of theoretical values in the last chapter, in which the two rates were expected to differ by 15%. This agreement is well within the statistical uncertainties of the two measurements.

13.2.2 Model Fits

Because counting statistics were low, a nonstandard chi-squared statistic was employed to calculate goodness-of-fit. This statistic is Lucy's Z^2 statistic, described in reference [101]. (This statistic is designed to be used in sparse or meager data sets, where Poisson rather than Gaussian statistics are applicable.)

$$"\chi^2" = Z^2 = \sum_i u_i \tag{13.6}$$

$$\text{where} \tag{13.7}$$

$$u_i = 1 + \eta_i (t_i - 1) \tag{13.8}$$

$$\eta_i^2 = \frac{2 + 1/y_i^{fit}}{2} \tag{13.9}$$

$$t_i = \frac{(y_i - y_i^{fit})^2}{y_i^{fit}} \quad (13.10)$$

Note that in this calculation the model variance is used rather than the sample variance. (In practice, the Z^2 statistic behaves similarly to an ordinary χ^2 statistic, if the model variance is used in the latter.)

The angular distribution was fit to two models: the no-oscillation model, and the Super-Kamiokande best-fit parameters for active neutrino oscillation $\nu_\mu \rightarrow \nu_\tau$ ($\sin^2 2\theta = 1$, $\Delta m^2 = 0.003$). In each case, the data was fit only for absolute normalization, which was allowed to float freely. The chi-squared values found for these fits are shown in Table 13.5. Although the fit to the neutrino oscillation model is favored, both models fit the data to within a 68% confidence interval. This offers no discrimination of hypotheses.

The fit values for the overall normalization were parameterized as in [98] as

$$\Phi_{meas}(\theta) = \alpha \times \Phi_{theory}(\theta) \quad (13.11)$$

Table 13.5: Fits to Oscillation Models. The χ^2 values and normalizations are shown for fits to no oscillation and Super-K best fit active oscillation (1.0, 0.003 eV^2). Normalization was allowed to float freely.

Fit	χ^2/d.o.f.	α^{SNO}
No Osc	6.29/6	1.07 % ± 0.15 (stat) ± 0.035% (sys)
SK Best Fit	3.90/6	1.18 % ± 0.16 (stat) ± 0.035% (sys)

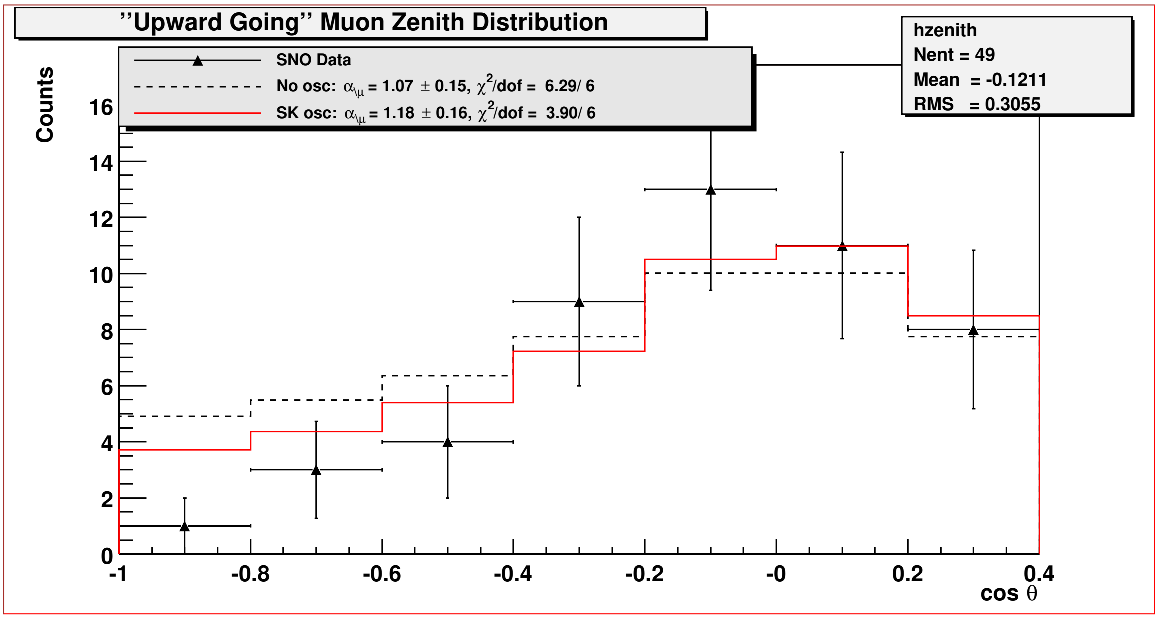

Figure 13.19: Neutrino-Induced Muon Zenith Angle Distribution. Data for neutrino-induced muon is shown for 149 days live time. Fits to the data are for no oscillation, and for Super-Kamiokande best-fit parameters of $\sin^2 2\theta = 1$, $\Delta m^2 = 0.003$. Models are fit only to overall normalization. Error bars are simply $\sqrt{(y_i)}$.

13.2.3 Parameter Fits and Excluded Regions

The above fits allow normalization to float freely. We now expand our evaluation over large parameter space in $sin^2 2\theta_V$ and Δm^2. We continue to fit each point for overall normalization, but now account for the knowledge of the normalization, which is known to 20%. Our new chi-squared statistic is computed as

$$\chi^2 = Z^2 + \left\{ \frac{\alpha - 1}{0.2} \right\}^2 \tag{13.12}$$

The extra term accounts for one extra degree of freedom in the fit. This method was used by Hatekyama [74] for Super-Kamiokande analysis [98].

We define excluded regions by computing chi-squared statistics for each point in parameter space, allowing the normalization (α) to vary for each point. A simple calculation of the excluded region is done by finding the best global fit (χ^2_{min}) and then mapping out regions with $\chi^2_{min} + 2.79$, $\chi^2_{min} + 4.61$, and $\chi^2_{min} + 5.99$ to represent areas excluded to 67%, 90% and 95% confidence limits respectively.[4]

Figures 13.20 and 13.21 show the resulting excluded regions for active and sterile neutrino mixing respectively. Both cases have a best fit position at $Deltam^2 \simeq 2 \times 10^{-3}\mathrm{eV}^2$ and $sin^2 2\theta_V \simeq 1$. The chi-squared is approximately 4.59 per 5 degrees of freedom for the case of active oscillations, and approximately 5.55 per 5 d.o.f. for the sterile case. This best fit position cannot be taken as anything more than suggestive,

[4] The use of more complicated methodologies in the construction of exclusion plots, such as Feldman and Cousins [102], is not warranted given the preliminary nature of the data.

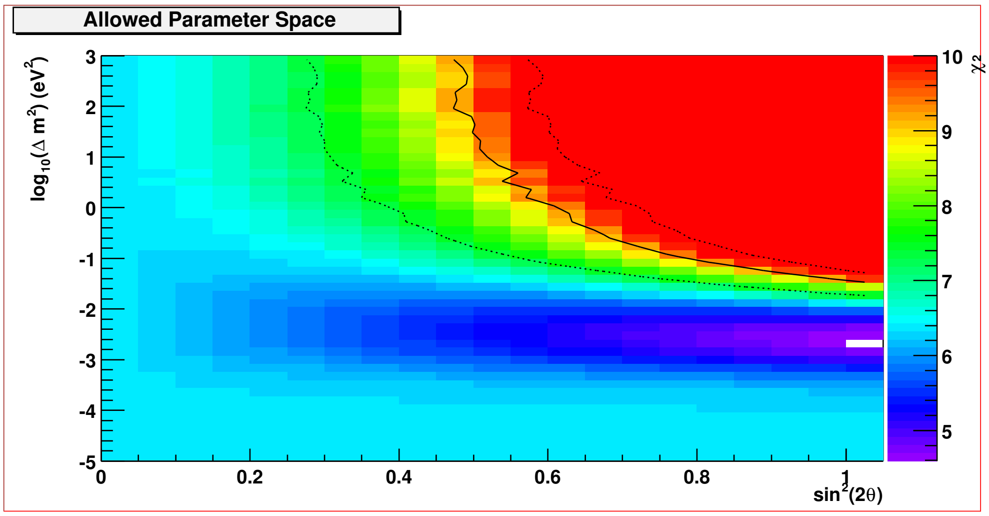

Figure 13.20: Exclusion Plot for $\nu_\mu \to \nu_\tau$ with Normalization Restriction. The chi-squared value for 7 degrees of freedom is computed including normalization constraint as in Eq. (13.12). Contours indicate regions allowed to 68%, 90%, and 95% C.L.

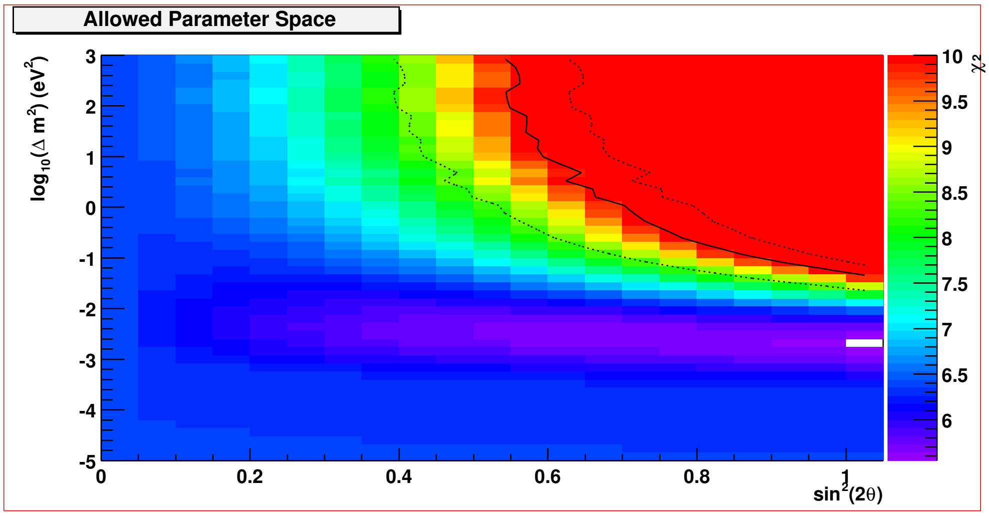

Figure 13.21: Exclusion for $\nu_\mu \to \nu_{sterile}$ with Normalization Restriction. The χ^2 value for 7 degrees of freedom is indicated by shading. The chi-squared value is computed including the normalization restriction of Equation (13.12). The lines indicate regions allowed to 68%, 90%, and 95% C.L.

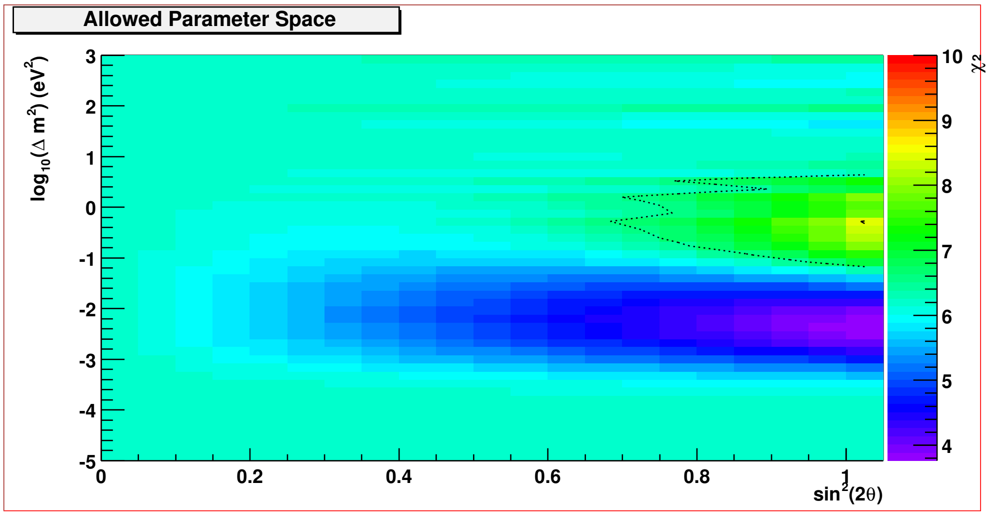

Figure 13.22: Exclusion for $\nu_\mu \to \nu_\tau$ with Free Normalization. The χ^2 value for 6 degrees of freedom is indicated by shading. Normalization is allowed to float freely. The line marks the region disallowed to a 68% confidence interval. (The entire plot is allowed to 90% C.L.)

due to low statistics.

A region of $\Delta m^2 \gtrsim 0.1\text{eV}^2$ and $\sin^2 2\theta \gtrsim 0.5$ is excluded (90% C.L.) in both cases, although the region excluded by sterile mixing is smaller. (This is because the distortion of the angular distribution is less severe than for active mixing, because of flavor regeneration in the earth.) This exclusion is mostly due to the measured overall flux (rather than the angular distribution). Large mass-mixing creates short oscillation lengths, which will tend to suppress neutrinos at all angles (not just angles with long baselines). This creates large normalizations, which are penalized.

It is also interesting to see what regions are excluded, using no knowledge of the absolute flux normalization. The normalization is allowed to float freely, so only shape distortions are used. This is shown, for active neutrino mixing ($\nu_\mu \rightarrow \nu_\tau$), in Figure 13.22. The best fit occurs at $\Delta m^2 \simeq 4 \times 10^{-3}\mathrm{eV}^2$, $\sin^2 2\theta \simeq 1.0$, with a$\chi^2$ of 3.76 over 5 degrees of freedom. No region in the plot was excluded at the 90% confidence level. However, one interesting region of Figure 13.22 is the region excluded to 68% C.L., at $sin^2 2\theta \simeq 1$, $\Delta m^2 \simeq 1\mathrm{eV}^2$. This region is disfavored due to critical mixing from downward-going neutrinos going through about one oscillation length, while upward-going neutrinos are completely mixed between the two flavors. This region demonstrates the value of measurements above the horizon.

13.2.4 Discussion

Despite limited data, a region of large Δm^2 and large $\sin^2 2\theta$ can be excluded. This regime has been excluded by other neutrino oscillation experiments, but nonetheless serves as an additional measurement.

More important than the current results are the promises for the future. The angular distributions show that there appears to be no major contamination in the analysis. This is evidenced most clearly in Figure 13.18, which shows distinct separation between atmospheric muons and neutrino-induced muons and closely tracks predictions over nearly 4 orders of magnitude. The angular distributions agree reasonably with established models, providing proof that the experiment lacks only running time to produce more interesting results.

The best of the future results will be the measurement of the absolute flux of muon neutrinos at high energies, by observation of events with zenith angle above the horizon. This is demonstrated in Table 13.5: the difference between values of α for the no-oscillation case and the oscillation case is much less for SNO than for Super Kamiokande. This is because the extra range of data available between 0 and 0.4 in $\cos\theta$ allows for better normalization of the absolute rate. This absolute rate is theoretically calculable to only about 20%, but with more data SNO will be able to find this normalization in a model-independent fashion by using these two downward-going bins. Approximately 2 years of live-time reduce the uncertainty to 10% (to 68% CL) using these two bins alone. This will allow model-dependent fits (in SNO and other experiments) much more limited values of the absolute flux, which may substantially improve their measurements.

Another measurement that will be made is that of the ratio of upward through-going muon rate to the rate of stopping upward, through-going muons. Such a measurement is difficult (due to the narrow width of the SNO detector, which catches fewer muon stops than larger detectors), but can in principle be made. Such a measurement allows for an estimation of the energies of the neutrinos interacting in the rock as well as the directions.

This work on preliminary data demonstrates that SNO is providing a previously unexplored measurement which is nicely complimentary to Super-K and other experiments. In addition, SNO is supplying a small but substantive set of data exploring angular distributions, which will contribute to the general understanding of high-energy neutrinos.

References

[1] **SNO** Collaboration, J. Boger *et al. Nucl. Instrum. Meth.* **A449** (2000) 172–207, `nucl-ex/9910016`.

[2] G. Ewan *et al.*, "Sudbury Neutrino Observatory Proposal," Tech. Rep. SNO-87-12, SNO Collaboration, 1987. (unpublished).

[3] G. Ewan *et al.*, "Scientfic and Technical Description of the Mark II SNO Detector," Tech. Rep. SNO-89-15, SNO Collaboration, 1989. (unpublished).

[4] A. S. Hamer, *Energy Calibration of SNO for Measurement fo the Charged-Current Neutrino Reaction.* PhD thesis, Queen's University, 1999.

[5] Welford and Winston, *The Optics of Non-Imaging Concentrators.* Academic Press, 1978.

[6] D. F. Cowen *et al. IEEE Trans. Nucl. Sci.* **42** (1995) 925.

[7] H. R. Adarkar *et al. Phys. Rev.* **D57** (1998) 2653–2664.

[8] H. Sobel *et al. Phys. Rev.* **C7** (1973) 1564.

[9] J. N. Bahcall, S. Basu, and M. H. Pinsonneault *Phys. Lett.* **B433** (1998) 1–8, `astro-ph/9805135`.

[10] J. N. Bahcall, M. H. Pinsonneault, and S. Basu `astro-ph/0010346`.

[11] Y. Suzuki *Nucl. Phys. Proc. Suppl.* **38** (1995) 54–59.

[12] **Super-Kamiokande** Collaboration, Y. Suzuki, "Solar Neutrino Results from Super-Kamiokande," in *Proceedings of the Neutrino 2000 Conference*. 2000.

[13] B. T. Cleveland *et al. Astrophys. J.* **496** (1998) 505.

[14] **GNO** Collaboration, E. Belloti, "Measurement of Low Energy Solar Neutrino Rate," in *Proceedings of the Neutrino 2000 Conference*. 2000.

[15] **SAGE** Collaboration, V. Gavrin, "Russian-American Gallium Experiment at the Baksan Neutrino Observatory," in *Proceedings of the Neutrino 2000 Conference*. 2000.

[16] J. Bachall. World Wide Web, `http://www.sns.ias.edu/~jnb/`. Updated version of figure shown in *Solar Neutrinos: Where We Are, Where We Are Going*, *Astrophys. J.* **467**, 475 (1996).

[17] J. Bachall, *Neutrino Astrophysics*. Cambridge University Press, April, 1989.

[18] L. Wolfenstein *Phys. Rev. D.* **17** (May, 1978) 2369–2374.

[19] S. P. Mikeheyev and A. Y. Smirnov *Nouvo Cimento* **C9** (1986), no. 17,.

[20] J. N. Bahcall, P. I. Krastev, and A. Y. Smirnov *Phys. Lett.* **B477** (2000) 401–409, `hep-ph/9911248`.

[21] N. Hata and P. Langacker *Phys. Rev.* **D56** (1997) 6107–6116, `hep-ph/9705339`.

[22] M. Gonzalez-Garcia and C. Peña-Garay, "Global and Unified Analysis of Solar Neutrino Data," in *Proceedings of the Neutrino 2000 Conference*. 2000.

[23] V. Barger, B. Kayser, J. Learned, T. Weiler, and K. Whisnant *Phys. Lett.* **B489** (2000) 345–352, `hep-ph/0008019`.

[24] C. Giunti, M. C. Gonzalez-Garcia, and C. Pena-Garay `hep-ph/0007154`.

[25] L. E. Marcucci *et al. Phys. Rev.* **C63** (2001) 015801, `nucl-th/0006005`.

[26] J. N. Bahcall, P. I. Krastev, and A. Y. Smirnov *Submitted to Phys. Rev. D* (2000) `hep-ph/0002293`.

[27] J. N. Bahcall and E. Lisi *Phys. Rev.* **D54** (1996) 5417–5433, `hep-ph/9607433`.

[28] G. Jonkmans, I. Towner, and B. Sur *Phys. Rev. C* **58** (1998), no. 2, 1278.

[29] V. S. Shirley, ed., *Table of Isotopes*. Wiley-Interscience, 8th edition ed., 1996.

[30] J. Bahcall, E.Lisi, D. Alburger, L. D. Braeckeleer, S. Freedman, and J. Napolitano *Phys. Rev.C* **54** (1996) 411.

[31] C. E. Ortiz, A. Garcia, R. A. Waltz, M. Bhattacharya, and A. K. Komives *Phys. Rev. Lett.* **85** (2000) 2909–2912, `nucl-ex/0003006`.

[32] R. J. Ford, *Calibration of SNO for the Detection of ^8B Neutrinos (SUDBURY NEUTRINO OBSERVATORY, LASERBALL SYSTEM)*. PhD thesis, Queen's University, Kingston, 1999.

[33] A. W. P. Poon *et al. Nucl. Instrum. Meth.* **A452** (2000) 115, `physics/9910011`.

[34] X. Chen, "An Improved Grid Fitter," Tech. Rep. SNO-00-004, Lawrence Berekely National Laboratory, April, 2000. (unpublished).

[35] S. Brice, "The Elastic Fitter," Tech. Rep. SNO-STR-95-040, Oxford University, 1995. (unpublished).

[36] T. Andersen *et al.*, "The SNOMAN User's Manual," 2000.

[37] S. Brice *et al.*, "Sacrifice and Contamination in SNO Data Cleaning Cuts," tech. rep., SNO Data Cleaning Group, November, 2000.

[38] B. Sur, E. Earle, R. Deal, and E. Gaudette, "^{8}Li: A β Calibration Source for SNO," Tech. Rep. SNO-STR-95-054, A.E.C.L. Chalk River Laboratories, Chalk River, 1995. (unpublished).

[39] B. Sur and E. Earle, "Gas Transport Calibration System for SNO: A Preliminary Design Document," Tech. Rep. SNO-STR-95-053, A.E.C.L. Chalk River Laboratories, Chalk River, 1995. (unpublished).

[40] B. Sur and E. Earle, "Safety Report for a Non-Medical Accelerator Facility at the Sudbury Neutrino Observatory," Tech. Rep. SNO-STR-95-031, A.E.C.L. Chalk River Laboratories, Chalk River Ontario K0J 1J0, 1995. (unpublished).

[41] R. B. Bird, W. E. Stewart, and E. N. Lightfoot, *Transport Phenomena*, pp. 51–54. John Wiley and Sons, 1960.

[42] A. Hamer, G. Jonkmans, B. Sur, N. Tagg, and R.Deal, "First Run of the SNO ^{8}Li Calibration System," Tech. Rep. SNO-STR-96-029, SNO, 1996. (unpublished).

[43] Y. Fung and E. E. Sechle, eds., *Thin-Shell Structure; Theory, Experiment and Design.* Prentice-Hall, Englewood Cliffs, N.J., 1974.

[44] A. S. of Mechanical Engineers, *ASME Section VIII: Boiler and Pressure Vessel Code.* ASME, 1992.

[45] K. MacFarlane. Private communication.

[46] The Americal Physical Society *Phys. Rev. D* **54** (1996), no. 1,. Particle Data Book.

[47] D. H. Wilkinson and D. R. Alburger *Phys. Rev. Lett.* **26** (1971) 1127.

[48] J. Birks, *The Theory and Practice of Scintillation Counting.* Oxford, Pergamon Press, 1964.

[49] G. F. Knoll, *Radiation Detection and Measurement.* John Wiley and Sons, New York, 2nd edition ed., 1989.

[50] W. Davidson, C. Dodd, and J. Zwinkels, "Light Transmittence in Acrylic." Sudbury Neutrino Observatory Annexes to Proposal SNO-87-12, December, 1987. (unpublished).

[51] A. Hamer. Private communication.

[52] M. Boulay, A. Hallin, and B. Moffat. Private communication.

[53] N. McCauley. Private communication.

[54] F. Duncan, "Comments on the PC Source Engineering Run Oct/Nov 2000," tech. rep., Queen's University, November, 2000. (unpublished).

[55] T. K. Gaisser, *Cosmic Rays and Particle Physics.* Cambridge University Press, 1990.

[56] T. Gaisser and T. Stanev *Phys. Rev* **D54** (July, 1996) 122–127. (1996 Review of Particle Physics).

[57] **LVD** Collaboration, M. Aglietta *et al. Phys. Rev.* **D60** (1999) 112001, `hep-ex/9906021`.

[58] M. Honda, T. Kajita, K. Kasahara, and S. Midorikawa *Phys. Rev.* **D52** (1995) 4985–5005, `hep-ph/9503439`.

[59] P. Lipari, "Review of Sources of Atmospheric Neutrinos," in *Proceedings of the Neutrino 2000 Conference.* 2000.

[60] G. Battistoni *et al. Nucl. Phys. Proc. Suppl.* **70** (1999) 358–360.

[61] Y. Tserkovnyak, R. Komar, C. Nally, and C. Waltham `hep-ph/9907450`.

[62] P. Lipari *Astropart. Phys.* **14** (2000) 153, `hep-ph/0002282`.

[63] Y. Totsuka *Nucl. Phys.* **A663** (2000) 218–230.

[64] **Super-Kamiokande** Collaboration, M. Nakahata *Nucl. Phys. Proc. Suppl.* **87** (2000) 125.

[65] **Super-Kamiokande** Collaboration, H. Sobel, "Atmospheric Neutrinos in Super-Kamiokande," in *Proceedings of the Neutrino 2000 Conference*. 2000.

[66] **MACRO** Collaboration, B. Barish, "Atmospheric Neutrinos in MACRO ?? DBL CHECK ??," in *Proceedings of the Neutrino 2000 Conference*. 2000.

[67] **Soudan** Collaboration, A. Mann, "New Results on Atmospheric Neutrinos from Soudan 2," in *Proceedings of the Neutrino 2000 Conference*. 2000.

[68] M. Apollonio *et al. Phys. Lett.* **B466** (1999) 415–430, `hep-ex/9907037`.

[69] **Palo Verde** Collaboration, G. Gratta, "Results from the Palo Verde Reactor Oscillation Experiment," in *Proceedings of the Neutrino 2000 Conference*. 2000.

[70] **Super-Kamiokande** Collaboration, S. Fukuda *et al.* `hep-ex/0009001`.

[71] **LSND** Collaboration, E. D. Church *Nucl. Phys.* **A663** (2000) 799–802.

[72] **LSND** Collaboration, G. Mills, "Final 1993-1998 LSND Results," in *Proceedings of the Neutrino 2000 Conference*. 2000.

[73] P. Harvey, *X-Windows SNO Event Display (XSNOED) User Guide*. Queen's University, August, 2000. Version 4.2.6. (unpublished).

[74] S. Hatekyama, *Search for Muon Neutrino Oscillations in Kamiokande and Super-Kamiokande*. PhD thesis, Tohoku Universty, 1988.

[75] N. Tagg, "Data Cleaning: The Muon Tag," tech. rep., University of Guelph, Nov, 1999. (unpublished).

[76] W. Lohmann, R. Kopp, and R. Voss. CERN-85-03.

[77] M. Cherry *et al.* in *Workshop on Very High Energy Cosmic Ray Interactions, Philadelphia*, p. 359. 1982. as described in [115].

[78] M. Boulay, "Data Selection." World Wide Web, `http://owl.phy.queensu.ca/~mgb/private/data_selection/`, 2000. (unpublished).

[79] P. Lipari and T. Stanev *Phys. Rev. D* **44** (1991), no. 11, 3543.

[80] N. McCauley, "Data Cleaning: The Neck Cut," tech. rep., Oxford University, 2000. (unpublished).

[81] R. V. de Water, "Data Cleaning: The Q/NHIT Cut," tech. rep., University of Pennsylvania, April, 2000. (unpublished).

[82] N. McCauley, "An estimate of contamination of neck events in neutrino data," tech. rep., Oxford University, October, 2000. (unpublished).

[83] A. Hamian. Private communication.

[84] W. H. Press, S. A. Teukolsky, W. T. Vetterling, and B. P. Flannery, *Numerical Recipies in Fortran 77*, ch. 15.5. Cambridge University Press, second edition ed., 1992.

[85] T. Gaisser and T. Stanev *Phys. Rev.* **D30** (September, 1984) 985–990.

[86] S. Bussino, C. Chiera, E. Lamanna, H. Bilokon, and L. Miller. LNGS-94-92.

[87] P. Antonioli, C. Ghetti, E. V. Korolkova, V. A. Kudryavtsev, and G. Sartorelli *Astropart. Phys.* **7** (1997) 357, `hep-ph/9705408`.

[88] V. Kudryavtsev. Private communication with SNO muon group, 2000.

[89] E. Earle *et al.*, "SNO: Collection of Annexes in Support of the Main Proposal." (unpublished), November, 1987.

[90] S. Maloney and P. K. Kaiser, "Determination of the Rock Strenth and its Stress-Path-Dependancy at the SOLAR NEUTRINO OBSERVATORY," tech. rep., Geomechanics Research Center, Laurentian University, F217, Science II Bldg, Ramsey Lake Road, Sudbury, Ontario, June, 1988.

[91] W. H. Press, S. A. Teukolsky, W. T. Vetterling, and B. P. Flannery, *Numerical Recipies in Fortran 77.* Cambridge University Press, second edition ed., 1992.

[92] C. Forti *et al.* *Phys. Rev.* **D42** (1990) 3668.

[93] **MACRO** Collaboration, M. Ambrosio *et al. Phys. Rev.* **D56** (1997) 1418–1436.

[94] **Fréjus** Collaboration, C. Berger *et al. Phys. Rev.* **D40** (1989) 2163.

[95] **LVD** Collaboration, M. Aglietta *et al. Phys. Rev.* **D58** (1998) 092005, `hep-ex/9806001`.

[96] V. Agrawal, T. K. Gaisser, P. Lipari, and T. Stanev *Phys. Rev.* **D53** (1996) 1314–1323, `hep-ph/9509423`.

[97] F. Stacey, *Physics of the Earth.* Brookfield, Brisbane, Australia, 1992.

[98] **SuperKamiokande** Collaboration, Y. Fukuda *et al. Phys. Rev. Lett.* **82** (1999) 2644–2648, `hep-ex/9812014`.

[99] "MINUIT, Function Minimization and Error Analysis Reference Manual." CERN Program Library Long Writup D506, March, 1992. (unpublished).

[100] R. Brun *et al.*, "ROOT Users Guide v.0.6.2." World Wide Web, `http://root.cern.ch/`, November, 2000. (unpublished).

[101] L. B. Lucy *Mon. Not. R. Astron. Soc.* **318** (Oct., 2000) 92–100.

[102] G. J. Feldman and R. D. Cousins *Phys. Rev.* **D57** (1998) 3873–3889, `physics/9711021`.

[103] N. Tagg, "^{8}Li Decay Chamber Design," Tech. Rep. SNO-STR-99-024, University of Guelph, November, 1999. (unpublished).

[104] A. Hamer and B. Sur, "Gas Flow Calculations for the SNO ^{8}Li Calibration Source," tech. rep., SNO, June, 2000.

[105] R. Becker-Szendy *et al. Nucl. Phys. Proc. Suppl.* **38** (1995) 331–336.

[106] K. McFarlane, "^{8}Li Stainless Steel Spherical Shell Source Preliminary Design and Fabrication Report," tech. rep., Sudbury Neutrino Observatory, December, 2000. (unpublished).

[107] T. Andersen *et al.*, "The SNOMAN Programmer's Manual," 2000.

[108] N. Tagg, "^{8}Li Decay Chamber Design," Tech. Rep. SNO-STR-99-024, University of Guelph, November, 1999. (unpublished).

[109] J. F. O'Hanlon, *A User's Guide to Vacuum Technology.* John Wiley and Sons, 1980.

[110] M. Neubauer, "Data Cleaning: The In-Time Channel Cut," tech. rep., U. of Pennsylvania, March, 2000. (unpublished).

[111] J. Klein and V. Rusu, "Data Cleaning: The QCluster Cut," tech. rep., U. of Pennsylvania, March, 2000. (unpublished).

[112] **MACRO** Collaboration, M. Ambrosio *et al. (CERN Desy Library)* (1997). INFN-AE-97-28.

[113] **MACRO** Collaboration, M. Ambrosio *et al. Phys. Rev.* **D 52** (October, 1995) 3793.

[114] **Kamiokande** Collaboration, K. Munakata *et al. Phys. Rev.* **D56** (1997) 23–26.

[115] P. Sokolsky, *Introduction to Ultrahigh Energy Cosmic Rays*, vol. 76 of *Frontiers in Physics.* Addison-Wesley, 1989.